Predicting future urban drought under climate change

Changsen Zhao

UNIVERSITÉ DE STRASBOURG

ÉCOLE DOCTORALE MSII (ED n°269)

Laboratoire des sciences de l'ingénieur, de l'informatique et de l'imagerie (ICUBE) - UMR 7357

THÈSE

présentée par :

Changsen ZHAO

soutenue le : 22 Décembre 2021

pour obtenir le grade de : **Docteur de l'Université de Strasbourg**

Discipline : Sciences de l'imagerie

Spécialité : Télédétection

Prédire les sécheresses urbaines dans le contexte du changement climatique

THÈSE dirigée par :

Mme F. NERRY	Directeur de Recherches, CNRS, France
M. Z-L. LI	Directeur de Recherches, CNRS, France

RAPPORTEURS :

M. J. SOBRINO	Professeur, Université de Valence, Espagne
M. H. WU	Directeur de Recherches, CAS, Chine

AUTRES MEMBRES DU JURY :

M. H. Yesou	Ingénieur de Recherches, UdS, France
M. G. YAN	Professeur, BNU, Chine

Acknowledgments

I want to express my thanks to all who have given me a lot of help during my Ph.D period. There are so many great people to whom I really want to thank in my heart.

My supervisor Nerry Françoise teaches students in accordance with their aptitude. To enlarge my research scope, she kindly invited Dr. Herve Yesou to guide my thesis together with her. She always tried her best to help me from the participation of summer schools to discussion on my research topic and encourage me with endless patience. It always warmed my heart to discuss with her every time. The thankfulness for her is written both in paper and in my mind.

I really must express my gratitude to my co-supervisor Li Zhao-Liang who helped me a lot both with study and life. Though he has very high academic achievement, he is always kind to every student. I remember when I was just arrived in France, when I was still having problems communicating with the local people, Professor Li and his wife Mrs. Zhao helped me solved a lot of problems. Dr. Li gave me the greatest patience on my study, using all he has to help me finish my research. I am so very glad for being under the supervision of Dr. Li. I herein express my most sincere respect and gratitude to him.

I cordially thank Dr. Herve Yesou whom I gained a lot of help from including not only the code processing GRACE data but also papers related to my thesis. What expressed me the most deeply is his detail comments on my manuscript, so carefully and so detail. Every time I learned a lot from his comments. Without his help, I can say I can not graduate successfully. I thank him for his patience and time in helping me, which took him a lot of time. I really need to give my great respect and thankfulness to him.

Many thanks to Professor José A. Sobrino, Guangjian Yan, Bo-Hui Tang, Hua Wu and Ronglin Tang for their helpful advice on my thesis. Also, I present my thankfulness to my friends, Dr. Ronghai Hu, Wenping Yu, Xiaopo Zheng, Xinyu Lan, Xiangyang Liu, Yazhen Jiang, Menglin Si. Thank you all for happy studying time spending together in Strasbourg.

I will remember all the help from all of you. I hope all of you can live happy and healthy forevere.

Contents

Figure List

Table List

Résumé

La sécheresse urbaine menace le bien-être des êtres humains et la durabilité du développement socio-économique des villes. Elle peut être estimée en fonction de la quantité d'eau douce disponible et de la consommation d'eau dans une ville. Pour réduire les risques induits par la sécheresse urbaine, il est urgent d'étudier les risques futurs de sécheresse urbaine. La plupart des recherches antérieures prennent habituellement la précipitation, l'humidité du sol, l'évapotranspiration et d'autres paramètres comme base pour calculer la sécheresse urbaine. Cependant moins d'intérêt est mis sur le flux d'eau - particulièrement dans les villes par manque de données. Pour la plupart des villes, le débit des cours d'eau et les eaux souterraines constituent la ressource en eau douce disponible. Mais dans les villes qui manquent de données, l'absence de longues séries de surveillance sur le débit et les eaux souterraines empêche de prédire avec précision la ressource en eau douce disponible dans le futur. Par conséquent, il est urgent de produire de longues séries de données sur cette ressource avant de prédire la sécheresse urbaine future. Cette thèse est consacrée au développement d'un cadre pour la prédiction de la sécheresse urbaine (consommation d'eau / eau douce disponible) pour les années 2030 et 2050 pour soutenir la politique de contrôle de la sécheresse dans les zones de manque de données. Cela comprend l'extension des séries de débits dans les zones de manque de données et la production de longues séries de données d'eau souterraine disponible liées au calcul de l'eau douce disponible afin de prédire la sécheresse en 2030 et 2050. L'étude a été menée dans le Bassin du Fleuve Jaune, en Chine, avec une superficie de 752,443 km^2, en prenant comme exemples les grandes villes avec une population supérieure à 5 millions d'habitants -- Jinan, Zhengzhou, et Xi'an.

L'organisation de cette thèse est la suivante. Le chapitre 1 présente le contexte de la recherche et l'état de l'art ainsi que la motivation du travail. Le chapitre 2 présente les données utilisées et les caractéristiques de la zone d'étude. Le chapitre 3 explore de nouvelles façons d'extraire le débit des cours d'eau dans les zones où les mesures in situ sont rares afin d'aider à calculer plus précisément la ressource en eau douce disponible dans les zones urbaines lors de l'évaluation de la sécheresse. Le chapitre 4 conçoit un nouveau cadre pour l'estimation de la ressource en eau souterraine disponible dans lequel la série de données de GRACE a été étendue des deux dernières décennies à plus de sept décennies depuis 1948. Le Chapitre 5 présente le calcul de la consommation d'eau des trois secteurs d'usage domestique, de l'industrie et des écosystèmes naturels et agricoles pour refléter la situation de la consommation d'eau en évaluant la sécheresse. Le Chapitre 6 prédit la sécheresse urbaine future en 2030 et 2050, y compris la prédiction de l'eau douce disponible et la consommation d'eau, basée sur les modèles établis dans les Chapitres 3-5 et les données présentées dans les scénarios CMIP5 IPCC ainsi que les littératures publiées. Le chapitre 7 conclut les résultats de la recherche et suggère des sujets connexes qui méritent une recherche continue.

Le **chapitre 1** donne une brève introduction sur le contexte et les objectifs de cette thèse. Avec le changement climatique, l'étendue, la sévérité et la fréquence des sécheresses dans le monde devraient augmenter. Les villes sont particulièrement vulnérables aux risques climatiques en raison de leur agglomération de personnes, de bâtiments et d'infrastructures. La

gravité de la sécheresse est généralement fortement liée à l'efficacité de la conservation de l'eau, en particulier dans les zones urbaines, et la conservation varie selon la région hydrologique, ou la variation du débit des cours d'eau. Cependant, l'évaluation de la sécheresse dans les zones où les données sont rares néglige souvent l'écoulement fluvial, ce qui induit de grandes incertitudes dans les résultats. Beaucoup de chercheurs ont consacré des d'efforts importants à l'inversion de la surface de l'eau ou à l'estimation du stockage de l'eau basale en utilisant des données multi-satellites, mais l'estimation du débit à partir d'observables "géométriques" de la surface d'écoulement reste un problème inverse difficile, en particulier dans le cas d'une mauvaise connaissance de la bathymétrie et de la friction de la rivière. Certains chercheurs ont essayé d'inverser le débit des rivières de grande largeur (i.e., plus de 100 mètres) et ont obtenu des résultats satisfaisants, mais la précision est faible lorsqu'elle est appliquée à des affluents plus étroits (ie moins de 40 mètres), ce qui induit de grandes incertitudes dans l'estimation de l'eau totale disponible dans une zone. Cela entrave grandement l'estimation précise de l'eau douce disponible et la prévision de la gravité des sécheresses futures. Le débit des cours d'eau, l'eau du sol et les eaux souterraines constituent la plupart des proportions d'eau douce disponible. Le débit des cours d'eau peut être récupéré en utilisant des images satellites et les deux derniers indicateurs peuvent être estimés en utilisant GRACE (Gravity Recovery and Climate Experiment de la NASA, série courte mais précise) combiné avec des données GLDAS (Global Land Data Assimilation System, série longue mais moins précise) visant à obtenir les champs optimaux d'états et de flux de la surface terrestre à partir de données satellites, de données in situ et de modélisation. Par conséquent, il est nécessaire et urgent de produire des séries de données longues sur la ressource en eau douce disponible (FWA) basées sur les sources de données ci-dessus afin de prédire la sécheresse urbaine future dans le cadre du changement climatique.

Le **chapitre 2** décrit les données et la zone d'étude, notamment la collecte des données (données satellitaires d'imagerie satellitaire Landsat TM, Sentinel et MODIS (spectroradiomètre imageur à résolution modérée) ; des produits géophysiques GRACE ; des données d'imagerie UAV (véhicule aérien sans pilote), des données d'états de sols issues de GLDAS, et des données hydrologiques au sol et des données statistiques locales sur le PIB (produit intérieur brut). Enfin ce chapitre présente les caractéristiques de la zone d'étude (utilisation des terres et végétation, rivières, eaux souterraines, population, économie et société). Les données GRACE et GLDAS ont été utilisées pour l'estimation des eaux souterraines ; les données Landsat TM, les données UAV ainsi que les données hydrologiques ont été collectées pour l'extraction et la vérification du débit des cours d'eau ; les données MODIS ont été utilisées pour calculer l'évapotranspiration des plantes dans la consommation d'eau et les données PIB ont été collectées pour calculer la consommation d'eau des ménages et des industries.

Les données GRACE TWSC (Terrestrial Water Storage Change) sont fournies par 11 instituts, dont le CSR (Center for Space Research, États-Unis), le GFZ (Geo Forschungs Zentrum, Allemagne), le JPL (Jet Propulsion Laboratory, Japon) et le GRGS (Groupe de Recherche de Géodésie Spatiale, France). L'analyse d'incertitude sur ces solutions montre que la solution CSR a l'incertitude minimale en Chine avec une erreur de 13,2 mm alors que celle du GRGS a l'incertitude maximale avec une erreur de 58,8 mm. Par conséquent, pour mener à bien cette étude, les solutions CSR ont été choisies comme source des données GRACE. La

nouvelle version de la solution CSR exprime l'anomalie de stockage de l'eau avec la hauteur équivalente de la colonne d'eau à une résolution spatiale de 0,25°× 0,25°, couvrant la période de 2002 à 2016. Des images Landsat TM, correspondant aux périodes de mesure in situ de 2007 à 2009, ont été utilisées. Parmi les sept bandes des images, la bande 4 (0,76-0,96 μm) avec une haute résolution spatiale (30 m) a été utilisée dans cette étude pour l'estimation de la vélocité, sur la base de laquelle le débit des cours d'eau en saison humide a ensuite été obtenu. Sentinel-1, une constellation de deux satellites en orbite polaire pour la continuité et l'amélioration des services opérationnels et des applications SAR, peut fournir une capacité d'observation de routine, jour et nuit, par tous les temps. Les données radar de Sentinel-1 peuvent répondre principalement à des applications de moyenne à haute résolution grâce à un mode de fonctionnement principal qui présente à la fois une large fauchée (250 km) et une haute résolution géométrique (5 m × 20 m) réechantillonée à un pixel spacing de 10m. Lonnées SAR Sentinel-1 ont été utilisées pour améliorer la précision de la surveillance de la largeur des cours d'eau dans cette étude et cela afin de permettre une meilleure estimation des débits des cours d'eau, les. Afin de réduire au maximum les incertitudes de la modélisation de l'évapotranspiration (ET) du GLDAS l'ET dérivée des données satellitaires MODIS a été utilisée pour l'ajustement sur les trois villes représentatives (Xi'an, Zhengzhou et Ji'nan), . L'ET ajustée a ensuite été exploité afin de'évaluer la consommation d'eau des écosystèmes dans les trois villes. Outre l'ET, le GLDAS peut également fournir des données globales sur l'humidité du sol (10, 30, 60 et 100 cm, à partir de la surface du sol), l'équivalent en eau de la neige, le stockage de l'eau dans la canopée, le ruissellement, etc. Nous avons recueilli les données mensuelles à des résolutions spatiales de 0,25°× 0,25°, de 1948 à 2016 et les avons utilisées pour étendre les séries de l'ET, du ruissellement ainsi que de GRACE TWSC dans les chapitres 3-6.

Le **chapitre 3** présente deux nouvelles méthodes pour l'estimation du débit dans les zones où les données sont rares afin de produire de longues séries de données sur la ressource en eau douce disponible (FWA). Deux nouvelles méthodes respectivement pour les saisons sèches et humides ont été développées dans un premier temps ; puis en utilisant les deux méthodes, les flux d'écoulement à long terme par les trois grandes villes ont été récupérés en utilisant des images de satellite ; finalement, basé sur le flux d'écoulement à long terme récupéré par satellite, la ressource en eau douce de surface disponible pour les trois villes représentatives a été estimée. Cette ressource estimée a pu être utilisée ensuite pour prévoir l'eau douce de surface disponible dans le futur 2030 et 2050. Parmi les deux méthodes, la première a été nommée VHR-AMHG (Virtual Hydraulic Radius at-many-stations hydraulic geometry) pour les saisons sèches, et la seconde a été nommée transcaled spatial C/M method pour les saisons humides. La première utilise uniquement la largeur de la surface en eau libre d'une rivière, tandis que la seconde se base sur la réflectance du sol du lit majeur et de l'eau pour estimer le débit de la rivière.

La méthode VHR-AMHG est utilisée pour estimer le débit des cours d'eau de taille moyenne à petite avec peu de mesures au sol en utilisant l'imagerie haute résolution de drones (UAV). Dans le cadre de VHR-AMHG, une nouvelle méthode de rayon hydraulique virtuel (VHR) a été proposée pour compléter la méthode AMHG (at-many-stations hydraulic geometry) ne nécessitant aucune mesure au sol lorsque des paramètres globaux sont utilisés (global-AMHG) dans les rivières à grande échelle, mais conduisant à de grandes incertitudes dans les

rivières à plus petite échelle. La VHR utilise un drone pour déterminer la topographie au-dessus de la surface de l'eau pendant les saisons sèches et calcule la valeur du rayon hydraulique, le périmètre mouillé et la zone d'écoulement dans l'équation de Manning en supposant que la largeur réelle de la surface de l'eau récupérée à partir des images du drone est le fond de la rivière, formant une section transversale virtuelle incomplète. Ainsi, le débit virtuel correspondant à la section transversale virtuelle, et non le débit réel, est alors calculé sur la base de l'équation de Manning. Notre analyse a montré qu'il existe une relation linéaire entre le débit virtuel et le débit réel. Ce dernier fait référence au débit calculé sur la base d'une section transversale réelle plutôt que virtuelle. Sur la base de cette relation linéaire, le débit réel à n'importe quel niveau d'eau peut être facilement calculé et peut ensuite être utilisé pour calibrer les paramètres dans AMHG, améliorant ainsi la précision du débit estimé par AMHG.

La vérification de la précision de la méthode VHR-AMHG a été effectuée en comparant les sorties de modèle aux données de mesure in situ et aux paramètres globaux de la méthode AMHG originale (global-AMHG). L'erreur quadratique moyenne (RMSE) calculée à partir de la méthode VHR-AMHG est inférieure de 32,15 m^3/s à la RMSE de la méthode originale (global-AMHG), qui était de 305,65 m^3/s, ce qui indique que la méthode VHR-AHRG offre une précision nettement supérieure pour l'estimation du débit des rivières de taille moyenne à petite.

Les résultats impliquent que la méthode VHR-AMHG proposée élargit le champ d'application de l'AMHG aux rivières de toutes tailles. La méthode VHR proposée dans cette étude fournit une méthode alternative de paramétrage pour les zones où les observations historiques de débit sont rares et améliore la précision du débit calculé par AMHG dans ces zones, en particulier pendant les saisons sèches. Lorsque les saisons humides arrivent, le débit peut être obtenu en utilisant la deuxième méthode, la méthode transcaled spatial C/M qui a été développée principalement pour l'estimation de la vitesse d'écoulement. La méthode Riba-zéro, a été développée et appliquée pour estimer la bathymétrie des rivières non jaugées afin de calculer la surface d'écoulement. En multipliant la surface d'écoulement par la vitesse d'écoulement, on obtient le débit. En d'autres termes, la méthode transcaled spatial C/M couplée à la méthode Riba-zero permet d'obtenir le débit des rivières non jaugées. La méthode transcaled spatial C/M surmonte les défauts de la méthode C/M originale de Tarpanelli et al (2013) (méthode originale nécessitant des données de plusieurs stations et négligeant l'hétérogénéité spatiale des rivières). Le principe de la méthode C/M est que l'augmentation de la surface de l'eau dans une zone donnée entraîne généralement une diminution de la valeur de réflectance NIR (proche infrarouge) de la zone et, par conséquent, le rapport (C/M) entre la réflectance de surface d'un pixel terrestre, nommé C (calibrage), et d'un pixel d'eau, nommé M (mesure), change en conséquence. Pour pallier les insuffisances de la méthode C/M originale, la plus grande surface de plan d'eau dans les images satellite dans une zone de 1 km * 1 km est utilisée comme limite, ou limite maximale de la rivière (MRB), sur la base de laquelle nous extrayons le proche infrarouge de tous les pixels de la zone. La valeur moyenne de la bande est prise comme M, et sa valeur change avec la zone inondée de la rivière. Toutes les zones urbaines sur l'image sont extraites, et la valeur moyenne des bandes du proche infrarouge dans les zones urbaines sur différentes images est comptée comme C. Pour surmonter l'inconvénient d'exiger des données de plusieurs stations, cette étude a développé de nouvelles méthodes pour n’utiliser

qu'une seule station hydrologique pour établir une relation régionale C/M~V à des stations non jaugées. Pour atteindre cet objectif, cette étude a d'abord utilisé des images Landsat TM et des données de vitesse d'écoulement mesurées à une seule la station hydrologique pendant la saison humide pour établir une relation régionale entre le pixel (C) et le pixel d'eau (M) avec la vitesse d'écoulement ; ensuite, pour surmonter le défaut de négliger l'hétérogénéité spatiale des rivières, nous avons établi la relation linéaire entre la valeur M d'une station non jaugée et d'une station de référence pour réduire l'influence de l'hétérogénéité spectrale sur les résultats. Grâce à ces étapes, la vitesse d'écoulement à une station non jaugée peut être calculée. La méthode C/M améliorée résout le problème des grandes différences spatiales dans la réflectance qui existait dans la méthode C/M originale, ce qui améliore l'applicabilité de la méthode C/M originale. En plus de la vitesse d'écoulement, la surface d'écoulement est une variable essentielle pour le calcul du débit. Comme les satellites ou les drones ne sont capables de surveiller qu'une section transversale au-dessus de la surface de l'eau, nous devons simuler la section transversale sous-marine par une méthode mathématique. Une section transversale peut être exprimée sous la forme d'une fonction de puissance dont la valeur est généralement inférieure à 2. Sur la base de ces principes, nous avons présenté la méthode Riba-zéro de modélisation de la section transversale sous-marine en prenant comme base la section transversale au-dessus de l'eau mesurée par drone, avec laquelle la surface d'écoulement de la section transversale peut être facilement calculée. Par la suite, le débit des rivières non jaugées peut être récupéré en couplant la méthode transcaled spatial C/M avec la méthode Riba-zéro. La vérification montre que l'erreur quadratique moyenne relative (rRMSE) et l'erreur relative (RE) de la vitesse simulée en utilisant la méthode transcaled spatial C/M dans notre zone d'étude est rRMSE : 0,36 (RE : 19,00%) pour l'année entière, 0,15 (14,56%) dans les saisons humides et 0,25 (20,88%) dans les saisons sèches, ce qui suggère que la performance de la méthode transcaled spatial C/M a une plus grande précision pour les saisons humides. En utilisant les deux méthodes couplées avec l'ensemble de données de ruissellement GLDAS de la NASA, le débit des cours d'eau à long terme (1948-2018) a été estimé en utilisant des images satellites pour les trois grandes villes représentatives (Xi'an, Zhengzhou et Ji'nan). Xi'an et Zhengzhou ont presque la même valeur moyenne de débit (~1000 m^3/s) de 1948 à 2018, et Jinan a une valeur moyenne de débit plus faible (~600 m^3/s). Sur la base du débit à long terme (1948-2018) et des données officielles du "Bulletin des ressources en eau" des trois villes, la quantité totale d'eau douce de surface disponible (SFWA) entre 2000 et 2017 pour les trois villes a été estimée, posant ainsi les bases de la prévision de la SFWA pour les années 2030 et 2050.

Suite aux résultats obtenus dans la production de séries longues de données SFWA au chapitre 3, un nouveau cadre pour estimer les séries longues d'eau douce souterraine disponible (UFWA) est développé dans le **chapitre 4**. Les longues séries de SFWA et d'UFWA sont constituées de longues séries de FWA (eau douce disponible). Parallèlement, la série de données de GRACE (ou TWSC : terrestrial water storage change) a été étendue des deux dernières décennies (2002-2016) à plus de sept décennies depuis 1948. Tout d'abord, les facteurs environnementaux entraînant la variation du TWSC ont été déterminés par des méthodes statistiques basées sur 11 facteurs potentiels sélectionnés dans la littérature. La méthode VIP (Very Important Projection) a été utilisée pour sélectionner les facteurs clés, VIP>1,0 signifiant une grande influence sur le TWSC. Pour sélectionner les facteurs clés optimisés, quatre scénarios avec trois périodes représentatives ont été établis. Pour le scénario 1, sept facteurs

clés ont été sélectionnés, dont la température de l'air, la fonte des glaciers, l'humidité du sol, le stockage de l'eau terrestre, l'évapotranspiration, les précipitations, la transpiration, qui varient selon les périodes ; dans le scénario 2, sept facteurs, dont la fonte des glaciers, la température de l'air, l'évaporation directe du sol nu, les précipitations, l'humidité du sol de 0 à 200 cm de profondeur, le ruissellement, les précipitations moins l'ET sont les plus importants ; quant au scénario 3, 10 facteurs, dont la transpiration, l'évapotranspiration, la température de l'air, l'humidité du sol dans la zone des racines, le stockage terrestre de l'eau, l'humidité du sol de 0 à 200 cm de profondeur, les précipitations, l'évaporation directe du sol nu, la fonte des glaciers, le ruissellement, sont d'une plus grande importance ; pour le scénario 4, les 11 facteurs environnementaux ont été sélectionnés. Ensuite, les facteurs sélectionnés ont été utilisés pour vérifier et améliorer un modèle de prédiction neuronal artificiel -LSTM-N (Long short-term memory network) dont les paramètres LSTM-N optimisés ont été déterminés. Pour la prédiction de GRACE TWSC, le paramètre optimisé "Unité" est 460, la fonction d'activation est la fonction "Sigmoïde", l'époque d'apprentissage est 650 pour le LSTM-N. En utilisant le LSTM-N avec les paramètres optimisés, la prédiction de performance des facteurs moteur sélectionnés dans les quatre scénarios a été testée. Les résultats montrent que le modèle LSTM-N basé sur le scénario 4 a le R2 le plus élevé (>0,8) dans tous les tronçons supérieurs, moyens et inférieurs de l'YRB ; toutes les valeurs de RMSE dans les tronçons supérieurs, moyens et inférieurs sont toutes inférieures à 5 cm. La comparaison de la valeur de prédiction avec l'observation GRACE montre que le modèle LSTM-N dans les zones du bief supérieur à la plus grande précision avec une RMSE inférieure à 0,1 cm, tandis que dans le bief moyen, il a une précision relativement plus faible avec une RMSE inférieure à 5,0 cm. Ces résultats indiquent que le modèle LSTM-N basé sur le scénario 4 donne des résultats satisfaisants dans l'ensemble de l'YRB, qui a ensuite été utilisé pour étendre les séries de données GRACE TWSC de 1948 à 2002 lorsque la surveillance GRACE est manquante. Sur la base de la longue série de données GRACE TWSC, les eaux douces souterraines disponibles (UFWA) dans les trois villes représentatives de 1948 à 2016 ont été produites. Parmi elles, Xi'an présente la moyenne la plus élevée de 1,92 milliard de m^3 et Zhengzhou la moyenne la plus basse de 0,46 milliard de m^3. Tous ces résultats serviront à la prédiction de l'UFWA souterrain pour les années 2030 et 2050 dans le chapitre 6.

Pour mieux prévoir la consommation d'eau future, le **chapitre 5** explore un ensemble de méthodes permettant de calculer la consommation d'eau des trois secteurs que sont le secteur domestique, l'industrie et les écosystèmes naturels et agricoles. La consommation d'eau domestique comprend celle des zones urbaines et des zones rurales. La consommation d'eau industrielle comprend la consommation d'eau dans les secteurs fabriquant des produits destinés au développement national et à la vie quotidienne. La consommation d'eau de l'écosystème comprend l'évapotranspiration des terres vertes urbaines, du sol nu et des terres cultivées. Pour évaluer la consommation d'eau des ménages, nous avons d'abord utilisé les données de la population mondiale de LandScan et ce afin egalement d'analyser le changement de population dans les trois villes représentatives. Des données de tatistiques locales ont été exploité afin de vérifier /qualifier ces données LandScan; puis nous avons utilisé la formule "Population*(consommation moyenne d'eau par personne)" pour estimer la consommation d'eau des ménages. Nous avons recherché la variable (utilisation de l'eau par personne) dans les livres de statistiques régionales des trois villes. Pour la consommation d'eau industrielle, nous

avons retenu la variable du PIB (produit intérieur brut) industriel à partir de statistiques régionales, puis nous avons utilisé la formule "PIB * (consommation d'eau par PIB)" pour estimer la consommation d'eau industrielle. Pour la consommation d'eau des écosystèmes, nous avons d'abord utilisé l'ET récupérée par MODIS pour rectifier l'ET modélisée par le GLDAS afin d'améliorer la précision de ce dernier ; ensuite, sur la base de l'ET GLDAS rectifiée (en mm), nous avons extrait l'ET dans les trois villes représentatives et calculé la consommation d'eau des écosystèmes (en milliards de m^3) en les multipliant respectivement par leur superficie. Les résultats montrent que pendant la même période avec les données de GRACE, la consommation d'eau domestiques dans les trois villes représentatives de Xi'an, Zhengzhou et Ji'nan a tendance à augmenter légèrement avec l'augmentation de la population. Elle est essentiellement affectée par la variation de la population. Xi'an a la plus forte consommation d'eau pour les ménages (0,35 milliard de m^3 en moyenne) et Ji'nan la plus faible (0,21 milliard de m^3 en moyenne). La consommation d'eau industrielle dans les trois villes fluctue autour de 1,60 milliard de m^3, sans tendance évidente à la hausse ou à la baisse. En moyenne, Zhengzhou a la consommation la plus élevée (1,73 milliard de m^3) tandis que Ji'nan a la plus faible (1,66 milliard de m^3). En ce qui concerne la consommation d'eau des écosystèmes, Xi'an et Ji'nan ont des valeurs similaires (moyenne : 7,13 et 7,11 milliards de m^3) tandis que Zhengzhou a la plus faible (moyenne : 5,05 milliards de m^3). La différence de superficie des trois villes (Xi'an, Ji'nan et Zhengzhou : 10752, 10244 et 7446 km2) a entraîné la différence de consommation d'eau des écosystèmes entre elles. En résumé, la consommation totale d'eau dans les trois villes a fluctué au cours de la période, Xi'an et Ji'nan ayant des processus similaires avec des valeurs moyennes de 9,17 et 8,99 milliards de m^3, tandis que Zhengzhou a la valeur la plus faible de 7,07 milliards de m^3. La consommation d'eau de l'écosystème domine la consommation d'eau totale avec des ratios de l'écosystème à la consommation d'eau totale allant de 71,45% à 79,06%. Tout ces calculs constituent une base solide pour l'analyse de la consommation d'eau dans les années 2030 et 2050 au chapitre 6.

Le **chapitre 6** vise à prédire la sécheresse urbaine future en 2030 et 2050, y compris la prédiction de l'eau douce disponible et de la consommation d'eau. Cela a été réalisé en mettant en place un ANN (Artificial Neural Network) avec l'eau douce de surface disponible (SFWA) estimée au chapitre 3 et l'eau douce souterraine disponible (UFWA) au chapitre 4, ainsi que les facteurs environnementaux influençant la variation de l'eau douce de surface, présentés dans les scénarios CMIP5 (Coupled Model Intercomparison Project Phase 5). Les facteurs environnementaux comprennent les précipitations, l'évapotranspiration, la température de l'air proche de la surface. Ensuite, à l'aide de l'ANN entraîné, nous avons utilisé les facteurs environnementaux en 2030 et 2050 présentés dans les scénarios CMIP5 du GIEC RCP 2.6, RCP 4.5 et RCP 8.5 pour prédire la SFWA et l'UFWA en 2030 et 2050. Par ailleurs, la consommation d'eau future pour les ménages, l'industrie et l'écosystème a été prédite sur la base des modèles établis au chapitre 5 et des données de base prédites présentées dans les publications. En ce qui concerne la future consommation d'eau des ménages, nous avons utilisé les projections démographiques de la Division de la population de l'ONU pour prévoir la population des trois villes en 2030 et 2050, en supposant que les trois villes ont le même taux de changement que la Chine ; puis nous avons estimé la "consommation d'eau par personne" en 2030 sur la base de la recherche de Guo et al. (2021) avec laquelle la consommation d'eau des ménages en 2030 est facile à estimer. Ensuite, nous avons estimé la consommation d'eau des ménages en 2050 sur la

base des recherches d'Ercin et Hoekstra (2012) en supposant que les trois villes ont le même taux de consommation d'eau des ménages que le reste de la Chine. En ce qui concerne la consommation d'eau industrielle, nous avons d'abord utilisé les projections du PIB de la Chine publiées par l'Organisation de coopération et de développement économiques (OCDE) pour estimer le PIB des trois villes en 2030 et 2050 ; puis nous avons estimé la " consommation d'eau par PIB " en 2030 et 2050 en nous basant sur les recherches de Meng et al. (2021) qui ont prévu la consommation d'eau annuelle dans 31 régions de la Chine avec un scénario d'augmentation future du PIB ; enfin, avec la formule " (PIB industriel) * (consommation d'eau par PIB) " présentée au chapitre 5, nous avons estimé la consommation d'eau industrielle en 2030 et 2050. En ce qui concerne la future consommation d'eau des écosystèmes, nous avons multiplié l'évaporation du sol et la transpiration de la végétation (ET, en mm) dans le cadre des trois scénarios CMIP5 du GIEC (RCP 2.6, RCP 4.5 et RCP 8.5) par la superficie des trois villes respectivement, ce qui nous a permis d'obtenir la consommation d'eau des écosystèmes (en milliards de m^3) pour les trois villes en 2030 et 2050. Avec la prédiction ci-dessus de l'eau douce disponible et la consommation d'eau en 2030 et 2050, nous avons estimé la sécheresse urbaine future dans les trois villes avec la formule "(consommation d'eau / eau disponible)". Les résultats montrent que comme et les facteurs environnementaux, présentés dans les scénarios CMIP5 (Coupled Model Intercomparison Project Phase 5), influençant la variation de l'eau douce de surface. Les scénarios CMIP5 du GIEC RCP 2.6, RCP 4.5 et RCP 8.5 ont été utilisés où les principaux facteurs environnementaux en 2030 et 2050 sont présentés. La consommation d'eau future, pour les ménages/industriels/écosystèmes, a été prédite sur la base des modèles établis au chapitre 5 et des données de base prédites présentées dans les ouvrages publiés. En ce qui concerne l'eau douce disponible, Xi'an, Zhengzhou et Ji'nan disposeront de 2,01-2,04, ~1,95 et 2,36-2,43 milliards de m^3 d'eau douce pour la consommation en 2030, et de 2,05-2,14, 1,95-1,96 et 2,33-2,43 milliards de m^3 en 2050. En détail, il y aura jusqu'à 1,14, 0,91 et 2,03 milliards de m^3 d'eau douce de surface, et 0,87-0,90, 1,04-1,06 et 0,33-0,40 milliards de m^3 d'eau douce souterraine pour la consommation en 2030, et 0,91-1,00, 1,04-1,05 et 0,30-0,40 milliards de m^3 en 2050 dans les trois villes. En ce qui concerne les eaux souterraines (évaluées à l'aide du LWE), Ji'nan présente le taux de diminution le plus élevé. Les trois PCR ont prédit un taux de diminution similaire de la LWE (~0,8 cm en moyenne). En ce qui concerne la consommation d'eau future en 2030 et 2050, la quantité totale d'eau consommée par les ménages, l'industrie et les écosystèmes à Xi'an, Zhengzhou et Ji'nan en 2030 sera de 17,23, 14,31, 14,06 milliards de m^3 en moyenne, et en 2050 de 16,84, 14,35, 13,62 milliards de m^3 en moyenne. La consommation d'eau des écosystèmes (EWC) domine la consommation totale d'eau (81-90% en 2030 et 75-91% en 2050). Dans le cadre des scénarios du GIEC CMIP5 RCP 2.6, RCP 4.5 et RCP 8.5, l'écosystème de la plupart des trois villes consommera plus d'eau en 2030 qu'en 2050 dans les trois villes représentatives. En 2030, l'écosystème consommera une quantité d'eau allant de 14,78-15,45, 10,91-12,72 et 12,15-13,21 milliards de m^3 respectivement à Xi'an, Zhengzhou et Ji'nan, alors qu'en 2050, l'écosystème consommera 14,05-15,19, 10,47-11,08 et 12,09-12,59 milliards de m^3 respectivement. La consommation future d'eau des ménages sous le RCP 2.6 est la plus élevée (15,32, 11,90 et 12,90 milliards de m^3 pour Xi'an, Zhengzhou et Ji'nan) alors que celle sous le RCP 8.5 est la plus faible (14,52, 10,98 et 12,18 milliards de m^3). Les ratios de la consommation d'eau des ménages par rapport au total sont les plus faibles, soit 1,0-3,0 % en 2030 et 1,0-2,0 % en 2050. L'ampleur du rapport

entre la consommation d'eau et l'eau douce disponible suggère le degré de sécheresse urbaine. En 2030 et 2050, la sécheresse urbaine est la plus sévère à Xi'an (avec un rapport supérieur à 8,0 en moyenne) et moins sévère à Ji'nan (moins de 6,0 en moyenne). La gravité de la sécheresse urbaine en 2030 est un peu plus élevée qu'en 2050. L'adaptation de l'évapotranspiration réelle de l'écosystème comme consommation d'eau de l'écosystème augmente le rapport jusqu'à environ 6 fois celui qui ne tient pas compte de l'évapotranspiration de l'écosystème. En d'autres termes, si l'évapotranspiration de l'écosystème n'est pas prise en compte dans l'estimation de la consommation totale d'eau, le rapport de la sécheresse urbaine en 2030 et 2050 sera de ~1,2, ce qui peut être facilement résolu en combinant les techniques d'économie d'eau et le détournement de l'eau des zones abondantes en eau comme le fleuve Yangtze.

Le **chapitre 7** résume les conclusions et les perspectives. Dans cette thèse, nous avons tout d'abord conçu deux nouvelles méthodes pour l'estimation du débit des cours d'eau dans les zones où les données sont rares afin de produire des séries longues de données sur l'eau douce de surface disponible (SFWA). Puis nous avons conçu un nouveau cadre pour l'estimation des séries longues d'eau douce souterraine disponible afin de produire des séries longues d'eau douce souterraine disponible (UFWA) et nous avons exploré un ensemble de méthodes pour calculer la consommation d'eau des trois secteurs des ménages, de l'industrie et de l'écosystème, et enfin nous avons prédit l'évolution de la sécheresse urbaine future des trois villes chinoises représentatives en 2030 et 2050. On peut conclure que la précision de l'estimation de la SFWA a été grandement améliorée en couplant le VHR-AMHG nouvellement développé et la méthode transcaled spatial C/M ; le premier a une plus grande précision en saison sèche tandis que le second a une plus grande précision en saison des crues. L'UFWA peut être estimée à l'aide de la TWSC surveillée par GRACE après avoir trouvé les facteurs de variation de la TWSC. En utilisant une méthode d'interpolation et de prédiction des valeurs TWSC dans les zones et les périodes où les données sont rares, les données GRACE ont été étendues de 2002-2016 à 1948-2016. Cela facilite grandement les études sur la gestion durable des ressources en eau, et peut également fournir un soutien scientifique à l'élaboration des politiques lors de la résolution des problèmes liés au changement climatique. Il ressort de ce travail que la sévérité de la sécheresse en 2030 pour les trois villes sera un peu plus élevée qu'en 2050 et, par conséquent, des techniques d'économie d'eau sont nécessaires de toute urgence à l'avenir. Pour les travaux futurs, davantage de facteurs environnementaux et d'images satellites à plus haute résolution spatiale, telle que Sentinel2, devraient être introduits afin d'améliorer la précision des estimations ; une analyse approfondie des simulations climatiques du CMIP5 devrait être menée afin de réduire les incertitudes des résultats actuels.

Chapter 1 Introduction

1.1 Background

In the history of the earth, though sometime strom occurs, drought threats the welfare of human beings and the sustainability of the socio-economic development of cities, especially with the severity of climate change. Urban drought can be estimated based on the quantity of available freshwater and of water consumption in a city. To sustain the welfare of human, risks induced by urban drought need to be reduced. Therefore, under climate change future risk of available freshwater and water consumption in urban areas is urgently necessitated to be studied.

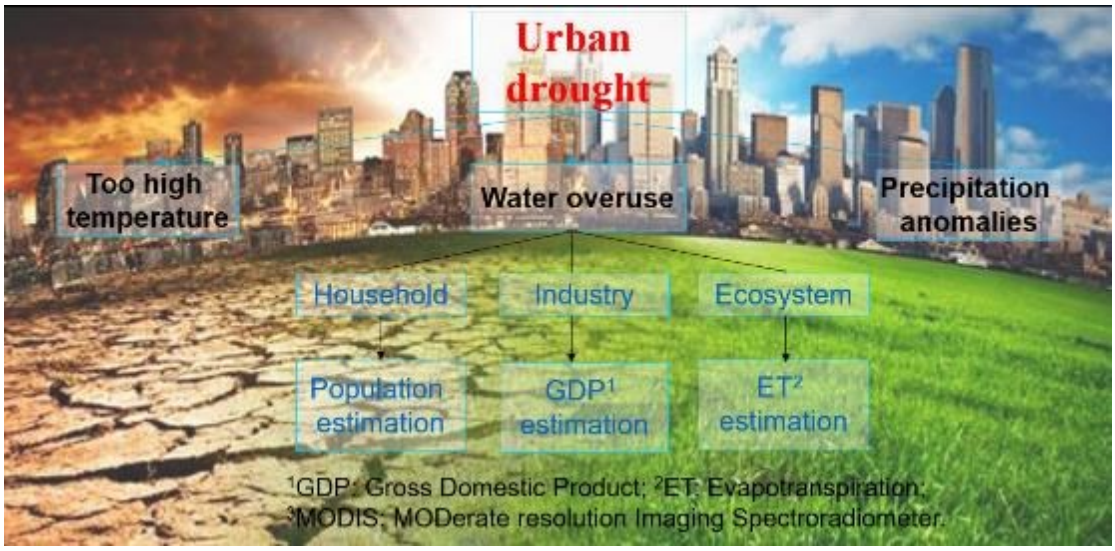

Fig. 1-1 Urban drought under climate change and intensive human activities

With climate change, the extent, severity, and frequency of droughts around the world are expected to increase (Palazzo et al. 2017), as illustrated in Fig. 1-1. Cities are particularly vulnerable to climate risks due to their agglomeration of people, buildings and infrastructure. In previous researches, urban drought was often assessed based on precipitation. Differences in methodology, hazards, and climate models limit the utility and comparability of climate studies on individual cities (Bryant et al., 1992; Phillips and McGregor, 1998; Guerreiro et al., 2018). Drought severity is usually highly related to the efficiency of water conservation -- especially in urban areas, and conservation varies by hydrologic region, or the change in streamflow (Svoboda,2000; Palazzo et al. 2017). However, drought assessment in data scarce areas often neglects the streamflow which induced great uncertainties in results.

The Surface Water and Ocean Topography (SWOT) satellite, to be launched in 2021, will bring observations of water surface with an unprecedented spatio-temporal coverage (Rodríguez et al., 2018). Many scholars devoted greatly to water surface inversion or basinal water storage estimation by using multisatellite data, such as MODIS imagery, ENVISAT satellite altimetry data or the derived virtual stations (Silva et al, 2010; Pham-Duc et al., 2019&2020; Kitambo et al., 2021). However, estimating streamflow from “geometric” observables of flow surface remains a difficult inverse problem particularly in case of poor knowledge on river bathymetry and friction. Moreover, few recent studies address the effective

modeling of ungauged river channels using multisatellite data, and the estimation of streamflow from SWOT water surface observations is a difficult inverse problem because of the correlated influence of flow controls on the observable water surface signatures, which may be solved when in situ depth/discharge data are available (Garambois et al., 2020; Pujol et al., 2020). Some scholars tried inversing streamflow in large-scaled rivers (e.g., more than 100 meter wide) and got a satisfactory results yet the accuracy is poor when applied to narrower tributary streams (e.g., less than 40 meter wide) (Gleason and Smith, 2014; Chen et al. 2016; Feng, et al., 2019; Zhao et al., 2019).

So far, urban drought was assessed by using the Drought Severity Index (DSI) where only precipitation was considered (Bryant et al., 1992; Phillips and McGregor, 1998; Guerreiro et al., 2018), or by using the most comprehensive data source for drought monitoring, e.g., the United States Drought Monitor (USDM) dataset (Svoboda,2000; Palazzo et al., 2017). However, water use information was often neglected. In addition, many methods were developed for local areas in which many data are not available in other regions, especially in the Yellow River basin (YRB) China. When assessing urban drought in these regions, it is highly necessary to set up a new framework for urban drought assessment by considering both water quantity available and water use / consumption in urban areas.

Water quantity available and water use information can be comprehensively reflected by the terrestrial water storage change (TWSC). Till now, the Global Land Data Assimilation System (GLDAS) is the mostly widely used dataset for hydrological study and disaster assessment. This dataset can also roughly calculate the TWSC in many regions globally. The GLDAS was jointly developed by scientists at NASA, GSFC, NOAA and NCEP to provide terrestrial water and energy storages data. It drives four land surface models: Noah, CLM (Community Land Model), VIC (Variable Infiltration Capacity) and Mosaic, incorporating both ground and satellite-based data (e.g., the global land cover and soil type dataset). The model output produced by the Noah land surface model includes soil moisture data (10, 30, 60 and 100 cm, from the soil surface down), snow water equivalent, evapotranspiration, LAI and canopy water storage (Rodell et al., 2004; Friedl et al., 2010).

In contrast, the NASA's Gravity Recovery and Climate Experiment (GRACE), or the GRACE satellite, can provide global monitoring on TWSC including the variation of groundwater, soil moisture, evapotranspiration, air moisture and precipitation as well as moisture in clouds. The GRACE data were widely used to regional drought, glacier melting monitoring as well as assessment of other disaster (Chen et al., 2013; Houborg et al., 2010; Nie et al., 2018; Yin et al., 2020).

In brief, when assessing urban drought in previous researches many scholars took precipitation as basis to calculate urban drought, yet less consideration is put on streamflow, especially in data-scarce areas. However, streamflow is significantly important for accurately estimation drought related variables (Lv et al., 2019). In addition, lack of long series of on-ground hydrological monitoring on streamflow in data scarce areas hinders accurately estimating freshwater available and predicting future drought severity. Streamflow, soil water and undergroundwater consist of most of proportions of freshwater available. Streamflow can be retrieved by using satellite imageries and the latter two indicators can be estimated by using

GRACE and GLDAS data (Bettadpur, 2012; Zhao et al., 2013; Gleason and Smith, 2014; Chen et al. 2016; Shen et al., 2016). Therefore, it is urgently necessitated to produce long series data of freshwater available based on GRACE and GLDAS data whereby to predict future urban drought with water consumption and freshwater availability.

1.2 Objectives

To develop a framework for the prediction of urban drought (water consumption / available water) in the year 2030 and 2050 to support making drought-control policy in data-scarce areas, inclusive of

(1) Extending streamflow series in data-scarce areas by exploring new ways to retrieve streamflow to help more accurately calculate available freshwater in urban areas when assessing future drought;

(2) Producing long series of available groundwater data related to calculation of freshwater available with the help of GRACE and GLDAS data for accurately predicting available freshwater;

(3) Predicting drought in 2030 and 2050 coupled with CMIP5 IPCC models and scenarios.

1.3 State of the art of drought assessment and prediction

Drought is often caused by a lack of rainfall or by intensive use of water resources(Trenberth et al., 2014). Climate change deteriorates it as higher temperature and less precipitation yielding runoff in urban areas. A lack of rainfall results in shortage of water available, and intensive use of water resoruces is the outcome of excessive water consumption. Generally, the ratio of water consumption to water available can reflect the degree of drought. Generally, the assessment methodologies can be categorized as four classes.

1.3.1 Meteorological drought

Meteorological drought can be defined as a prolonged lack of (or below normal) rainfall, possibly aggravated by hot temperatures causing high evapotranspiration rates (Spinoni et al., 2019). In general, the meteorological drought is the origin of the other three types of droughts, and the hydrological drought tends to be caused by the accumulation of meteorological drought. Once the hydrologic drought occurs, it is easy to lead to the shortage of agricultural water supply and socioeconomic drought (Yi et al., 2020). Till now, scholars developed many algorithms to calculate meteorological drought (e.g., SPI, SPEI, PET, PDSI, scPDSI, PHDI, Z-Index, PMDI, PNP etc.), among which three algorithms of SPI, SPEI and DPI were widely used. SPI and SPEI are multi-scale and can reflect different drought types (Hernandez and Uddameri, 2014; Stagge et al., 2015). DPI is based on the difference between the data and the average value. It does not impose any probability distribution on the precipitation data (Tayfur, 2021). It is a more representative drought assessment tool for arid climate regions. Moreover, these three indexes are also commonly used in drought assessment. Details are as follows:

(1) Standardized Precipitation Index (SPI)

The (SPI) is calculated in the following sequence. A monthly precipitation data set is prepared for a period of m months, ideally a continuous period of at least 30 years. A set of averaging periods are selected to determine a set of time scales of period j months where j is 3, 6, 12, 24, or 48 months. These represent arbitrary but typical time scales for precipitation deficits to affect the five types of usable water sources. The data set is moving in the sense that each month a new value is determined from the previous i months. Each of the data sets are fitted to the Gamma function to define the relationship of probability to precipitation. Once the relationship of probability to precipitation is established from the historic records, the probability of any observed precipitation data point is calculated and used along with an estimate of the inverse normal to calculate the precipitation deviation for a normally distributed probability density with a mean of zero and standard deviation of unity. This value is the SPI for the particular precipitation data point (Mckee et al., 1993).

(2) Standardized Precipitation-Evapotranspiration Index (SPEI)

Drought is not only affected by precipitation, but also closely related to evapotranspiration. In 2010, Vicente-Serrano used the difference between precipitation and evapotranspiration to construct SPEI (Vicente-Serrano et al., 2012), and used the log-logistic probability distribution function of 3 parameters to describe its changes. Through normalization processing, the cumulative frequency distribution of standardized precipitation and potential evapotranspiration was finally standardized to classify drought. Potential evapotranspiration (PET) means the maximum evapotranspiration that can be reached on a fixed underlying surface when the water supply is not restricted under certain meteorological conditions (Hernandez and Uddameri, 2014; Wu et al., 2021). Potential evapotranspiration is a key factor for the evaluation of regional dry and wet conditions, the estimation of crop water requirements, and the rational planning of water resources.

(3) Discrepancy Precipitation Index (DPI)

The DPI does not impose any probability distribution on the precipitation data, which is based on the discrepancy of the data with respect to the mean value (Tayfur et al., 2021). The drought classifications are proposed based on the D-score values. Its drought classification ranges are straightforward as those of the Standard Precipitation Index (SPI). The proposed drought index is based on the discrepancy of precipitation data with respect to the mean value and does not impose any transformation or any other probability distribution function. It does not require the normal distribution of the data yet requires only the long-term precipitation data which can be easily available in most part of the world (Tayfur et al., 2021).

In summary, both SPI and SPEI are standardized indicators that fit the input variable(s) with a statistical distribution over a baseline and classify the drought conditions with a simple scheme related to standard deviations from the median. Both indicators have been computed at multiple temporal accumulation periods (from 3 to 72 months), in order to let the user choose the accumulation period which best accounts for the sector of interest (Spinoni et al., 2019). It does not consider moisture condition and therefore it can be effectively used in both summer and winter, not affected by the topography. It is simply a fine transformation of precipitation

time series into a standardized normal distribution (z-distribution). The categories and the related ranges of the DPI are straightforward as the z-values of the SPI method (Tayfur et al., 2021).

However, the SPI is based on precipitation only and what is worth noticing is that semi-arid and arid areas can be problematic with meteorological indicators computed at short periods, especially with SPI (Spinoni et al., 2019) since the precipitation data in semi-arid and especially in arid regions have a strong discrepancy due to the sporadic rainfall occurring in such regions. Therefore, in the analysis of the drought for such regions, imposing any probability distribution function to the data could be futile (Tayfur et al., 2021). Moreover, SPI and SPEI may not be capable of identifying regions that may be more 'drought prone' than others (Tayfur et al., 2021). In addition, ftting the difference between precipitation and PET over a short baseline period can result in problems computing SPEI due to climate change effects (i.e. rising temperatures) that are manifest in PET over recent decades and SPEI values of recent years (or decades) may be unrealistic because recent differences between precipitation and PET fall outside the range recorded during the baseline period, thus biasing the fit of the statistical distribution (Spinoni et al.,2019). In this sense, these indices need to be applied to different climatic regions to show its capabilities and the limitations (Tayfur et al., 2021).

1.3.2 Agricultural drought

Agricultural drought is usually caused by the stress of soil moisture in the root zone, which results in chlorophyll content losses, vegetation wilting and even crop failure over time. The onset of agricultural drought may lag that of the meteorological drought depending on the previous effective soil water content. To monitor different kinds of droughts (severity or magnitude), over 70 drought indices and several drought information systems have been developed. Based on a review of previous studies, two aspects need to be considered. Firstly, agricultural drought is the result of meteorological drought in agriculture areas. One of the best statistical indicators of meteorological drought is precipitation. however, the drought indices that include this indicator, such as SPI or SPEI, may not be suitable for monitoring agriculture drought, especially in irrigated areas. The main reason is that irrigation leads to overestimations of drought severity by certain drought indices, Secondly, agricultural drought is affected by meteorological factors, soil properties, vegetation types and other factors (e.g., field management and disease) (Wu et al., 2021a). Agricultural drought occurs when a deficiency in soil moisture (SM) starts adversely affecting crop growth and ultimately reducing crop yield (Baik et al., 2019).

Three methodologies were widely used as follows:

(1) EDI (Evapotranspiration Deficit Index)

To highlight the soil moisture response to surface dryness, a simple EDI, following the evaporative stress index, is designed from the improved actual ET model and PET model, given by 1 minus the ET/PET ratio. Generally, EDI is sensitive to moisture stress and is comparable at different spatial scales. Higher EDI means more severe water stress or drying of the soil surface and lower EDI means less water stress or ample surface soil moisture (Yao et al., 2010). The sensitivity of vegetation drought response enhances drought detection capability. Also, EDI

highlights surface dryness integrated energy fluxes in response to soil moisture stress and can accurately monitor long term land surface drought (Wu et al., 2021b).

(2) SEDI (Standardized Evapotranspiration Deficit Index)

Kim et al., (2016) adopted the structure of SPEI to produce a probability-based relative drought index. The precipitation minus the reference ET of SPEI was replaced with the ET deficit obtained from the modified GG method. Since SPI and SPEI show strong correlations with PDSI at 9 to 12 months of duration, they hypothesized that the 9 months duration for accumulating ET deficit would show high correlations with the precipitation-based indices. The accumulation of ET deficit considers influence of moisture availability in the previous months on the drought conditions of the current month. Hence, the series of 9-month ET deficit for each grid cell of the PRISM data sets over 119 years. Using the fitted log-logistic distribution and the gridded 9 months ET deficit, they produced monthly drought indices from 1896 to 2014 at a 4 km grid resolution. While the SPEI uses the nonexceedance probability (p) of accumulated precipitation, the exceedance probability ($1 - p$) of the 9-month ET deficit was standardized because the ET deficit inversely indicates water availability. As such, the novel drought index derived from the ET deficit was referred to as the Standardized Evapotranspiration Deficit Index (SEDI) hereafter, which simplifies the computation of ET with meteorological data and performs well in identifying agricultural drought (Wu et al., 2021b).

(3) ETDI (Evapotranspiration Deficit Index) (Narasimhan et al., 2005)

The water stress anomaly during any week ranges from -100 to +100 indicating very dry to very wet conditions with respect to evapotranspiration. Adopting a similar cumulating procedure of SMDI, drought severity due to evapotranspiration deficit is given whereby Evapotranspiration Deficit Index (ETDI) were calculated. ETDI is a good indicator of short-term agricultural drought monitoring which comparable irrespective of climatic zones. It underscores the importance of LAI and vegetation type capturing well the two-peak seasonality of ET variations as well as the drought area and yield loss (Wu et al., 2021b).

However, EDI lacks physical basis and cannot easily quantify the wetness or dryness of a region in a given monthly or yearly period. SEDI does not consider wind speed yet decrease in wind speed will reduce evaporative demand. ETDI limits the river basin level and therefore remote sensing products are the only viable data for mapping ET and PET in large catchments. What is more, it performs poorly in mountain areas due to the lack of observed meteorological data (Wu et al., 2021b).

1.3.3 Hydrological drought

Hydrological drought refers to the deficit of river discharge. The impact of droughts typically increases when a meteorological drought turns into a hydrological drought, affecting the ecosystem (e.g., water quality), residents, as well as industrial and agricultural production. Following its onset, the lifecycle of a hydrological drought includes development and recovery or termination. Development is defined as the period from the onset of hydrological drought to the time when the maximum intensity is realized, while the recovery refers to the period from the maximum intensity of hydrological drought to complete recovery (Wu et al., 2020).

Three methodologies were widely used as follows:

(1) SSI (Standardized Streamflow Index)

If the probability distribution is suitable for fitting the monthly streamflow series, the average value of the SSI and the standard deviation must equal 0 and 1, respectively. The SSI is a standardized variable and can therefore be compared with other SSI values across time and space (Vicente-Serrano et al., 2012). Moreover, it applies to multiple timescales with simple calculation and less data input (Wu et al., 2020). SSI with the advantages of simplicity and effectiveness is viewed as the most commonly utilized method for quantifying the streamflow-based hydrological droughts (Wang et al., 2020).

(2) SRI (Standardized Runoff Index)

The procedure for calculating the SRI includes the following steps (Shukla et al., 2008): first, a retrospective time series of runoff is obtained by simulation, and a probability distribution is fit to the sample represented by the time series values. Second, the distribution is used to estimate the cumulative probability of the runoff value of interest (either the current accumulation or one from a retrospective date). Third, the cumulative probability is converted to a standard normal deviate (with zero mean and unit variance). It has been extensively used for hydrological drought assessment (Wang et al., 2020).

(3) SAP (Streamflow Anomaly Percentage)

The equation for SAP is $F_{dy} = \frac{(\overline{lnQ_d} - lnQ_{dy})}{\sigma(lnQ_d)}$ where Fdy, is the flow anomaly occurring on day d of year y and Qdy is the flow occurring on day d of year y. Qd represents the set of flows occurring on day d (where d can range between 1 and 365), hence $\overline{\ln Q}_d$ is the mean value of lnQd over a period of n years, whilst σ (lnQd) is the standard deviation of the lnQd values within the n year period (Zaidman et al., 2002).

What is worth noticing is that SSI does not directly reflect the amount of water required for recovery as they are dimensionless indices. Belonging to standardized drought index family, the SSI is developed directly under the assumption that the distribution of streamflow is statistically stationary. However, the non-stationarities in long-term observations cannot be ignored under a changing environment, which to some extent becomes the main obstacle to the validity and usefulness of the traditional indices. SRI does not directly reflect the amount of water required for recovery as they are dimensionless indices and suffered from the lack of appropriate universal approaches at basin scale. As to SAP, it employs a fixed timescale (e.g., monthly or annual) and average streamflow as the calculation parameter. Consequently, the cumulative effects of drought for a prolonged event are neglected (Wang et al., 2020; Wu et al., 2020).

1.3.4 Socio-economic drought

Different from meteorological, hydrologic, and agricultural drought, socioeconomic drought is an only non-physical phenomenon among these four types of drought, which refers to that available water cannot satisfy the demand, and directly results in negative effects on industrial, irrigation, hydroelectric power and environment. However, socioeconomic drought

is difficult to quantify(Guo et al., 2019; Mehran et al., 2017; Mehran et al., 2015). In addition, it should be noted that as an unnatural phenomenon, once the socioeconomic drought occurs, it will directly affect the stability of human production and living (Guo et al., 2019a). In the socioeconomic system, its population is most influenced by drought due to the direct impact of drought on the water and food supply. Still, various economic sectors can be seriously affected by drought, and the huge economic impact of drought is most important in developing countries. The spatial distributions of populations and economic activity are also highly correlated, which has enabled the effects of climate change on socioeconomic systems to be assessed, although economic impacts have not received the same attention as population (Liu et al., 2020).

There are three wide-used methods for this kind of drought.

(1) MSRRI (Multivariate Standardized Reliability and Resilience Index)

The index MSRRI is not only a hybrid index (consisting of two fundamentally different indicators) but also covers both common approaches in vulnerability studies (top-down and bottom-up). MSRRI can be considered as a measure of socioeconomic drought since it evaluates the supply and storage relative to the demand. Similar to other standardized drought indicators, positive values indicate sufficient water to satisfy demand, while negative values indicate shortage of water relative to the demand. Here the standardization is based on a nonparametric approach that does not require parameter estimation or any a priori assumption on the underlying distribution function of the original data. The values of MSRRI and the corresponding socioeconomic drought severity can be interpreted similar to the commonly available drought indicators such as the Standardized Precipitation Index (SPI) -- i.e., a negative value indicates socioeconomic drought, while a positive value represents a wet period (Mehran et al., 2015). In fact, given that MSRRI is based on the joint distribution, MSRRI indicates the onset of the stress based on the onset of the hydrologic drought and recovery of the system from a socioeconomic perspective. This behavior of MSRRI provides an assessment of the overall stress on the system including the system resilience (Mehran et al., 2015); MSRRI has better performance in assessing socioeconomic droughts than Inflow-Demand Reliability index (IDR) and Water Storage Resilience index (WSR) (Huang et al., 2016); Multivariate Standardized Reliability and Resilience Index (MSRRI) framework to quantify the socioeconomic drought, which provided complementary information on socioeconomic drought development and recovery based on reservoir storage and demand (Guo et al., 2019a).

(2) IDR (Inflow-Demand Reliability index)

IDR is designed to investigate socioeconomic drought and is a multivariate approach that relies on two individual (univariate) indicators. At first, a time frame is defined based on the type of reservoir system (within-year or over-year). After defining the time frame, two new indicators are defined as follows: water storage resilience indicator and inflow-demand reliability indicator. Inflow-demand reliability (IDR) indicator is derived by computing the sum of the percent change of inflow with respect to water demand during the projected time frame. This indicator (inflow-demand reliability) corresponds to the “top-down” approach where the available inflow is assessed relative to the water demand. In other words, this indicator shows whether the available water (inflow to the system) is sufficient to satisfy water demand, regardless of the storage in the reservoir (Mehran et al., 2015).

(3) WSR (Water Storage Resilience index)

WSR in respect to “bottom-up” methodology is the water storage resilience indicator. This indicator is defined based on monthly inflow, monthly water demand, monthly storage, and total water demand during the time frame. Water storage resilience (WSR) indicator is computed monthly and shows whether the reservoir storage is enough to satisfy water demand for the selected period (Mehran et al., 2015).

In summary, MSRRI is overly sensitive to inflow, and could not accurately depict the reservoir operation process and the capacity to resist the future drought, especially in flood season. IDR and WSR cannot clearly reveal the severity of water stress. In the IDR index framework, the outflow of a reservoir was regarded as the demand, but the outflow cannot accurately represent the demand, especially during the drought period when the outflow is small, the demand is large, and the outflow is much less than the actual demand. It could not accurately monitor the drought situation of the reservoir during the flood season (Mehran et al., 2015; Guo et al., 2019b).

1.4 Large-scaled drought assessment with multi-source data inclusive of satellite imageries

When assessing drought at large scales, using the method (water comsumption / freshwater available) is the best way due to the lack of ground observations.

FWA includes surface freshwater available and underground FWA. Surface freshwater is usually stored in large waters (such as lakes, reservors and wetland), and transported via surface streamflow.

1.4.1 Assessment of surface freshwater storage with satellite images

The water storage of surface waters is frequently monitored by using satellite imageries with which hydrological models were developed (Donchyts et al., 2016; Feng et al., 2016; Pekel et al., 2016). Song et al., (2018) used the Landsat archived images, including those from the Landsat 4 & 5 Thematic Mapper (TM), the Landsat 7 Enhanced Thematio Mapper-plus (ETM+) and the Landsat 8 Operational Land Imager (OLI), to detect surface water dynamics in New Area during the past three decades; Kim et al. (2020) used C-band Sentinel-1A and -1B SAR images to derive reservoir surface water areas; in addition, Yésou et al. (2011) monitored the variation of water resource over the Yangtze middle reaches by coupling satellite imageries of ENVISAT, MODIS, altimetric data and field measurements; Hulth et al. (2020) monitored water dynamics based on Sentinel-1 Time Series; Xing et al. (2018) monitored monthly surface water dynamics of Dongting Lake using Sentinel-1 data at 10 m spatial resultion; Yang et al., (2020) estimated monthly variation of surface water extent in metropolitan France at a 10-m resolution using Sentinel-2 data; Che et al. (2019) estimated seasonal water cover and change in arid and semi-arid Central Asia by using Landsat imagery; Paul et al. (2020) developed Satellite-based hydrological model (SHM) on 1 km × 1 km spatial grid resolution to estimate and forest surface water, snowmelt, groundwater and study runoff routing processes.

1.4.2 Assessment of stream flow with satellite images

As to surface streamflow, estimation methods with satellite imageries are products of in-

depth research in the fields of computer science and spatial science during recent years. Using these methods, researchers can perform the inversion of discharge under difficult geology and harsh conditions without gauging the water (Fisher et al., 2020; Hirpa et al., 2013; Syvitski et al., 2000). There are two main types of inversion methods: near-surface remote sensing and satellite remote sensing. Near-surface remote sensing mainly includes stereo vision—particularly imaging (Li et al., 2016), Doppler radar and ground penetrating radar (Costa et al., 2006; Costa et al., 2000), aircraft–radar–water surface elevation (LeFavour & Alsdorf, 2005), water-level/slope/hydraulic method (Bjerklie et al., 2018; Jung et al., 2010; Pujol et al., 2020), etc. However, the expensive instruments limit the wide application of such methods. In contrast, satellite remote-sensing methods have the advantages of low cost, high speed and convenience, and ease of implementation. They have been widely used in large rivers and can be approximately divided into five types: water surface area (satellite–water surface area), water surface width (satellite–water surface width), water level (satellite–water level) and hydrological multi-parameter set (satellite–multiparameter) and coupling of satellite data and hydrological model (satellite–hydrological model).

The satellite–water surface area method uses in the 1990' ERS-1 radar satellite images and simultaneous ground measurement data to establish a correlation between water surface area and discharge for the inversion of streamflow (Smith et al., 1996; Smith et al., 1995; Song et Al., 2011). The satellite–water surface width method uses water surface width information obtained from satellite images such as QuickBird-2 together with fitting curves generated from survey stations to invert streamflow (Pavelsky et al., 2014; Xu et al., 2004). The satellite–water level method converts the information on the underlying surface water level estimated using TOPEX/Poseidon satellite data into a series of water level values. It establishes the relationship between the water level values from satellite data and the measured discharge from adjacent hydrological stations. Thus, the discharge can be estimated using TOPEX/Poseidon (TP) satellite data (Zhang et al., 2002; Zhang et al., 2004) or by directly using satellite altimetry data of Jason 3, Jason CS, Sentinel3 and the coming SWOT, etc., to estimate discharge for areas with no data (Getirana et al., 2013; Papa et al., 2010). The satellite–multiparametric method measures hydrodynamic and hydrological parameters such as water surface width, hydraulic gradient, and water level to invert the discharge of large rivers with widths >100 m (Biancamaria et al., 2016; Birkinshaw et al., 2014; Durand et al., 2016; Gosling Et al, 2011; Pavelsky et al., 2014). Alternatively, it calculates water cycle components from satellite inversions by linking remote sensing and synchronized ground measurement (Li et al., 2012; Lu et al., 2010). The satellite–hydrological modeling method combines satellite data, surface climate data, and hydrological modeling to measure the discharge of large rivers (Andreadis et al., 2007; Vörösmarty et al., 1996).

Among the five methods previously described, most are highly dependent on ground measurement data, whereas the global parameters in at-many-stations hydraulic geometry (AMHG) is one of McFLI (Gleason et al., 2016). It calculates the streamflow solely from the variation in river width, making it among the mainstream methods widely used for streamflow estimation via remote sensing (Bonnema et al., 2016; Durand et al., 2016; Gleason et al., 2014; Gleason et al., 2018). However, satellite-induced scale problems (Wu and Li, 2009), restricted its wide application in medium and small rivers. In other words, because of the limitations of

satellite spatial resolution or sensor capacity, the accuracy of this method is relatively high for large rivers (average river width ≥100 m) but unstable for medium-to-small rivers (average river width ≤ 100 m, and small rivers with width <40 m) (Gleason et al., 2014; Feng et al., 2019), thus greatly limiting its application to medium-to-small rivers lacking hydrological monitoring data. Therefore, there is an urgent need to explore new methods to enhance the AMHG method and to expand the scope of its application.

1.4.3 Estimation of underground water variation with satellites

In aspect of underground water study, Gravity Recovery and Climate Experiment (GRACE)(Tapley et al., 2004) observations and DInSAR Data were often combined with other models as the water balance method and Darcy's law (Ramillien et al., 2011, 2012 & 2015). GRACE observations were used to assess underground water exchange patterns. GRACE-derived TWS anomalies are the sum of all components, including GWS, soil moisture, snow water equivalent (SWE), and canopy water storage (CWS) (Yin et al., 2020). DInSAR Data were often used to derive ground displacements based on SAR-derived deformation series as DInSAR processing allows the evaluation of the temporal evolution of surface displacement using SAR images over large areas since the first SAR satellites became operational in 1992 (Massonnet et al., 1993; Ezquerro et al., 2017).

In addition, variaious satellite products were integrated together to set up mathematical model to study groundwater variation. Shu et al. (2018) modeled groundwater processes using remote sensing data and took the results as input variables of distributed hydrological modelling. They merged ground observations and the RS data by forcing the RS data to obey the measurements at the gauge stations.

1.4.4 Estimation of precipitation with satellite imageries

Precipitation, as the most active element in the water cycle, and its tempo-spatial distribution play an important role in accurate prediction and assessment of factors in hydrology, meteorology and agriculture (Shi et al., 2019). With the techniques of high-speed computation and remotely sensed satellite, meteorological satellite has been a new tool to estimate precipitation. Through satellite imageries, researchers can calculate high- spatial-resolution and high-accuracy precipitation observations (Amitai, et al., 2009). Globally, there emerged many satellite precipitation datasets, such as GPCP (global precipitation climatology project), TRMM (tropicalrainfall measuring mission), CMORPH (climate predictioncenter morphing technique), PERSIANN (precipitationestimation from remotely sensed information usingartificial neural networks), GSMaP (global satellitemapping of precipitation), GPM (global precipitationmeasurement mission) etc. (Amitai, et al., 2009; Jiang et al, 2010; Shi et al., 2019; Guo et al, 2021). These datasets lay solid foundation for the researches of hydrology and meteorology in data-scarce and ungauged areas. However, spatial resultion of most satellite dataset is not very high, e.g., GPCP has a spatial resolution of 1.5°×1.5°; CMORPH, PERSIANN and TRMM have a spatial resolution of 0.25°×0.25°. Though GSMaP and GPM have a relative higher spatial resolution (0.1°×0.1°) (Guo et al, 2021).

1.5 Assessment of water consumption

This section will evaluate water consumption from three aspects: household water

consumption, industrial water consumption and agricultural and naturals ecosystem water consumption.

1.5.1 Household water consumption

In the estimation of household water comsumption, population is an important variable. Several principle global databases for population such as Landscan (with historical values and some forecast one, https://landscan.ornl.gov/), the GUF from DLR (http://www.dlr.de/eoc/en/desktopdefault.aspx/tabid-9628/16557_read-40454/), GHSL from JRC (http://ghsl.jrc.ec.europa.eu/) are available (Bhaduri et al., 2002; Florczyk et al., 2019; Mück et al., 2017).

Among the three datasets, ORNL's LandScan™ (Dobson et al., 2000 & 2003) is a community standard for global population distribution data with approximately 1 km (30″ by 30″) spatial resolution, it represents an ambient population (average over 24 hours) distribution. LandScan is now available at no cost to the research and education communities. Dataset from 2000 to 2018 are available now. It is developed using best available demographic (Census) and geographic data, remote sensing imagery analysis techniques within a multivariate dasymetric modeling framework to disaggregate census counts within an administrative boundary. Since no single population distribution model can account for the differences in spatial data availability, quality, scale, and accuracy as well as the differences in cultural settlement practices, LandScan population distribution is essentially a combination of locally adoptive models that are tailored to match the data conditions and geographical nature of each individual country and region.

The second dataset, the "Global Urban Footprint" (GUF) project aims at mapping the worldwide settlements with unprecedented spatial resolution of 0.4 arcsec (~12 m). A total of 180 000 TerraSAR-X and TanDEM-X scenes have been processed to create the GUF. The resulting map shows the Earth in three colors only: black for "urban areas", white for "land surface" and grey for "water". This reduction emphasizes the settlement patterns and allows for the analysis of urban structures, and hence the proportion of settled areas, the regional population distribution and the arrangement of rural and urban areas. For scientific and non-commercial applications, the GUF data are free for use. Global coverage of the Earth's land surface (generated based on ~180.000 single TerraSAR-X/TanDEM-X image products) for the reference year 2011. Data collection of satellite imagery between 2011 and 2012 (93 %); single scenes with more recent acquisition dates (2013 / 2014) used to fill data gaps.

The third dataset of GHSL is a new open and free tool for assessing the human presence on the planet. It produces new global spatial information, evidence-based analytics and knowledge describing the human presence on the planet and operates in an open and free data and methods access policy (open input, open method, open output). The GHSL Data Package 2019 consists of multitemporal products, that offers an insight into the human presence in the past: 1975, 1990, 2000, and 2014.

Except for population there exist five other ways to measure household water consumption, directly or indirectly, as follows:

（1） By water meters

Traditionally, the primary source of household water usage data is water meters (Willis et al., 2013). Water meters is a household instrument to measure how much water the household consumes. The temporal resolution of the data obtained differs significantly depending on the generation of meter used to collect the data — from monthly to yearly intervals with ordinary manually read ('dumb') meters (Sønderlund et al., 2016) to smart meters capable of generating real-time or near real-time usage data (Cole and Stewart, 2013; Nguyen et al., 2018a). Some of the more modern generations of ordinary meters have Automatic Meter Reading (AMR) technology, which allows remote meter reading and data transfer (Pericli and Jenkins, 2015; Abu-Bakar et al., 2021).

（2） Via surveys

A primary survey pertaining to water consumption pattern was conducted by means of structured questionnaire as main research instrument. The survey instrument contained both closed and open-ended questions. The household survey incorporated questions on daily and activity wise consumption, sources, quality, duration and frequency of water supply, distance of different sources and the level of awareness about rainwater harvesting technology in the village. What is worth noticing using this method is that the season impacts the populations water needs (Singh et al., 2013).

（3） Dividing the household's reported monthly bill by the unit tariff

In this method, the key dependent variable water consumption was obtained by dividing the household's reported monthly bill by the unit tariff corresponding to the household's water delivery system (Basani et al., 2008).

（4） Statistical forecasting methods

Statistical forecasting methods rely on historic data to define relationships between independent and dependent variables (Memon and Butler 2006). These relationships can then be used to predict future household water demand but forecast accuracy is highly dependent on the quality of the underlying data (Tate 2000). Water demand forecasts are typically derived from explanatory variables (e.g., population, household size and climate variables) using linear regression methods. Alternatively, water companies employ geodemographic profiling to estimate household demand via factor analysis of census data to identify areas with common attributes. For example, the ACORN (A Classification of Residential Neighbourhoods) metric is widely used with household demand coefficients (derived from sample surveys) to estimate household consumption across the regional population (Parker et al., 2013).

Water companies also base predictions on ownership-frequency-volume models which consider the number of waters using fixtures, how often they are used, and the average quantity of water per use. 'Microsimulation' techniques have also been applied to household demand estimation and forecasting (Clarke et al. 1997; Williamson et al. 2002).

（5） Basing on household population

Domestic water consumption (DWC) depends on the living habits of communities. The

registered population during 2006–2015 (without taking account of the non-registered population) living in Chao Phraya watershed was collected from the Bureau of Registration Administration of the Department of Provincial Administration of Thailand. According to the Government Gazette (2010) of Thailand, 80% of domestic water demand (DWD) was set at an average rate of domestic wastewater for Thailand. Consequently, 20% of DWD was determined as DWC in this study. The DWD was calculated from using a DWD coefficient of each community multiplied by the population (Kaewmai et al., 2019).

（6）Via household water demand prediction model

There are four attributes of a household agent: total water consumption, water consumption per capita, household population and education. Economic, climate and some other factors are usually considered to drive water consumption (Arbués et al.2003). Each household may be affected by surrounding households to change its water consumption in reality. Thus, the household agent in the HWDP has self-learning ability which is related to education. Not only does it enhance interpretations by defining the behavioral characteristics of elements, but also it makes the model more realistic by revealing internal feedbacks. Therefore, when modeling water demand by agents, factors including geographic, cultural, socio-economic, behavioral etc. are needed (Athanasiadis et al. 2005; Barthel et al. 2008; Galán et al. 2009; Valkering et al. 2009; Chu et al. 2009). The complexities and uncertainties caused by the randomness and feedbacks in the system can be deeply investigated to show the variations of urban household water demand (Yuan et al., 2020).

However, most traditional meters have significant limitations (Pericli and Jenkins, 2015), making them unsuitable for consumption measurement without being linked to data loggers (Giurco et al., 2008). Other methods of surveys, monthly bill and statistics are conducted with ground investigation house by house, which is impossible for large-scaled estimation of household water consumption. The last two methods based on household population are good way yet collection of registered household population data is difficult in China. Also, the data for spatial distribution of educated household population are hard to get in China. Fortunately, the role of educated household population in the prediction model is only slight adjustment and can be ignored at large scales. The most suitable way is firstly estimating population via satellites or other sources like Landscan, secondly estimating water use per captia by way of investigation in representative areas like Ercin and Hoekstra (2012), Yuan et al. (2020) and Guo et al. (2021), and thirdly estimating household water consumption, or the total water consumption in the prediction model of Yuan et al. (2020), via formula of (population* water consumption per captia). In other words, a simplified household water demand prediction model of Yuan et al. (2020) will be used in this study.

1.5.2 Industrial water consumption

There are four ways to calculate water consumption by industry (IWC) as follows.

（1）Data collection

The bottom-up data collection method is often used, and the comprehensive data sources include but are not limited to the following: government statistics, official park websites, and open sources, such as Google Maps. These data can be classified into the following categories:

Resource-environment data include the source and quantity of water withdrawal, water consumption, energy consumption, wastewater treatment and emission, and reclaimed water use; economic data include the industrial added value (IAV) (BEA, 2006), the annual growth rate of IAV, and leading industries in NIPs; geographical data include the geographical location of the parks; other related data include local economic development, availability of local water resources, and local water consumption performance (Hu et al., 2021).

（2）Statistic

The water comsumption of an industry (IWC) depends on the type of industry (Kaewmai et al., 2019), e.g., a food industry requires the most water in Thailand at 75 m^3 hectare (ha)−1 day−1, followed by the chemical and non-metal industries at 50 $m^3\,ha^{-1}\,day^{-1}$ (RID, 2011a). The historical data on the daily water demand of industry were multiplied by the number of workdays in each month to obtain the monthly water demand by the industry. The IWC for the Southeast Asian countries in 2010 was set at 31.7% of the total industrial water withdrawal (Flörke et al., 2013; Shiklomanov, 2000).

（3）Water Input–Output model

Mohan, et al. (2021) developed a water I-O model which defines total water consumption and differentiates between direct and indirect water consumption. These concepts can be presented in the model, which allows us to formulate a matrix of intersectoral water relationships and analyze the relative importance of direct and indirect water consumption. The sum of the entire round of consumption is called total indirect water consumption (Wang et al., 2009).

（4）Aggregated IOT and the direct water consumption data

FWS is based on the Leontief I-O framework (Leontief,1986). In a general I-O framework, an economy has N sectors where each sector i produces aunique good. To better reflect the economic structure and water consumption conditions, the IOT is further aggregated. Thus, the water consumption among different industries can be obtained through using the aggregated IOT and the direct water consumption data (Chen et al,2010; Zhang et al., 2014; Zheng, et al., 2021).

（5）Industrial GDP-based model

This model firstly analyzes the water consumption variation with the industrial GDP of different industries whereby to determine the representative industry. Secondly, the water consumption per GDP is determined for every representative industry. When calculating industrial water consumption, what people need do is to classify local industries based on the class of representative industries and then uses “water consumption per GDP for every representative industry” multipied by GDP of local industries to get water consumption by every individual industry. All water consumption quantities total up to the water consumption for a region (Zhou and Xu, 2012; Ayiguli et al., 2015).

In summary, the bottom-up approach is a vital tool that provides the most accurate information and gathers reliable data from an industrial facility (Hu et al., 2021). However, due to its time consuming and confidentiality obstacles, such approach is avoided (Hu et al., 2021).

LDMI has been argued to be a superior IDA approach (Ang, 2004), as it satisfies all of the key desirable properties for a decomposition approach, including (1) a perfect decomposition (i.e. does not result in a "residual" element), (2) it is robust to negative or zero values, and (3) and is straightforward to implement and explain to non-specialists (Wang et al., 2017). The last method of industrial GDP-based model needs to determine "water consumption per GDP for every representative industry" which can be accessed via local industrial statistic report. But it is a little difficult for large-scaled study. If the method can be simplified with the variable being replaced by region-averaged value, industrial water consumption will be easily calculated.

1.5.3 Ecosystem water consumption (EWC)

Ecosystem includes natural and wetland, crop land, meadow etc. In a broader sense, ecosystem includes vegetation and the surrounding environment, or land without vegetation. A constructed wetland (CW) is an artificial wetland to treat sewage, greywater, stormwater runoff or industrial wastewater. It may also be designed for land reclamation after mining, or as a mitigation step for natural areas lost to land development(Lu et al., 2015). Water consumtion for this vegetation can be evaluated based on their life cycle with a temporal scale of monthly, e.g., the methods of IWRC, evapotranspiration which are usually applicable for humid areas. But in the arid areas distributing groundwater-dependent vegetation, the phreatic evaporation method is applicable. In detail,

（1）Irrigation water requirement of crops (IWRC)

Crops include rice, maize, sugarcane, cassava, para rubber, soybean, coffee, oil palm, longan, mungbean, and peanuts etc. The monthly planted area of each crop within the irrigation zone can be collected from several agencies, e.g., the RID, the Office of Agricultural Economics, the IWMD, and the Department of Agriculture Extension of Thailand (Kaewmai et al., 2019). For the calculation of the monthly IWRC within the irrigation zone of the watershed, the monthly planted areas of each crop should be multiplied by an irrigation demand coefficient for each crop based on the crop evapotranspiration, the effective rainfall, the infiltration rate and irrigation efficiency (RID, 2011b). Then, the total irrigation water requirement of all crops was summed up.

（2）Evapotranspiration from vegetation

The EWCs were calculated with evpotranspiration using the Penman–Monteith formula, and the characteristics of the spatial-temporal evolution of EWCs were analyzed. The EWCs of vegetation are affected by vegetation type, climate and soil moisture. The water conditions in the YRB can fully support the growth of vegetation, while the coefficient of Penman-Monteith K values of grassland, cropland and forestland are 0.4, 0.35 and 0.5, respectively (Zhang and Yang, 2002; Zhang, 2003; Zhang, 2017; Zhao et al., 2019). Under given climatic conditions, if a region with expansive land, adequate fertility, and appropriate soil moisture, which promote vegetation growth to achieve standard conditions of healthy production without pest and disease damage, then, according to recommendations from FAO (Allen et al., 1998), vegetation evapotranspiration rate can be determined. Under nonstandard conditions, vegetation growth is affected by soil water content. When soil water content is below a specified threshold, vegetation will be subject to water stress, and the effect is determined by the soil moisture

limitation coefficient (Ks). Vegetation degradation is therefore significant. For the incomplete coverage and destroyed natural vegetation, the calculation of the EWC must be done under nonstandard conditions and take the area of vegetation coverage into account (Chi et al., 2018).

（3）The phreatic evaporation method

The phreatic evaporation method is applicable for the vegetation of arid regions and is mainly related to groundwater. The actual evapotranspiration of the riparian vegetation is supplied by soil water (generated by upward phreatic water), and the soil water condition is thus determined by the evaporation of phreatic water (Chen et al., 2008). On a larger spatial scale, when the soil has a stable evaporation rate, the surface evaporation intensity is stable, and the soil water content also remains unchanged (Chen et al., 2008). The phreatic water evaporation intensity, soil water flux and soil evapotranspiration intensity are all equal (Li, 1988). Accordingly, the phreatic evaporation method is applicable in calculating the EWR of desert riparian vegetation. The phreatic evaporation method can be applied to estimate indirectly the EWC of the desert riparian vegetation, as based on the remote sensing interpretation (Song et al., 2000; Ling et al., 2014).

In summary, when estimating ecosystem water consumption evaptranspiration is the core. Among all the widely used three method, that for irrigation water requirement of crops are more applicable for crop areas, and the infiltration rate and irrigation efficiency vary with regions and crop types which need local experiment to determine and therefore it is hard to apply at large scales; the phreatic evaporation method is applicable for the vegetation of arid regions in stead of urban areas; the method of evapotranspiration from vegetation is applicable for studies in urban areas especially in the YRB as the coefficient of Penman-Monteith K values of grassland, cropland and forestland are given in advance. Therefore, the second method “evapotranspiration from vegetation” will be adopted in this study.

1.6 Flow chart and outline of the dissertation research

1.6.1 Flow chart of the dissertation research

To describe the routine of this research, we draw the flowchart of this dissertation as shown in Fig. 1-2.

Urban drought can be estimated by using the ratio of the quantity of freshwater available to the quantity of water consumption in a city. To reduce risks induced by urban drought, future risk of freshwater available and water consumption is urgently necessitated to be studied. But lack of long series of monitoring on freshwater (streamflow and groundwater storage) hinders accurately predicting future available freshwater. It is urgently necessitated to produce long series data of freshwater available. Freshwater available consists of surface freshwater available (SFWA) and underground freshwater available (UFWA). Surface freshwater includes streamflow dynamically flowing in rivers and water quietly stored in lakes and reservoirs. Underground freshwater includes water stored in shallow soil layer and deep underground layer.

The variation of freshwater available can be indicated by using TWSC (terrestrial water storage change). Streamflow is significantly important for accurately estimate TWSC. But difficulties in collection of ground-observed streamflow (instead of water-height) data resulted

in high uncertainties in TWSC estimation. To overcome this, two novel methods for streamflow retrieval with multisource data were developed in **Chapter 3**. The first one was named VHR-AMHG (Virtual Hydraulic Radius and at-many-stations hydraulic geometry) based on river water-surface width for streamflow retrieval in dry seasons, and the second one was named transcaled spatial C/M method based on the reflectance of soil and water more accurate in wet seasons. After validating the methods, we coupled the results with runoff data from GLDAS (Global Land Data Assimilation System) dataset to recitiy the latter whereby to get long-series streamflow (runoff) data (1948-2018). With the long series streamflow, the SFWA in the three representative cities (Xi'an, Zhengzhou, Jinan in the Yellow River basin, China) was estimated. The long-termed data of past SFWA can be used to predict SFWA in future 2030 and 2050.

As surface and underground freshwater available （SFWA+UFWA）consist of total freshwater available, we secondly put forward a new framework in **Chapter 4** to estimate UFWA where factors driving the variation of underground water were identified based on which the whole Yellow River basin was clustered. All factors are from GLDAS dataset and underground variation is from GRACE (NASA's Gravity Recovery and Climate Experiment) monitoring. With the driving factors and spatial clusters, an ANN (artificial neural network) prediction model –LSTM-N (Long short-term memory network) was trained and validated to extend the GRACE data from 2002- to 1948-, almost 70 years long. Then the extended GRACE data were used to calculate long termed UFWA (1948-) which will be finally used to predict underground FWA in future 2030 and 2050.

With total freshwater available (of surface and underground) estimated, water consumption in the three representative cities was further calculated in **Chapter 5** as our goal is to predict future drought, or the ratio of water consumption to freshwater available, in 2030 and 2050. Since water consumption for household, industry and ecosystem totals up the most of water consumption in urban areas, the three types of water consumption were estimated based on the data of population, GDP (gross domestic product) and ET (evapotranspiration). LandScan global population data was used to analyze the change in the three representative cities by using local statistical data to verify them. MODIS (moderate-resolution imaging spectroradiometer) derived ET (evapotranspiration) was used to rectify GLDAS modeled ET to make the latter able to represent the whole study area.

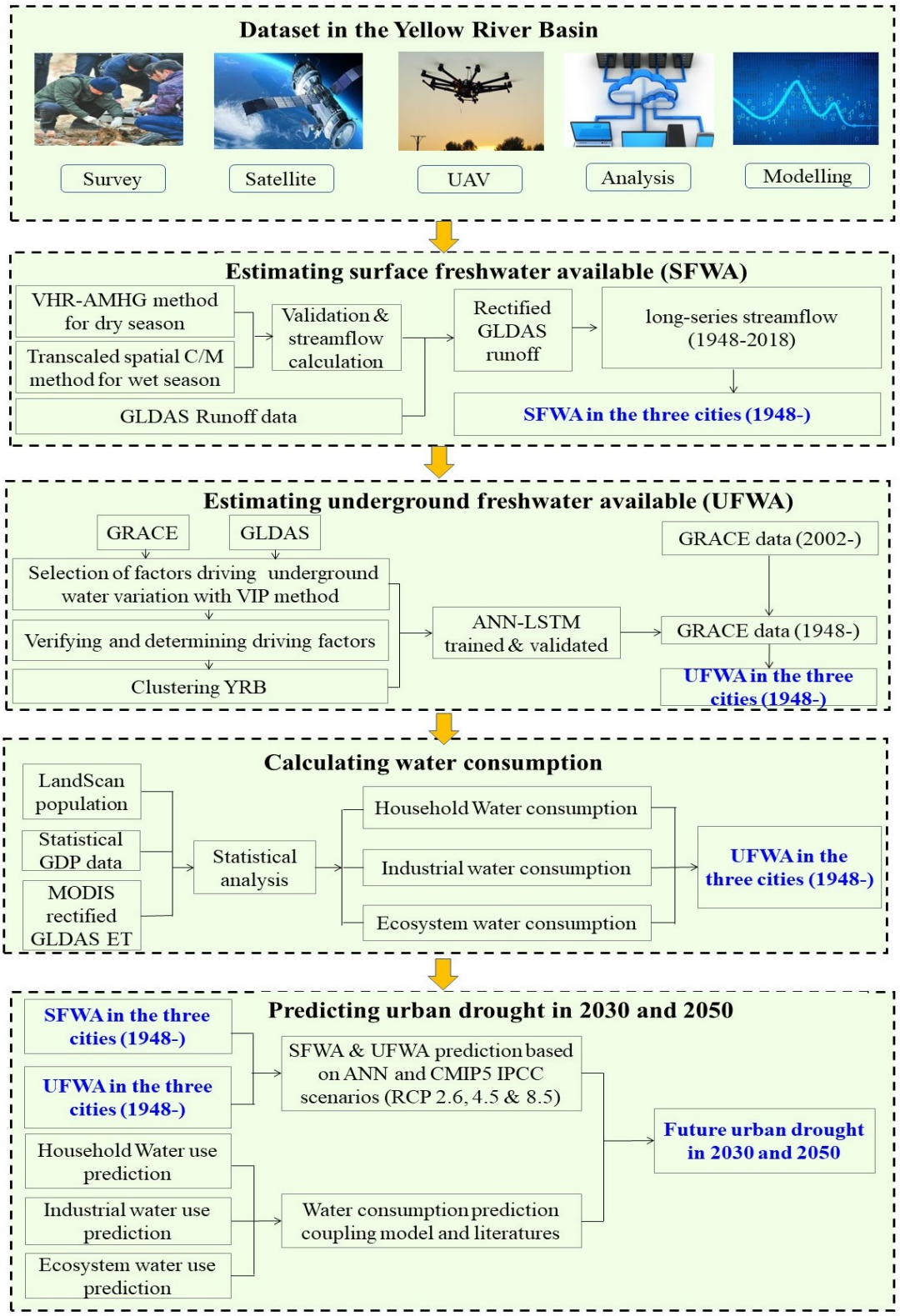

Fig. 1-2 Flow chart of this dissertation conducted in the Yellow River basin (YRB). UAV: Unmanned Aerial Vehicle; ANN: artificial Neural Network; GRACE: NASA's Gravity Recovery and Climate Experiment; GLDAS: Global Land Data Assimilation System; GDP: Gross Domestic Product; ET: Evapotranpiration.

Finally, with CMIP5 (Coupled Model Intercomparison Project Phase 5) IPCC senarios and based on the results for total freshwater available and water consumption, future urban drought,

or the ration of total water consumption to total freshwater available, for 2030 and 2050 was analyzed with help of literature and ANN predictions in **Chapter 6**. The total freshewater available includes SFWA and UFWA. The SFWA was predicted by setting up ANN (Artificial Neural Network) with SFWA estimated in Chapter 3 as output and environmental factors presented in CMIP5 influencing the variation of surface freshwater.as input variables. Likely, UFWA was predicted by setting up ANN with UFWA estimated in Chapter 4 and CMIP5-environmental factors. CMIP5 IPCC scenarios of RCP 2.6, RCP 4.5 and RCP 8.5 were used where principal environmental factors in 2030 and 2050 were presented. The future water consumption in 2030 and 2050 for household/industrial/ecosystem, was predicted based on models established in Chapter 5 and predicted data presented in published literatures.

1.6.2 Outline of the dissertation research

This disseratation focuses on the prediction of future urban drought in 2030 and 2050. Its organization is as follows: Chapter 1 introduces the research background and state of the art as well as motivation. Chapter 2 introduces data used and the characteristics of the study area. Chapter 3 explores new ways to retrieve streamflow in data-scarce areas to help more accurately calculate available freshwater in urban areas when assessing drought. Chapter 4 designs a new framework for estimating underground freshwater available wherein the data series of GRACE was extended from the last two decades to more than seven decades from 1948. Chapter 5 calculates the water consumption of three-sectors of household, industry and ecosystem to reflect the situation of water consumption when assessing drought. Chapter 6 predicts future urban drought in 2030 and 2050 including prediction of freshwater available and water consumption, based on models established in Chapters 3-5 and data presented in CMIP5 IPCC scenarios as well as published literatures. Chapter 7 concludes the research results and suggests related topics worth ongoing research.

.

Chapter 2 Data and study area

This chapter introduced all data used in this study as well as the study area. In the data collection section, satellite and UAV (unmanned aerial vehicles) data—imageries and their derived geophysical products, GLDAS (Global Land Data Assimilation System) data, ground observed and statistical data were introduced. Afterwards, study area characteristics of land use, river, underground water, vegetation and economy /society were introduced.

2.1 Data collection and verification

In this section, satellite / UAV data, GLDAS data and ground observed / statistical data are collected.

2.1.1 Satellite and UAV data

Satellite and UAV imageries (including Landsat, Sentinel and UAV), their derived geophysical products (derived from GRACE--the Gravity Recovery and Climate Experiment, MODIS-- moderate-resolution imaging spectroradiometer), and data from GLDAS are introduced in this section.

(1) Satellite and UAV imagery

(a) Landsat

Landsat satellite data have been available since the early 1970s. Onboard the early series Landsat satellites 1–5 were MSS sensors with four spectral bands in the visible to near-infrared spectral range at an approximate spatial resolution of 60 m; band 4 of Landsat 5 MSS failed in 1995. The TM onboard Landsat 4 and 5 satellites with seven spectral bands covered the shortwave range at a resolution of 30 m from 1984 to 2011 (He et al., 2018). Since then its imagery has become an important data resource in environmental remote sensing due to its moderate spatial resolution, multiple spectral bands and continuous observation (Kun 2008). Landsat Thematic Mapper (TM), launched in 1984 and retired in 2012, provided nearly 30-year continuous imaging of the Earth. TM collects seven multispectral bands: six bands in 30 m pixel size from blue to mid-infrared regions of the electromagnetic spectrum and one band in 120 m pixel size on thermal-infrared region. The major application of Landsat TM imagery is to detect the land use and land cover changes over time (Jensen 1986). Landsat TM imagery has seven spectral bands, and information in certain bands is redundant, which can reduce the accuracy in water extraction (Zhong and Wang, 2006). In this study Landsat TM images, corresponding to the ground-measurement periods (2007-2009), will be used. Among the seven bands the band 4 (0.76-0.96 μm) with a high spatial resolution (30 m) is used in this study for velocity estimation. By cloud filter and NIR value anomaly filter, we select 27 images covering the study area. All the images were acquired from https://earthexplorer.usgs.gov.

(b) Sentinel

To better monitoring the water surface in the study area, we also used Sentinel-1 radar data. In the frame of the Global Monitoring for Environment and Security (GMES) Space

Component program, the European Space Agency (ESA) undertook the development of a European Radar Observatory (Sentinel-1), a polar orbiting two-satellite constellation for the continuation and improvement of SAR operational services and applications. Satellite and payload are being built to provide routine, day-and-night, all-weather medium (typically 10 m) resolution observation capability. Ground infrastructure is provided for planning, mission control, data processing, dissemination and archiving. Free and open data access is provided. Data quality of the Sentinel-1 data products is shown along with uncertainty estimation of retrieved information products confirming specified performance and indicating application growth potential. The unique data availability performance of the Sentinel-1 routine operations makes the mission particularly suitable for emergency response support, marine surveillance, ice monitoring and interferometric applications such as detection of subsidence and landslides. Sentinel-1 is designed to work in a pre-programmed conflict-free operation mode, imaging global landmasses, coastal zones, sea–ice, polar areas, and shipping routes at high resolution, and covering the global ocean with imagettes. The Sentinel-1 mission comprises a constellation of two polar-orbiting satellites, operating day and night performing C-band synthetic aperture radar imaging, enabling them to acquire imagery regardless of the weather (https://sentinel.esa.int/web/sentinel/missions/sentinel-1). This ensures a reliability of service required by operational services and a consistent long-term data archive built for applications based on long time series. Sentinel-1 revisit and coverage are dramatically improved with respect to the ERS-1/2 SAR and ENVISAT ASAR. The two-satellite constellation offers six s free operations based on two main operational modes allowing exploiting every single data take. To deal with user requirements for both high and medium resolution data conventional SAR system designs include different operational modes that either optimize the spatial resolution (at the expense of the swath, hence the coverage) or the swath width (at the expense of the resolution). Taking account of data access through GMES to complementary national very high-resolution SAR missions (TerraSAR-X by DLR/Astrium GmbH, Cosmo-SkyMed by ASI) Sentinel-1 has been designed to address primarily medium to high resolution applications through a main mode of operation that features both a wide swath (250 km) and high geometric (5 m × 20 m) and radiometric resolution. Over sea–ice and polar zones or certain maritime areas, an extra-wide swath mode may be used to satisfy the observation requirements of certain service providers (e.g. sea–ice monitoring), to ensure in particular wider coverage and better revisit time by sacrificing geometric and radiometric resolution (Torres R et al.2012).

The Sentinel-1 mission is designed as a two-satellite constellation. The identical satellites orbit Earth 180° apart and at an altitude of almost 700 km. This configuration optimises coverage, offering a global revisit time of just six days. This study did not exploited Sentinel-2 imagery because we used landsat imageries for the purpose of long-termed stream flow retrieval as landsat has been launched more than 50 years and has a very long series of imageries. Meanwhile, satellite data with higher spatial resolution but shorter time-series than landsat TM as Sentinel-1 imagery were also used as complement of landsat imageries.

(c) UAV

A large-scale field survey of the entire study area was carried out during September of 2016 in the Jinan City, downstream the YRB. The UAV flew across nine rivers (for one river, a

total of 11 river segments in the upper, middle, and lower reaches were covered) and collected a total of 2,477 photographs. From 200 to 300 images per station were taken using a controlled flight method, with the photograph shooting overlap rate set to 90% to ensure the accuracy of the subsequent software-generated data such as stereo image pair, point cloud, and digital surface model (DSM) datasets. The generated DSM had a spatial resolution of from 2.22 cm (flight altitude: 50 m) to 4.23 cm (flight altitude: 50 m) (Zhang et al., 2018).

The UAV used in this study was DJI Phantom-3-pro small drone, which has the advantages of light weight, low cost, flexibility, portability, and high speed. It was equipped with a DJI FC300X camera with a field of view of 94°, which produced photographs 4000 × 3000 pixels in size. The basic parameters of the UAV are shown in Figure 2-1. The flight control software used was Pix4Dcapture developed by the Pix4D team (https://pix4d.com/).

Basic parameter of UAV

UAV Product	Phantom-3-pro
Camera	FC300X
Camera Sensor	Sony Exmor R CMOS
Max Photo Resolution	4000×3000
Max Aperture	f/2.8
Focal Length	20mm
Field of View (FOV)	94°
Max Flight Altitude	500m
Max Flight Time	23min

Fig. 2-1 DJI Phantom-3-pro drone and its basic parameters

UAV were used to collect the topography data of rivers at lower Yellow River where flight environment is favorable and river cross-section is stable, permitting the produce of high precision topography data. The basic parameters of the UAV are shown in Table 2. The UAV flew across 2 rivers (BDK, ZGNL) and collected 200 to 300 images per river using a controlled flight method, with the photograph shooting overlap rate set to 90% so as to ensure the accuracy of the subsequent software-generated data such as stereo image pair, point cloud, and digital surface model (DSM) datasets, which are generated in Pix4dMapper Software (Version 2.0.104). The generated DSM had a spatial resolution is 2.22 cm when flight altitude is set on 50 m (Zhang et al., 2018), and the elevation precision were verified by Total Station, which were implemented during flight. The results show that the RMSE between UAV data and Total Station measured data is 24 cm in BDK, where the channel is dried up, while the RMSE between UAV data and field data in ZGNL is 23.6 cm above the water, where the channel is partly drown by water, indicating that UAV can obtain high precision above-water cross-section data (Zhao et al., 2017; Zhao et al., 2019).

(2) Geophydical products

(a) From GRACE

The GRACE mission was launched by NASA and the Germany Aerospace Centre in 2002, to provide global mass change information by detecting gravity field changes. It is the first

dedicated satellite time-variable gravity mission and provides an alternative and unique approach for monitoring large-scale mass changes in the Earth system (Tapley et al., 2004). Since its launch in March 2002, GRACE has been measuring global gravity changes monthly, with unprecedented accuracy (Wahr et al., 2004). Earth gravity changes are caused by mass redistribution within different components of the Earth's system, including the atmosphere, ocean, hydrosphere, cryosphere, and solid Earth. GRACE-observed gravity changes can be used to infer terrestrial water storage (TWS, the sum of snow water equivalent, surface water, soil water, and groundwater storage) changes, given that other geophysical causes of gravity change can be estimated and removed (e.g., Wahr et al., 2004; Chen et al., 2009). As atmospheric and oceanic contributions to gravity change have been removed in GRACE data processing using estimates from numerical models (Bettadpur 2012), over non-glaciated land areas, GRACE-observed mass changes mostly reflect TWS changes. The TWS anomaly (TWSA) data are provided by 11 institutes including CSR (Center for Space Research, USA), GFZ (Geo Forschungs Zentrum, Germany), JPL (Jet Propulsion Laboratory, Japan) and GRGS (Groupe de Recherche de Géodésie Spatiale, France), as shown in Table 1. Yao (2017) estimated the uncertainties of the solutions in China, showing that the solution of CSR has the minimum uncertainty with an error of 13.2 mm as that of GRGS has the maximum uncertainty in China with an error of 58.8 mm. Therefore, this study selected CSR monthly solutions as the source of GRACE data. The new version CSR solutions were pre-processed with a Gaussian filter and can be directly used after downloading. The new version GRACE TWSA (or TWSC) dataset expresses the water storage anomaly with equivalent water column height at a spatial resolution of 0.25°× 0.25°, covering the period of 2002 to 2016.

(b) From MODIS

To calculate ecosystem evaporation, this study used the method developed by Twine et al. (2000) and Yao et al. (2013) to calculate the latent heat (LE) according to $\mathrm{LE} = (R_n - G)/(\mathrm{LE}_{ori} + H_{ori}) \times \mathrm{LE}_{ori}$ where LE is the corrected latent heat flux, and H_{ori} and LE_{ori} are the uncorrected sensible heat flux and latent heat flux, respectively. The 8-day MODIS FPAR/LAI (MOD15A2) product (Myneni et al., 2002) with 1 km spatial resolution was used to drive the LE algorithms in this study, and the daily FPAR/LAI values were temporally interpolated from the 8-day averages using linear interpolation. Similarly, the 16-day MODIS NDVI/EVI (MOD13A2) (Huete et al., 2002) and MODIS albedo (MOD43B3) products (Liang et al., 1999; Schaaf et al., 2002) were also used to validate the LE models. The basis of the above research is GLASS system. The GLASS system can be used to generate five land surface remote sensing products: Leaf Area Index (LAI), shortwave broadband albedo, broadband emissivity (BBE), downwelling shortwave radiation (DSR), and photosynthetically active radiation (PAR). The newest algorithms that utilize multi-source remote sensing data, such as MODIS and AVHRR, to generate GLASS products are integrated into the system. The GLASS product generation system was designed to implement high-performance computing (HPC) on a clustered environment. The system also has relatively high efficiencies for utilizing the distributed and parallel computing techniques. Five GLASS products have been generated with the system. The five products are eight-day LAI, albedo and BBE products with resolutions of 5 km and 1 km for the years before and after 2000, respectively, and three-hour DSR and PAR

datasets with a 5-km resolution from the years 2008 to 2010. In the GLASS system, MODIS and AVHRR data were used as input data to generate GLASS products. The data quality of the MODIS and AVHRR images was greatly influenced by clouds, cloud shadows, snow, and other abnormal climate conditions, which hindered the surface reflectance inversion and further impacted the GLASS products' quality. Some data, such as AVHRR, MOD09A1, MOD09GA, MCD43B3 and MOD02, were preprocessed before they were used to produce the GLASS products. To improve the data quality, the existing MODIS snow and cloud mask and the reflectance characteristics of the non-snow/cloud pixels were used in combination to identify pixels of snow, clouds and abnormal values. All of the identified values were filled by the clear pixel values over a long period of time to remove the effects of snow, clouds and cloud shadows (Zhao et al.2013).

Another important source for ecosystem evapotranspiration estimation is MODIS satellite data. To take full advantage of MODIS's multi-angular and multi-spectral observation ability, a physical algorithm based on Radiative Transfer (RT) was developed for generating MODIS LAI/FPAR products (MOD15) (Knyazikhin et al.1998; Knyazikhin 1999). The MODIS science team aims to provide users with better products by updating product cohorts that are called collections. Since the launch of Terra in December 1999, MODIS land data records have been reprocessed four times. Having stage one validation status, Collection 3 (C3) is the first release of MODIS LAI/FPAR products and covered the period of November 2000 to December 2002. The product accuracy of this version has been estimated using ground measurements obtained from some field campaigns (Yang et al.2006a). Collection 4 (C4) covered the period from February 2000 to December 2006 and benefited from the improved inputs and updated look-up-tables (LUTs) (Yang et al.2006b). Aimed at reducing the impact of environmental conditions and temporal compositing period, Collection 5 (C5) combined Terra- and Aqua-MODIS sensor data and generated four LAI/FPAR products from February 2000 to present (Yang et al.2006c). In addition, C5 used a static 8-biome land-cover map instead of previous 6-biome one. Algorithm refinements were carried out over all biomes but with a major focus on woody vegetation for which a new stochastic RT model was utilized (Shabanov et al., 2000; Yan et al., 2016).

(3) GLDAS database

The Global Land Data Assimilation System (GLDAS) was jointly developed by scientists at NASA, GSFC, NOAA and NCEP to provide terrestrial water and energy storages data. It drives four land surface models: Noah, CLM (Community Land Model), VIC (Variable Infiltration Capacity) and Mosaic, incorporating both ground and satellite-based data (e.g., the global land cover and soil type dataset). The model output produced by the Noah land surface model includes soil moisture data (10, 30, 60 and 100 cm, from the soil surface down), snow water equivalent, evapotranspiration, canopy water storage. In this project, we collected the monthly data simulated by Noah from NASA (http://ldas.gsfc.nasa.gov/index.php) at spatial resolutions of 0.25°× 0.25°, from 1948 to 2010 and from 2011 to 2016, respectively.

Subsequently, a theoretical uncertainty analysis was conducted showing that the GLDAS has an averaged standard deviation (Std) of random error value of less than 3.6 mm/8 day. For various vegetation structures considered, the absolute uncertainties generally follow the order

of best to worst (grassland < rice paddy < forest) for GLDAS. Similarly, the relative uncertainty analysis also demonstrated better performance of the GLDAS dataset with less (20%, 11% and 32%) uncertainties compared to those obtained for MOD16 (15%, 38% and 36%), and flux tower (25%, 32% and 27%) measurement (forest, rice paddy, and grassland) at point scale, respectively. The ranking of grid-based uncertainties for three (MOD16, GLEAM, GLDAS) datasets showed their tendency to produce better estimations in the respective proportion of (12.3%, 55.5%, 32.2%) in forest, (4.9%, 46.2%, 48.9%) rice paddy, and (5.3%, 39.4%, 55.4%) grassland which constitutes approximately ~75% of the total study area. The merged product developed by combining the least uncertainties of the three datasets revealed the better accuracy for GLDAS (47%) followed by GLEAM (42%) and MOD16 (11%) over the entire study region (Khan et al., 2018).

2.1.2 Ground data

(1) Hydrological data

In total, ground monitored hydrological data of eight stations in the Yellow River basin (YRB) were collected. Two in the lower reach—Jinan City, and six in the middle reach of YRB—Shaanxi City. In the lower reach, the cross-sections data of two stations (BDK & ZGNL) were collected by Total Station during UAV flight. In middle Yellow River, or the Wei River, river discharge, river velocity, water level and cross-sections of six typical stations during the period of 2007–2009 were obtained and qualified by the hydrological bureau of the Yellow River Conservancy Commission, whose main responsibility is monitoring, collecting and distributing this information regarding the Yellow River. The measurement criteria of the data for different years were consistent through the entire recorded period, and the data quality for the discharge and velocity was strictly controlled before the data were released. The collected river discharge and river velocity were linearly interpolated to daily scale for matching the satellite images, while river velocity is used for calibration and validation of newly developed method in this study, the river discharge is only used for validation. Cross-section data were used to inverse the shape and area of the underwater cross-section.

(2) Local / regional statistics (GDP)

The gross domestic product (GDP) data for the three representative cities of Xi'an, Zhengzhou, and Jinan can be found in the Provincial Statistic Yearly book. A few past yearly book can be accessed via China Academic Journal Network Publishing Database (CNKI) https://kns.cnki.net/, or statistic book share websites, e.g., https://www.yearbookchina.com/index.aspx. The statistic data can be accessed from before 2000 to 2019.

2.2 Characteristics of study area

The studies will be conducted taking as the study area the Yellow River Basin (YRB), China with an area of 752,443 km^2 (Fu et al., 2004), taking as examples big cities with population great than 5 million as example, e.g., Jinan, Zhengzhou, Xi'an in the Yellow River Basin. Accordingly, the middle reach where Zhengzhou and Xi'an locate, and the lower reach where the Jinan locates will be taken as key area for studying. The middle and upper reaches

of the basin are affected by climate, topography, water resources and economic development where the population is sparse and increasing rate is slow. The conflict in water use between human and nature is severe. The downstream area is economically developed and is the densely populated area of the entire basin (Song, 2018).

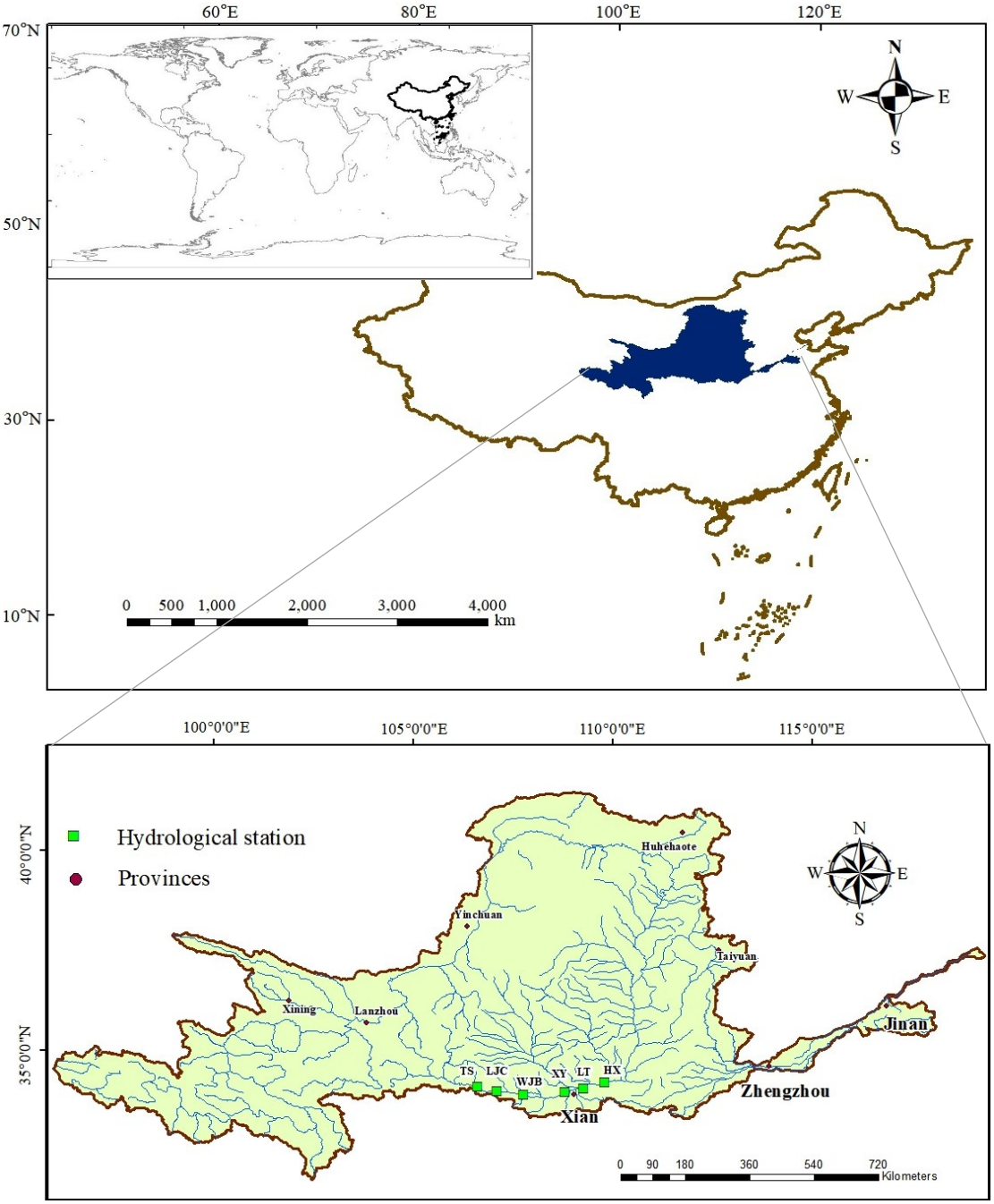

Fig. 2-2 Location of stations and important cities in the YRB.

2.2.1 Land use &vegetation

There are many types of vegetation in the YRB where the type of land use is complex and

diverse (Figure 2-3). The principal land use type in the entire basin is agricultural land, while non-agricultural land and water areas account for a relatively small proportion. The principal type of agricultural land includes cultivated land and grassland, which respectively account for 28.84% and 48.48% of the agricultural land area in the entire basin (Yan et al., 2006; Xie, 2020). The Yellow River Basin is an important base of agricultural products and grain production area in China. The area of agricultural arable land is 15.509 million hm^2, accounting for 13% of the country (Jiang et al., 2017; Zhang, 2019).

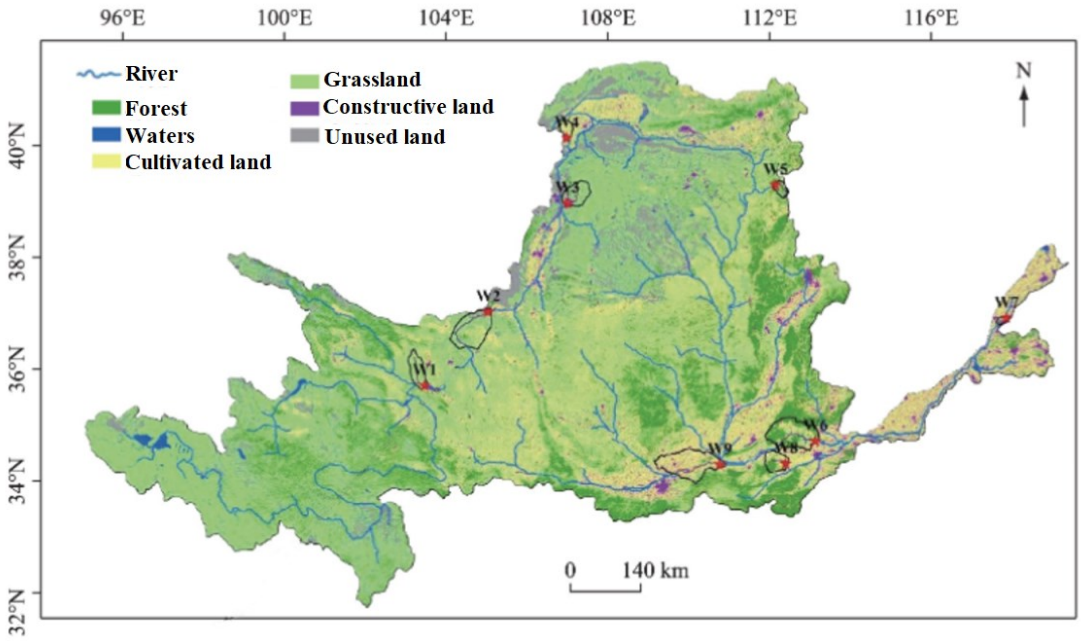

Fig. 2-3 Land use and rivers in the YRB (modified from Guo et al., 2021)

Affected by climate, hydrology and topography, the vegetation in the Yellow River Basin mainly includes grasslands, alpine vegetation, meadows and swamps, artificial woodlands, temperate coniferous forests, temperate broad-leaved forests, shrubs, deserts and sand plants. The distribution of vegetation is in a synchronous trend with the distribution of precipitation, which is distributed in strips from southeast to northwest. The vegetation types in the upper reaches of the Yellow River are dominated by grasslands. Meadows and grasslands account for more than half of the vegetation area of the Yellow River Basin. Grasses, meadows and alpine vegetation are widely distributed in plateau areas. Among them, meadows are mainly distributed in the Qinghai-Tibet Plateau, and grasslands are distributed in the Loess Plateau; grasses and shrubs are mostly distributed in the middle reaches of the YRB; coniferous and broad-leaved forests are mixed in the lower reaches of the YRB (Zhu, 2019). The diverse types of ecosystems in the Yellow River Basin have created favorable conditions for the development of various types of vegetation, and the vegetation types are regionally representative and typical. The vegetation of crops, grasslands, forests and shrubs account for 98% of the entire watershed, and the remaining 2% are vegetation types such as tundra and herbaceous swamps (Fan, 2017). Vegetation in the YRB is affected by horizontal zonality and monsoon. From east to west, it is crops, broad-leaved forest, coniferous forest, grassland and sparse shrub grassland (Zhang, 2019). The YRB includes many plateaus, plains, valleys, and many rain-fed irrigated agricultural areas. From the perspective of crop planting structure, wheat and corn are the

largest and most widely distributed crops in the YRB, accounting for 30% and 27% of the total sown area respectively (Song, 2017; Zhang, 2019).

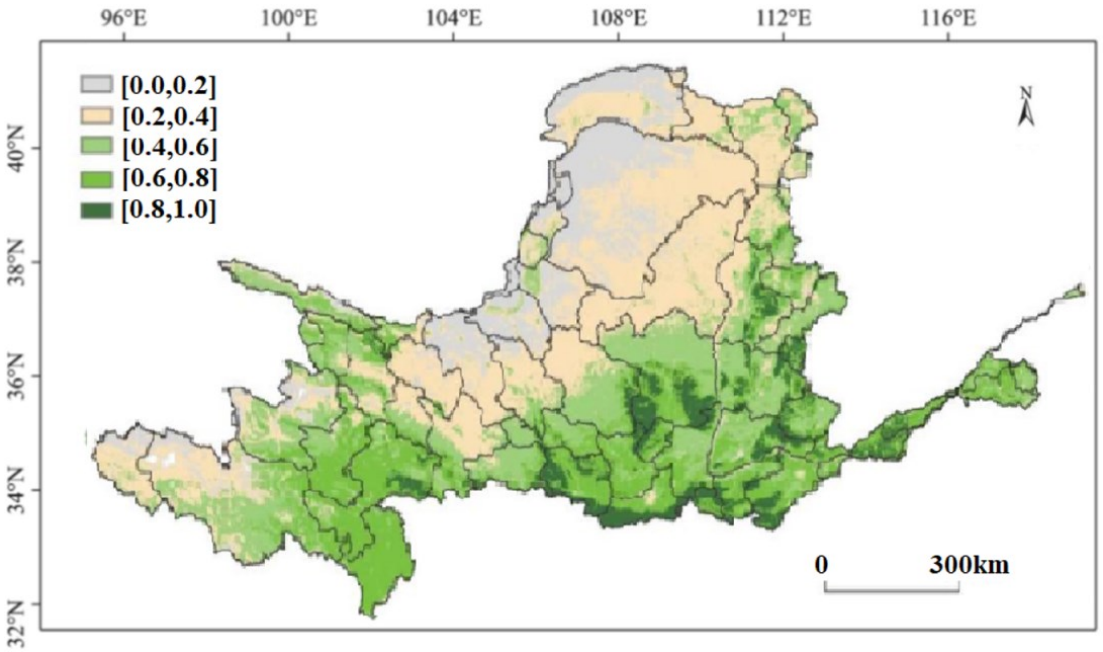

Fig. 2-4 Multi-year averaged fractional vegetation cover in the YRB (modified from Zhang et al., 2021)

2.2.2 Rivers

The Yellow River is the second longest river in China (after the Yangtze River) and the fifth longest river in the world. The main river is about 5,464 kilometers in length. It originates from the Qinghai-Tibet Plateau, or the third polar of the world. After flowing through Qinghai, Sichuan, Gansu, Ningxia, Inner Mongolia, Shanxi, Shaanxi, Henan and other provinces in turn, it finally flows into the Bohai Sea of China (Huang et al., 2015; Xie, 2020). There are many tributaries of the Yellow River. From the source to the estuary, there are 220 tributaries with a drainage area greater than 100 km^2; 76 of the tributaries have an area greater than 1000 km^2 with the drainage area is 580,000 km^2, accounting for 77% of the total river catchment area; there are 11 tributaries larger than 10,000 km^2 with a drainage area of 370,000 km^2, accounting for 50% of the river catchment area. The principal tributaries of the Yellow River have more than 20 among which the Wei River is the largest (Zhou, 2020). The representative city studied in this paper -- Xi'an City is in the tributary--Wei River; Zhengzhou and Jinan are located on the main stream of the Yellow River.

The Yellow River Basin (YRB) is located between 95°E-119°E and 32°N-41°N. The drainage area is about 795,000 km^2 (including the internal flow area of 42,000 km^2). The drainage area crosses the Qinghai-Tibet Plateau, the Inner Mongolia Plateau, the Loess Plateau and the North China Plain, with the average altitude more than 3000 m. and the terrain gradually low from west to east. There are great differences in climatic types and landforms among the sub-basins (Wang et al., 2012). According to its hydrological characteristics and geographical types of the Yellow River basin, the entire basin can be roughly divided into upstream, middle and lower reaches (Figure 2-3). The total length of the upstream river is 1206.4 km with a control area of ~428,000 km^2, accounting for 53.8% of the total drainage area. The boundary

between the middle and lower reaches of the Yellow River is located at Zhengzhou City, Henan Province. The total length of the middle reach is about 1206.4 km with a control area of ~344,000 km, accounting for 43.3% of the entire basin area. The total length of the downstream river is about 785.6 km with a control area of 23,000 square kilometers, accounting for about 3% of the entire basin area (Xie, 2020).

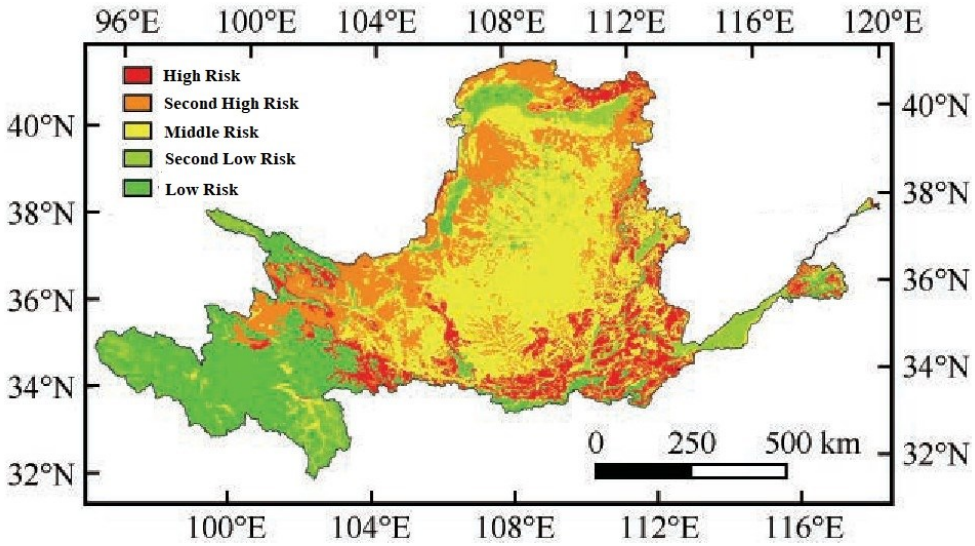

Fig.2-5 The spatial distribution of comprehensive drought disaster risk assessment in Yellow River Basin (Han et al, 2021)

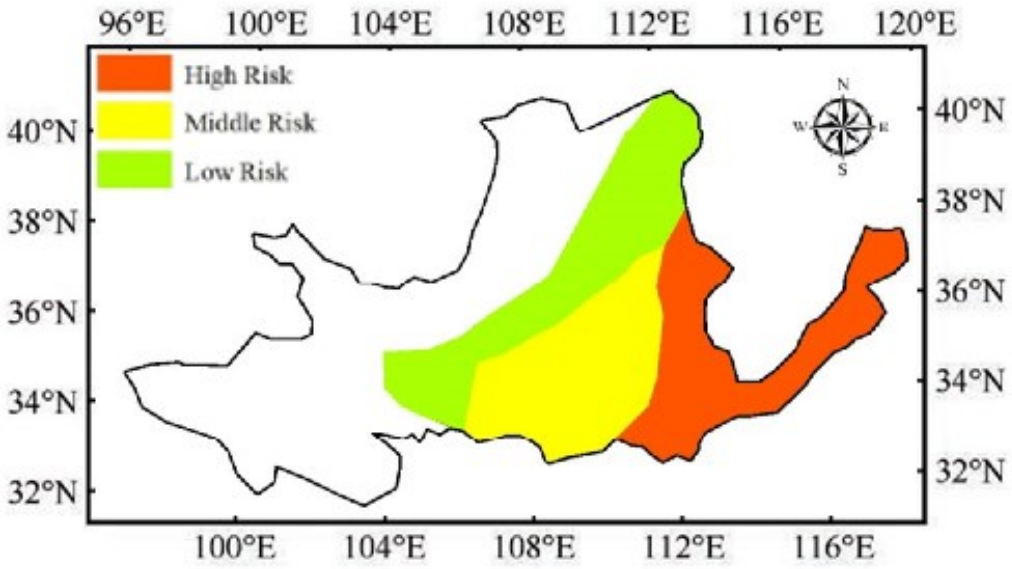

Fig.2-6 Regions Divided by risk of drought and flooding (modified form Lv 1998)

2.2.3 Underground water

The annual-average total water resources of the YRB are 71.9 billion m^3, of which surface water resources are 60.7 billion m^3 and groundwater resources are 11.2 billion m^3 (Tao, 2020). The Yellow River Basin seriously over-exploited groundwater. The total groundwater withdrawal has increased from 336 k m^3 in 2003 to 412 k m^3 in 2015. In recent years, the amount of groundwater extraction has gradually increased. In some areas, 12 shallow

groundwater funnels have been formed, and three of them are serious over-exploited. In general, the Yellow River Basin has insufficient and uneven inter-annual distributed water resources, which limits the sustainable development of the social economy to a great extent (Wang, 2020).

The total amount of groundwater withdrawal in the basin was 12.327 billion m^3 in 2015, of which urban public water withdrawal was 576 million m^3 accounting for 4.7%; residents water withdraw was 1.975 billion m^3 accounting for 16.0%; that for ecological environment was 267 million m^3 accounting for 2.2%. The proportions of groundwater withdrawal in different industries of the YRB in 2015 are shown in Figure 2-7.

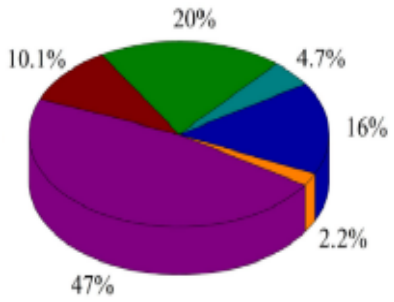

Fig. 2-7 Ground withdraw in the YRB in 2015 (modified form Zhang 2019)

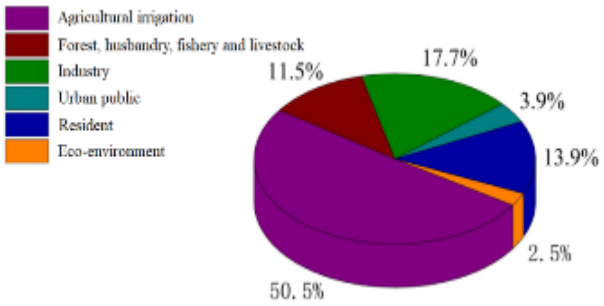

Fig. 2-8 Ground water consumption in the YRB in 2015 (modified form Zhang 2019)

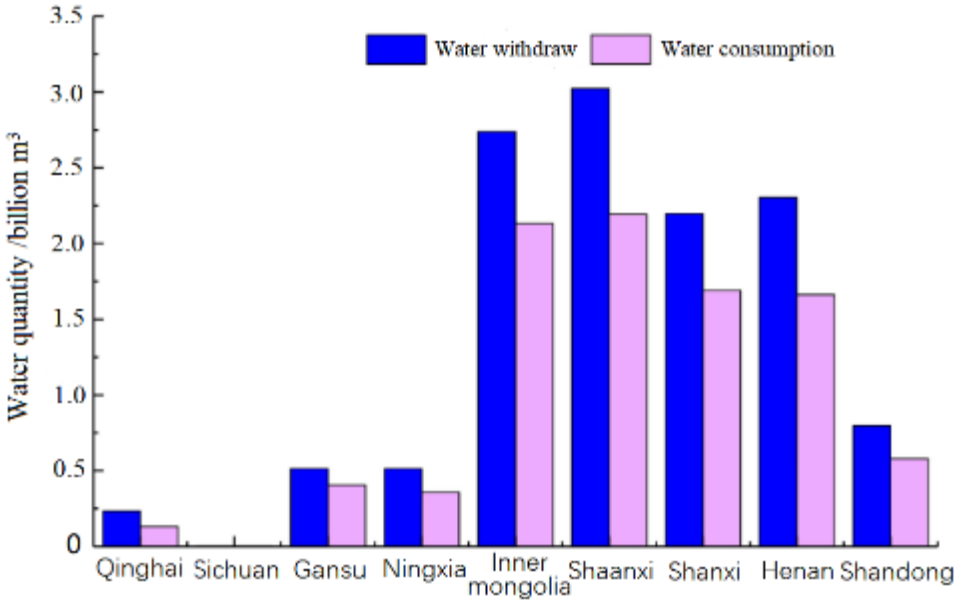

Fig. 2-9 Groundwater withdraw and consumption in provinces crossed by the Yellow River (modified form Zhang 2019)

As to the total water consumption of groundwater in the basin in 2015 was 9.171 billion m^3, of which 4.633 billion m^3 was consumed by agricultural irrigation, accounting for 50.5% of the total groundwater consumption in the whole basin. The water consumption of forest, animal husbandry, fishery and livestock are ~11.5% of the total. Water consumption by industry accounted for 17.7%, by urban public accounted for 3.9%, by residents accounted for 13.9%, by ecological environment accounted for 2.5%. The proportion of total groundwater

consumption of various industries in the YRB is shown in Figure 2-8.

Among all provinces the Yellow River crossed, Shaanxi Province, where Xi'an is located, has the largest amount of groundwater withdrawal and the largest water consumption, with a water withdrawal of 3.024 billion m^3 accounting for 24.5% of the total groundwater withdrawal in the basin; also with a water consumption of 2.193 billion m^3, accounting for 23.9% of the total groundwater consumption in the basin, as shown in Figure 2-9.

Human activities and climate change together resulted in a decrease in the amount of water resources. With the increasing population size year by year and the rapid economic growth in the river basin, water consumption has increased by 3.130 billion m^3 in the past 20 years, which further intensified the contradiction between water supply and demand, and therefore restricts the sustainable development of the economy and society (Zhang, 2019). The impact of climate change on the water resources of the YRB has two aspects: climate change affects the hydrological cycle of precipitation and evapotranspiration, and causes changes in surface runoff; climate change has also led to changes in the temporal and spatial distribution of hydrological elements such as surface-, ground-, and soil-water in the basin, which in turn caused the migration and redistribution of water resources in the basin (Xie, 2020).

2.2.4 Population

The YRB is the birthplace of Chinese civilization. Since the reform and opening up of China, the total population of the basin has continued to grow. The total population in 2000 was 135.42 million, accounting for 10.45% of the total population of China. In 2015, the total population was 160.44 million, accounting for 11.67% of the total population of China, with an average annual growth rate of 7.89%. The population density in 2000 was 184.35 people/km^2, and in 2015 it was 218.43 people/km^2. At the same time, due to the large differences in natural conditions and economic conditions between the upstream and downstream, the population growth within the YRB is also regionally unbalanced (Song, 2018).

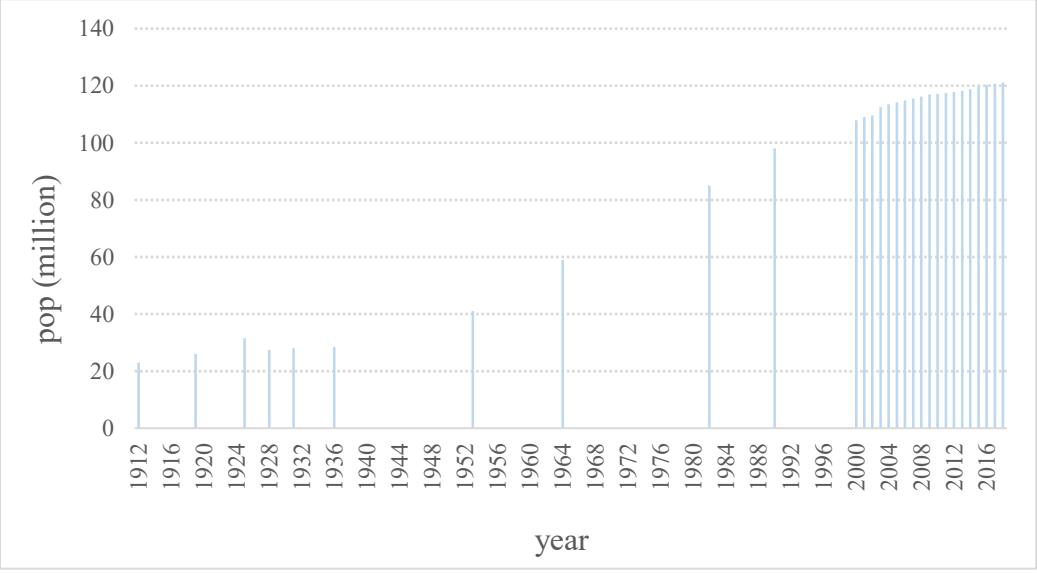

Fig.2-10 Total population in the YRB from 1912 to 2018 (Wang et al., 2009)

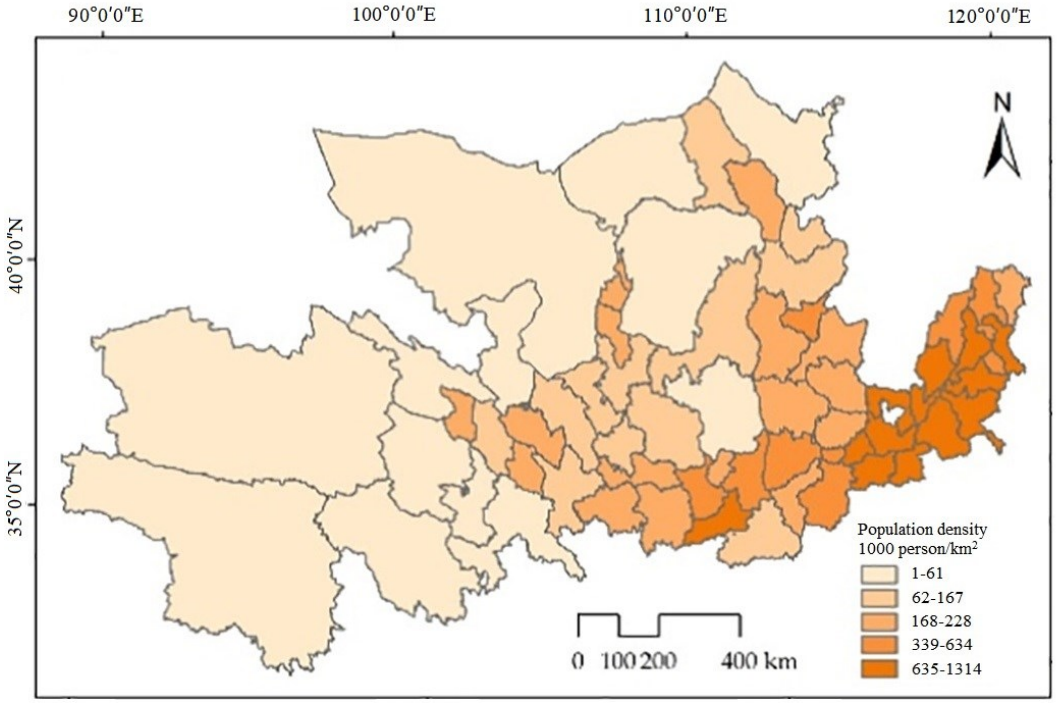

Fig.2-11 The population density in the YRB (Zhang et al 2021)

2.2.5 Economy and society

The gross national product (GDP) of the YRB is about 8 trillion RMB (about 14% of China's GDP), and the agricultural land area is about 200,000 km^2 (about 15% of China's total arable land), Mainly distributed in Henan, Shaanxi, Inner Mongolia and Shanxi provinces. Due to its important role in social and economic development, in ecological resource protection, and in agricultural and food production, the YRB has always been regarded as one of the most important research areas in China (Cai et al., 2004; Xie, 2020).

In 2017, the GDP of the basin was 6,148.8 billion RMB, and the industrial added value was 2,386.6 billion RMB. At present, the total arable land area is 191.58 million Mu, and the effective irrigation area of farmland is 81.37 million Mu (Tao, 2020). Cultivated land accounts for about 14% of China's total cultivated land, and it is an important grain producing area in China. The upper reaches of the Yellow River are highly different in topography and are rich in hydropower resources. The cities in the middle reaches of Ordos, Yulin, and Jincheng are important coal producing areas in China. The lower reaches are rich in hills, plains and rich in natural gas and oil resources, laying an important foundation for China's social and economic development (Zhu, 2019). The average GDP growth rate was 7.4%, which was higher than the national average growth rate of 6.9%. The lower Yellow River has a highly-developed economy with the area only accounts for 3% of the entire basin (Song, 2018).

Chapter 3 Estimation of surface freshwater available

This chapter aims at the first objective of this thesis to explore new ways to retrieve streamflow in data-scarce areas to help more accurately calculate available freshwater in urban areas when assessing drought. For this goal, two new methods respectively for dry and wet seasons were developed firstly; and then by using the two methods the long-termed streamflow in the Yellow River flowing by the three representative cities were retrieved by using satellite imageries; finally, based on the satellite retrieved streamflow the surface freshwater available (FWA) for the three representative cities was estimated which can be used to predict surface FWA in future 2030 and 2050.

3.1 Retrieval of long-termed streamflow for the three representative cities

3.1.1 Development of new methodologies for estimating surface streamflow by using satellite imageries

Two methods for streamflow retrieval by using satellite imageries were developed. The first one was named VHR-AMHG which is derived from Glob AMHG (Gleason et al., 2018), and the second one was named transcaled spatial C/M method, an improved version of C/M method (Tarpenelli et al., 2013). The first one has a higher accuracy in dry season yet the second one is more accurate in wet season.

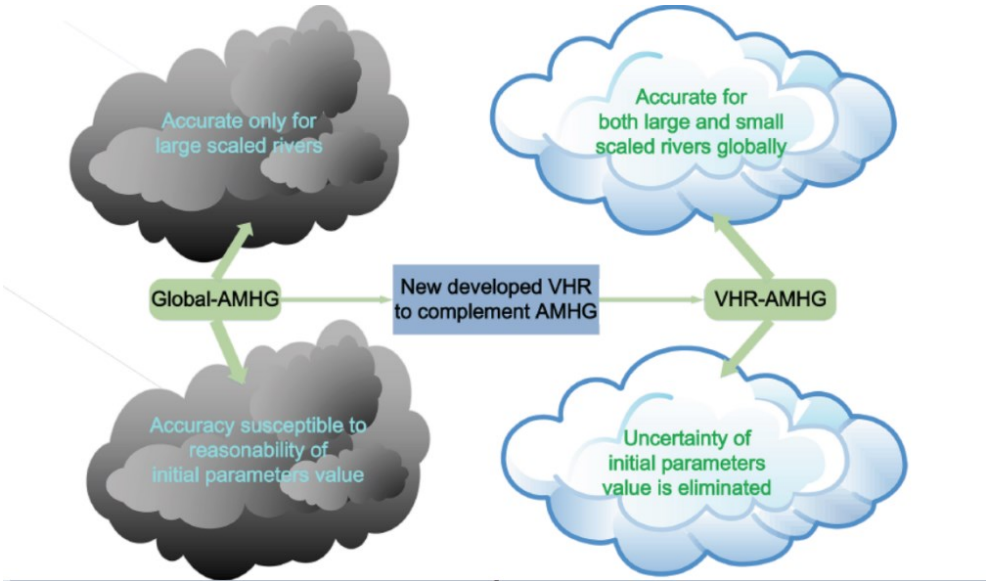

Fig. 3-1 Graphical illustration of VHR-AMHG comparing with original AMHG applicable to rivers without historical streamflow observations (priori knowledge)—Global-AMHG

(1) Surface streamflow estimation in dry seasons

Across the world many tributaries of rivers including the Yellow River have a few ground measurements on streamflow. Therefore, we developed a new framework for estimation of streamflow with few ground measurements based on high-resolution imageries, e.g., from

unmanned aerial vehicle (UAV). Among the framework a new Virtual Hydraulic Radius (VHR) method was proposed to improve AMHG (at-many-stations hydraulic geometry by Gleason et al., 2018), a method not requiring any ground measurements when global parameters are used (global–AMHG) in large-scaled rivers (with width larger than 100m) but yielding great uncertainties in smaller scaled rivers (with width less than 40 m). It is named as VHR-AMHG method for medium-to-small rivers. The accuracy verification of the proposed method was performed by comparing it to field measurement data and the global parameters of the original AMHG (global–AMHG), as shown in Figs. 3-1 and 3-2.

Gleason and Wang (2015) give a derivation of the original AMHG which is formulated as

$$b = -\frac{1}{\log(Q_c)} * \log(a) + \frac{1}{\log(Q_c)} * \log(w_c) \quad (1)$$

where 1/logQc and logwc/logQc respectively represent two important parameters, AMHG slope, AMHG intercept as described by Gleason and Smith (2014).

AMHG calculates the streamflow solely from the variation in river width, making it widely used for streamflow estimation via remote sensing (Bonnema et al., 2016; Durand et al., 2016; Gleason et al., 2014; Gleason et al., 2018). AMHG needs priori knowledge of long-termed streamflow observations to ensure its accuracy. For rivers lacking long-termed streamflow observations, it gives a set of global parameters to estimate streamflow. Trials shows that the global parameters are not applicable to medium and small rivers without long-termed past streamflow observations as priori knowledge (Zhao et al., 2019). In other words, the accuracy of AMHG with global parameters is relatively high for large rivers (average river width ≥ 100 m) but unstable for medium-to-small rivers (average river width ≤ 100 m) (Gleason et al., 2014; Feng & Gleason, et al., 2019), thus greatly limiting its application to medium-to-small rivers lacking hydrological monitoring data such as streamflow. Therefore, there is an urgent need to explore a new way to enhance the AMHG method making it applicable in medium and small rivers, especially in small tributary rivers with width less than 40 m and lacking streamflow observations.

With this method, Feng et al. (2019) presented the first assessment of the suitability of CubeSat satellite data for river discharge estimation by using Landsat 8, Sentinel-2 individual and fused satellite data sets on rivers from <20 to >1,000 m wide. Their research shows that small rivers (<40 m wide) are too small for Landsat and Sentinel-2 data sets, and their discharge is also not well estimated using CubeSat data alone. For small rivers, the method does not perform well, probably due to both the poor width extractions and worsened prior information. More importantly, a precise measurement of widths at cross section scales requires high resolution images, which makes most of the current remote sensing imagery with moderate spatial resolutions (e.g., MODIS) poor for small rivers. In addition, although Landsat and Sentinel-2 have coarser spatial resolutions (30/10/20 m) as compared to Planet (3 m), SPOT 6/7 (1.5 m), GF-7 (0.8 m) etc., the widths from these governmental satellites have lower uncertainties than those from the CubeSat due to the higher quality of Landsat 8 and Sentinel-2 imagery compared to Planet imagery. Landsat 8 can provide very accurate flow width information for large rivers, but has a very long revisiting period (~16 days), i.e., its temporal

data density is very low. Sentinel-2 can provide more usable images at finer scales, but the quality of the extracted widths is not as good as that of Landsat, likely due to cloud classification issues that introduces bias to water masks. The impact of cloud reduces the usable images of the optical satellites (Feng, Gleason, et al., 2019).

To overcome the shortcomings above, the present study used an UAV combined with SAR-based Sentinel-1 image (with 10 m resolution) to determine the topography above the water surface during dry seasons. We directly measured the water surface width from UAV-derived DEM and SAR-based Sentenel-1 image.

Based on the principle of Manning Equation, the value of R (hydraulic radius) was calculated under the assumption that the actual water surface width was the river bottom forming an incomplete virtual cross-section.

$$Q = A \cdot v = \frac{1}{n} A \cdot R^{\frac{2}{3}} \cdot S^{\frac{1}{2}} = \frac{1}{n} A \cdot \left(\frac{A}{P}\right)^{\frac{2}{3}} \cdot S^{\frac{1}{2}} \quad (2)$$

where A is the area of the cross-section (m^2); V is the cross-sectional flow rate (m/s); R is the hydraulic radius (m), which is the ratio of the cross-sectional area A to the wetted perimeter P(m); S is the gradient; and n is the roughness.

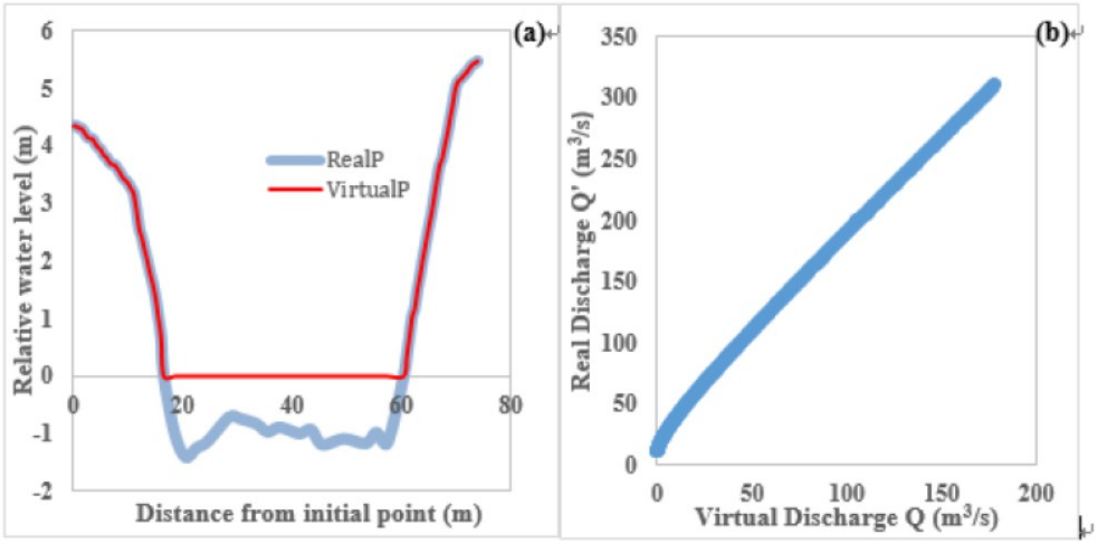

Fig. 3-2 VHR method and the Q-Q' relationship. (a) VHR diagram, in which the y axis is the relative elevation with the water surface as a reference; (b) scatter plot of the virtual streamflow (Q) and real streamflow (Q') bothcalculated from the Manning Equation at different water levels according to VirtualP and RealP

Then, the virtual streamflow (Q), instead of the real streamflow (Q'), was calculated according to the Manning Equation. If a reference station with a complete cross-section was selected in a study area, the equation for determining the real streamflow (Q') from Q could be established. The method is named as VHR (virtual hydraulic radius) method, as shown in Fig. 3-2 and Equations 7,8, and 9. In VHR, the wetted perimeter P and the water area A were calculated based on the assumed river bottom, then the hydraulic radius R at different water levels was calculated using the equation R=A/P. In Fig. 3-2a, the thin red line indicates the

assumed wetted perimeter (VirtualP) and the thick blue line indicates the true wetted perimeter (RealP). Combined with the Manning Equation (Equation 6), the virtual streamflow (Q) and real streamflow (Q') at different water levels were calculated. Regression analysis was then performed to determine the correlation between Q and Q' (Eq. 3, Fig. 3-2b) to deduce the real streamflow Q'.

Fig. 3-2a shows that there is a strong linear relationship existing between Q and Q'

$$\mathrm{Q}' = m * Q + \mathrm{n} \tag{3}$$

where m and n are linear regression coefficients. Using the streamflow Q calculated using the VHR method and Eq. 3, the Manning-Equation-based streamflow with complete cross-section data or the real streamflow Q' could be obtained. Because of the scarcity of hydrological monitoring stations along medium-to-small rivers, there is usually a lack of cross-section and streamflow data for such rivers. To apply this method to the calculation of streamflow at actual cross-sections of all rivers using the Manning Equation, a reference station must be selected to determine the initial values of m and n in Eq. 3. Considering that river width is an important characteristic reflecting the streamflow magnitude, and that medium-to-small rivers within the same study area have similar cross-section formation mechanisms, a river width ratio was introduced to obtain the coefficients m and n of other stations, as shown in Eq. 4:

$$\mathrm{WRatio} = \frac{W_1}{W_i} (\mathrm{i} = 1, \ldots, \mathrm{k}) \tag{4}$$

where WRatio is the river width ratio; W1 is the average river width (m) at the reference station; Wi is the average river width at the other stations, where i represents the station number; and k represents the total number of stations (k is equal to number of rivers we study). By combining Equations 7 and 8, a universal equation for estimating the actual streamflow at each station was obtained (Eq. 5) as follows:

$$Q' = WRatio * (m * Q + n) \tag{5}$$

By substituting Q calculated with the VHR method using UAV data into Eq. 5, the real streamflow Q' at other stations in the study area can be estimated. The results from VHR are then used to provide initial values for parameters in the AMHG. The coupled method is named as VHR-AMHG.

To validate the results from VHR-AMHG method, we compared them with that from the original AMGH method with and without priori knowledge (historical streamflow observations) as well as ground observations, as shown in Fig. 3-3.

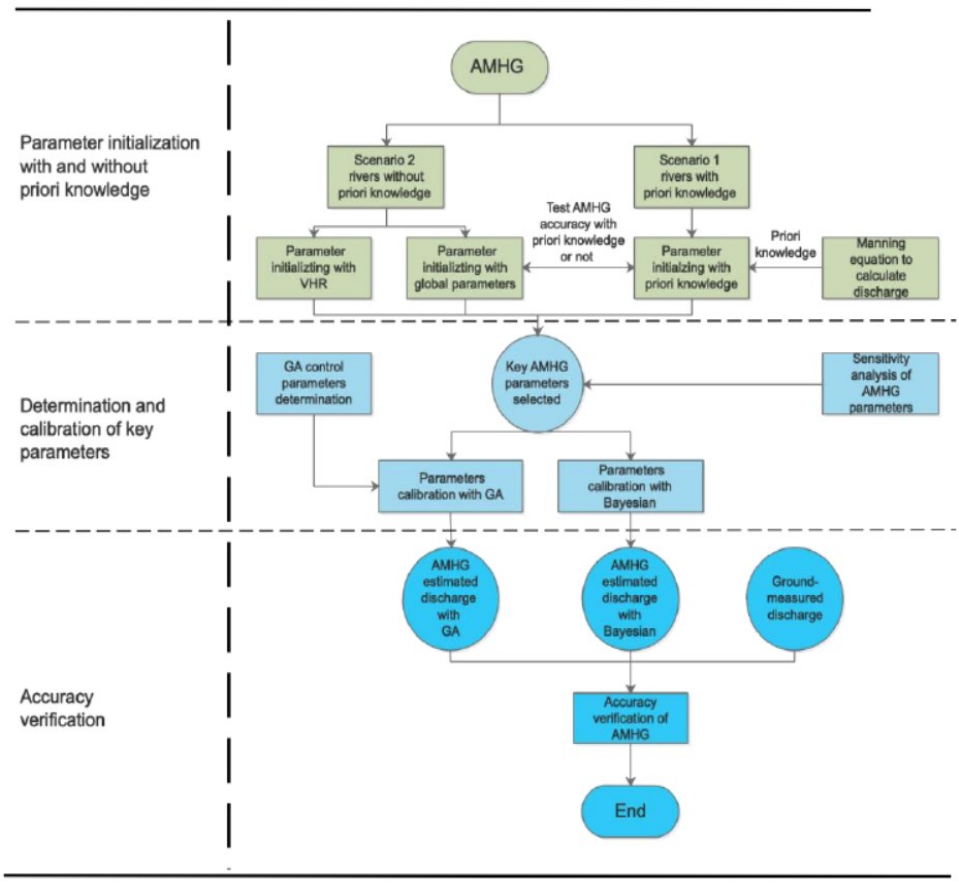

Fig. 3-3 Flowchart for VHR-AMHG validation. Two scenarios were designed: Scenario 1 with priori knowledge or long-term historical streamflow observations; Scenario 2 without priori knowledge.

The results by using the Manning Equation and the original AMHG with and without priori knowledge in medium-to-small rivers were calculated as shown in Fig. 3-4.

Fig. 3-4 shows that the Manning Equation has the best performance in streamflow calculation when comparing its results (dark blue line) with the ground measurements (gray circles). Therefore, the streamflow calculated using the Manning Equation was used to verify the AMHG accuracy. The simulations by AMHG with priori knowledge (Scenario 1) and those by the Manning Equation share the same trend, with some small errors occurring at low values. The calculated NSE (Nash–Sutcliffe efficiency coefficient) and RMSE (root mean square error) were 0.94 and 5.12 m^3/s, respectively. Results from the t-test show $P=0.73>0.05$, implying that there were no statistically significant differences between the results calculated using the AMHG with priori knowledge and those calculated using the Manning Equation. In other words, the Manning Equation based VHR method can well provide priori knowledge for AMHG.

To perform an in-depth evaluation of the error, the results of the AMHG method under these two scenarios were further verified using ground-measured streamflow data, as shown in Fig. 3-5.

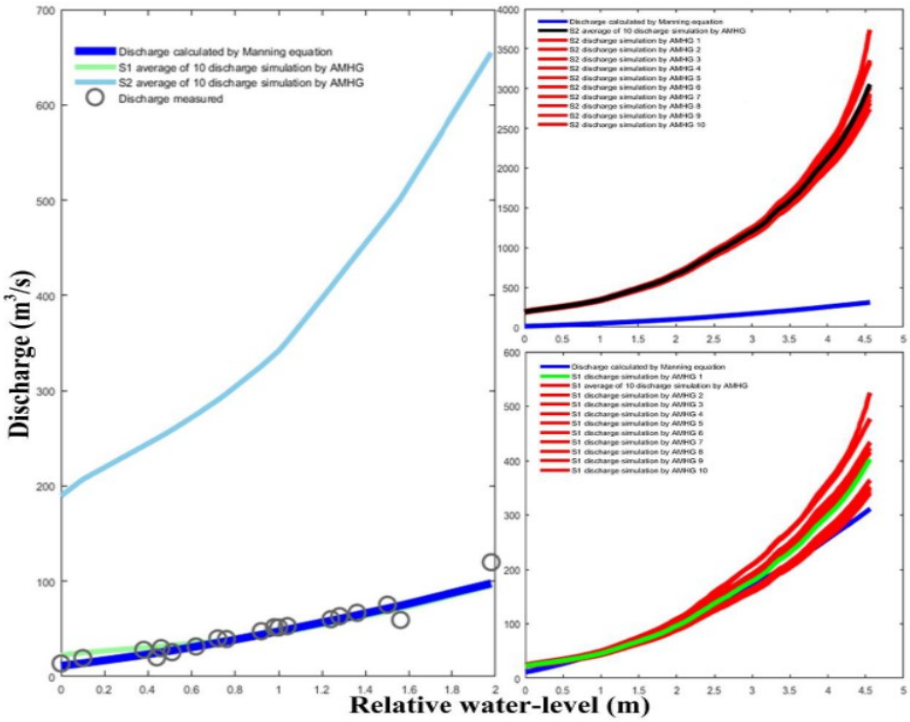

Fig. 3-4. Medium-to-small river streamflow (or discharge) calculated using the AMHG under two scenarios. Scenario 1 (S1, green line) represents the streamflow estimated by the AMHG driven by priori knowledge. Scenario 2 (S2, light blue line) represents the AMHG-estimated streamflow driven by the global parameters by Gleason et al. (2014) without priori knowledge. Gray circles stand for ground-measured streamflow; dark blue thick line is discharge calculated based on Manning equation.

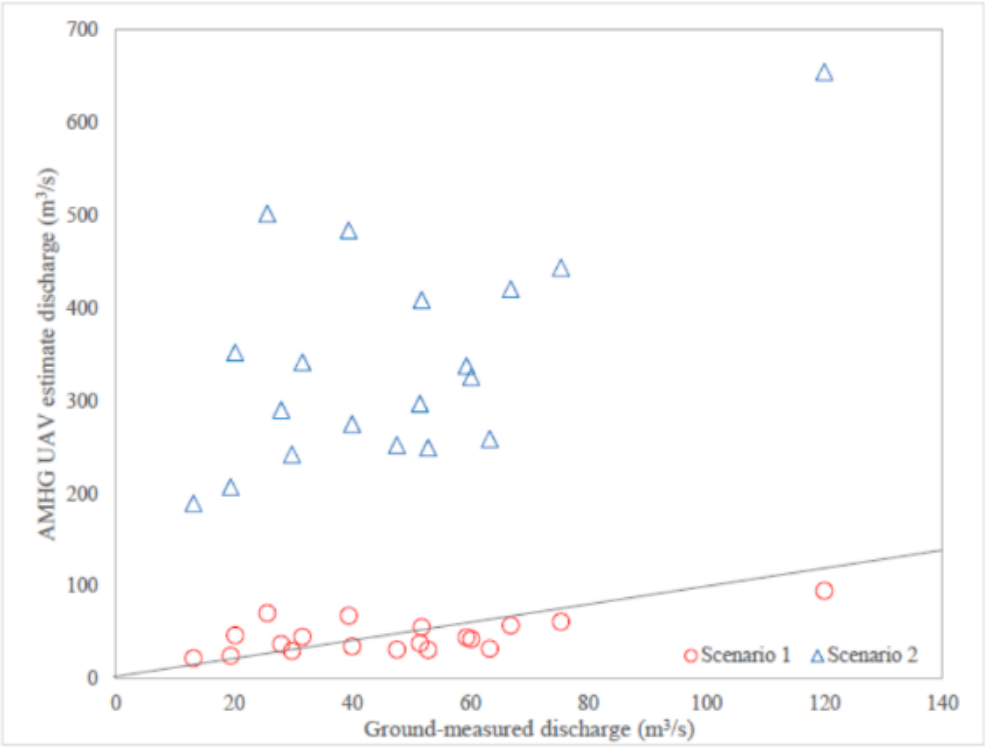

Fig. 3-5 Error analysis diagram of the VHR-AMHG (or AMHG-UAV) estimated streamflow; the grey line represents the 1:1 line

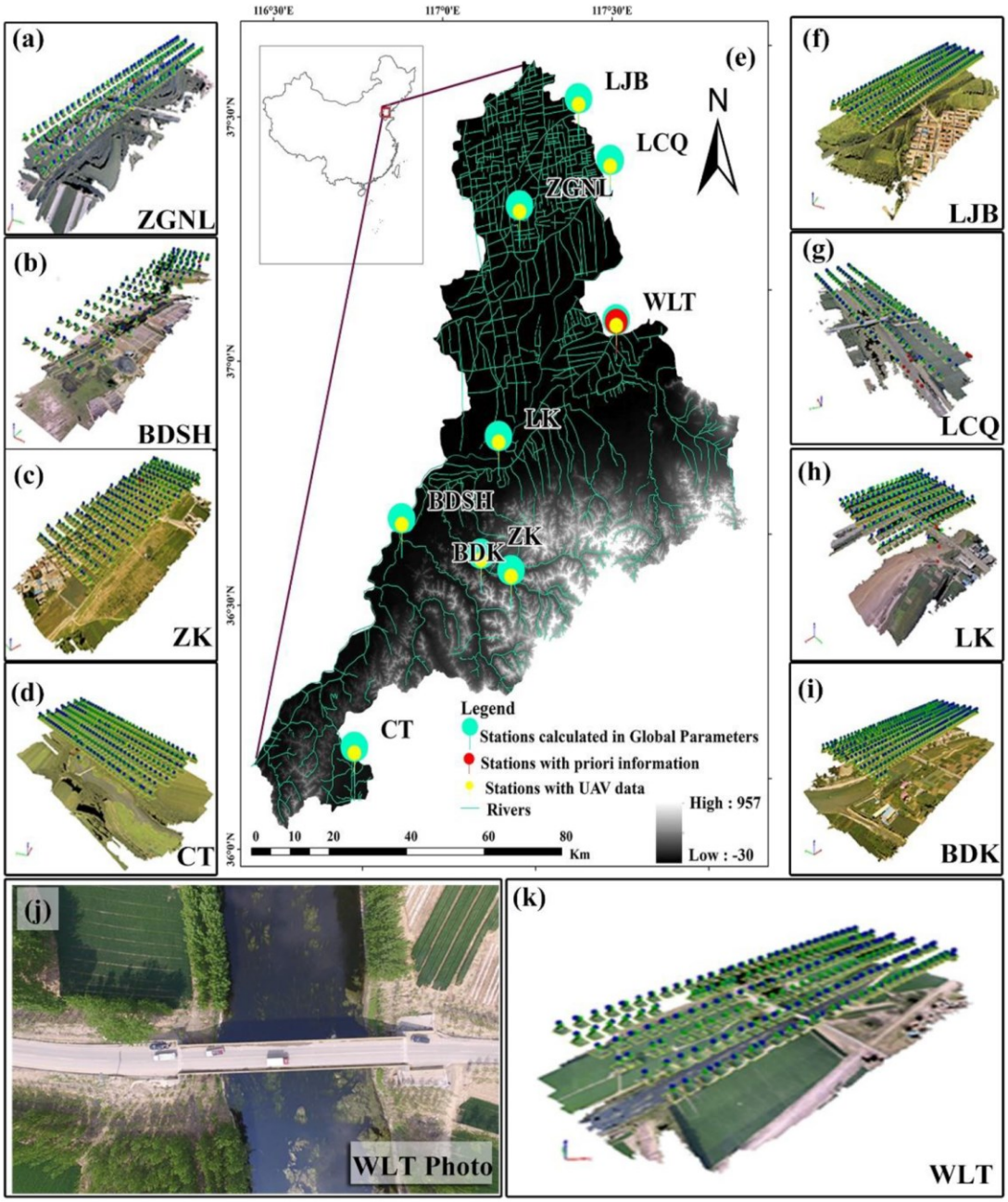

Fig. 3-6 Stations selected in different rivers of Jinan City. (a)–(d), (f)–(i), and (k) represent the generated digital surfacemodel (DSM) and point cloud using UAV imagery; (e) shows the locations of the representative monitoring stations; and (j) is an aerial photo corresponding to k via UAV.

As shown in Figure 3-6, Scenario 1 had an NSE of 0.88, an RMSE of 8.38 m^3/s, and an average relative error of 15.99% for all data. Therefore, the AMHG had high accuracy and can be applied when priori knowledge exists. Scenario 2 had an NSE of -161.54, an RMSE of 310.23 m^3/s, and P=0.00<0.05, meaning that the calculation accuracy of the global-AMHG was low. Here we also respectively discussed streamflow in dry and wet periods to evaluate errors: in dry season, scenario 1 had an RMSE of 15.27 m^3/s and scenario 1 had an RMSE of 226.04 m^3/s; while in wet season, scenario 1 had an RMSE of 24.25 m^3/s and scenario 1 had an RMSE of 403.82 m^3/s, indicating that AMHG perform better in dry season.

Relatively speaking, because Scenario 1 is highly dependent on historical data, the global–AMHG (scenario 2) is more likely to be used in medium-to-small rivers where historical data (cross-section and streamflow) is scarce. However, global–AMHG has low calculation accuracy. To further verify its accuracy, eight representative stations in Jinan City were selected, as shown in Fig. 3-6. The ground-measured streamflow data of these stations were used for further error analysis of the Global-AMHG, as shown in Table 3-1 and Fig. 3-7.

Table 3-1 Medium-to-small streamflow estimation results using the global parameters

Station	Ground-measured Discharge (m^3/s)	Global-AMHG Discharge (m^3/s)	Absolute Error (m^3/s)
BDK	5.37	215.31	209.94
BDSH	2.37	5.84	3.47
LK	263.00	956.85	693.85
ZGNL	1.14	132.24	131.10
LJB	3.93	39.51	35.58
LCQ	33.93	485.10	451.18
ZK	0.31	268.23	267.92
CT	2.73	139.30	136.57

As shown in Fig. 3-7 and Table 3-1, the estimation accuracy for medium-to-small rivers using the global parameters was poor, with the RMSE and average absolute streamflow error of each station being 332.64 m^3/s and 234.37 m^3/s, respectively.

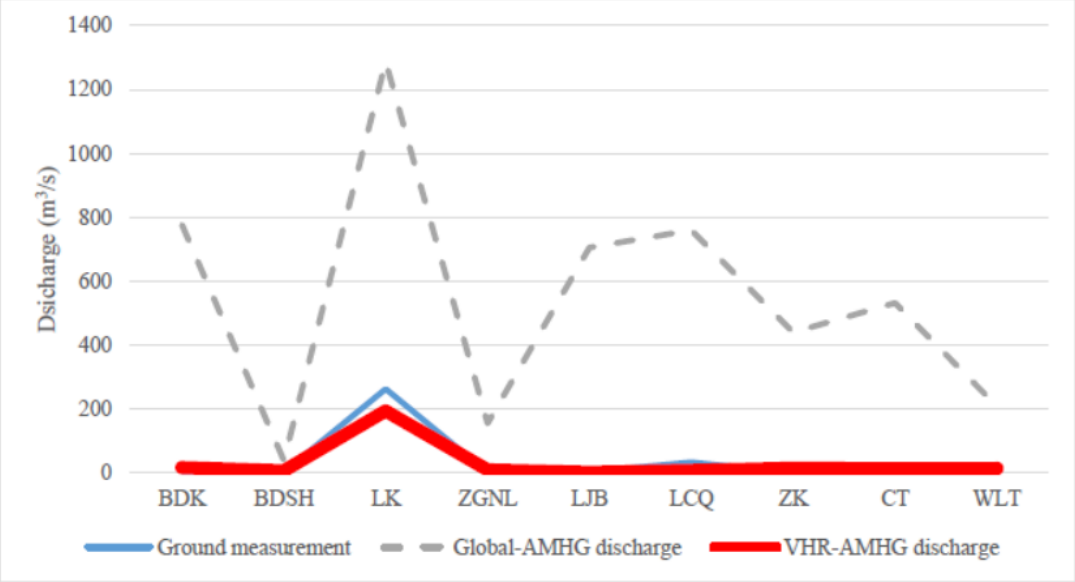

Fig. 3-7 Streamflow estimated via VHR-AMHG compared with that via Global-AMHG and ground measurement.

Fig. 3-7 also shows that the VHR-AMHG (Red) was more suitable for the estimation of medium-to-small streamflow. The RMSE between the estimation and ground measurement (dark blue) was 32.15 m^3/s, while the average error was 24.06 m^3/s. However, the RMSE between the streamflow estimated using global–AMHG (gray dotted line) and the ground

measurement was 301.80 m^3/s, while the average error was 220.33 m^3/s. Moreover, the results at each station were unstable compared to the ground measurement values (dark blue). When the proposed VHR-AMHG method was used to calculate streamflow in data-scarce medium-to-small rivers in the Ji'nan City, an RMSE of 32.15 m^3/s and an average absolute error of 24.06 m^3/s were obtained, which were superior to those of the global parameter-AMHG method and indicated a significant enhancement of calculation accuracy. Therefore, the proposed VHR-AMHG method expanded the application range of AMHG to rivers of all sizes. Overall, it is feasible to use the AMHG method to calculate the streamflow of global medium-to-small rivers with proper initial value setting of the parameters. The VHR method proposed in the present study provides an alternative parameter-setting method for areas with scarce historical data and improves the accuracy of the AMHG for streamflow calculation in these areas. In conclusion, the VHR-AMHG method (Equations 7–9) proposed in the present study is suitable for streamflow calculation in medium-to-small rivers, especially in dry seasons.

(2) Surface streamflow estimation in wet seasons

To facilitate streamflow calculation in wet seasons, this section proposed a rapid and accurate framework for estimating the streamflow of ungauged rivers by combining satellite and unmanned aerial vehicle (UAV) data, which includes a newly developed C/M method (transcaled spatial C/M method) for flow velocity estimation, and a newly method to estimate river bathymetry with zero ground measurement at ungauged rivers (the Riba-zero method). Both two methods were verified by field-measured data. To conduct the research, six representative hydrological stations in the middle reach of the Yellow River were selected for this study, as shown in Fig. 3-8.

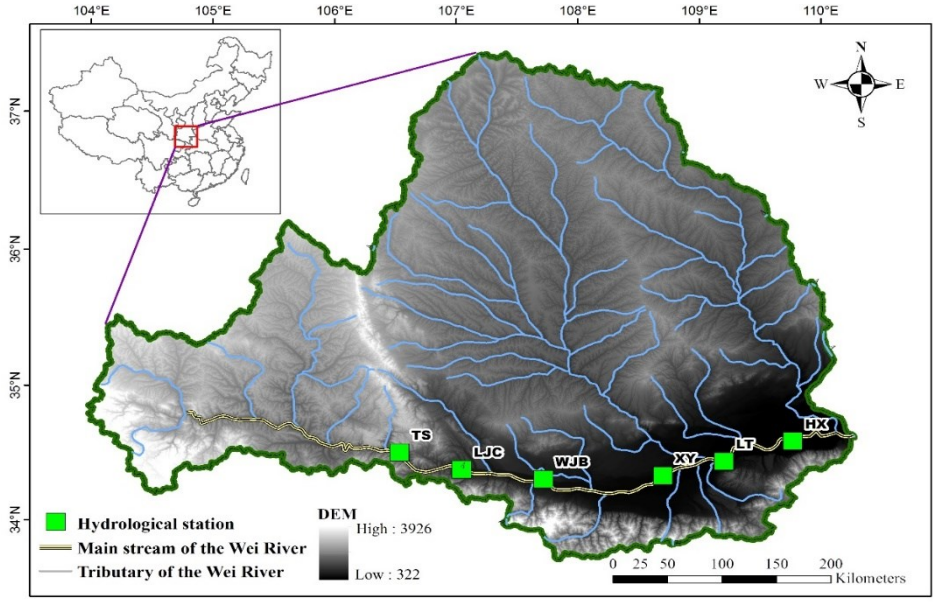

Fig. 3-8 Six representative hydrological stations along the middle reach of the Yellow River.

TS: Tianshui, LJC: Linjiacun, WJB: Wujiabao, XY: Xianyang, LT: Lintong, HX: Huaxian.

(a) Development of the transcaled spatial C/M method—an improved method for estimating river velocity for ungauged rivers

The transcaled spatial C/M method is an improved version of the orginal C/M method by Tarpanelli et al (2013). The former overcomes the shortcomings of the latter (requiring data from multiple stations and overlooking the spatial heterogeneity of rivers). According to Tarpanelli et al.(2013 & 2015), water surface increase in any given area usually causes a decrease in the NIR (near infrared) reflectance value of the area. As results, the ratio (C/M) between the surface reflectance of a land pixel, named C (calibration), and of a water pixel, named M (measurement), changes accordingly. This principle is then used for calculating river velocity. In previous studies, exploiting water and land in the NIR portion of the electromagnetic spectrum by computing the ratio (C/M) and then establishing the regional relationship between C/M and river velocity would require data from multiple hydrological stations, which is difficult in ungauged basin, besides, the established relationship is not stable in large scale because of the failure to consider the spatial heterogeneity of both spectral behavior and river morphology. Considering that relationship between C/M and flow velocity (V) established by one-pixel method have difficulties in being applied at large scale area, especially when the relationship was only determined by limited hydrological stations. Besides, due to best location for wet pixels M are supposed to be near the river in zone not only completely full of water but also sensitive to variations of the inundated area during flood events, while dry pixels C of calibration are supposed to be determined by selecting all the urban areas that are not affected by the seasonal cycle of vegetation (Tarpanelli et al., 2018). In addition, the inconsistent reflectance caused by different surface water bodies with different complex heterogeneous backgrounds and spectral noise characteristics, e.g. the variable sand content in different segment of a river, usually result in the spectral heterogeneity in space.

To overcome these shortcomings, we improved the original C/M method in this section. The water body area corresponding to the largest water body area in the image recording within 1km * 1km area is used as a boundary, or maximum river boundary (MRB), to extract the near-infrared reflectance (or luminance) values of all the pixels in the area. The mean value of the band value is taken as M, and its value changes with the flooded area of the river, and all urban areas on the images are extracted, and the average value of the near-infrared bands in the urban areas on different images is counted as C. The improved method can effectively overcome the shortcomings of requiring data from multiple stations and overlooking the spatial heterogeneity of rivers. The improved C/M method can establish a reliable regional relationship between C/M and V based on solely one (not multiple any longer) hydrological station.

In order to use a single hydrological station to establish a regional C/M~V relationship at ungauged stations, this study first uses Landsat TM images and measured flow velocity data at the single hydrological station during the wet season to establish a regional pixel (C) and water pixel (M) regional relationship with the flow velocity during non-wet seasons, such as Eq. 6; secondly, as there is spectral heterogeneity in space, we established the linear relationship between the M value of the ungauged station and of the reference station (Eq. 7) to remove the influence of spectral heterogeneity on results. With these steps, the flow velocity at an ungauged station (V_u) can be calculated by using Eq. 8. The improved method solves the problem of large spatial differences in reflectance existed in the original C/M method, which enhances the applicability of the original C/M method. Therefore, the improved method is named as transcaled spatial C / M method.

$$V = p \cdot C/M + q \tag{6}$$

$$M_{ref} = g \cdot M_u + h \tag{7}$$

$$V_u = p \cdot C/(g \cdot M_u + h) + q \tag{8}$$

(b) Estimation of flow area

To calculate the flow area the shape and size of cross section has to be gotten. But nowadays sensors of both satellite and UAV can not "see" the cross section under water surface. In other words, one can only use satellite or UAV to monitor the cross section above water. Therefore, we must simulate the underwater cross section by mathematical method. From the viewpoint of mathematics, the cross section of a river, i.e. the width and depth of the river can be expressed in the form of a power function, and the power value of the function is usually less than 2 (Dingman, 2007).

In this section, we monitored the above-water cross section by using UAV and developed a new algorithm for modelling underwater cross-section taking as basis the UAV-measured above-water cross-section. To model underwater cross-section the whole one (above plus under water) is firstly to be formulated by using information of the starting point distance and water depth, as shown in Eq. 9 and Fig. 3-9.

$$\begin{cases} y_r = a_r(|x_r - b_r|)^{t_r} + c_r \\ y_l = a_l(|x_l - b_l|)^{t_l} + c_l \end{cases} \tag{9}$$

where *y* represents the water depth of the river; *x* represents the starting distance; *t* represents the power of the river shape; *a* represents the opening size of the river; *b* represents the central axis point of the fitting function; the subscript *r* and *l* respectively stands for right- and left-side cross-section.

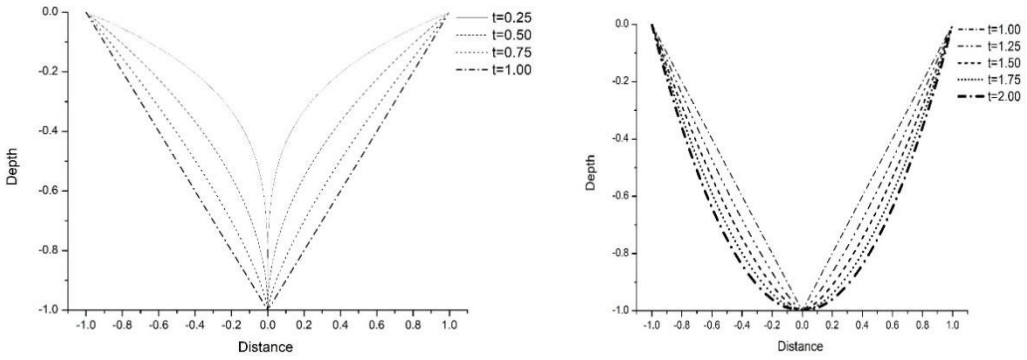

Fig. 3-9 Ideal cross-section or relationship between water depth and distance in Eq. 9 with t <= 1 (Left) and t>= 1 (Right).

In Fig. 3-9 and Eq. 9, the difference in power value represents the shape of the cross-section of the river. For instance, the curve with t = 1 represents a triangle-type cross section, t = 1.75 the 'Lane Type B stable channel', t = 2 a parabola shape cross-section (Dingman, 2007; Bjerklie et al., 2018).

So far, the cross-section formula are established. But in a real river there will be slope

break points in a cross-section not as smooth as in Fig. 3-9 due to the frequent eroding and sedimentation, as shown in Fig. 3-10.

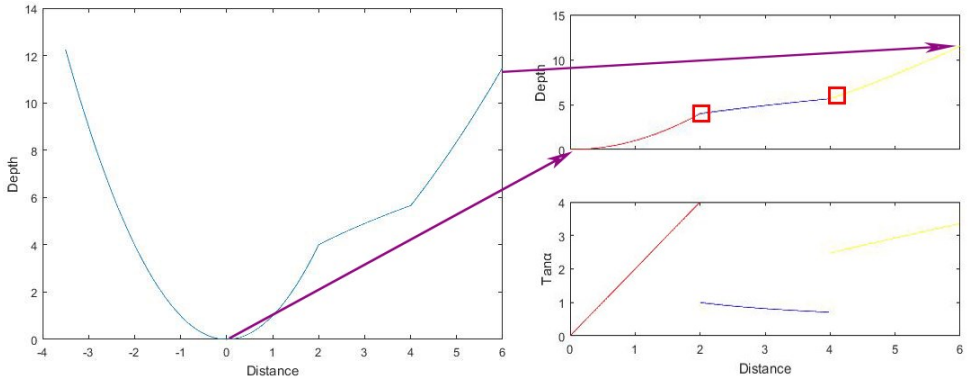

Fig. 3-10 Examples of slope break point on cross-sections

To model the actual across-section in Fig. 3-10, the slope (dy/dx) and the change rate of slope (d^2y/dx^2) of the above-water cross-section is calculated and local maximum of d^2y/dx^2 is used as the slope mutation point for extracting the segment of above water cross-section that is closest to water surface. The relationship between the slope of the cross-section and the starting distance can be formulated as Eq. 10.

$$\begin{cases} \text{slope}_r = a_r \cdot t_r \cdot (x_r - b_r)^{t_r - 1} \\ \text{slope}_l = a_l \cdot t_l \cdot (x_r - b_l)^{t_l - 1} \end{cases} \quad (10)$$

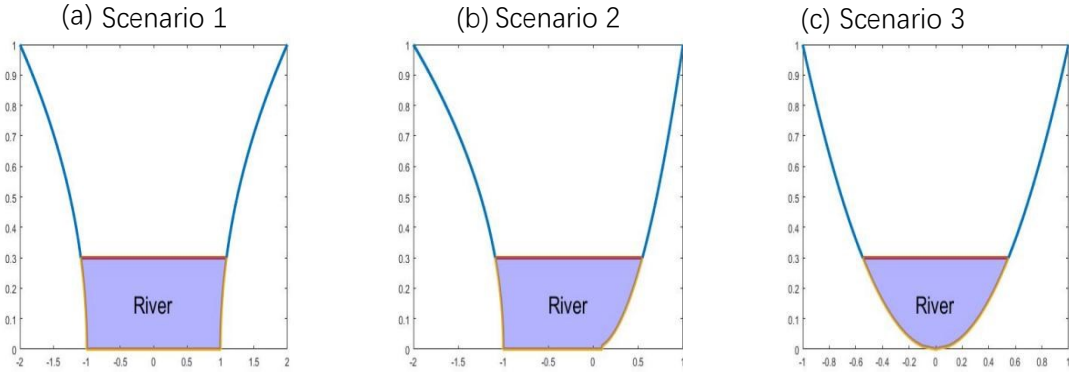

Fig. 3-11 Example of 3 scenarios when determine the below water cross-section. a) Scenario 1, b) Scenario 2, c) Scenario 3

Depending on whether the power of the fitted relationship is less than 1, the segmented cross-sections of the cross section closest to the water surface are divided into convex cross section or concave cross section, and underwater cross-section is determined according to 3 scenarios: (a) Scenario 1: $t_r < 1$ and $t_l < 1$ (Fig. 3-11a), that is, both the left and right sides of the cross-section are convex cross-section. In order to fit the underwater cross-section with Eq. 9 using segments that are closest to the water surface, we uses the points with $x_r = b_r$ and $x_l = b_l$ (i.e., slope equal to infinite) as the bottom points of the river on two sides; (b) Scenario 2: $t_r < 1$, $t_l > 1$ or $t_r > 1$, $t_l < 1$ (Fig. 3-11b), i.e., only one side of the cross-section is convex cross-section. We detect the bottom point of cross-section by finding the point with slope equal to infinite; (c) Scenario 3: $t_r > 1$ and $t_l > 1$ (Fig. 3-11c), the intersection of the formulas fitted by left and right sides of the above water cross section are used as river bottom point, thereby determining the

underwater cross-section.

Combined with Eq. 9 and Eq.18, we can model the underwater cross-section using above water cross-section produced by UAV, which do not require any ground-measured data. The method is named Riba-zero method.

After modelling underwater cross-section with the Riba-zero method (Eq. 9 and Eq. 10), we can then calculate flow area (or underwater cross-section area) based on two scenarios in Fig. 3-12 according to the principle whether the left and right fitting formulas cross under water. In Scenario 1, the left and right fitting formulas do not cross under water (Fig. 3-12a), we calculate flow area with Eq. 11. In Scenario 2, the left and right fitting formulas have intersections (shown in Fig. 3-12b), and we calculate flow area with Eq. 12.

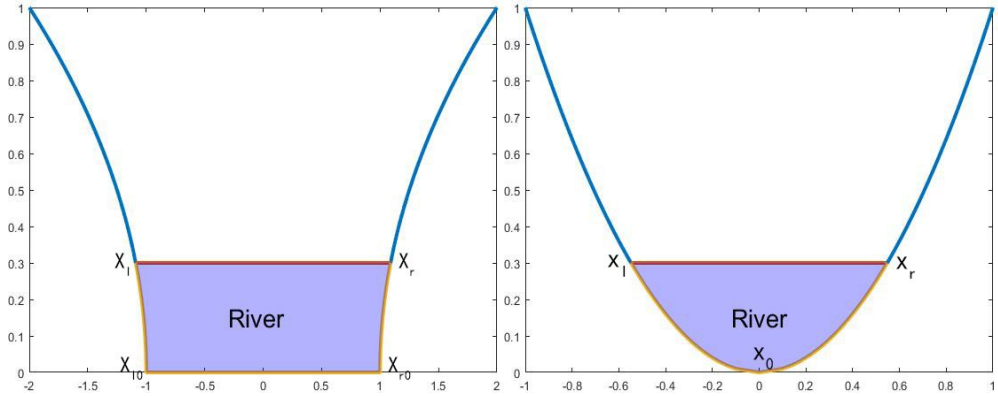

Fig. 3-12 Scenarios. Left-Scenario 1: no intersection in fitting formula of two side of cross-section; Right-Scenario 2: intersection is found in fitting formula of two side of cross-section.

$$\begin{cases} \mathrm{A} = |x_{r0} - x_l| \cdot \mathrm{y}_l - (\int_{x_l}^{x_{lo}} (a_l(x - b_l)^{t_l} + c_l) + \int_{x_{r0}}^{x_r} (a_r(x - b_r)^{t_r} + c_r) \\ \mathrm{y}_l = |(a_l(x_l - b_l)^{t_l} + c_l) - (a_l(x_{lo} - b_l)^{t_l} + c_l)| \end{cases} \quad (11)$$

$$\begin{cases} \mathrm{A} = |x_0 - x_l| \cdot \mathrm{y}_l - (\int_{x_l}^{x_o} (a_l(x - b_l)^{t_l} + c_l) + \int_{x_0}^{x_r} (a_r(x - b_r)^{t_r} + c_r) \\ \mathrm{y}_l = |(a_l(x_l - b_l)^{t_l} + c_l) - (a_l(x_o - b_l)^{t_l} + c_l)| \end{cases} \quad (12)$$

where A represents the flow area, x_l and x_r represent the distance of the left and right sides of the cross-section crossed by water surface. In addition, in Eq. 11, x_{l0} and x_{r0} represent the lowest underwater points on the left and right sides, and y_l represents the water surface line to the height difference between the lowest point underwater; in Eq. 12, x_0 represents the underwater intersection point, and y_l represents the height difference from the water surface line to the underwater intersection point.

with the flow velocity (V) determine in Section 3.1.2.2 (1) and flow area (A) in Section 3.1.2.2 (2), we can finally calculate the streamflow with Eq. 13.

$$\mathrm{Q} = \mathrm{A} \cdot \mathrm{V} \quad (13)$$

(c) Test and validation of the transcaled spatial C/M method

To make the result more accuracy, we further tested the methods in the middle reach of the Yellow River.

The flow velocity was firstly estimated. Before determining the C / M-V relationship, one first need to extract the corresponding areas from the image according to the C and M calculation methods specified in 3.1.2.2 (1). For the range of C a large number of town pixels both far from and near the Wei River, a tributary in the middle reach of the Yellow river, were extracted from the Landsat TM 127 and 128 image, as shown in Fig. 3-13.

For the extraction of M value, we visually extract the water body area corresponding to the largest water body area recorded in the image during 2007-2009 as the boundary, called maximum river boundary (MRB), as shown in Fig. 3-14.

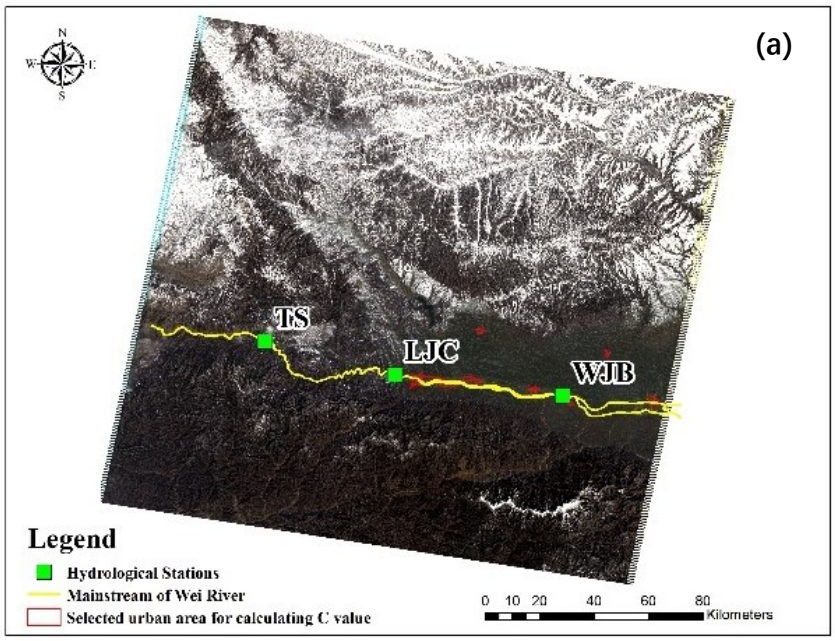

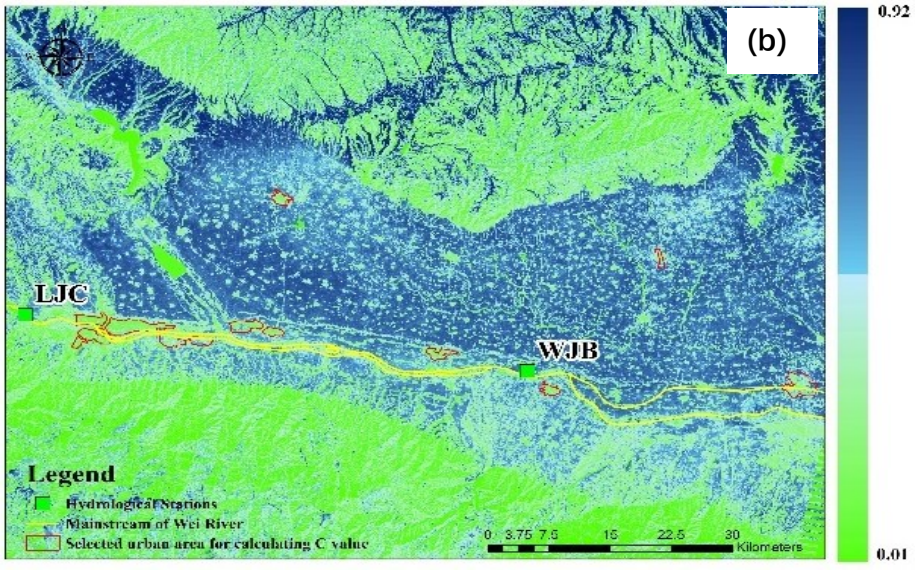

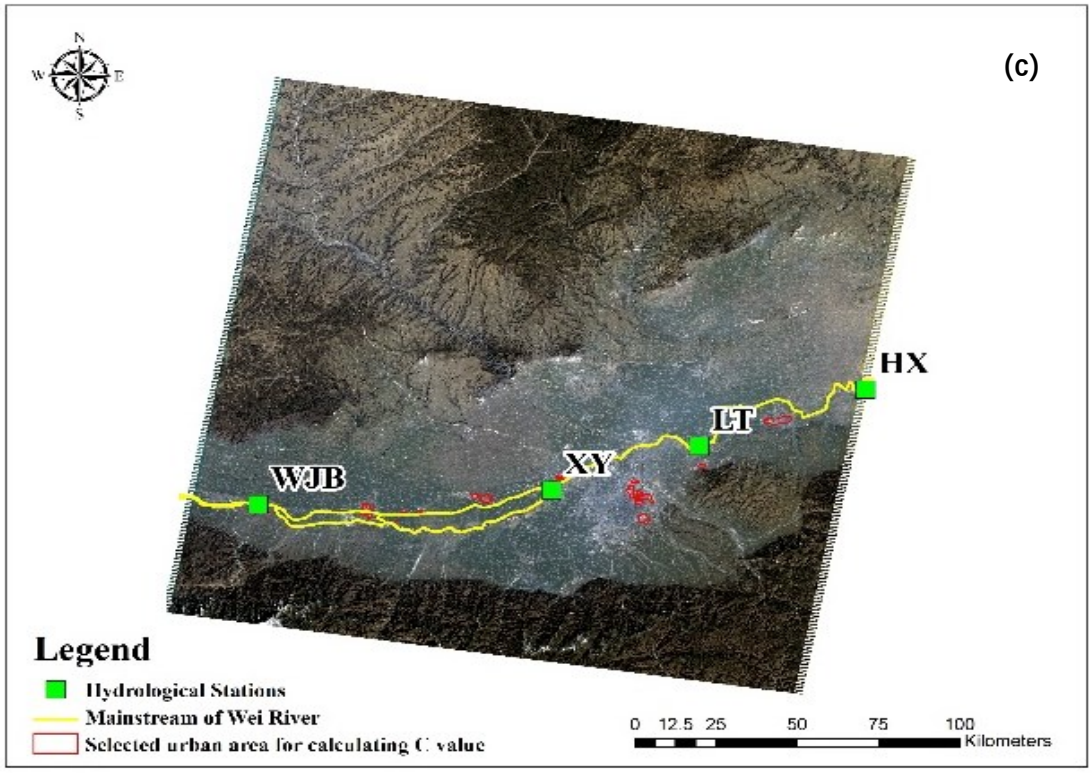

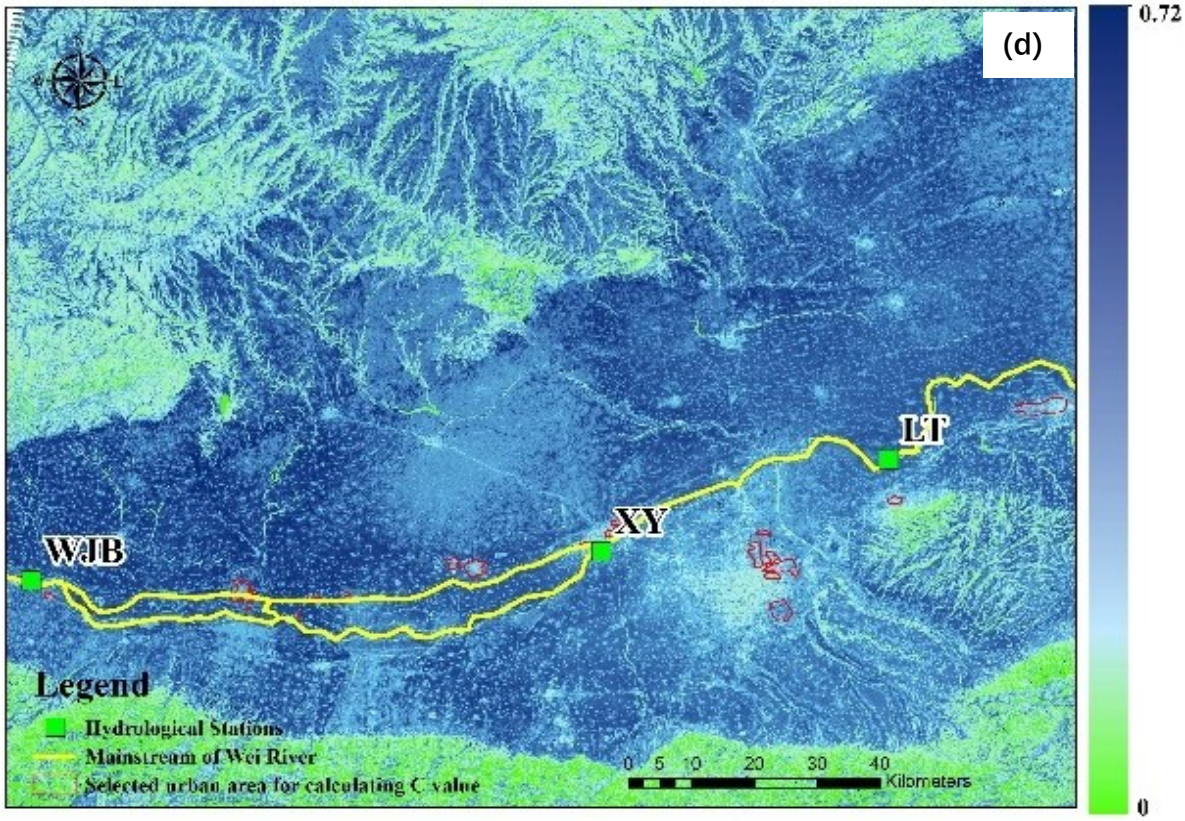

Fig. 3-13 Extracted boundary for C value calculation from Landsat TM. Sub-figures a & b: image No. 127; c & d: image No. 128. Images a&c are true color images, and b&d are near-infrared images. Red circles stand for urban area selected with lower reflectivity in the near-infrared band.

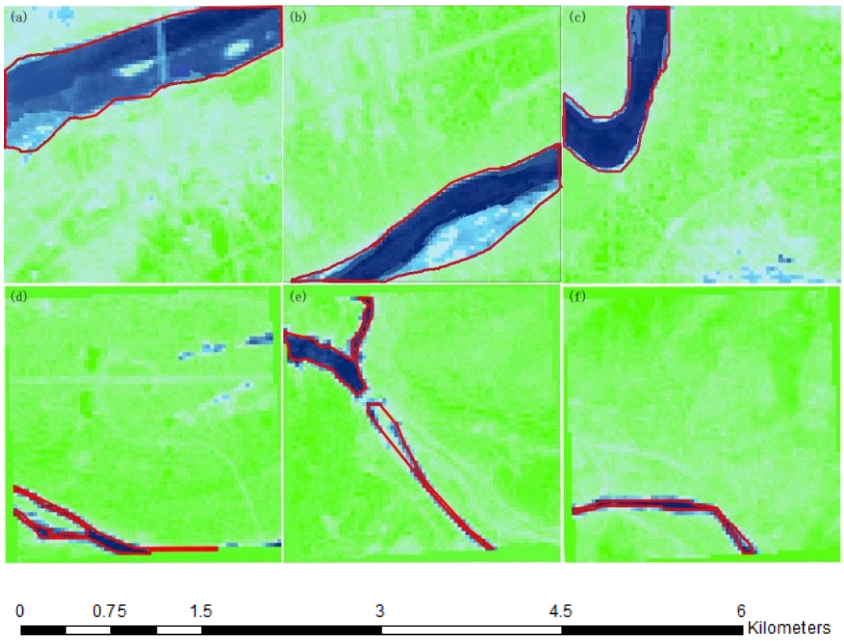

Fig. 3-14 Extracted boundary for M value calculation based on TM imagery, the red line represents the maximum river boundary. (a) XY, (b) LT, (c) HX, (d) WJB, (e) LJC, (f) TS. Blue and green colors show the value of landsat NIR channel, like Fig. 3-13.

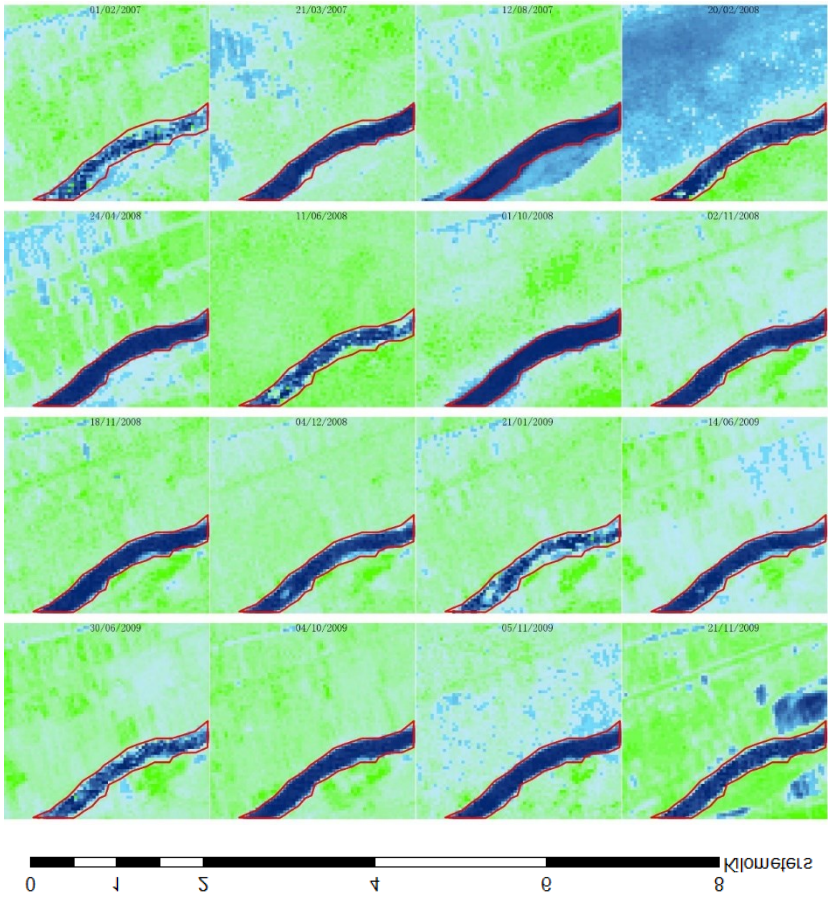

Fig. 3-15 Actual water surface (dark blue) variation over time within the maximum river boundary (MRB, red line) of the LT (a downward hydrological station in Figs. 3-8 & 3-13) based on TM images. Blue and green colors show the value of landsat NIR channel, like Fig. 3-13.

The MRB extracted at each station is different, the largest is XY with an area of 853233 m^2, and the smallest is TS with an area of 61586 m^2. We used the average reflectance within the MRB at different times as M value. Within every MRB, the internal reflectance changes significantly over time, as shown in Fig. 3-15 by taking LT as an example. When water level rises, the water pixels increase and land pixels decrease, and vice versa, as shown in Fig. 3-15.

After obtaining the values of C and M at each station, we first select 27 pairs of C / M and V of reference station (WJB), and establishes the relationship between wet season and non-flood season, as shown in Fig. 3-16.

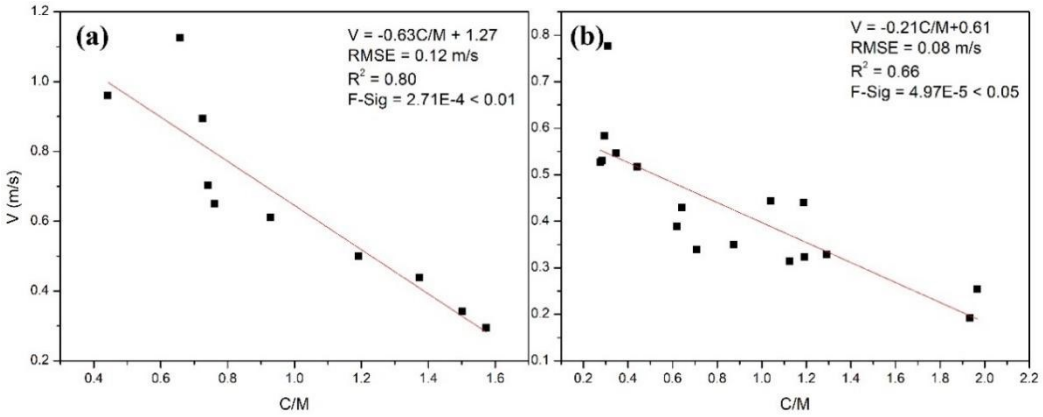

Fig. 3-16 The relationship between C / M and the velocity of the reference station (WJB) in different seasons. (a) during the wet season, and (b) during the dry season. R2 value is used to evaluate the correlation between flow velocity and C/M, while RMSE represents Root-mean-square error.

According to Fig. 3-16, the relationships between C / M and V at the reference station WJB in wet and dry seasons are different. During wet season, the absolute value of the fitting-curve slope is higher than 0.63, and R^2 is 0.83, with V =-0.63C / M + 1.29; while in dry season, the absolute value of the slope is 0.21, and R^2 is 0.68, with V = -0.21C / M + 0.61. This is because that the Wei River basin lies in the semi-arid area of the northern hemisphere. Majority of rainfall falls in the wet season from May to October. During the wet season, the river velocity changes greatly (0.30-1.13m / s). As water level rises, the value of M changes less (0.13-1.10), so the slopes of V and C / M are larger; while in the remain dry season the variability of flow velocity is small (0.19-0.78m / s) due to sparse rainfall. Therefore, the slope of V and C / M is small.

According to the fitting formula, for all periods, the overall average error of the inversed velocity is 0.07 m/s, the RMSE is 0.09 m/s, and the average relative error is 14.07%, which indicate a high accuracy. In wet season, the average velocity error is 0.09 m/s, the RMSE is 0.11 m/s, and the average relative error is 14.57%. In dry season, the average velocity error is 0.06 m/s, the RMSE is 0.08 m/s, and the average relative error is 15.16%. The precision of velocity estimation in the wet season is higher than that in the dry season.

The fitting relationship between M values at the reference station and ungauged stations is established according to Eq. 7 in wet and dry seasons, as shown in Table 3-2.

Table 3-2 Fitting of M value relationship between ungagged stations and the reference station (WJB).

Station	MRB (m^2)	Wet season	R^2	F-Sig	Dry season	R^2	F-Sig
XY	853233	M_{WJB}=1.00M_{XY}-0.04	0.95	8.16E-4	M_{WJB} = 1.25M_{XY}+0.03	0.94	4.06E-6
LT	78262	M_{WJB}=0.76M_{LT}+0.01	0.68	0.04	M_{WJB} = 0.58M_{LT}+0.05	0.78	6.94E-4
HX	61586	M_{WJB}=0.74M_{HX}+0.08	0.74	0.02	M_{WJB} = 1.09M_{HX}+0.05	0.80	3.51E-3
LJC	377855	M_{WJB}=0.41M_{LJC}+0.10	0.87	0.04	M_{WJB} = 0.59M_{LJC}+0.02	0.91	9.24E-4
TS	121003	M_{WJB} = 2.92M_{TS}-0.56	0.99	0.03	M_{WJB} = 0.94M_{TS}-0.03	0.93	3.41E-6

According to Table 3-2, in wet seasons, the highest R^2 fitted by the TS station is 0.99, and the lowest R^2 fitted by the LT is 0.68; in the dry season, the highest R^2 fitted by the XY station is 0.94, and the lowest R^2 fitted by the HX is 0.78. After obtaining the fitting relationship between the M value of each station and the reference station, one can calculate flow velocity with Eq. 8 for each ungauged station. We used satellite imagery to extract the M value of the corresponding station at different times and calculated flow velocity for the stations other than the reference station (WJB), and performed error analysis with the measured flow velocity, as shown in Fig. 3-17.

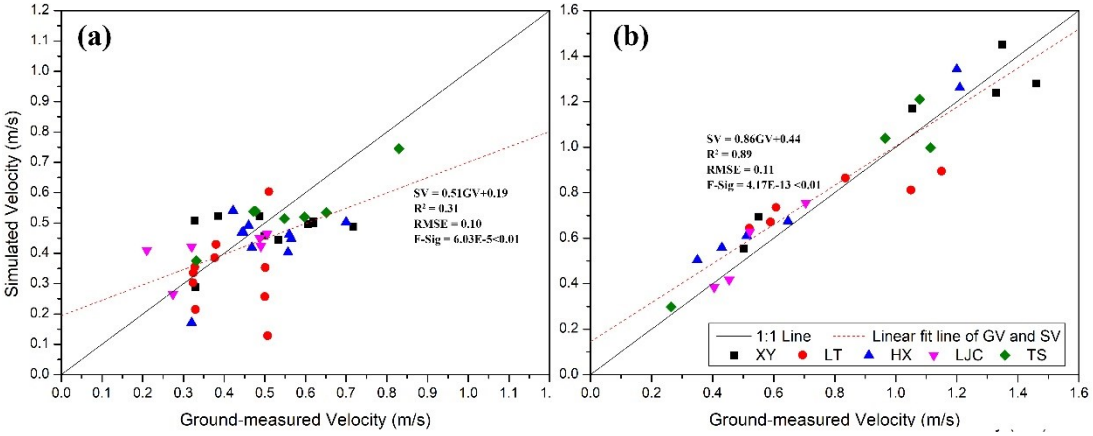

Fig. 3-17 The errors between estimated velocity and ground-measured velocity. The red dash line represents the linear fit line of ground-measured velocity (GV) and simulated velocity (SV), the black lines represent 1:1 line. (a) dry season, (b) wet season.

According to Fig. 3-17, the simulated velocity RMSE of all station in the whole period is 0.12 m/s, the average relative error is 19.00%, and the rRMSE is 0.36 with a F-test significance of 0 < 0.01, indicating the relationship is reliable. In wet season, the simulated velocity RMSE of all stations is 0.12 m/s, the average relative error is 14.56%, and the rRMSE is 0.15. In dry season, the simulated velocity RMSE of all stations is 0.12 m/s, the average relative error is 20.88%, and the rRMSE is 0.25. It can be concluded from the above results that our improved method (transcaled spatial C / M method) gives better simulation in wet season instead of dry season and is especially better at estimating big flow velocity than small one. The rRMSE of each station is shown in Table 3-3.

Table 3-3 rRMSE of flow velocity of all stations in middle Yellow River. relative root-mean-square error (rRMSE)

	XY	LT	HX	LJC	TS
Wet season	0.116057	0.207085	0.153012	0.119668	0.112241
Dry season	0.243814	0.387174	0.227191	0.237509	0.131788
All periods	0.173656	0.29033	0.192475	0.190149	0.123728

As shown in Table 3-3, among all stations, the result of TS performed best both in wet and dry seasons, with rRMSE values of 0.11 and 0.13, respectively; while LT performed worst with rRMSE values of 0.21 in the wet season and 0.39 in the dry season. The regional relationship between C/M and V is established by introducing Eq. 7 to address reflectance differences caused by optically active substances in water body on the absorption and scattering of solar radiation (Beck et al., 2016). However, due to some instinctive differences in the water bodies of stations caused by sediment and chlorophyll, the reliability of the M value relationship is different at 5 stations. It can be concluded that the stations with higher R^2 in the M value relationship of ungauged- referenced stations (e.g., XY, TS) performed better in velocity calculation.

After the formula for flow velocity calculation have been tested, flow area estimation model is subsequently tested and validated. The above-water cross-sections collected by UAV in the lower Yellow River area were used to analyze the precision of our underwater cross-section modelling method (Riba-zero method). Specifically, based on the recorded historical minimum and maximum water level interval, 9 water levels are taken at equal intervals between the highest and lowest water level to analyze the error of the simulated underwater cross section, as shown in Fig. 3-18.

According to Fig. 3-18, the Riba-zero method performed better in ZGNL, where the shape of the cross-section is more similar to a parabola, the RMSE of the 9 simulations is 29.81 m^2, the rRMSE is 0.18, the lowest relative error in the 9 simulations is 1.47% when the relative water level is 1.0, and the highest relative error in the 9 simulations is 25.12% when the relative water level is 5.0. Interestingly, based on our data, the lowest relative error occurred when the bias between the elevation of the simulated and real river bottom was the least, while the highest relative error occurred when the bias was the largest. In BDK, where the shape of the cross-section is close to a trapezoid, the RMSE of the 9 simulations is 417.13 m^2, and the rRMSE is 4.76, indicating that the Riba-zero method did not perform well in dealing with such a cross section, of which the lowest point of the cross section is not easy to simulate by the above-water cross section.

After verifying the applicability of the Riba-zero method with precise UAV data in the lower Yellow River, we then validated it with non-trapezoidal cross section in the middle Yellow River, as shown in Fig. 3-19. There we used the measured flow area as a benchmark to analyze the accuracy of the modelled flow area at each station.

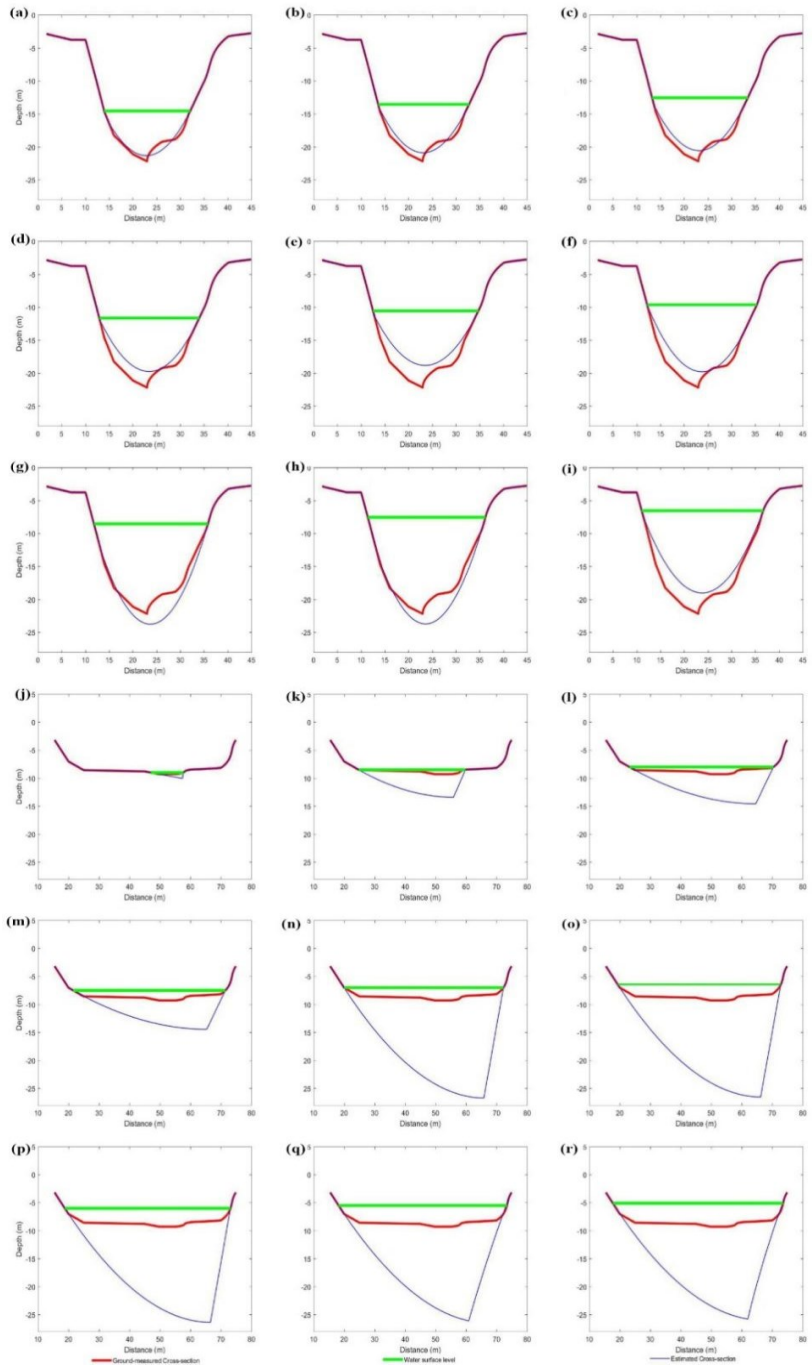

Fig. 3-18 Cross-section simulated by UAV data in Lower Yellow River. (a) the simulation of ZGNL, relative water level is 1m; (b) the simulation of ZGNL, relative water level is 2m; (c) the simulation of ZGNL, relative water level is 3m; (d) the simulation of ZGNL, relative water level is 4m; (e) the simulation of ZGNL, relative water level is 5m; (f) the simulation of ZGNL, relative water level is 6m; (g) the simulation of ZGNL, relative water level is 7m; (h) the simulation of ZGNL, relative water level is 8m; (i) the simulation of ZGNL, relative water level is 9m; (j) the simulation of BDK, relative water level is 0.5m; (k) the simulation of BDK, relative water level is 1.0m; (l) the simulation of BDK, relative water level is 1.5m; (m) the simulation of BDK, relative water level is 2.0m; (n) the simulation of BDK, relative water level is 2.5m; (o) the simulation of BDK, relative water level is 3.0m; (p) the simulation of BDK, relative water level is 3.5m; (q) the simulation of BDK, relative water level is 4.0m; (r) the simulation of BDK, relative water level is 4.5m.

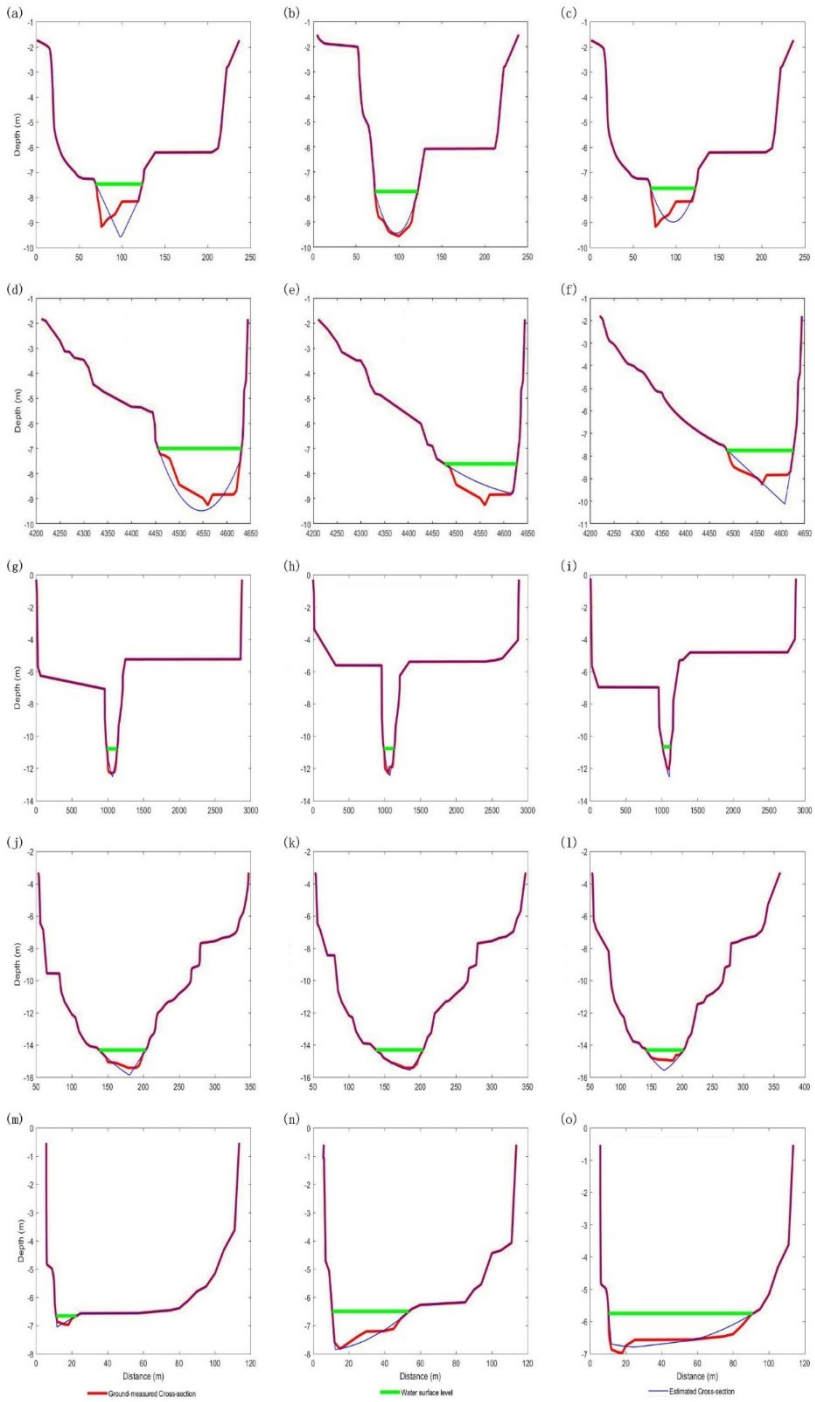

Fig. 3-19 Five cross-section simulated in middle Yellow River. (a), (b), and (c) are 3 of 16 typical underwater cross-section simulations of 2007,2008 and 2009 at XY; (d), (e), and (f) are 3 of 16 typical underwater cross-section simulations of 2007,2008 and 2009 at LT; (g), (h), and (i) are 3 of 16 typical underwater cross-section simulations of 2007,2008 and 2009 at HX; (j), (k), and (l) are 3 of 11 typical underwater cross-section simulations of 2007,2008 and 2009 at LJC; (m), (n), and (o) are 3 of 11 typical underwater cross-section simulations of 2007,2008 and 2009 at TS.

According to Fig. 3-19, the RMSE of the estimated flow area of all stations in the middle Yellow River regardless of season is 69.59 m^2, the relative error is 27.76%, the rRMSE is 0.49, and the relationship between the ground-measured and the simulated flow area was tested by

using the F-test method and has a significance of 0 < 0.01. In the wet season, the RMSE of estimated flow area of all stations in the middle Yellow River regardless of season is 102.52 m^2, the relative error is 34.12%, the rRMSE is 0.57, and the relationship between the ground-measured and simulated flow area is verified by the F-test with significance of 4.10E-10, less than 0.01. In the dry season, the RMSE of the estimated flow area of all stations in the middle Yellow River regardless of season is 59.06 m^2, the relative error is 24.00%, the rRMSE is 0.40, and the relationship between the ground-measured and simulated flow area is verified by the F-test with significance of 0, less than 0.01. The precision of estimating the flow area in the wet season is worse than that in the dry season.

Similar to the results in the lower Yellow River, among all the 5 stations, the estimated flow area error of LJC, where the shape of the cross section is most similar to a parabola, is the lowest, and the rRMSE is 0.23; while in HX, where the shape of the cross section is long and narrow, the rRMSE is 0.40, which is the biggest among the 5 stations. In other words, errors are from (positively correlated with) the degree of bias (from an ideal parabola curve) of the actual cross section. Based on the results on both the lower Yellow River and middle Yellow River, it can be concluded that the Riba-zero method is more suitable for parabola-shaped cross sections.

After having obtained flow area and flow velocity, we then used Eq. 13 to calculate the streamflow at each station. Results are as shown in Fig. 3-20.

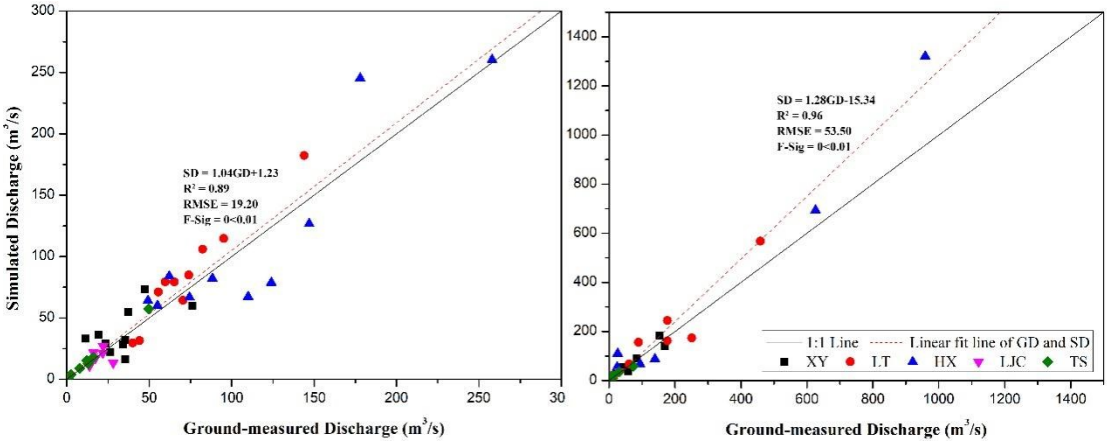

Fig. 3-20 The errors between estimated and ground-measured streamflow (discharge). The red dash line represents the linear fit line of ground-measured discharge (GD) and simulated discharge (SD), the black lines represent 1:1 line. (a) dry season, (b) wet season.

According to Fig. 3-20, the simulated streamflow RMSE of all stations in the whole year is 36.42 m^3/s, the average relative error is 35.31%, NSE is 0.86, the rRMSE is 0.41, and the relationship between the ground-measured and the simulated streamflow is verified by the F-test with significance of 0, less than 0.01, indicating that the relationship is reliable. In the wet season, the simulated streamflow RMSE of all stations is 82.49 m^3/s, the average relative error is 45.81%, the NSE is 0.85 and the rRMSE is 0.56, and the F-test shows that the relationship between the ground-measured and the simulated streamflow is reliable with a significance of 0, less than 0.01. In the dry season, the simulated streamflow RMSE of all stations is 19.17 m^3/s, the average relative error is 29.10%, the NSE is 0.86 and the rRMSE is 0.34, and the F-test

indicaes that the relationship is reliable with significance of 0, less than 0.01. It can be concluded that, unlike the simulated velocity, the result of the simulated streamflow is similar to that of the flow area estimation, which is more precise in the dry season than in the wet season and is caused by the uncertainties of estimating the flow area from the above-water cross section. Among all the stations, the simulated streamflow of TS shows the least rRMSE (0.31), in which the precision of velocity is the highest and the flow area is the second highest among all the stations. The performance of our method is worst in HX, which is mainly due to the error in the estimated underwater cross-sectional area caused by its irregular shape (Fig. 3-20).

To discuss the application potential of our method, we compared the streamflow result of our proposed method with previously developed methods. Based on four hydrological stations in the Po River, Italy, Tarpanelli et al. (2013) established a regional relationship of C/M and V to calculate the river streamflow at ungauged stations. The NSE value of their results is between 0.59–0.83, which is lower than that of our result in the middle Yellow River (0.86), indicating that our improved method successfully managed using data from one hydrological station to establish a more robust regional relationship for estimating streamflow at ungauged stations. Li et al. (2019) proposed a multiple-pixel ratio (MPR)-based C/M calculation method that is like our MRB-based C/M calculation but overlooked the spatial heterogeneity of spectral information when applying their method in small rivers of the Tibetan Plateau, China. The rRMSE of their result is between 0.67-0.81, which is higher than that of our result of 0.41, indicating that considering spectral information can successfully improve the performance of C/M-based streamflow estimation. However, Tarpanelli et al. (2015) proposed using the relationship between velocity and C/M to calculate river streamflow in ungauged basins, and the rRMSE is 0.37, which is slightly better than that of our result (0.41) because they applied river bottom elevation information that is absent in our study in inversing cross-section.

Apart from estimating river streamflow through spectral information, there are also many remote sensing-based streamflow estimation methods based on river width and height that can easily be observed by remote sensing sensors (Zhao et al., 2019; Huang et al., 2018). Gleason & Smith (2014) proposed the at-many-stations hydraulic geometry (AMHG) method for river streamflow estimation in ungauged rivers based on Landsat Thematic Mapper images and tested their method over 3 large rivers in the United States, Canada, and China; the rRMSE was within 0.20-0.30. We expand this method into medium- to small-sized rivers by using unmanned aerial vehicles (UAV), proposing a virtual hydraulic radius AMHG (VHR-AMHG) and found that in global scale, AMHG can now only be suitable for large rivers with high river streamflow. Huang et al. (2018) proposed multisource remote sensing (including satellite altimetry data, Landsat TM data and UAV data) to extract river width and water level to estimate the streamflow of rivers on the Tibetan Plateau, China. Their results indicated that large rivers show less uncertainty in the errors of river width and water level than that of small rivers (width <400 m). However, Li et al. (2019) exploited spectral information by the C/M ratio in estimating the streamflow of rivers with widths less than 100 m in China, and the NSE value of their result is 0.45, indicating the potential of using the C/M-based method to monitor the streamflow of small ungauged rivers. Apart from being applied in small rivers, Tarpanelli et al. (2018) applied the C/M method in estimating the streamflow of the Niger River (width is approximately 2800 m) at Lokoja and achieved great results (rRMSE is 0.12), indicating that the C/M-based method

can also be applied on large rivers.

In conclusion, previous research on estimating river streamflow through extracted width and height from satellites is generally suitable for large rivers, while using spectral information from satellite images, e.g., Chinese GF-7 (0.8 m), has the potential for river streamflow in both small and large rivers.

3.1.2 Long-termed streamflow estimation by using satellite imageries for the three representative cities

(1) Selection of stations for long-termed streamflow estimation for three cities

Surface freshwater in rivers, or streamflow is important water sources for a city. To accurately estimate surface water resources for the three representative cities, one has to select stations on rivers crossing by or flowing nearby the three representative cities. Since Xi'an lies near two tributaries (Jing River and Wei River) in the middle reach of the Yellow River, two stations were selected for Xi'an; while Zhengzhou and Ji'nan are located near the main stream of the Yellow River, two stations (HYK and LK) were respectively selected for the two cities. Selected stations are as shown in Fig. 3-21 and Table 3-4

.

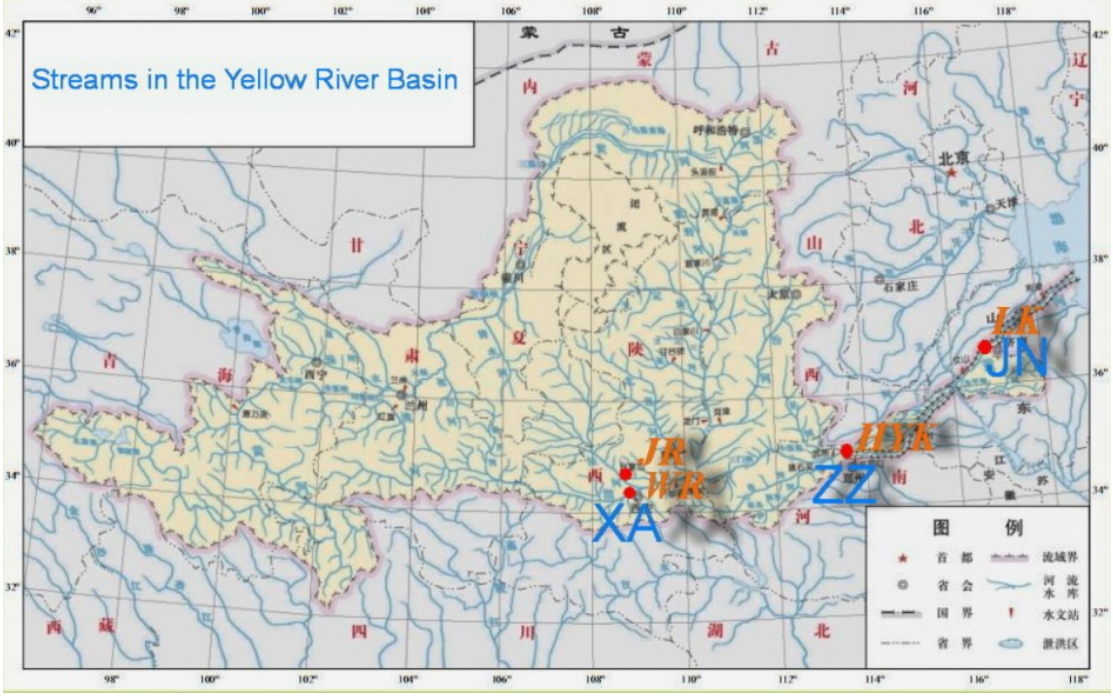

Fig. 3-21 The four selected stations for streamflow retrieval with satellite and UAV imageries (red point) for the three representative cities*. XA: Xi'an City; ZZ: Zhengzhou City; JN: Ji'nan City; JR: Jing River Station; WR: Wei River Station; HYK: Huayuankou Station; LK: Luokou Station.

Table 3-4 The position of the four stations

City	Station for streamflow retrieval	Long	Lat	Streamflow (m^3/s)	Maximum water-level(m)
XA (Xi'an)	JR (Jing River)	108.9932	34.4574	100-9200	451.98
	WR (Wei River)	108.9993	34.4404	50-13300	385.40
ZZ (Zhengzhou)	HYK	113.8693	34.8922	20-22300	94.42
JN (Ji'nan)	LK	117.0241	36.7542	200-11000	35.19

(2) Long-termed streamflow estimation for representative stations

With the selected four stations, we begin to calculate streamflow value series at the four stations in Table 3-4 by using VHR-AMHG with Sentinel-1 imageries in dry seasons and transcaled spatial C/M method with Landsat TM imageries in wet seasons.

After downloading Sentinel-1 data, it is necessary to pre-process the data by using ESA SNAP (Java) (https://senbox.atlassian.net/wiki/spaces/SNAP/overview) to improve the image data that suppresses unwanted noise, distortions and enhances some image features important for further applications. First, we need to apply precise orbit files to know where the satellites are. Second, we're going to convert Digital Numbers (DNs) to Backscatter. The conversion is mission-specific. Then we have to perform Specckle-Filter, including Multi-look processing and Image Filtering. Finally, we need to complete the geometric correction. To derive a precise geolocation for each pixel of the image, the Range-Doppler approach is the most appropriate way to perform geometric correction. With the corrected Sentinel-1 data, we can easily recoginize water from land via visual interpretation whereby to produce multiple water surface widith values of a river section which are then used by the VHR-AMHG method. Water surface widith values are validated by manually checking the randomly selected Sentinel-1 images to ensure the accuracy of results.

Likely, after downloading TM images, radiometric calibration is conducted under ENVI environment converting DN values to spectrial radiance values. Then, FLAASH is used for atmospheric correction converting the spectrial radiance values into surface reflectance values. With the reflectance values, we can estimate C and M values in the transcaled spatial C/M method.

In total, more than 200 tiles and 2,000 Sentinel-1 images were explored to retrieve dry-season streamflow at the four stations from 2014 to 2021. And more than 1,000 tiles and 15,000 landsat TM images were used to retrieve wet-season streamflow from 1980s. To incorporated with Sentinel-retrieved streamflow in dry seasons, TM-retrieved wet-season streamflow from 2014 to 2021 were used and retrieved streamflow in upper (Xi'an: JR&WR), middle (Zhengzhou: HYK), down-stream (Ji'nan: LK) of the Yellow River are shown in Fig. 3-22. Monthly imageries of Sentinel-1 and Landsat TM were used. In other words, multiple images of Sentinel-1 or TM for a station and its adjacent cities were fused together as an imagery. The first imagery of Sentinel-1 or TM of every month was downloaded and explored as the monthly imagery.

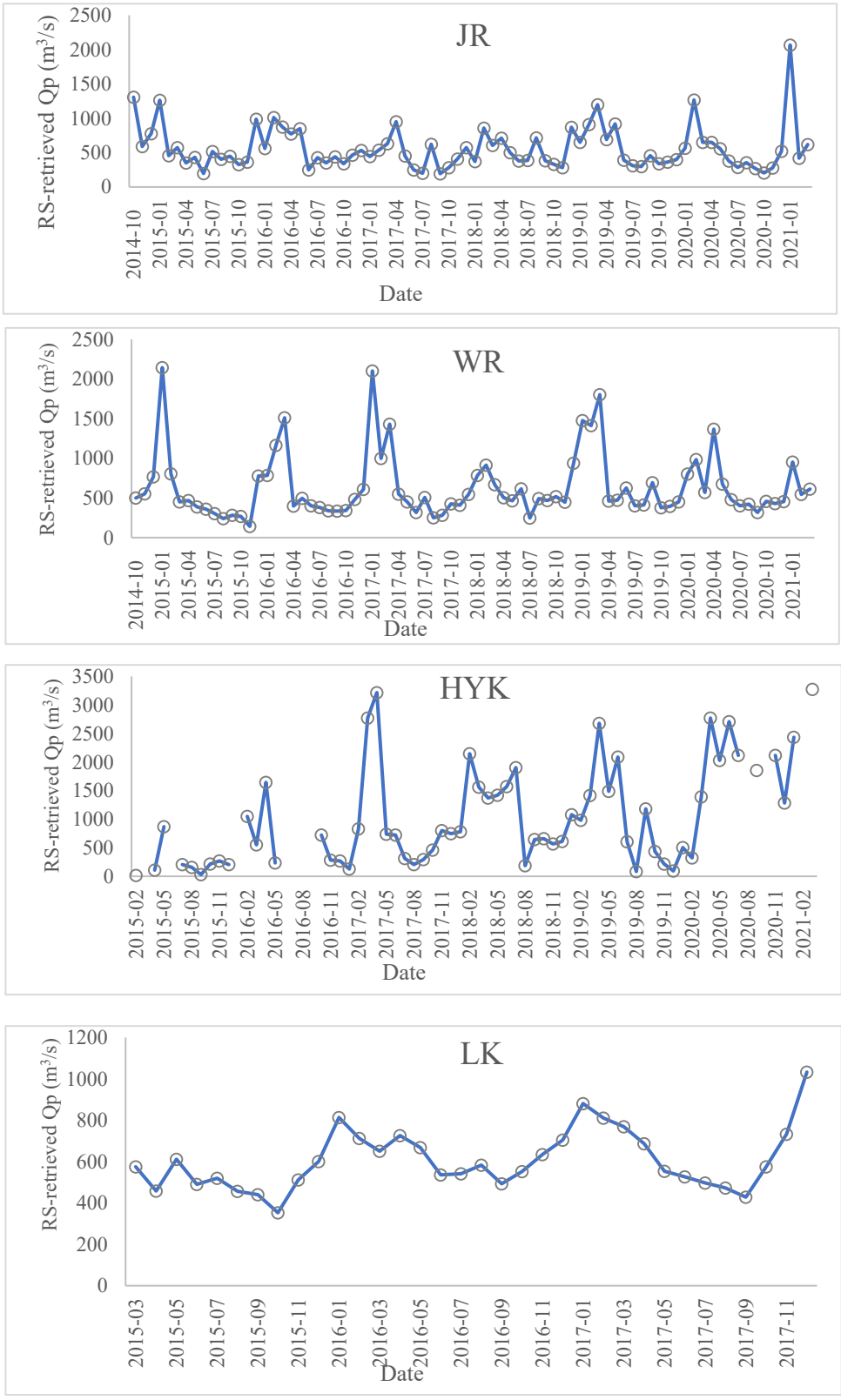

Fig. 3-22 RS-retrieved streamflow in the four stations for past dates with VHR-AMGH method plus Sentinel-1A data used in dry seasons as transcaled C/M method plus TM imageries were used in wet seasons. Streamflow in some dates are missing due to the availability of satellite imageries.

If the percentage of cloud area in a TM image is greater than 50%, the image is replaced by

another image on other day of the month. What is worth noticing is that the image has to be replaced if the station-located river section is covered by cloud (even if the percentage is less than 5%) whereby to ensure the estimation of M value in the transcaled spatial C/M method not to be affected by any cloud. All these imageries were processed via the platform of Google Earth Engine (https://developers.google.cn/earth-engine/).

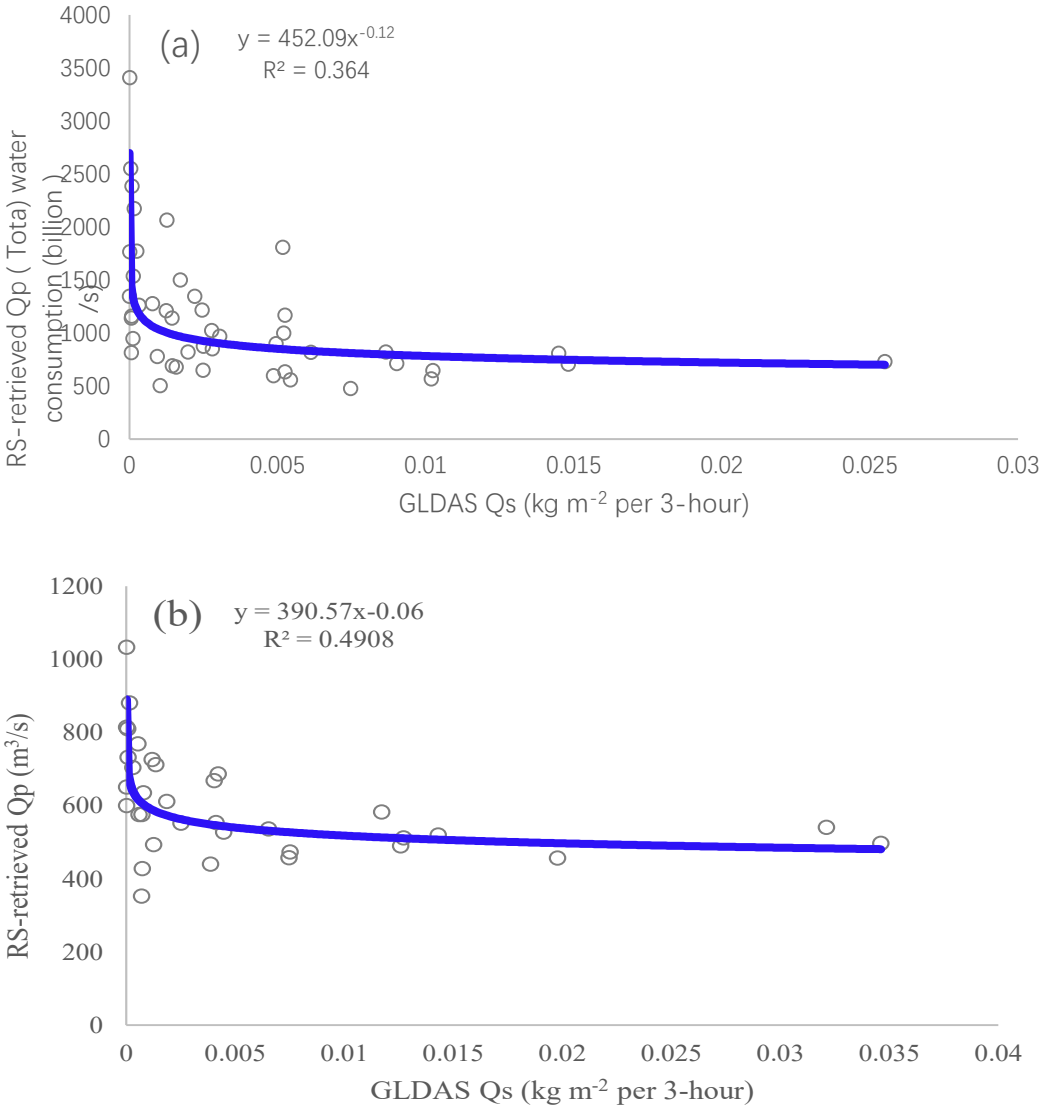

Fig. 3-23 Relationship between RS-retrieved streamflow (Qp) and runoff modeled in the dataset of NASA GLDAS 2 NOAH with (a) for JR and WR, and (b) for HYK and LK.

Fig. 3-22 shows that streamflow in the four stations fluctuates with dry and wet seasons. Due to continually withdrawing water out of the Yellow River from upper to downward reaches, streamflow increases in the upper and then decreases in the downward reach. In the upper reach (JR&WR) the averaged streamflow is ~600 m^3/s and in the middle reach (HYK) it is ~1000 m^3/s, but in the downstream (LK) it is ~600 m^3/s which implies that in the downstream water withdraw greatly decreases the quantity of streamflow in the Yellow River.

With streamflow RS-retrieved in the four stations, relationship between it and runoff modeled in the dataset of NASA GLDAS 2 NOAH (or GLDAS Noah Land Surface Model L4

monthly 0.25×0.25 degree, V2.0 (DOI: 10.5067/9SQ1B3ZXP2C5) (Hiroko and Rodell, 2016)) can be established. By using the relationship as a bridge, RS-retrieved streamflow in the four stations can be extended from the last decade to the period of almost 70 years (from 1948 to current). The relationships established are as shown in Fig. 3-23.

Fig. 3-23 shows that there is an evident power relationship between the RS-retrieved streamflow (Qp) and the runoff from NASA GLDAS. By using the relationships, the RS-retrieved streamflow can be extended to 1948-, as shown in Fig. 3-24.

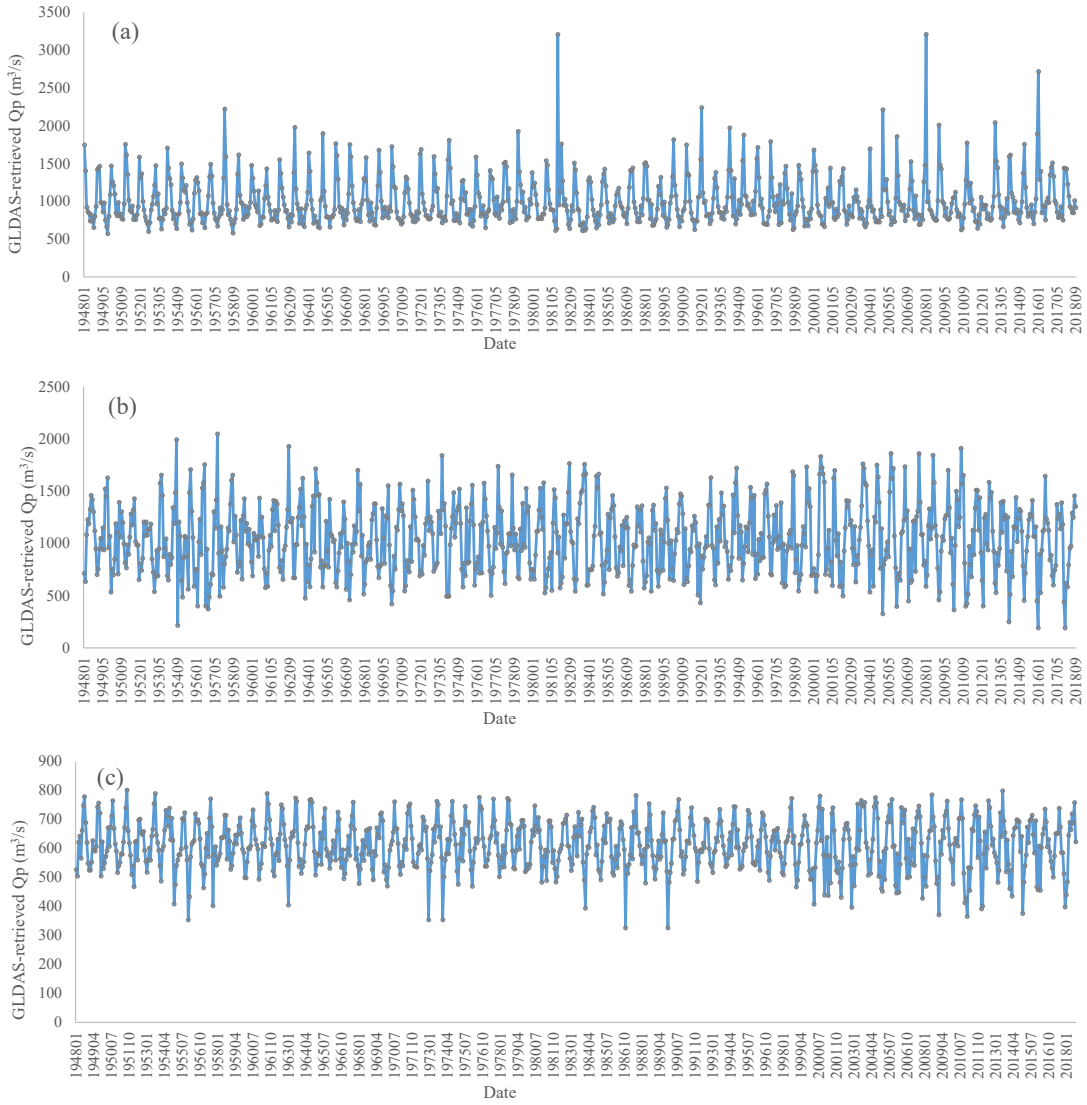

Fig. 3-24 Streamflow or FWA retrieved based on GLDAS runoff data from 1948 year with (a) for Xi'an, (b) for Zhengzhou, and (c) for Ji'nan.

Fig. 3-24 shows that Xi'an (a) and Zhengzhou (b) have almost the same averaged streamflow value (~1000 m^3/s) from 1948 to 2018, and Jinan (c) has a lower averaged streamflow value (~600 m^3/s). With these streamflow values, FWA can be estimated in the next section. Streamflow in the upper reach (Xi'an in Fig. 3-24a) fluctuates more intensively than the lower reaches (Fig. 3-24b & c: Zhengzhou and Ji'nan). The reason is that there are a fewer tributaries concentrated into the mainstream of rivers in upper reaches than in the low- and

middle- reaches and therefore the streamflow process in Xi'an fluctuates more intensively than in Zhengzhou and Ji'nan. In addition, Xi'an lies adjacent to the two tributaries of the Yellow River -- Jing river and Wei River (see Table 3-4 and Fig. 3-22) while Zhengzhou and Ji'nan lie in the mainstream. The maximum magnitude of streamflow of the two tributaries (9200~13300 m^3/s) is much lower than these in the mainstream (11000~22300 m^3/s). As for the two tributaries, streamflow in the Wei River fluctuates more intensively than in the Jing River (WR & JR in Fig. 3-22). In othe words, the fluctuations in streamflow of Xi'an are mostly contributed by the Wei River.

Also, we looked up the flood in the cities and found historical extraordinary high flood all occurred in Summer and Fall. In addition, as an example, the food years of the Wei River flowing through Xi'an include 1933, 1954, 1981 and 2019 NOT in accordance with the peak values in Fig. 3-24a. Therefore we further investigated the input data of our model and found that the extraordinary high peak values in 198105, 200801 and 201601 are resulted by the uncertainties in GLDAS data. In other words, uncertainties in GLDAS dataset also induced uncertainties in the results of Fig. 3-24, especially in the Fig. 3-24a, the extraodinary peak values occurred in 198105, 200801 and 201601 come from the extraordinary low value of GLDAS: $8.06*10^{-8}$, $8.06*10^{-8}$, and $3.23*10^{-7}$ kg m^{-2} per 3-hour while the average value is $8.17*10^{-3}$ kg m^{-2} per 3-hour. During the stage of application, the extraordinary peak values are suggested to be interpolated by using the before- and after-month values.

In addition, in the year 1998 floods occurred through most basins in China including Yangtze River, the Nen River, the Songhua River and the Pearl River as well as the YR. But because of most floods occurred in the tributaries of the YR, so the food of the mainstream of YR is not as severe as in Yangtze River. As literatures recorded, the extraordinary peak flood in the mainstream of the YR occurred five times in 1761, 1843, 1933, 1958, 1982.

3.2 Surface freshwater available (FWA) for the three representative cities

Water resources or streamflow in the Yellow River are assigned by the Yellow River administrators to cities along the Yellow River proportionally for use. Literatures show that in the year 1987, 1.58 billion m^3 streamflow in the Yellow River was assigned to Xi'an, 0.42 billion m^3 to Zhengzhou*(Nie, 2008). The averaged quantity of streamflow in the Yellow River (0.58 billion m^3 in the period from 2011 to 2013) was assigned to Ji'nan (Zhou et al., 2015).

From Fig. 3-24, we can learn that in the year 1987, the Yellow River flowing by Xi'an has an annual runoff of 382.39 billion m^3, that flowing by Zhengzhou has an annual runoff of 378.09 billion m^3; in the period from 2011 to 2013, the average annual runoff in the Yellow River flowing by Ji'nan is 229.57 billion m^3. With these data we can calculate the allowable proportions of water withdraw from the Yellow River for Xi'an, Zhengzhou, and Ji'nan, which are respectively 0.41%, 0.11%, and 0.25%. With these proportions, we can get the surface freshwater available (FWA) from the Yellow River, and those from 2013 to 2017 are as shown in Table 3-5 (2).

According to "Water Resource Bulletin of Xi'an (2013-2017)", "Water Resource Bulletin of Zhengzhou (2013-2017)", and "Water Resource Bulletin of Ji'nan (2013-2017)", surface

freshwater available (FWA) for the three cities varies are as shown in Table 3-5 (1). With the averaged ratio of surface FWA from the Yellow River to that from "Water Resource Bulletin" in Table 3-5 (which are respectively 1.01, 1.14, and 1.22), we can derive total surface FWA quantity for the three cities in other prediction years. Surface freshwater available for the three representative cities from the year 2000 are as shown in Fig. 3-25.

Table 3-5 Surface FWA variable from the Yellow River, from "Water Resource Bulletin" and their ratios. XA: Xi'an, ZZ: Zhengzhou, JN: Ji'nan.

Year	Surface FWA variable (billion m^3)	XA	ZZ	JN
2013	(1) Quantity from "Water Resource Bulletin"	1.56	0.35	1.16
	(2) Quantity from the Yellow River	1.61	0.41	0.58
	(3) Ratio=(2)/(1)	**1.03**	**1.18**	**0.50**
2014	(1) Quantity from "Water Resource Bulletin"	1.73	0.35	0.25
	(2) Quantity from the Yellow River	1.56	0.44	0.56
	(3) Ratio=(2)/(1)	**0.90**	**1.24**	**2.23**
2015	(1) Quantity from "Water Resource Bulletin"	1.71	0.42	0.52
	(2) Quantity from the Yellow River	1.62	0.42	0.58
	(3) Ratio=(2)/(1)	**0.95**	**0.99**	**1.13**
2016	(1) Quantity from "Water Resource Bulletin"	1.42	0.44	0.89
	(2) Quantity from the Yellow River	1.90	0.41	0.57
	(3) Ratio=(2)/(1)	**1.34**	**0.92**	**0.64**
2017	(1) Quantity from "Water Resource Bulletin"	2.03	0.28	0.35
	(2) Quantity from the Yellow River	1.63	0.38	0.56
	(3) Ratio=(2)/(1)	**0.80**	**1.37**	**1.60**

* What is worth noticing is some of the ratios in Table 3-5 are great than 1.0 due to uncertainties in the estimation of surface FWA above. The uncertainties were mostly resulted from the relatively lower spatial resolution (the minimum: 10 m) of satellite imageries when we estimate streamflow. Fortunately, the ratios greater than 1.0 have little influence on the derived total surface FWA in other prediction years because they act only as a bridge (or an adjusting coefficient to the real values from "Water Resource Bulletin").

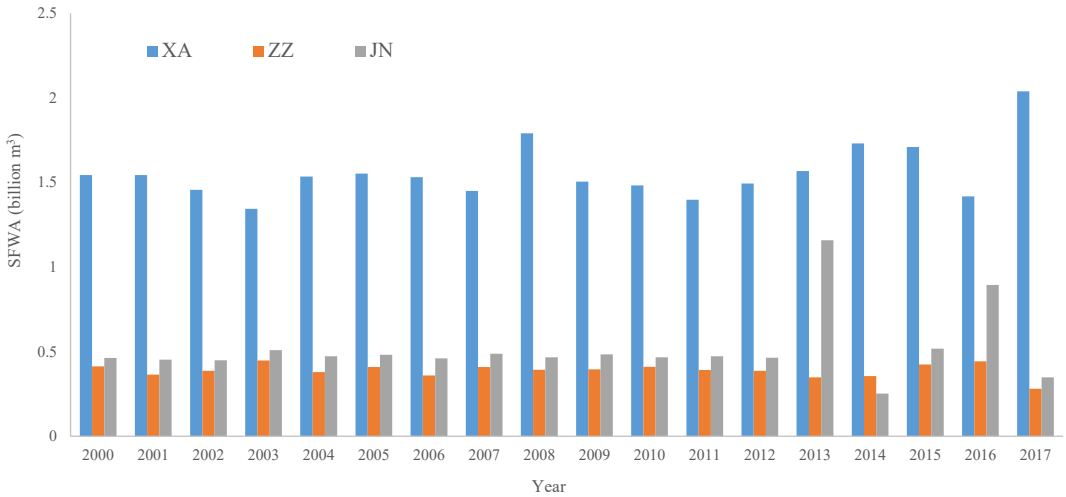

Fig. 3-25 Surface FWA for the three representative cities of Xi'an (XA), Zhengzhou (ZZ), and Ji'nan (JN).

With the surface freshwater available for the three representative cities in Fig. 3-25, ANN (Artificial Neural Network) model can be set up based on environmental factors, presented in CMIP5 (Coupled Model Intercomparison Project Phase 5) scenarios, influencing the variation of surface freshwater. By using the ANN models, future surface FWA in the year 2030 and 2050 can be predicted with environmental factors in CMIP5 scenarios. Details can be found in Chapter 6.

3.3 Summary

This chapter firstly two new methods to estimate streamflow respectively for dry (VHR-AMHG) and wet seasons (transcaled spatial C/M method). The accuracy verification of VHR-AMHG was performed by comparing it to field measurement data and the global parameters of the original AMHG (global–AMHG).The root mean square error (RMSE) calculated from VHR-AMHG was 32.15 m^3/s lower than the RMSE from original method (global–AMHG) of 305.65 m^3/s, indicating that the VHR-AHRG method yields a significantly higher accuracy for streamflow estimation for medium-to-small rivers. The second method, transcaled spatial C/M method was developed mainly for flow velocity estimation. Complementally the Riba-zero method was developed to estimate river bathymetry at ungauged rivers. The transcaled spatial C/M method coupled with the Riba-zero method can be used to retrieve streamflow at ungauged rivers. Verification show that the relative root mean square error (rRMSE) and the relative error (RE) of the simulated velocity by using the transcaled spatial C/M method in our study area is rRMSE: 0.36 (RE: 19.00%) for the whole year, 0.15 (14.56%) in wet seasons and 0.25 (20.88%) in dry seasons, suggesting the performance of the transcaled spatial C/M method has higher precision in wet seasons. The streamflow estimation at ungauged rivers using transcaled spatial C/M plus Riba-zero is better than that of previous studies.

Using the two methods coupled with NASA GLDAS runoff dataset, long-termed streamflow (1948-2018) was estimated by using satellite imageries for the three representative cities (Xi'an, Zhengzhou and Ji'nan). Xi'an and Zhengzhou have almost the same averaged streamflow value (~1000 m^3/s) from 1948 to 2018, and Jinan has a lower averaged streamflow value (~600 m^3/s).

Based on the long-termed streamflow (1948-2018) and official data from "Water Resource Bulletin" of the three cities, total surface freshwater available (SFWA) in the period from 2000 to 2017 for the three cities was estimated, laying foundation for SFWA prediction in future 2030 and 2050.

Chapter 4 Estimation of underground freshwater available

Following on the achievement of the first objective in Chapter 3, this chapter, aiming at the second objective and designed a new framework for estimating underground freshwater available. Meanwhile the data series of GRACE (or named as TWSC: terrestrial water storage change) was extended from the last two decades to more than seven decades from 1948. For this goal, environmental factors driving the variation of TWSC were firstly determined via literature analysis and statistic methods. Secondly, the selected factors were used to verify and improve an artificial neural prediction model –LSTM-N (Long short-term memory network) wherein the optimized LSTM-N parameters were determined. By using the LSTM-N with optimized parameters, the prediction performance of driving factor selected in the four scenarios was tested. Finally, using the driving factors which perform the best along with the LSTM-N with optimized parameters the data series of GRACE TWSC were extended from the period of 2002-2016 to the period of 1948-2016 with which the corresponding underground freshwater available (UFWA) were produced to serve for the prediction of UFWA in future 2030 and 2050 in Chapter 6.

4.1 Determining factors driving the variation of underground FWA (vertical water flux)

4.1.1 Potential factors driving the variation of underground FWA

Globally, GRACE observations were often used to assess terrestrial water storage change (TWSC), or the sum of all components, including groundwater storage (GWS), soil moisture, snow water equivalent (SWE), and canopy water storage (CWS) (Massonnet et al., 1993; Ezquerro et al., 2017; Shu et al, 2018; Yin et al., 2020). TWSC is usually expressed as LWE (Liquid Water Equivalent) in the GRACE dataset. From previous literatures, all potential factors that may influence the temporal and spatial variation of underground FWA, e.g., ET, precipitation, irrigation, air temperature, runoff, glacier melting etc. were determined meanwhile the spatiotemporal characteristics of TWSC were often validated or downloaded against hydrological model simulations and precipitation data (Döll et al., 2014; Cao et al., 2015; Pellet et al., 2020; Vishwakarma et al., 2021). The rest factors can be accessed through GLDAS dataset. Correlation between underground FWA and other factors were analyzed. The variation of underground FWA was surrogated by using the terrestrial water storage (TWS), or the sum of surface FWA and underground FWA whereby to select potential driving factors for underground FWA variation.

Terrestrial water storage (TWS) variation is crucial for global and basinal hydrological cycles and water resources management under climatic changes. As to the whole China, the inner-annual variations in TWS exhibited remarkable downward trends with decreased rate of 0.1 cm/yr (Chen et al., 2017). Spatial patterns of TWS in China can be divided into three distinct sub-regions of TWS region with increased (Fig.4-1 (A)), TWS region with decreased (Fig.4-1 (B)), TWS region with insignificant variation (Fig.4-1 (C)). The TWSC decline in the Hai River basin can be largely attributed to GWS depletion, and meanwhile the decrease of consumptive agricultural water use alleviated the TWSA reduction rate by 4.1% in the basin. The increase

of irrigation consumption accelerated the TWSA depletion trend by 4.9% and 13.4% in the Yellow River and Huai River basins, respectively. The correlation coefficients were 0.742-0.952 between TWSC and the residual of precipitation, ET, flow into the sea, and irrigation consumption over the four river basins (Lv et al., 2021). In addition, the human activities (e.g., irrigation and inter-basin water diversion) are very important factors influencing regional water-cycle inclusive of TWSC as the TWSC is an important factor of regional water budget (Lv et al., 2017 & 2019).

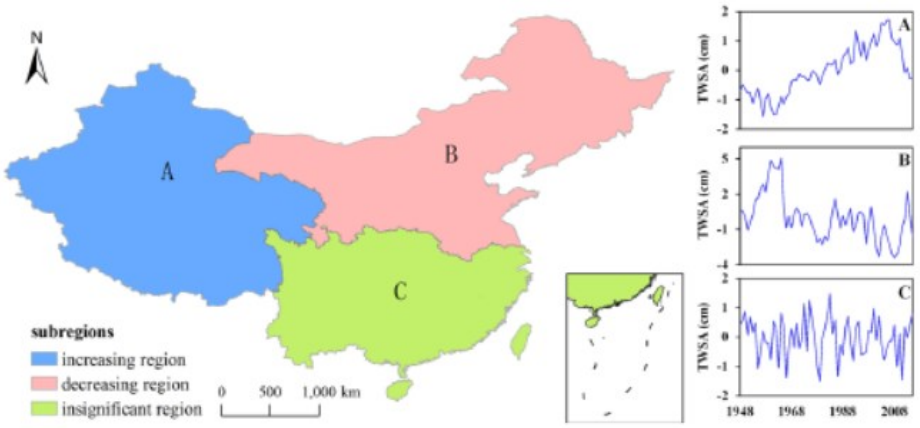

Fig. 4-1 Spatial distributions of the TWS variation sub-regions: (A) increasing TWS region, (B) decreasing TWS region, and (C) the insignificant change region (from Chen et al., 2017)

Chen et al. (2017) took West, Northeast and South China as examples and studied the dominant factors influencing the variation of TWS with GRACE and GLDAS (Global Land Data Assimilation System Version 2) data between 1948 to 2015. Results show that the Northeast had decreased trends (−0.05 cm/yr) due to climate change and anthropogenic activities. Urban expansion is a non-ignorable factor to TWS reduction in Jing-Jin-Ji region ($r = 0.61$); the west had increased from 1948 to 2015 (0.03 cm/yr) due to precipitation increased and recharge by glacier melt; the south had insignificant trends and TWS varied with precipitation ($r = 0.78$). As to the dominant factors influencing the variation of TWS, precipitation, air temperature and glacier mass loss dominate the TWSC in the west of China (Sub-region A); LUCC and human activities (especially, urbanization and population growth) dominate the variation of TWS in the Northeast of China (Sub-region B); Sub-region C is one of the most densely populated parts of China and the depletion of water storage should not be ignored. In addition, the high number of dams influences the hydrological regime. However, anthropogenic activities have lower influence on water storage changes in the sub-region C. Overall, TWS variation exhibits a high correlation to climate change and land cover and land use changes or constructions of dams. TWSC variations in different regions of China depend on the certain climate condition and geographical characteristics (land cover change and regional development plan).

The Yellow River basin crosses some regions of Sub-region A and Sub-region B and therefore factors may vary with the geographical position. Further analysis (Lin et al., 2019) on the GRACE datasets suggests that the groundwater storage had an overall decreasing trend ($R^2=0.57$) during the last 14 year, and over the whole basin decreased significantly ($p<0.0001$,

slope changed from −0.0137 cm/month to −0.0684 cm/month) since 2010 (2010–2016) and showed stronger fluctuations than the time before (2003–2009). Despite the overall trend, the changes were heterogeneous if looking at finer scales: spatially, there was a gradual decline of storage from west to east (e.g. the change in December 2016 was −3.6, −9.1 and −25.8 cm for the upper, middle and lower reach, respectively); and temporally, the timeseries among the reaches were significantly different (p=0.023). Hotspot analysis also indicated the heterogeneity in groundwater decline across the basin and through the time. Additionally, it showed that human factors (e.g. groundwater consumption) become dominant in determining the groundwater change pattern over climatic variations (Lin et al., 2019).

In addition, the TWS data present an overall downward trend and the variation of TWS, or TWSC, is influenced by runoff, or surface streamflow most directly. The reason is that surface streamflow usually recharges underground water in wet seasons and is recharged by the latter in dry seasons, therefore the variation of surface streamflow has great influence on TWSC. Additionally, the main hydrological and meteorological factors influencing TWSC are precipitation and temperature.

The research of (Lv et al., 2019) suggests that, as for the source regions of the Yellow River, decline of evaporation and degradation of permafrost had led storage capacity increasing significantly and then surface runoff increasing. Moreover, one of the potential factors for the TWSC in the whole YRB is precipitation mimus ET (Fig. 4-2) as ET is highly influenced by LAI (Fig. 4-3) which was directly influenced by groundwater. Another important influencing factor for TWSC is irrigation in the YRB, as shown in Fig. 4-4.

As to the middle reaches of the Yellow River Basin, TWS had an increasing trend from 2003 to 2012. The increase of water storage was caused by the decrease in runoff loss in the middle reaches of the Yellow River Basin, that the average annual decreasing amount was 2.93 mm equivalent water depth. There was obvious spatial variation of the water storage change. The most obvious increasing of water storage is at Longmen-Sanmenxia section, where the average annual increasing amount was 4.59 mm equivalent water depth. The second is at the Hekou-Longmen section, where the average annual increasing amount was 3.47 mm equivalent water depth. And the last one is at Sanmenxia- Huayuankou section, where the average annual increasing amount was 2.71 mm equivalent water depth.

As to the Loess Plateau, precipitation has a greater influence on the TWSC in the southwest and south of Loess Plateau, but the surface temperature plays dominated role in the southeast and east. Human activities have a greater impact on TWSC in Shanxi province and the border zone of Shaanxi, Shanxi and Henan. The TWS has decreased (increased) more and more quickly (slowly) in the Loess Plateau (headwater region). The TWS increase corresponded to increased runoff and soil moisture in the headwaters, and the TWS depletion corresponded to decreased runoff and groundwater in the Loess Plateau and downstream regions. The increase in evapotranspiration (ET) dominated the basin-averaged TWSC reduction, while the increase in ET was highly related to the increases in vegetation cover and irrigation water use. For spatial TWSC variations, the value of precipitation minus ET could account for most changes in TWSC, except for those in the headwater region and a region near the internally drained area. Importantly, the irrigation-induced TWSC was considerable and varied with different irrigation

water sources (i.e., surface water and groundwater). Overall, the impacts of afforestation and irrigation on TWS are sufficiently important (Lv et al., 2019).

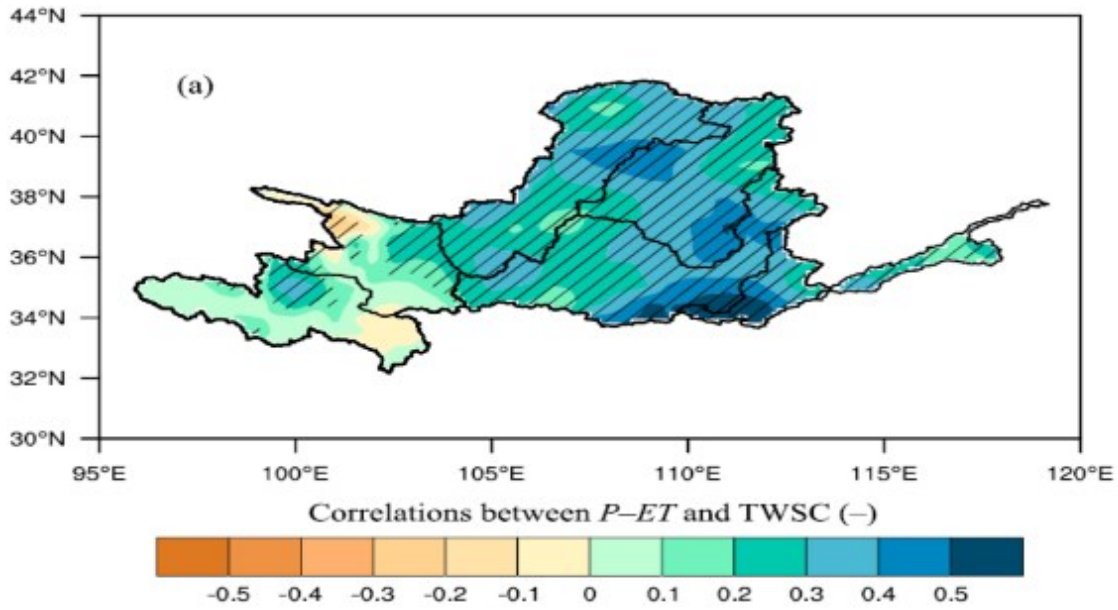

Fig. 4-2 Correlations between P-ET and TWSC (Lv et al., 2019)

Fig. 4-2 shows that, in most areas of the YRB P-ET has positive correlation with TWSC, except for very small proportion of upstream area in the west. This reveals P-ET is an important factor influencing the TWSC in most areas of the YRB.

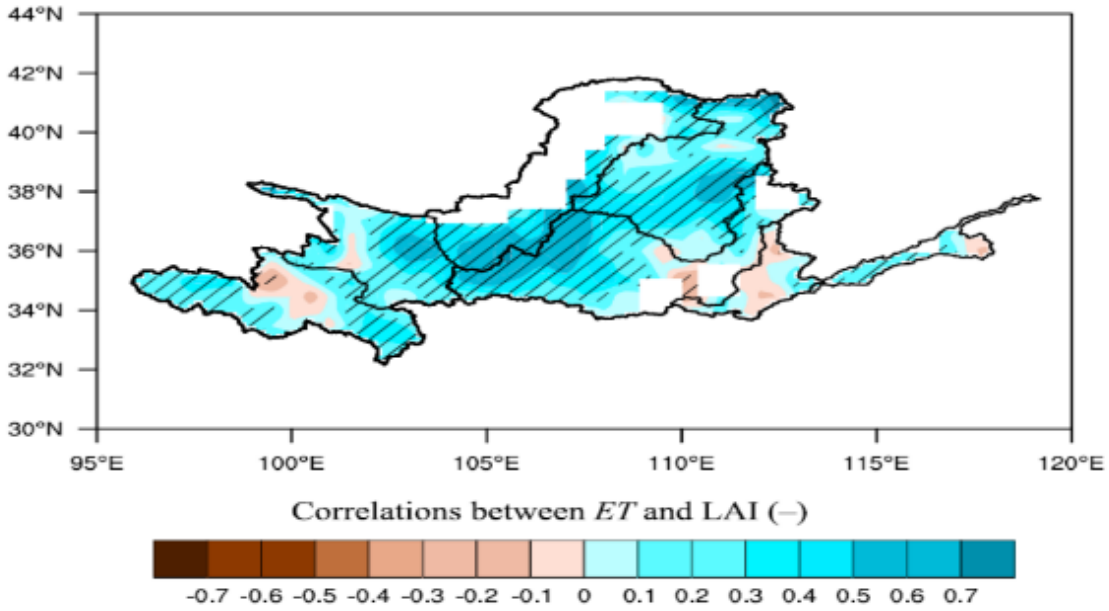

Fig. 4-3 Correlations between ET and LAI (Lv et al., 2019)

Fig. 4-3 shows that, in most areas of the YRB ET has positive correlation with LAI, except for very small proportion of upstream area in the west and downstream area in the east. This reveals ET changes with LAI positively in most areas of the YRB.

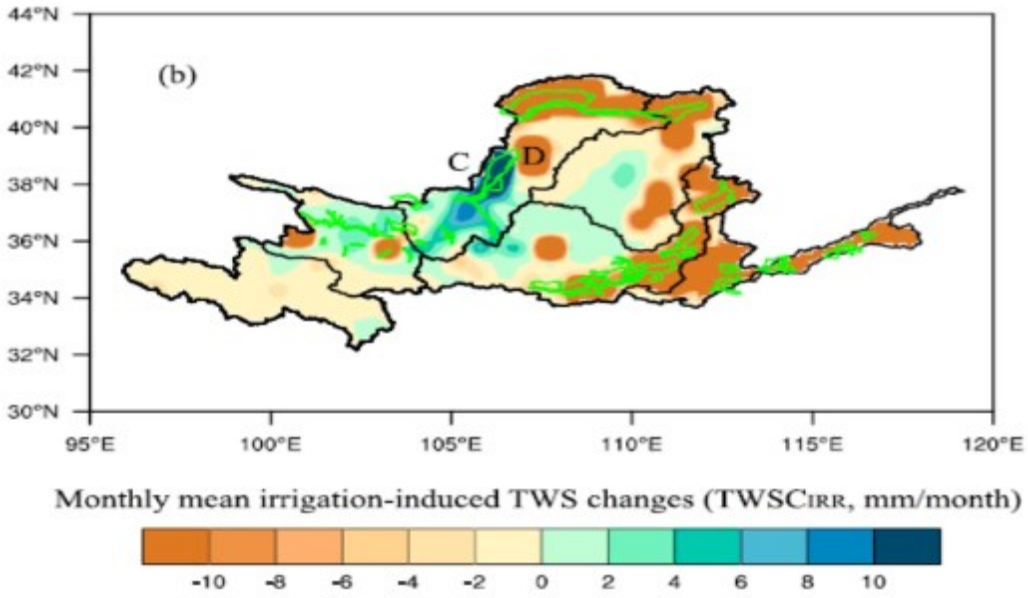

Fig. 4-4 Irrigation-induced TWSC (Lv et al., 2019)

Fig. 4-4 shows that, in most areas of the YRB intensive irrigation reduced the TWS. The TWS in the north and east decreases the most and decrease a little in the west. In contrary, in some areas of the middle reach of the YRB, irrigation resulted in increase of TWS. The reason maybe because of the withdraw of surface water from the Yellow River and its tributaries. Overall, irrigation is a very important factor influencing the TWSC in most areas of the YRB but varies with space.

All in all, literatures (Lin et al., 2019; Lv et al., 2019; Pellet et al., 2020; Vishwakarma et al., 2021) show that potential factors for underground FWA include precipitation, air temperature, evaptranspiration, precipitation minus evaptranspiration, human activities or groundwater consumption, and surface runoff. In details, the source regions of YRB have declined evaporation, degraded permafrost, and increased soil moisture / streamflow which had led underground FWA increasing significantly. Differently, the middle and lower reaches of YRB have decreased runoff and groundwater leading to underground FWA decreasing.

4.1.2 Determination of factors driving underground FWA variation

Based on data series of all potential factors, mainly from GLDAS dataset, I use VIP (Very Important Projection) method to refine the factors influencing underground FWA variation whereby to lay foundation for GRACE data series extension, i.e. underground FWA.

(1) Determination of representative periods for underground FWA variation

With climate change, FWA in different periods has variable driving factors. So, respectively selecting representative periods to set up prediction models is helpful for prediction precision improvement.

To determine factors for the different representative periods by using VIP method. Three representative periods were determined by using trend analysis plus Mann-Kendall method.

Of most GRACE solutions in China, the solutions from Jet Propulsion Laboratory (JPL)

and the Center for Space Research (CSR) are more reliable than others (Lv et al., 2021) and the RMSE of the two solutions in mainland China is respectively 31.3 mm and 13.2 mm (Yao, 2017). So this study selected the CSR RL06 monthly solutions (with a resolution of 0.25°) as the database. GRACE TWS, or underground FWA increased from July 2003 to Nov. 2005, and kept a recharge-use balance between Dec. 2015 and Oct. 2006. After the ~1 year balance period, TWS decreased first abruptly within a half year (Nov. 2006-Jun. 2007), then slowly in the following 6 years (July 2007-Oct. 2013), and finally abruptly within nearly 3 years (Nov. 2013-May 2016).

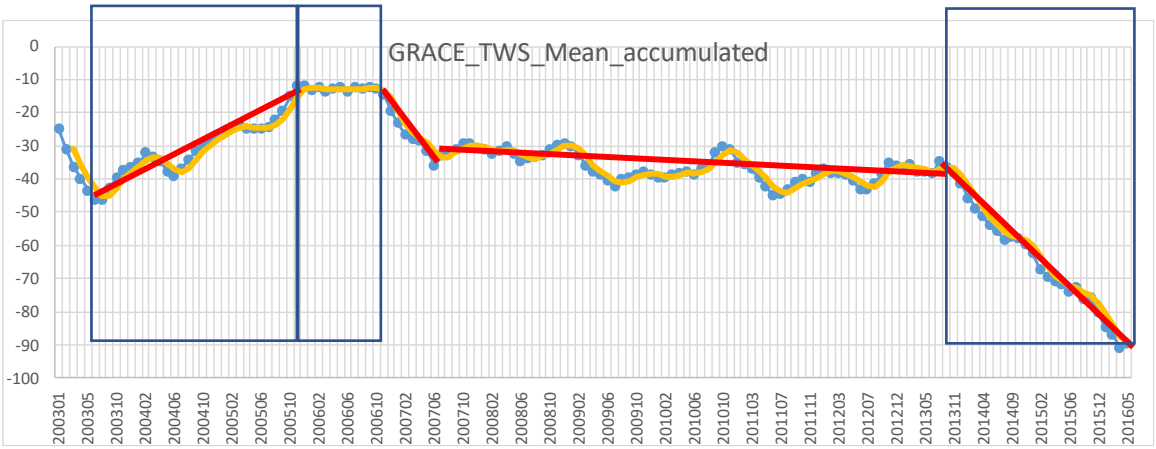

Fig. 4-5 Three representative periods in the GRACE TWS data at monthly scale

Therefore, there are three representative periods of TWS-increasing period (July 2003-Nov. 2005), TWS-balancing period (Dec. 2005-Oct. 2006), and abruptly TWS-decreasing period (Nov. 2013-May 2016).

To further verify the change-point identification results, I used the Mann-Kendall change point identification method to verify them, as shown in Fig. 4-6.

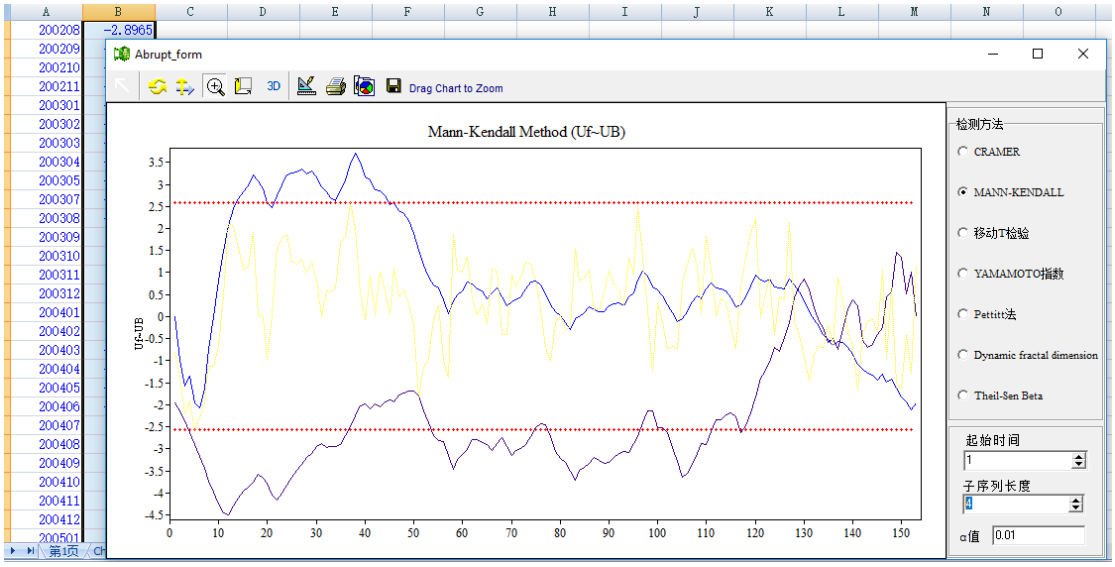

Fig. 4-6 Change point analysis on the GRACE TWS data by using Mann-Kendall change point identification method.

Fig. 4-6 shows that the change point (CP) firstly appeared in 201311.After CP, increased

amount (recharged water amount) was less than decreased amount (water usage amount) and therefore lasting decrement in TWS appeared.

Therefore, three representative periods were selected to further explore the TWS spatial heterogeneity and its driving factors and extend the data series of GRACE-TWS.

- TWS-increasing period (07/2003-11/2005)
- TWS-balancing period (12/2005-10/2006)
- TWS abruptly -decreasing period (11/2013-05/2016)

(2) Determination of driving factors for representative periods

VIP method was used to determine the driving factors for the three representative periods. VIP method is often used to explain the weight of the independent variable in explaining the dependent variable, which is usually considered to have important roles in the partial least squares discriminant analysis process, suggesting the variables are important when VIP values exceed 1.0 (Gao et al., 2018; Lee et al., 2018; Wang et al., 2020). The VIP was calculated with:

$$VIP_k = K \times \sum_j W_{jk}^2 \left(\frac{SSY_j}{SSY_t} \right) \quad (1)$$

where VIP_k is the kth wavelength for a partial least square regression (PLSR) algorithm with jth factors, W_{jk} denotes the loading of the kth wavelength in the jth PLSR factor, SSY_j and SSY_t represent the explained and total sum of squares of target Y (soil property of interest), respectively, and K is the total number of wavelengths. The VIP value greater than 1.0 indicates that the factor is significant for spatial-temporal variation of underground FWA.

Based on the GLDAS dataset, the five potential factors from literatures (precipitation, air temperature, evapotranspiration, precipitation minus evapotranspiration, and surface runoff) (Lin et al., 2019; Lv et al., 2019; Pellet et al., 2020; Vishwakarma et al., 2021) were calculated as shown in Table 4-1. Factor indicating human activities or groundwater consumption was not calculated because in the GLDAS dataset no variables can be used to calculate the factor. Moreover, in the statistical book only annual (not monthly) values are presented and hard to match with the monthly variables in GLDAS dataset. In addition, only data in the unit of district instead of footprint are presented in the statistical book which are hard to match to the other variables in the GLDAS dataset (at footprint scale).

To make up the mistake missing groundwater abstraction data, I collected other factors (transpiration, glacier melting, root zone soil moisture, soil moisture from 0 to 200 cm in depth, terrestrial water storage, direct evaporation from baresoil) from GLDAS likely influencing groundwater variation to complement the potential factor list, as shown in Table 4-1.

The ultimate goal of this study is to extend the series of GRACE dataset from 2002-2016 to 1948-2016. Finding the key driving factors is the primary step. But only finding factors for the whole YRB is far from enough. Therefore, this research tries different ways to find factors driving the variation of TWS of every spatial classes and even every pixel (0.25°×0.25°) for the three representative periods whereby to set up prediction model with a temporal scale of month.

For this purpose, I set up other four scenarios to select key driving factors for TWS variation and in the next section accordingly use them to predict TWS in the period of 2002-2016 whereby to verify the precision of prediction model. The four scenarios uses different scale of data as input: Scenarios No.1 uses the YRB-averaged environmental factors which are separated into three periods; Scenario No.2 uses cluster-averaged factors to replace YRB-averaged ones with three periods; Scenario No.3 is an improved version of Scenario No.2 where all factors were rearranged by using the same principal as the GRACE data used; Scenario No.4 uses pixel environmental factors to replece YRB- or cluster-avearaged environmental factors where the analysis was conducted one month after another from 2002 to 2016 instead of using the three periods. The key-factor-driving model with the highest accuracy will finally be selected to predict TWS from 1948 to 2016.

(a) Scenario No. 1: using the YRB-averaged environmental factors to determine key driving factors for the three periods (3 sets of key driving factors)

Scales have great influence on the results of driving factors selection. To begin with, I try to get factors driving the variation of TWS at the scale of the whole YRB. In other words, I averaged footprint values of a factor in Table 4-1 in the whole basin into one value. E.g., as the whole YRB has 1271 pixels or footprints in the GRACE dataset (CSR GRACE/GRACE-FO RL06 Mascon Solutions with a spatial resolution of 0.25° or ~120 km), I averaged the 1271 values of air temperature per month into one value per month and then a series of values of air temperature from 07/2003 to 05/2016 was formed. In this way 11 series of values of the 11 potential factors in Table 4-1 from 07/2003 to 05/2016 along with a series of GRACE TWS values from 07/2003 to 05/2016 were inputted into VIP methods to determine driving factors at the scale of the whole YRB. The results are listed in Table 4-1.

Table 4-1 Potential factors corresponding to the GLDAS data: VIP value and formula

Priority	Potential factor	VIP value	Fomula with GLDAS data
1	Air_temperature	1.611	Tair_f_inst
2	Precipitation	1.215	Rainf_f_tavg
3	Evapotranspiration	1.205	Evap_tavg
4	Transpiration	1.142	Tveg_tavg
5	Glacier_melt	0.958	Qsm_acc
6	Root zone soil moisture	0.907	RootMoist_inst
7	Soil moisture from 0 to 200 cm in depth	0.821	SoilMoi0_10cm_inst+SoilMoi0_40cm_inst+SoilMoi0_100cm_inst+SoilMoi0_200cm_inst
8	Terrestrial_water_storage	0.821	(SoilMoi0_10cm_inst+SoilMoi0_40cm_inst+SoilMoi0_100cm_inst+SoilMoi0_200cm_inst)+SWE_inst+CanopInt_inst
9	Direct Evaporation from Bare Soil	0.794	ESoil_tavg
10	Precipitation_minus_ET	0.498	Rainf_f_tavg-Evap_tavg
11	Runoff	0.453	Qs_acc+Qsb_acc(Storm surface runoff+Baseflow-groundwater runoff)

Overall, at the scale of the whole YRB driving factors detected (with VIP value great than 1.0, from big to small) include air temperature, precipitation, evapotranspiration, and transpiration, as shown in Column 2 of Table 4-2.

Likely, I selected the driving factors at the scale of the whole YRB for the three representative periods, as shown in Column 3-5 of Table 4-2. The results show that driving factors in the three representative periods differ from those in the whole period from 2002-2017 except for the last periods of 11/2013-05/2016, or TWS abruptly -decreasing period. In other words, TWS abruptly -decreasing period has the same driving factors as the whole period: air temperature, precipitation, evapotranspiration, and transpiration. However, the TWS-increasing period (07/2003-11/2005) and TWS-balancing period (12/2005-10/2006) have the same driving factors (with VIP values great than 1.0 and in the order from big to small) of air temperature, glacier melting, soil moisture from 0 to 200 cm in depth, and terrestrial water storage. In other words, the YRB in the period from 2002 to 2017 has an overall trend of decreasing.

Table 4-2 driving factors in the whole period from 2002 to 2017 and in the three representative periods

Priority of driving factor	Monthly mean			
	Year 2002 through 2016	07/2003-11/2005	12/2005-10/2006	11/2013-05/2016
air_temperature	1	1	1	1
precipitation	2			3
evapotranspiration	3			2
Transpiration	4			4
glacier_melt		2	2	
Soil moisture from 0-200 cm depth		3	3	
Terrestrial_Water_Storage		4	4	

Table 4-2 shows that every one of the three periods has four key driving factors. The key driving factors shared by periods 1, 2 and 3 is air temperature the VIP value of which is the largest. The driving factors selected for the period 1 and period 2 are the same. According to the VIP value from high to low, the four key driving factors are air temperature, glacier melt, soil moisture, and Terrestrial Water Storage. The driving factors selected for period 3 have four members of air temperature, evapotranspiration, precipitation, transpiration.

(b) Scenario No. 2: using cluster -averaged environmental factors to determine key driving factors for the three periods (9 sets of key driving factors)

Based on the results in the last section this section lowers the scale of the whole YRB to sub-basins of the YRB. In other words, the whole YRB will be divided into several sub-basins for this research. To unveil the inner rule driving the variation of TWS in every sub-basin, this study takes as sub-basins those classes with 12 factors (11 potential factors and one TWS factor) having similar variation trend.

In detail, averaged values of individual factor and TWS at every pixel (0.25°, ~25 km) of the YRB from 2002 to 2017 are calculated. In this way 12 temporal-averaged spatial maps are produced. Every spatial map has 1271 pixels with values of an individual factor. Using the 12 maps as input, the K-mean method was used to cluster the whole YRB into different classes. In details, firstly, every one of the environmental factors (Table 4-1) plus lwe within the 163

months from 2002 to 2016 are averaged into that for one averaged month. In this way, we get 12 averaged monthly variable values for every one of the total 1271 pixels in the whole YRB. Secondly, the K-means method is used to spatially cluster the 1271 pixels with 12 averaged variables into three classes, as shown in Fig. 4-7 (a). Finally, in the same way, 1271 pixels in the 3 representative periods (07/2003-11/2005, 12/2005-10/2006, 11/2013-05/2016) are also respectively clustered into three classes, as shown in Fig. 4-7 (b,c,d).

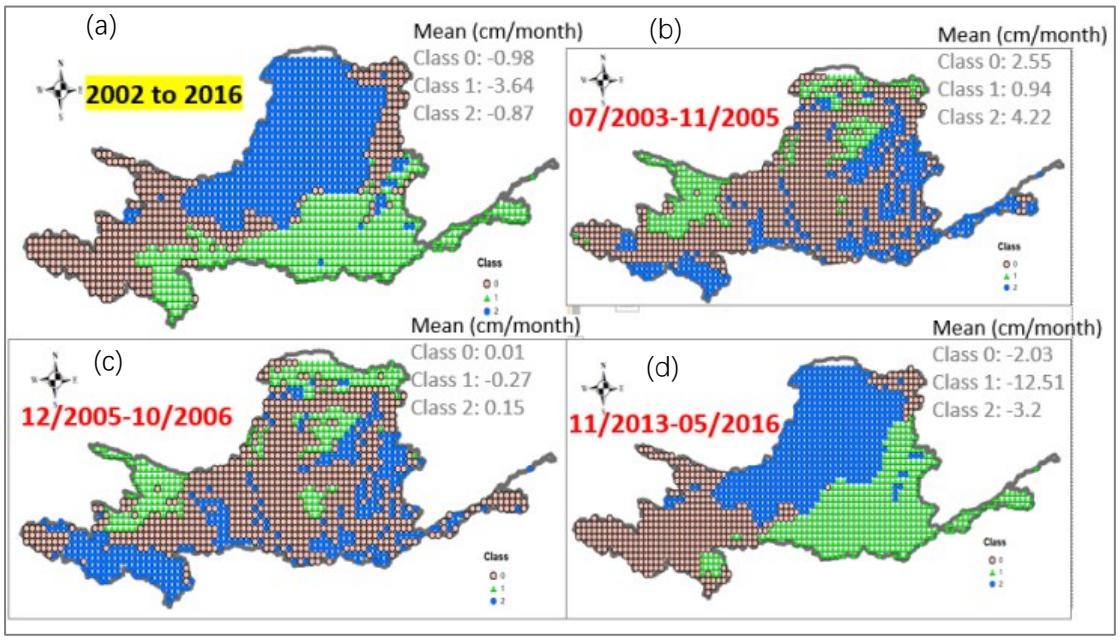

Fig. 4-7 Clustering the 1271 pixels of the YRB into three classes for the whole period (2002-2016) (Upper left-(a)), and for the three representative periods (Upper right-(b), Lower left-(c), and Lower right-(d)).

Overall, the 1271 pixels in YRB are clustered into three classes with clear boundaries which are in the north-central, western and southeast of the basin. The classes for the first and second periods are roughly the same. They are scattered, and the boundary is not very clear. Based on the classes for the three representative periods in Fig. 4-7, the VIP method is used to determine the key driving factors respectively for the three classes in every one of the three periods, as shown in Table 4-3.

In Table 4-3, the VIP value of a certain impact factor exceeding 1 indicates that the factor has a significant impact on lwe. The larger the proportion of VIP>1 in the 9 groups within one column, the greater the importance of the factor. To avoid missing important factors, a screening scheme of fuzzy membership degree is introduced, with (1±0.1) as the fuzzy standard. The factor with its value greater than the standard can be selected as the key driving factor of the period, as shown in red bold letters in rows 5, 9, and 13 in Table 4-3. Generally, as can be seen from Table 4-3, there are 7 influencing factors with a larger proportion of VIP>1 in the 9 groups, including glacier melt (8/9 of the VIP values are greater than 1): air temperature (8/9), and evaporation2 (Direct Evaporation from Bare Soil) (5/9), precipitation (4/9), soil moisture2 (or soil moisture from 0 to 200 cm in depth)(3/9), runoff (3/9), precipitation minus ET (3/9), which indicates that the 7 factors are of higher importance.

Table 4-3 VIP values of the 11 environmental factors for the three classes in the three representative periods respectively. VIP>1.0 (in bold font) means the corresponding factor has great influence on LWE.

Representative period	Class	Evapotranspiration	Glacier melt	Transpiration	Evaporation 2	Soil moisture 2	Precipitation	Air temperature	Runoff	Soil moisture1	Terrestrial water storage	Precipitation minus ET
1	0	0.63	**1.14**	0.63	**1.15**	**1.31**	0.57	**1.49**	0.44	**1.17**	**1.16**	0.64
	1	0.55	**1.83**	0.81	**1.50**	0.13	0.23	**1.72**	0.68	0.60	0.60	0.50
	2	0.95	**1.01**	0.91	0.54	0.74	**1.41**	**1.11**	**1.23**	0.83	0.83	**1.15**
	Mean	0.71	**1.33**	0.78	**1.06**	0.73	0.74	**1.44**	0.78	0.87	0.86	0.76
2	0	0.44	**1.00**	0.53	0.80	**1.40**	0.79	**1.40**	**1.17**	0.95	0.94	**1.09**
	1	0.71	**1.65**	0.57	**1.08**	0.93	**1.09**	**1.71**	0.34	0.55	0.55	0.75
	2	0.98	**1.31**	0.88	0.71	0.93	**1.09**	**1.68**	0.74	0.82	0.82	0.54
	Mean	0.71	**1.32**	0.66	0.86	**1.09**	**0.99**	**1.59**	0.75	0.77	0.77	0.79
3	0	**1.16**	0.79	**1.05**	**1.21**	**1.33**	0.84	**1.33**	0.35	**1.00**	0.99	0.34
	1	0.26	**1.42**	0.37	**1.44**	0.27	0.28	**2.04**	**1.22**	0.28	0.28	0.85
	2	**1.14**	**1.02**	**1.08**	0.69	0.86	**1.58**	0.96	0.79	0.79	0.79	**1.02**
	Mean	0.85	**1.08**	0.84	**1.11**	0.82	0.90	**1.44**	0.79	0.69	0.69	0.74

(c) Scenario No. 3 — improvement of Scenario 2: using the same principal of GRACE to rearrange GLDAS dataset (9 sets of key driving factors)

This section continues to select key driving factors with VIP method by using similar steps in the Scenario No.2. Actually, this section is an improvement of the Scenario No.2. The idea of improvement comes from the difference between GRACE data and GLDAS data. The GRACE satellite dataset reflects the abnormality of LWE based on the reference value (the average value from 2004 to 2009). In other words, the GRACE observations users downloaded are the original observations subtracted by the reference value year by year. However, environmental factors from GLDAS dataset are the original values instead of abnormality. To keep consistent with the GRACE LWE data we used, the GLDAS data must be rearranged to get abnormalities. Therefore, GLDAS data are processed with the principles of GRACE data. In details, environmental factors in GLDAS dataset are firstly subtracted by the reference values (average values in the period of 2004-2009) whereby to obtain the abnormal values of environmental factors.

After obtaining the abnormal values of environmental factors in the GLDAS dataset, the 1271 pixels of the whole YRB are re-clustered by using the GLDAS abnormality data stage by stage in the three representative periods (as determined in Fig. 4-5). Clustering results are shown in Fig. 4-8 ~ Fig. 4-10.

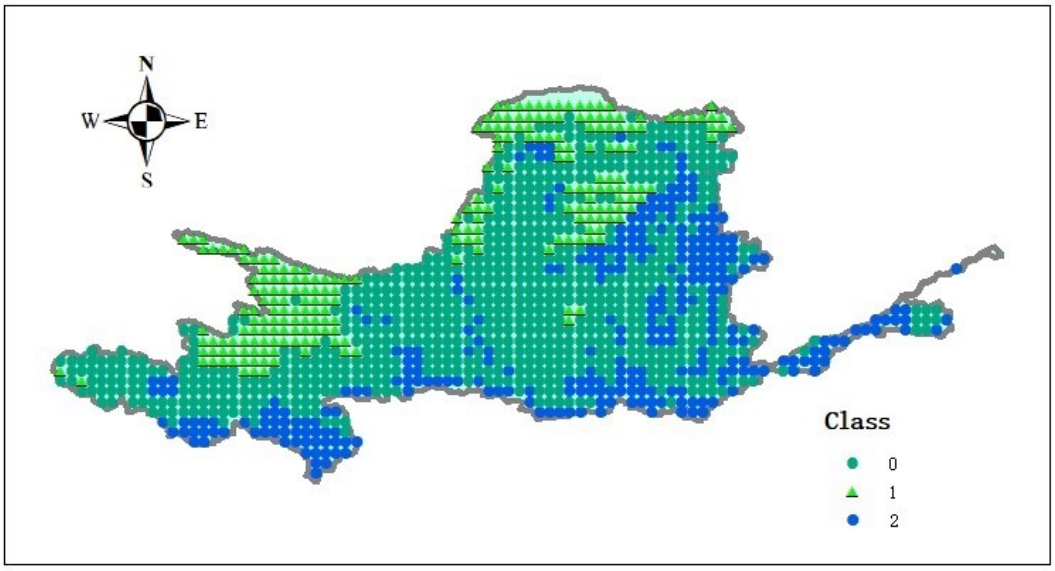

Fig. 4-8 Clustering in the first representative period of 07/2003-11/2005

Fig. 4-8 shows that, after having been reclustered the first stage has similar clusters with Fig. 4-7(b) and as a whole there are no clear boundaries among the three clusters having a direction of north-south. Most clusters lie in the middle reach of the Yellow River.

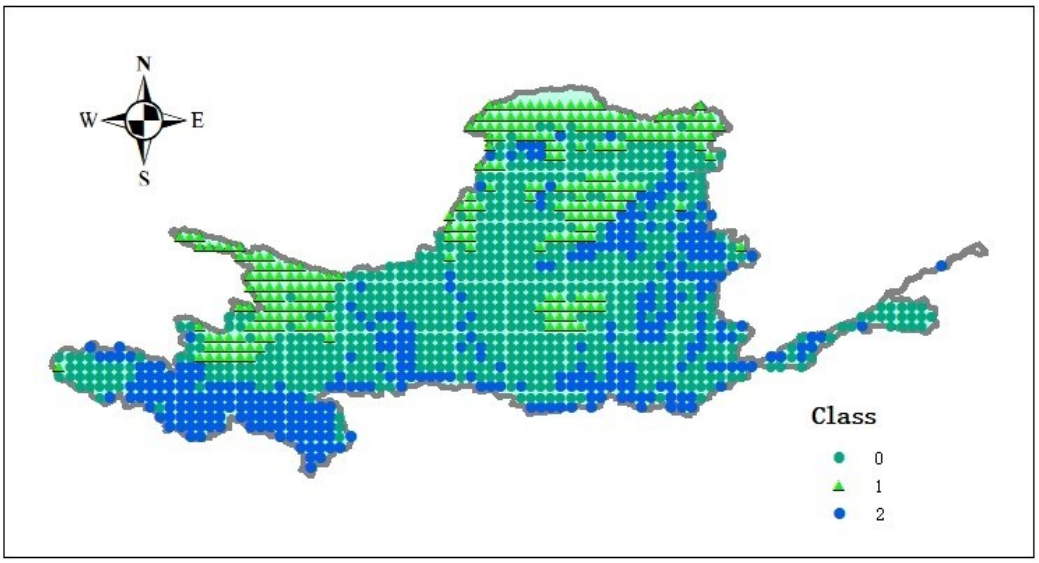

Fig. 4-9 Clustering in the second representative period of 12/2005-10/2006

Fig. 4-9 shows that, after having been reclustered the second stage has similar clusters with Fig. 4-7(c) and the three clusters have a direction of north-south. The three clusters have almost the same number of pixels.

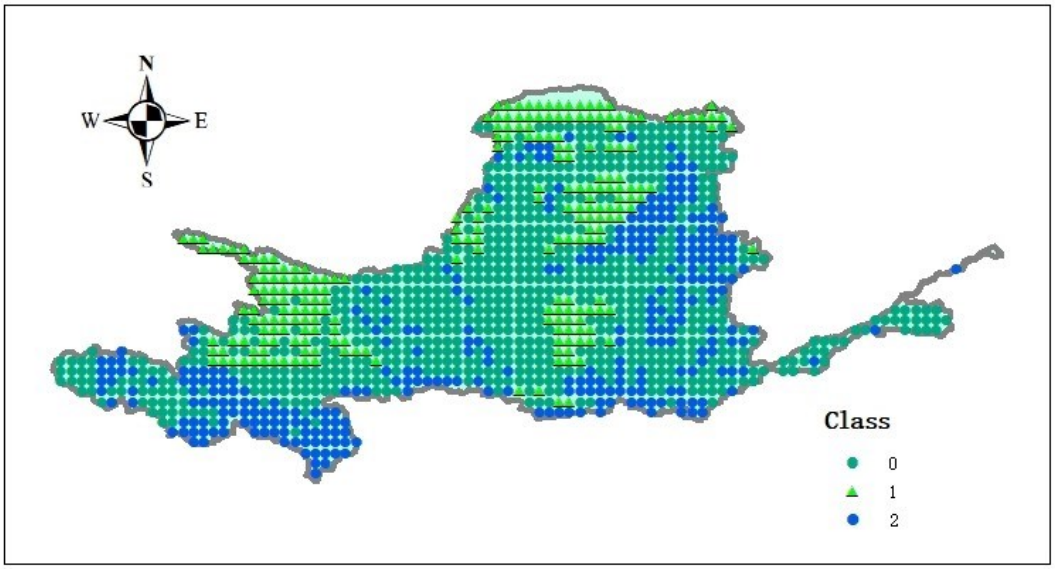

Fig. 4-10 Clustering in the third representative period of 11/2013-05/2016

Fig. 4-10 shows that, after having been reclustered the third stage has different clusters with Fig. 4-7(d). On the whole there are no clear boundaries among the three clusters with an evident direction of north-south. The pixel number of the three clusters are almost equal.

Overall, it can be seen from Fig. 4-8 ~ Fig. 4-10 that the three classes in the three periods are relatively similar in overall distribution, with little difference. Basically, three classes are distributed from north to south, and the main differences of the three figures lie in the west, east and the middle of YRB.

Comparison of the clustering results in Figs. 4-8 ~ Fig. 4-10 with those of Scenario 2 (Figs. 4-7 (b)~(d)) shows that the rearrangement of GLDAS dataset has little impact on the first and second period but has great impact on the third period (11/2013-05/2016). Comparison of Fig. 4-10 with Fig. 4-7 (d) shows that regular pattern of the three classes in Fig. 4-7 (d) was changed into spatially irregular pattern.

Based on the new classes in Fig. 4-10, the key driving factors are further screened by using the VIP method, as shown in Table 4-4. There are 10 factors with a larger proportion of VIP>1 in the 9 groups, including transpiration (8/9 of the VIP values are greater than 1), evapotranspiration (7/9), air temperature (7/9), moisture1 (or root zone soil moisture) (6/9), terrestrial water storage (6/9), soil moisture2 (or soil moisture from 0 to 200 cm in depth) (5/9), precipitation (5/9), evaporation2 (or direct evaporation from bare soil)(3/9), glacier melt (2/9), runoff (1/9) indicating the 10 factors are of higher importance.

Table 4-4 VIP values of the 11 environmental factors for the three classes in the three representative periods respectively. VIP>1.0 (in bold font) means the corresponding factor has great influence on LWE.

Representative period	Class	Evapotranspiration	Glacier melt	Transpiration	Evaporation 2	Soil moisture 2	Precipitation	Air temperature	Runoff	Soil moisture1	Terrestrial water storage	Precipitation minus ET
1	0	**1.05**	0.64	**1.09**	0.65	**1.33**	0.84	**1.03**	0.52	**1.39**	**1.39**	0.46
	1	0.97	0.51	0.95	0.81	**1.37**	0.94	0.90	0.76	**1.34**	**1.43**	0.48
	2	0.96	0.49	**1.05**	0.70	**1.36**	0.76	0.95	0.86	**1.41**	**1.41**	0.45
2	0	**1.11**	0.81	**1.14**	**1.00**	**1.15**	**1.03**	**1.12**	0.70	**1.11**	**1.10**	0.48
	1	**1.28**	0.89	**1.27**	**1.21**	0.74	**1.21**	**1.30**	0.88	0.47	0.55	0.69
	2	**1.09**	0.72	**1.08**	0.99	**1.01**	**1.05**	**1.13**	**1.02**	**1.00**	**1.01**	0.83
3	0	**1.43**	0.55	**1.32**	**1.39**	0.74	**1.36**	**1.39**	0.08	0.44	0.48	0.47
	1	**1.16**	**1.60**	**1.07**	0.98	0.66	**1.14**	**1.10**	0.66	0.78	0.82	0.59
	2	**1.06**	**1.50**	**1.02**	0.95	0.81	0.96	**1.02**	0.61	**1.11**	**1.11**	0.48

(d) Scenario No. 4 —using pixel-scaled all environment factors to determine key driving factors without clustering and without using the three-representative period (1271 sets of key driving factors)

Scenarios No. 1-3 are all using averaged environmental factors which dismissed many details at the pixel scale. In other words, the heterogeneity of the relationship between environmental factors and the LWE value at the pixel scale were neglected, which inevitably induce uncertainties on the results. To avoid this, this scenario begins at the pixel scale, i.e., every pixel has all its environmental factors as the last key driving factors to force prediction model (LSTM-N model) to work. Thus, there will produce 1271 sets of key driving factors. However, the workload of model prediction will increase dramatically (consuming much more working time) because over the whole YRB 1271 pixel-based LSTM-N model will be set up for verification and prediction in the current Scenario No. 4 while at most 9 LSTM-N model need be set up in Scenarios No. 1-3.

To ensure the objectivity of the screening results, the screening results were further verified against four scenarios. The one with the highest prediction accuracy will be used to extend LWE from 1948 to 2016, nearly 70 years.

4.1.3 Verification and improvement of prediction model with four-scenario-selected key driving factors

This chapter will use the key driving factors determined in the four scenarios to set up models for LWE prediction in the period of 2002-2017 whereby to verify the precision of prediction model. There are many prediction models can be selected, such as back propagation neural network (BP network), recurrent neural network (RNN), Feedback neural network, multi-layer perception, linear artificial neural network, radial basis function neural network (RBF) and so on (Broomhead and Lowe, 1988; Gao and Sun, 2000; Kong et al., 2014; Rukonuzzaman et al., 2001; Sharmeela et al., 2003; Wang et al., 2014). Among them, RNN

have been widely used in the research fields involving sequence data, such as text, audio, and video. The typical feature of the RNN architecture is a cyclic connection, which enables the RNN to have the ability to update the current state based on the past state and current input data. However, when the input gap is large, RNN composed of sigma cells or tanh cells cannot learn the relevant information of the input data. To deal with "long-term dependence", (Hochreiter and Schmidhuber, 1997) proposed the method of Long short-term memory (LSTM-N). By introducing the gate function into the unit structure, LSTM-N can handle the problem of long-term dependence well. Generally, the performance of LSTM-N is much better than RNN.

LSTM-N is a very popular RNN in recent years (Xie et al., 2019; Yu et al., 2019a; Yu et al., 2019b). Deep LSTM-N is one of the most important deep learning models. By using gate cells, LSTM-N avoids the problem of gradient degradation. Deep LSTM-N has been widely used in many fields, especially in time series modeling, including speech recognition, natural language processing and sequence prediction. Simplified LSTM-N is very effective for modeling time series. In addition to time series modeling, LSTM-N can also be applied to modeling nonlinear systems (Yu et al., 2019a; Yu et al., 2019b). This algorithm could avoid the interference of the redundant information in the output of the bottom layer to the effective information in the upper layer. In the term of speech-based emotion recognition task, the weighting on the time dimension reflects the difference of emotion saturation among periods, while that on the feature dimension reflects the distinguishability of different features (Xie et al., 2019).

This section uses the LSTM-N neural network model to carry out the verification work. The specific prediction processes have two steps. Firstly, data preparation: reading GRACE data containing terrestrial water storage and GLDAS data containing all environmental factors. Secondly, according to the VIP results (Table 4-2,4-3,4-4,4-5), the key driving factors of the corresponding three periods of 2002-2016 selected from the GLDAS dataset (acting as the X variable of LSTM-N) and the corresponding GRACE LWE (acting as the Y variable of LSTM-N) are input into the model for training the LSTM-N model. Then the trained LSTM-N model is used to predict the LWE of the unknown month and then calculate the statistical error according to the GRACE LWE observations.

To display the effectiveness of the key driving factors, we randomly selected three pixels in the upper, middle, and lower reaches of the Yellow River basin to verify the driving factors in every scenario. To begin with, LSTM-N model was set up inclusive of analysis on parameter-sensitivity and the determination of optimized value of parameters.

(1) LSTM-N model set up

(a) Analysis on parameter-sensitivity

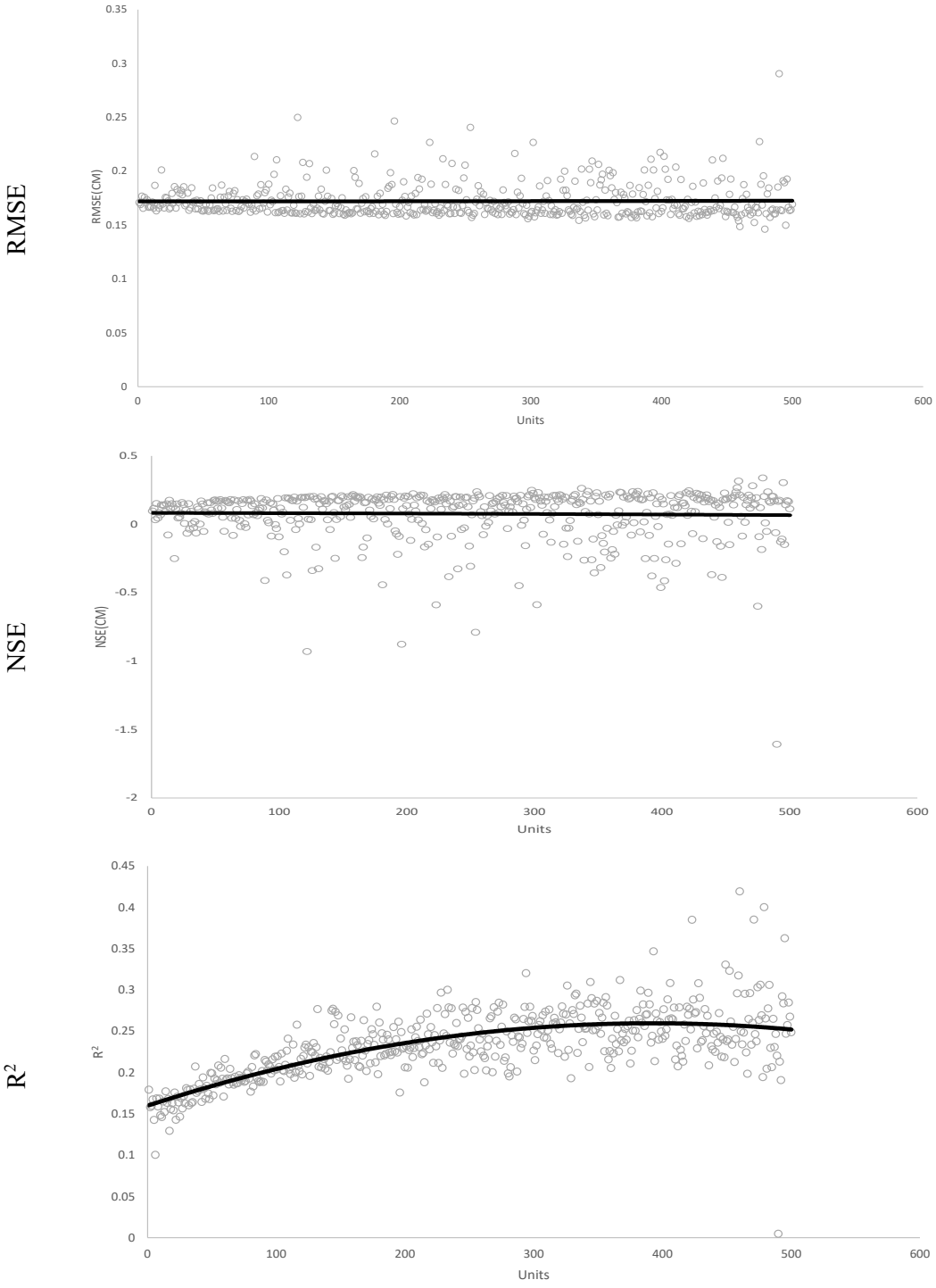

Fig. 4-11 Effect of function selection on prediction accuracy

This section analyzes and optimize the three parameters of the LSTM-N model, including the Unit number, Activation functions (of Sigmoid, Relu, Leakyrelu) and training epochs. Firstly, when analyzing the Unit number, we set Sigmoid as Activation function, and set the training epoch to 1. Afterwards the Unit number loops 500 times to find the optimal value of the Unit number. Secondly, when analyzing the Activation function, we set the Unit number to its optimal value, the training epoch to 1, the Activation functions are in turn tried to find the optimized function. After determining the Unit numbers and the Activation function, we set the training epoch from 1 to 800 to evaluate the influence of the training epoch on the accuracy of

the LSTM-N model. The optimized values of Unit number and training epoch, as well as the optimized function usually leads to the highest R^2, NSE yet lowest RMSE.

- **Unit**

The influence of the parameter Unit on the accuracy indices (RMSE, NSE, and R^2) is shown in Fig. 4-11.It can be seen from the RMSE in Fig. 4-11 that when the Unit number is between 0 and 500, the RMSE is between 0.14 and 0.29, and the relationship curve between the units and the RMSE is basically level, which shows that the Unit number has little effect on the RMSE. NSE in Fig. 4-11 shows that when the Unit number is between 0 and 500, the NSE is between -1.6 and -0.34, and the relationship curve between Unit number and NSE is basically level, which shows that Unit number has little effect on NSE. R^2 in Fig. 4-11 shows that when the Unit number is between 0 and 500, the value of R^2 is roughly between 0.1 and 0.42. The relationship curve between units and R^2 rises slightly and then becomes gentle showing the Unit number has little effect on the accuracy of LSTM-N model. Overall, the model parameter Unit number is not sensitive.

- **ActivationFunction**

In the LSTM-N model, there are three widely used functions: Sigmoid, Relu, and Leakyrelu. The influence of the three functions on the accuracy indices (RMSE, NSE, and R^2) is shown in Fig. 4-12.

It can be seen from the RMSE in Fig. 4-12 that the range of influence of different activation functions on NSE is (0.15, 0.18). When the activation function is set to Sigmoid, the RMSE is 0.15 cm yet when the activation function is set to Leakyrelu, the RMSE is 0.18 cm, which shows that the Sigmoid function performs the best. NSE in Fig. 4-12 shows that the range of influence of different activation functions on NSE is (-0.22, 0.31). When the activation function is set to Sigmoid, the NSE is 0.31 as when the activation function is set to Leakyrelu, the NSE is -0.22, showing the Sigmoid function performs the best. R^2 in Fig. 4-12 shows that the range of influence of different activation functions on R^2 is (0.22, 0.42). When the activation function is set to Sigmoid, the R^2 is 0.42 but when the activation function is set to Leakyrelu, the R^2 is 0.22. All in all, the Sigmoid function performs the best.

- **Training epoch**

The influence of the parameter training epoch on the accuracy indices (RMSE, NSE, and R^2) is shown in Fig. 4-13.

It can be seen from the RMSE in Fig. 4-13 that when training epoch loops in the range of 1-800, the value of RMSE is 0.007-0.166. There produces a large fluctuation when training epoch changes showing training epoch has a great influence on RMSE. NSE in Fig. 4-13 shows that when training epoch loops in the range of 1-800, the value of NSE is 0.154-0.999 showing training epoch has a great influence on NSE. R^2 in Fig. 4-13 shows that when training epoch loops in the range of 1-800, the value of R^2 is 0.292-0.997. When training epoch reaches 500 times, R^2 is 0.988, the curve tends to be steady. The above analysis shows that showing training epoch has a greater impact on the LSTM-N model prediction accuracy.

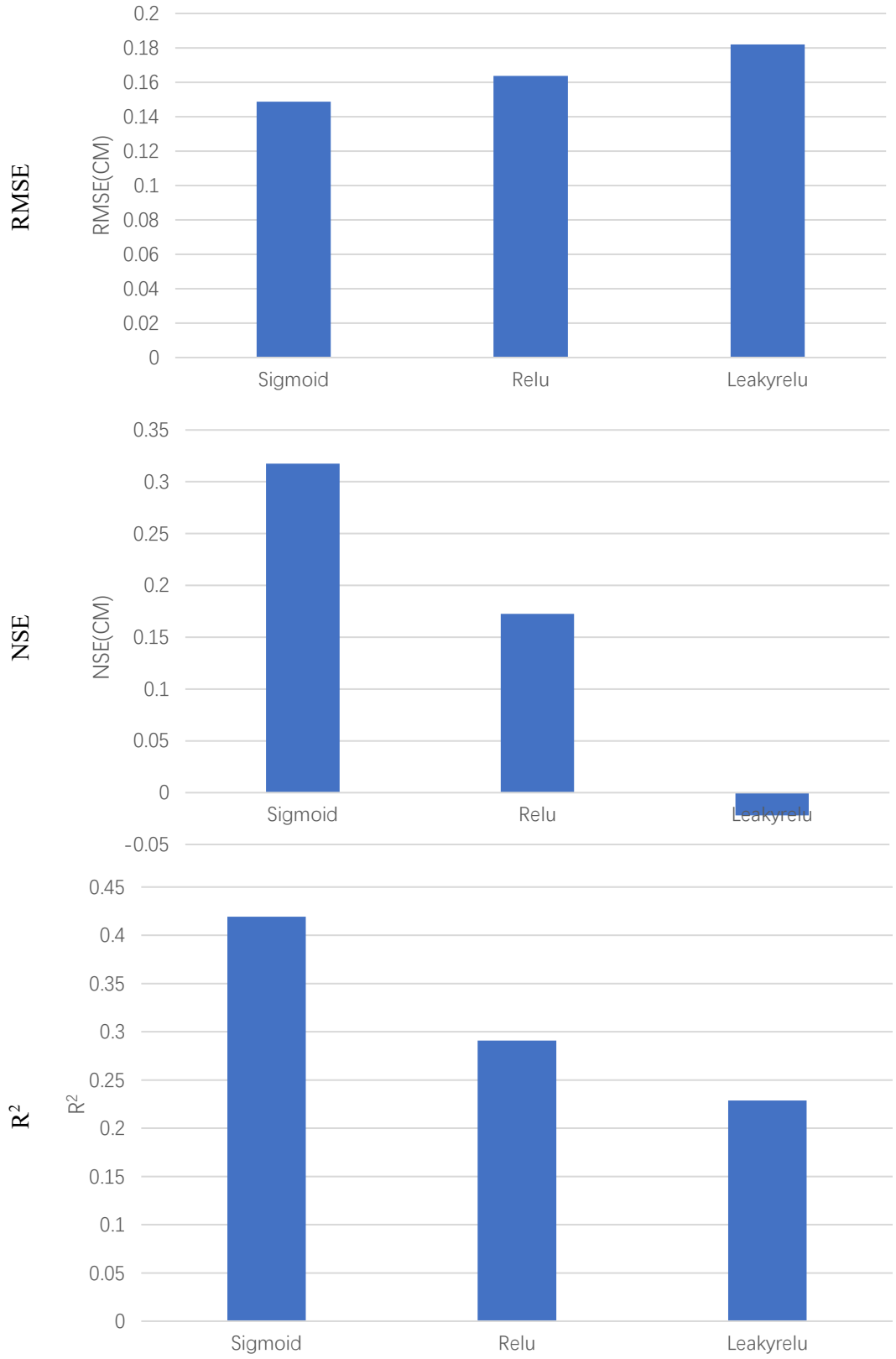

Fig. 4-12 Effect of function selection on prediction accuracy

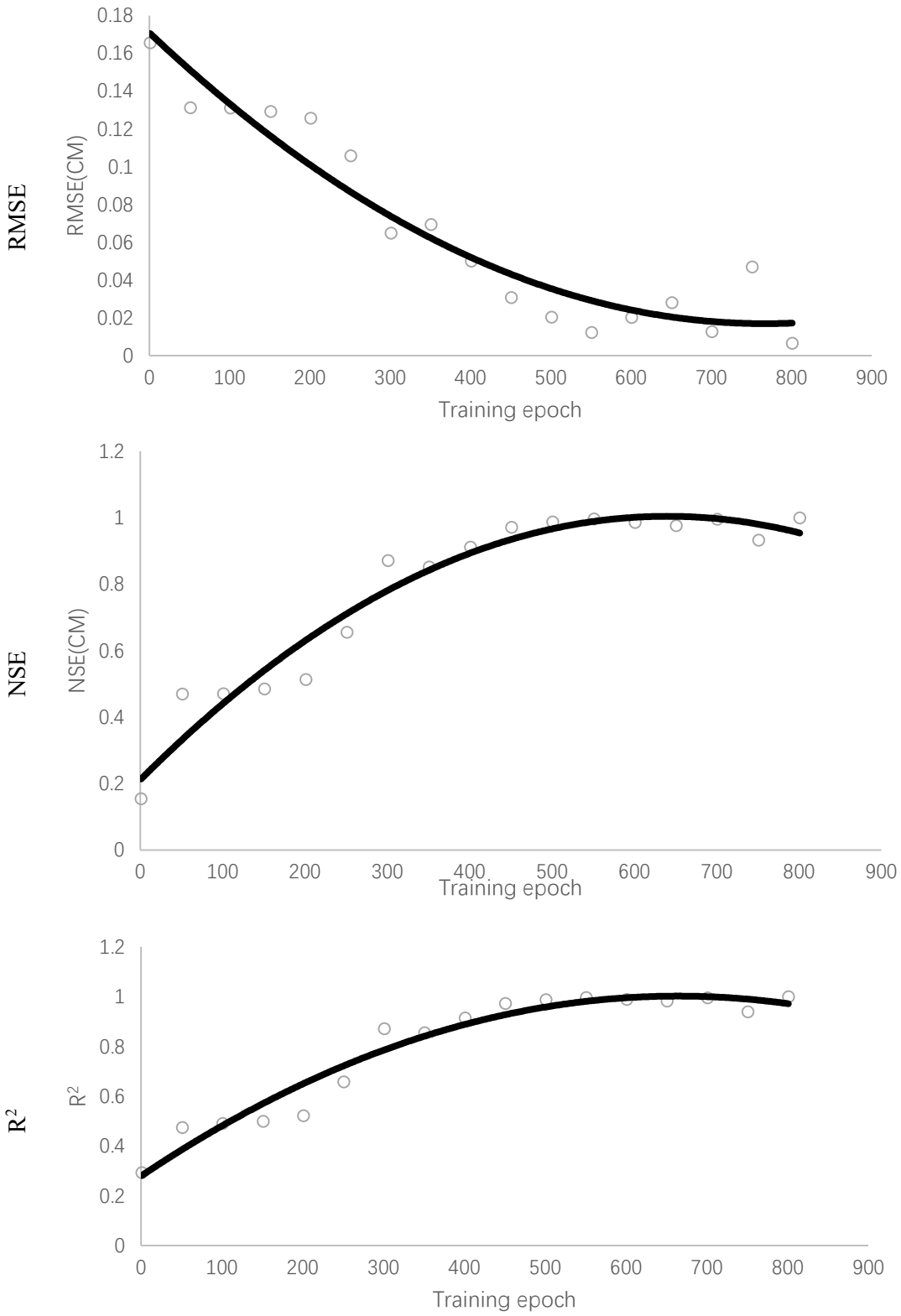

Fig. 4-13 Effect of function selection on prediction accuracy

(b) Determination of parameter-optimized value

The optimized parameter "Unit" is 460. Though the influence of "Unit" on RMSE and NSE is neglectable, that on the correlation coefficient (R^2) is not neglectable, that on R^2 has the highest value when the "Unit" has a value of 460. Therefore, the value of 460 is determined as

the optimized value for “Unit” (Fig. 4-11).

The optimized activation function is “Sigmoid” function as among the three functions of Sigmoid, Relu and Leakyrelu, the Sigmoid function has the maximum NSE and R^2 yet minimum RMSE (Fig. 4-12).

The optimized training epoch is 650. The parameter of “training epoch” has remarkable influence on all the three indices of RMSE, NSE, and R^2 (Fig. 4-13). When the training epoch increases, RMSE decrease yet NSE and R^2 increase remarkably. The RMSE decreases to its minimum value, yet NSE and R^2 increase to their peak values when the training epoch gets value of 650.

(2) verification of scenario prediction accuracy

This section uses the LSTM-N model set up in the above section to predict LWE in the period from 2002 to 2017 based on the sets of key driving factors determined in Scenarios 1-4. Then GRACE LWE observations in the period from 2002 to 2017 were coupled to calculate the accuracy indices inclusive of RMSE and R^2 whereby to verify the accuracy of every scenario-based LSTM-N models. To make the results objective and universe, verification was made respectively in the upper, middle, and lower reach of the YRB.

(a) Scenarios No. 1

The screening of key driving factors in Scenario No. 1 is based on the whole YRB. According to the optimal parameters of LSTM-N (Unit”: 460, activation function: “sigmoid”, and training epoch: 650) in the above-discussed, a total of 3 LSTM-N models (with optimized parameters) are established in the three representative periods in this section. Three models were used to predict the upper, middle, and downstream LWE from 2002 to 2016, verified by using the GRACE observed LWE values, as shown in Fig. 4-14.

Fig. 4-14 shows that the Scenario-1-based LSTM-N model has higher R^2 in the upper (R^2>0.6) yet lower in the middle and lower reaches (R^2<0.5). Contrary for RMSE, the upper reach has a RMSE of 0.66 cm yet the middle and lower both have their RMSE higher than 1.0 cm. The results imply that prediction accuracy in the upper reach is higher yet in the middle and lower reaches is lower.

Fig. 4-15 shows that the Scenario-2-based LSTM-N model performs poor all in the upper, middle and lower reaches of the YRB due to the extraordinary low R^2 (<0.1) and much higher RSME (>1cm). The maximum R^2 of the Scenario-2-based LSTM-N model in the upper, middle and low reaches of the YRB is 0.06 as the minimum is 0.0002. The maximum RMSE is 32.23 cm and the minimum is 3.69 cm. The very low R^2 (<0.1) and very high RMSE (>1cm) suggest poor performance of the model in the whole YRB.

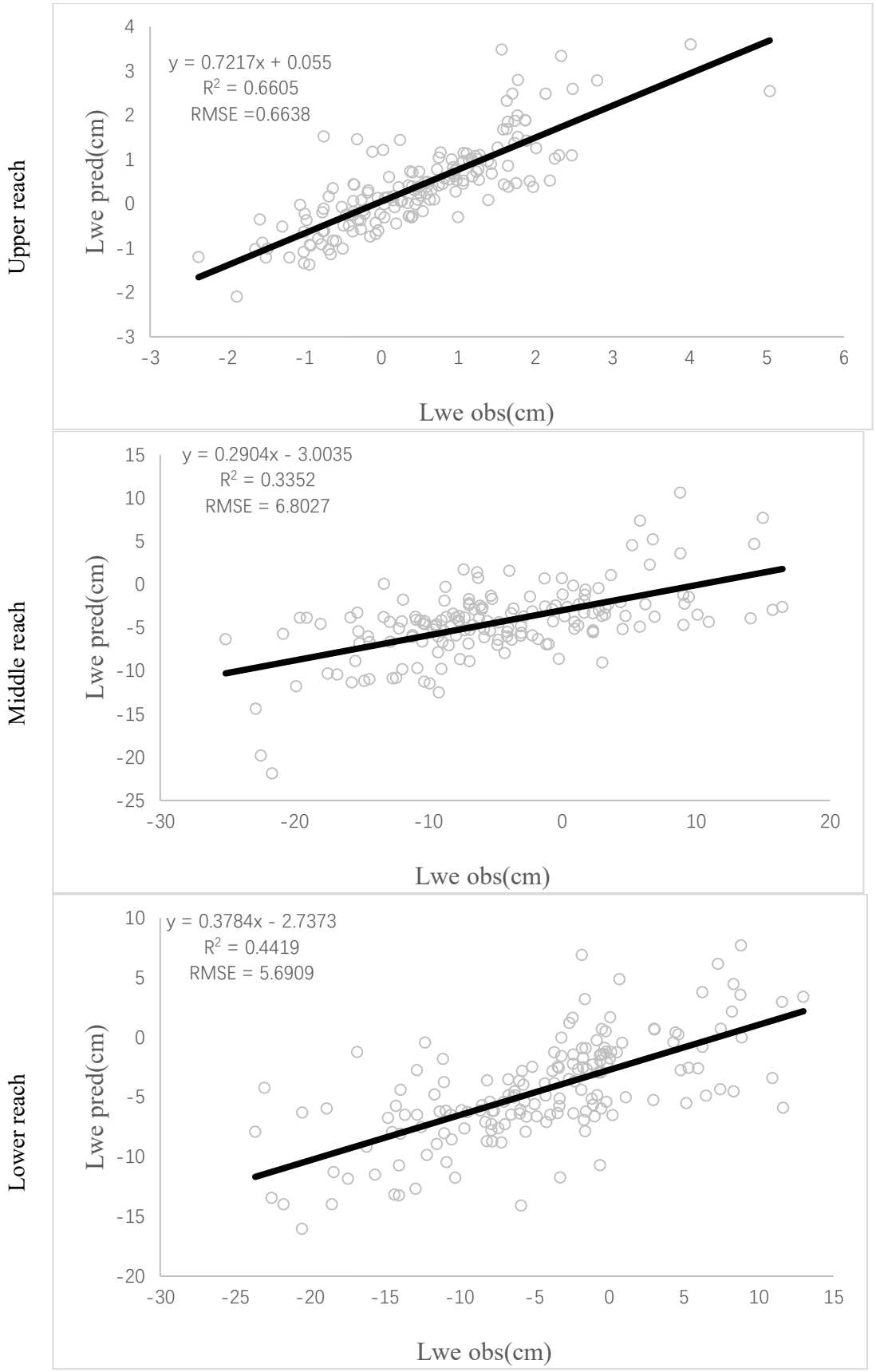

Fig. 4-14 LSTM-N prediction in upper, middle and lower reaches of the YRB by using the set of driving factors determined in Scenario No.1. Pred: prediction; obs: observation.

(b) Scenarios No.2

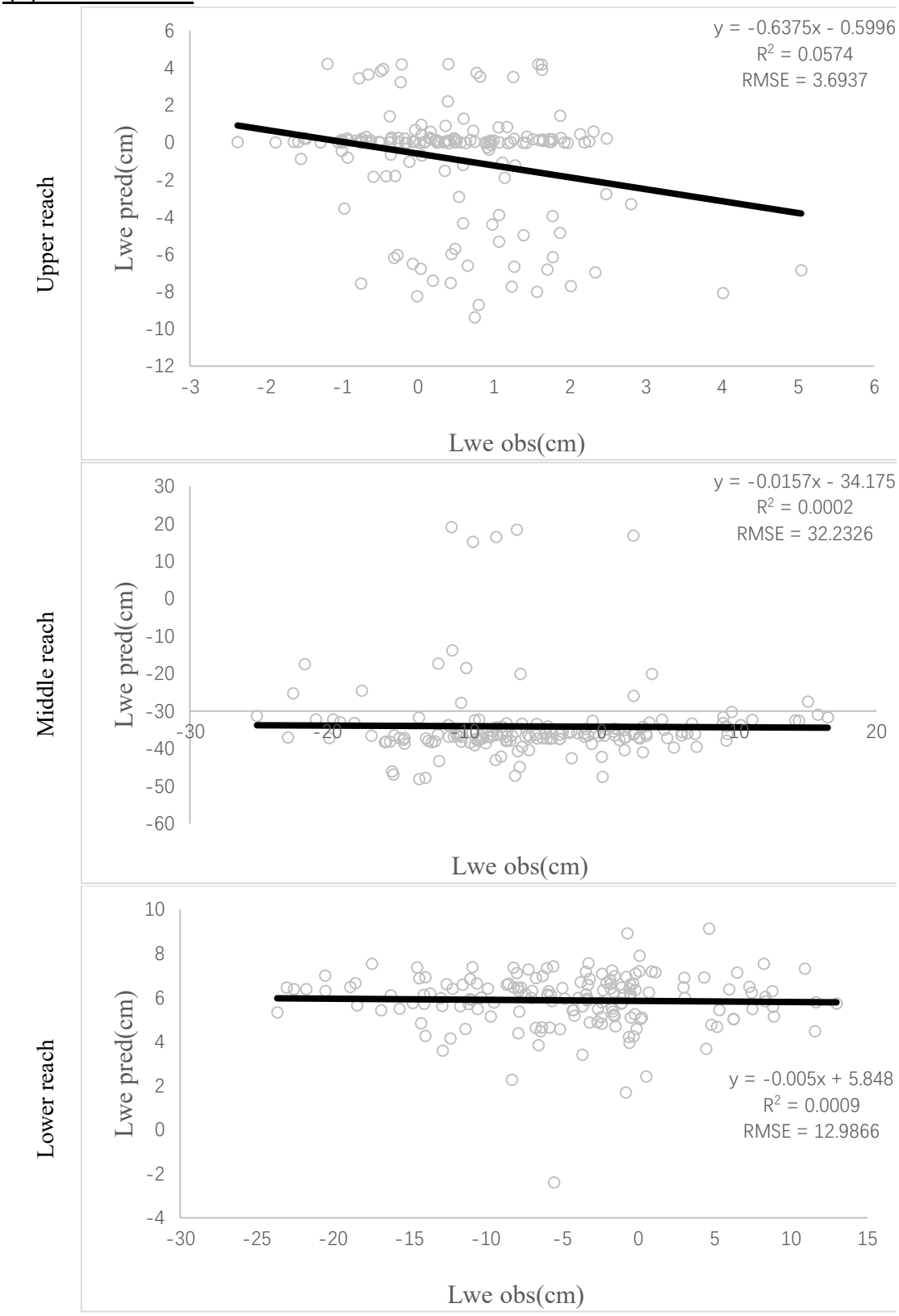

Fig. 4-15 LSTM-N prediction in upper, middle and lower reaches of the YRB by using the set of driving factors determined in Scenario No.2. Pred: prediction; obs: observation.

(c) Scenarios No. 3

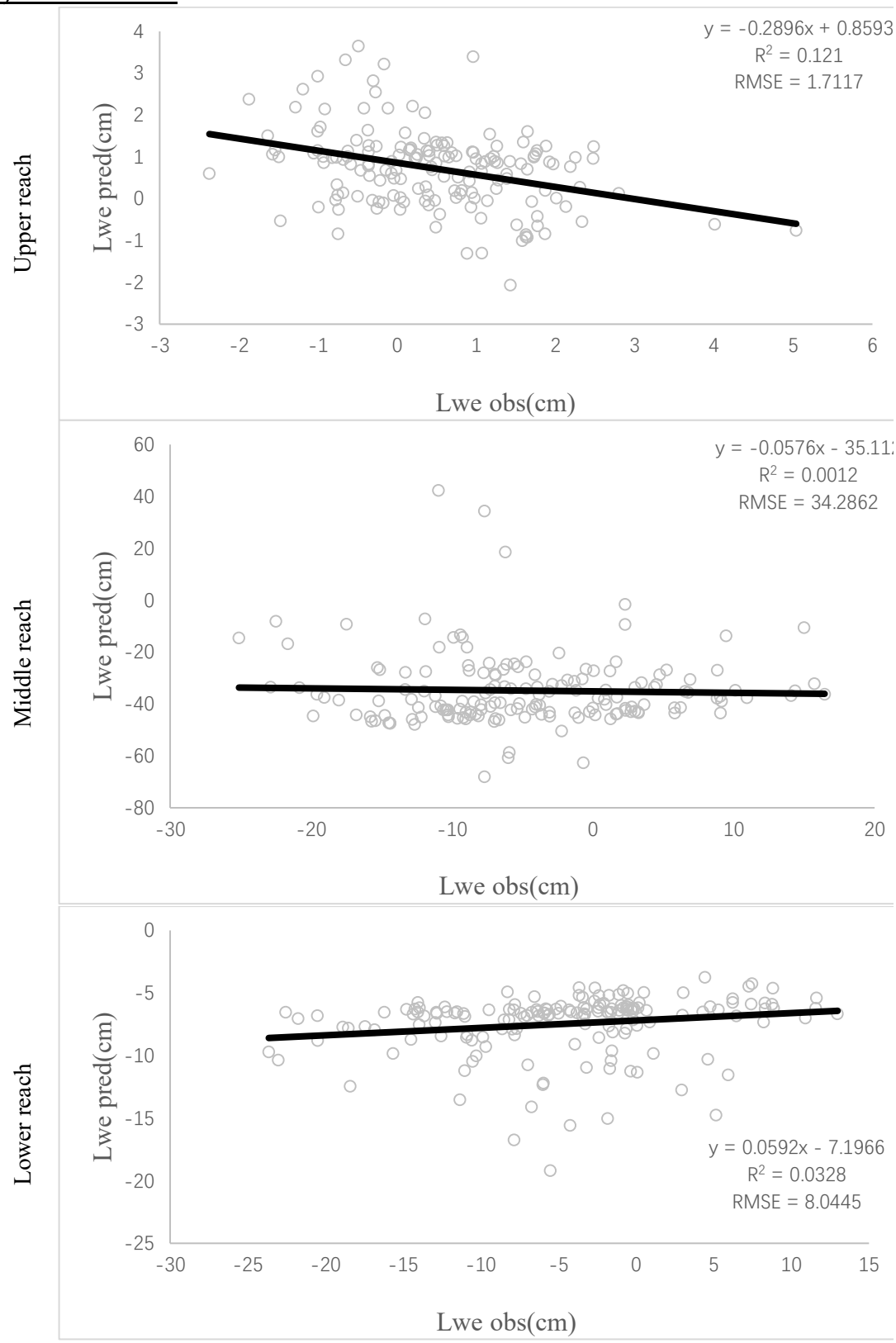

Fig. 4-16 LSTM-N prediction in upper, middle and lower reaches of the YRB by using the set of driving factors determined in Scenario No.3. Pred: prediction; obs: observation.

Better but similar with Scenario 2, the Scenario-3-based LSTM-N model also performs poor all in the upper, middle and lower reaches of the YRB due to the low R^2 (<0.2) and much

higher RSME (>1cm), as shown in Fig. 4-16. The maximum R^2 of the Scenario-3-based LSTM-N model in the upper, middle and low reaches of the YRB is 0.12 as the minimum is 0.0012. The maximum RMSE is 34.29 cm and the minimum is 1.71 cm. Although the Scenario-3-based LSTM-N model performs better than the Scenario-2-based one, the low R^2 (<0.2) and very high RMSE (>1cm) suggest poor performance.

(d) Scenarios No. 4

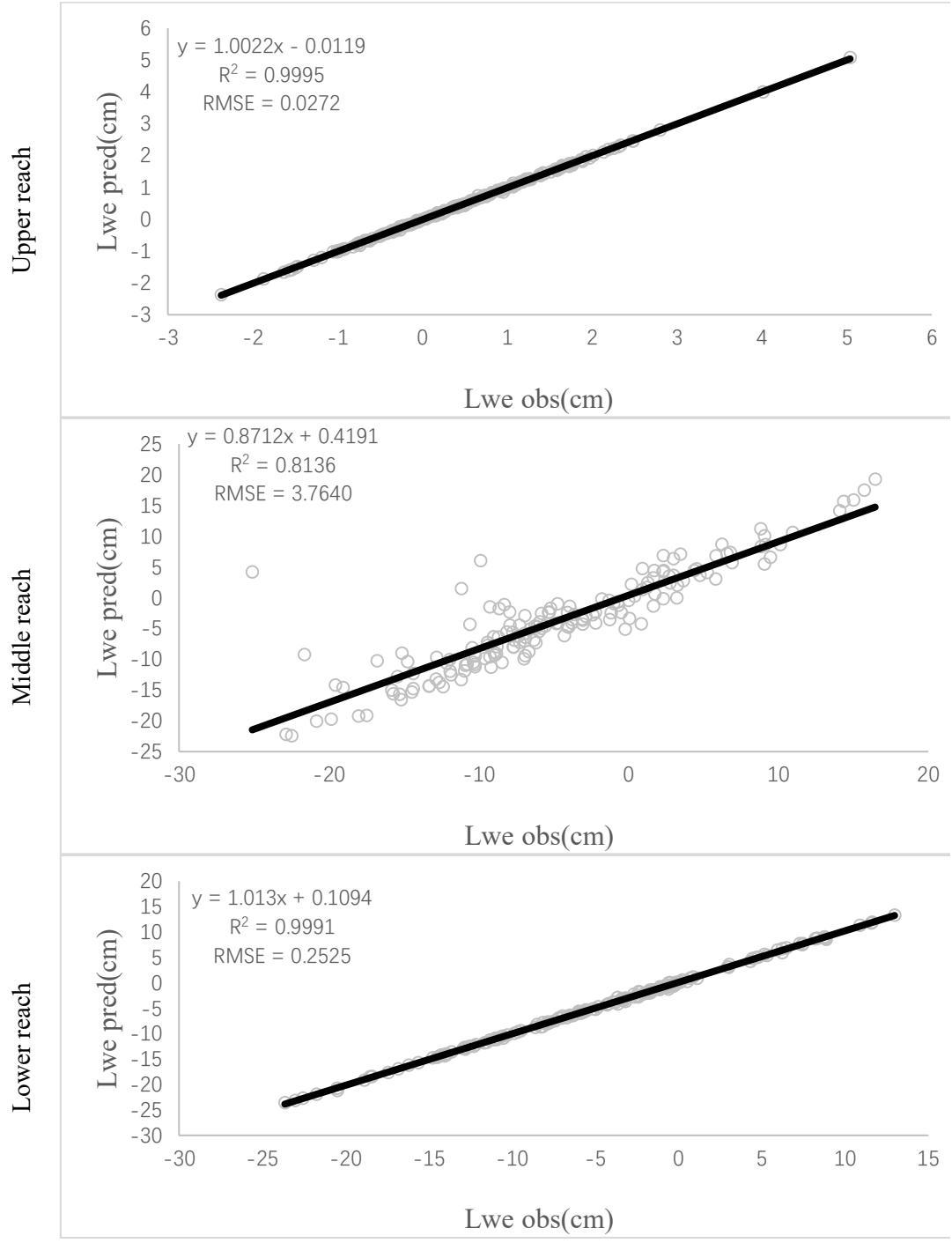

Fig. 4-17 LSTM-N prediction in upper, middle and lower reaches of the YRB by using the set of driving factors determined in Scenario No.4. Pred: prediction; obs: observation.

In the above Scenarios 1-3, we make model predictions based on the key driving factors

obtained through VIP screening. Scenario No. 4 does not select but use all environmental factors as the final key driving factors for every pixel. Therefore, this section adopts the principle of point-by-point modeling. That is to say, at one point all environmental factors and all LWE observations are used inputted into the optimized LSTM-N model to predict and verify without spatially clustering and temporally period-division. The predicted and GRACE-observed LWE values in the upper, middle and lower reaches are shown in Fig. 4-17.

Greatly differently from the above three scenarios-based model, the Scenario-4-based LSTM-N model has the highest R^2 in the upper (R^2>0.9), middle (R^2>0.8) and lower reaches (R^2>0.9). As to the RMSE, the upper and lower reaches have RMSEs both lower than 1.0 cm. The RMSE for the middle is relatively lower (RMSE=3.76 cm) but still smaller than 5 cm, as shown in Fig. 4-17. The results imply that prediction accuracy in all the three reaches is high. In other words, the Scenario-4-based LSTM-N model performs satisfactory in all the whole YRB. Therefore, the Scenario-4-based LSTM-N model will be employed to extend LWE data, or underground FWA from 1948 to 2002 when the GRACE LWE monitoring is missed.

4.2 Extension of data series of underground FWA

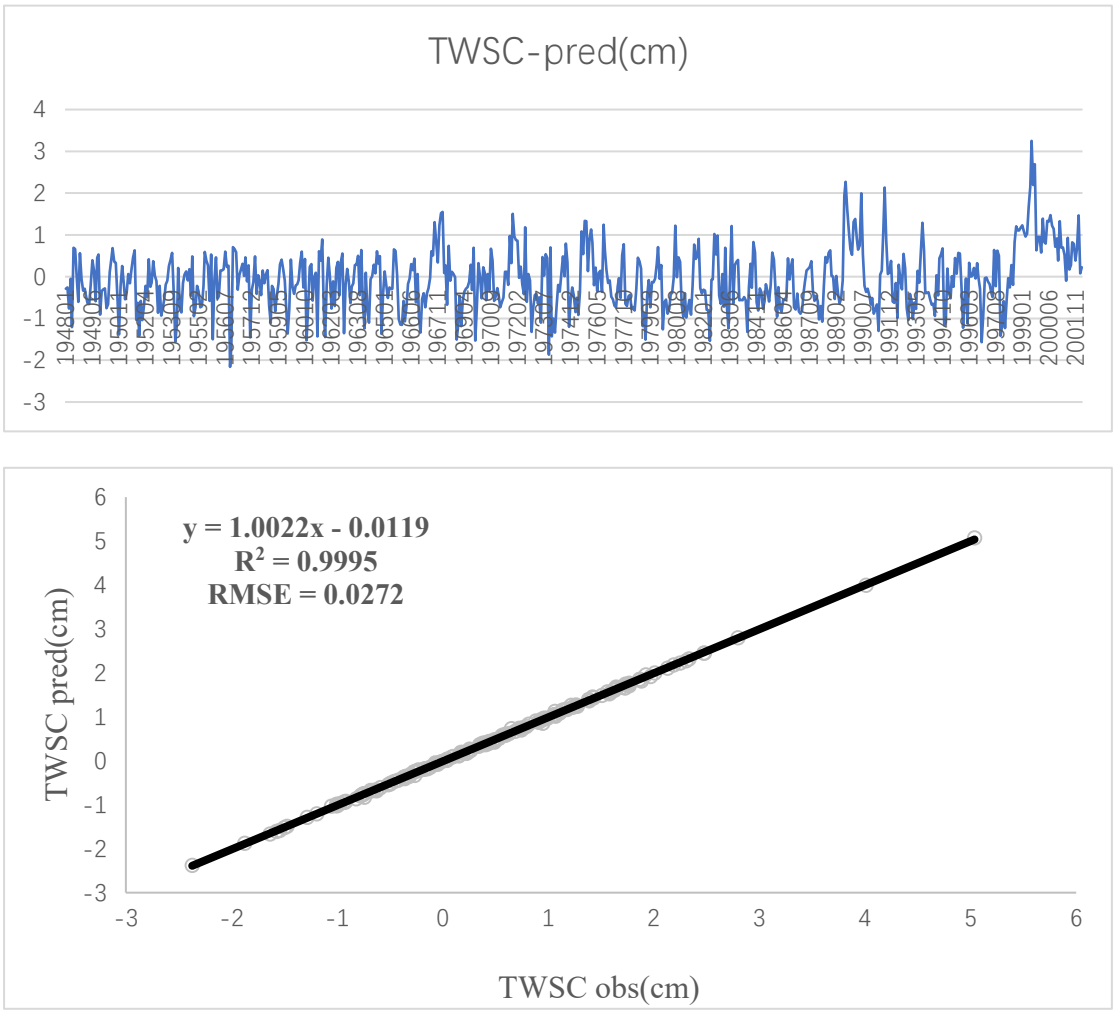

Fig. 4-18 Predicted LWE (TWSC) from Jan. 1948 to Dec. 2001 (Upper) and the accuracy of prediction model (Lower) in the upper reach of the YRB.

With the optimized parameter values above, 1271 Scenario-4-based LSTM-N models were firstly set up one pixel after another in the whole YRB. Then underground FWA, or LWE values in the period of Jan. 1948-Dec.2001 were predicted by using all the environmental factors (Scenario 4). Fig.4-18~20 display the results respectively in the upper, middle and lower reaches of the YRB.

Fig. 4-18 (upper) shows the reconstructed TWSC from 1948 in the upper reach which fluctuates between -1.5 cm and 1.0 cm. Some peaks (> 1.0 cm) occur in the periods of 1989-1991 and 1999-2000. Most TWSC values are greater than 0 yet the magnitude of the reconstructed TWSC is small. The lower figure shows the uncertainties in the training with a R^2 of 0.9995 and a RMSE of 0.03 cm which reveals a very high accuracy.

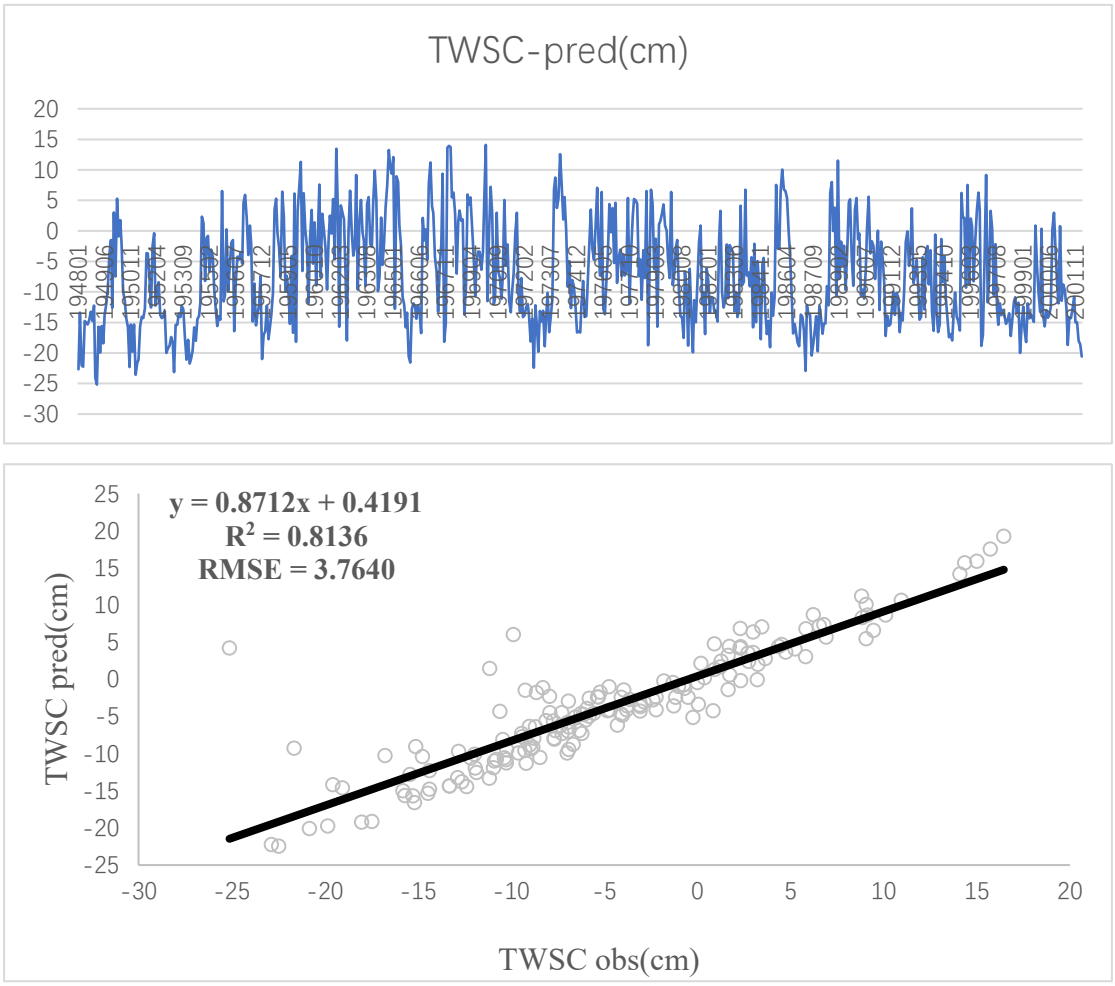

Fig. 4-19 Predicted LWE (TWSC) from Jan. 1948 to Dec. 2001 (Upper) and the accuracy of prediction model (Lower) in the middle reach of the YRB.

Fig. 4-19 (upper) shows the reconstructed TWSC from 1948 in the middle reach which fluctuates between -20 cm and 5 cm. Some peaks (> 10 cm) occur in the periods of 1959-1974 and some vallies occur in 1948-1953. The magnitude of the reconstructed TWSC is big. The lower figure -- uncertainties in the training has a R^2 of 0.81 and a RMSE of 3.76 cm which reveals a high accuracy though it lower than in the upper reach.

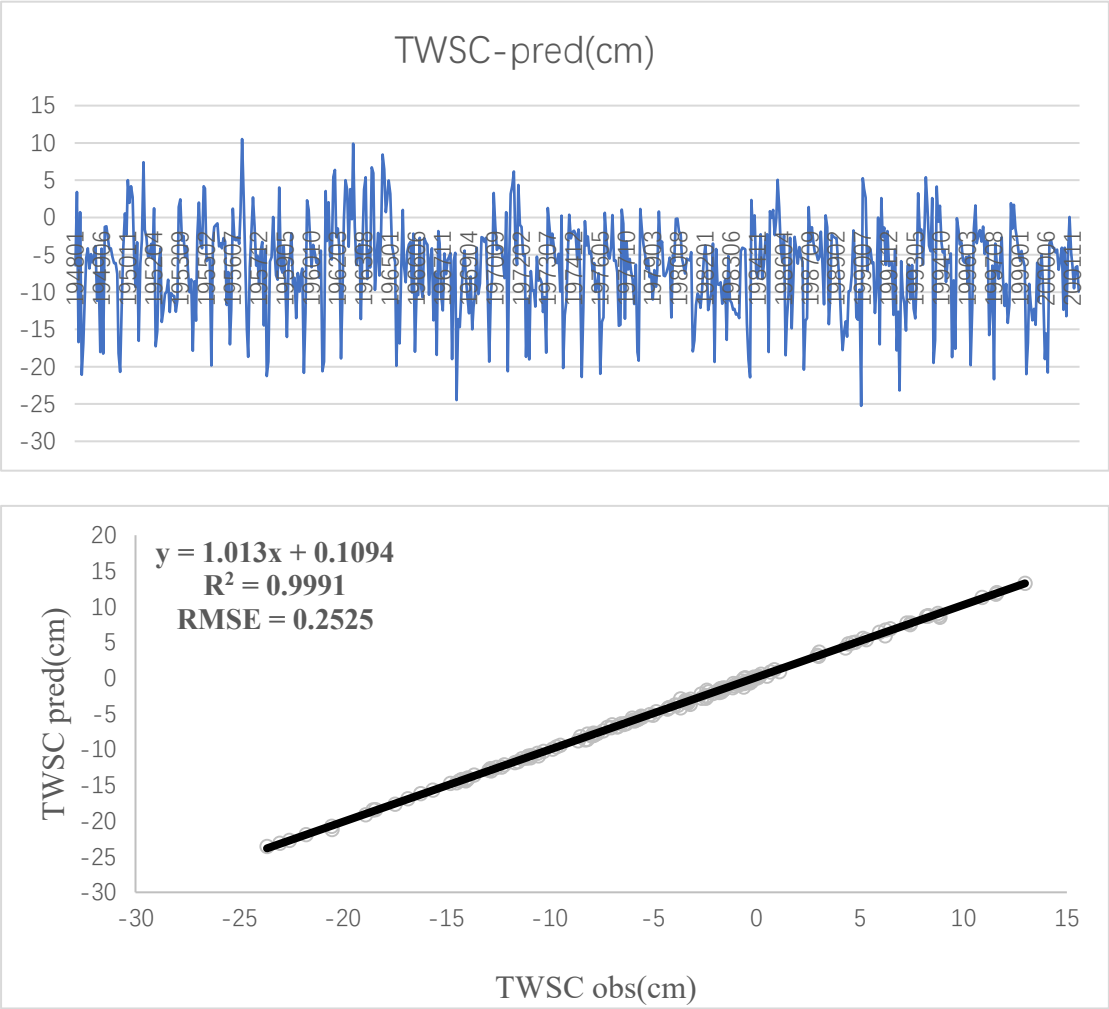

Fig. 4-20 Predicted LWE (TWSC) from Jan. 1948 to Dec. 2001 (Upper) and the accuracy of prediction model (Lower) in the lower reach of the YRB.

Fig. 4-20 (upper) shows the reconstructed TWSC from 1948 in the lower reach which fluctuates between -20 cm and 5 cm. Some peaks (> 5.0 cm) occur in the periods of 1951, 1957, and 1961-1964 while two very low values occur in 1968, 1990, and 1992. Most TWSC values are less than 0 yet the magnitude of is big. The lower figure shows the uncertainties in the training with a R^2 of 0.9991 and a RMSE of 0.25 cm which reveals a very high accuracy like in the upper reach.

With the predicted TWSC in Figs. 4-18~20 and taking the underground water available in the date corresponding to the TWSC (from "Water Resource Bulletin of Xi'an (2013-2017)", "Water Resource Bulletin of Zhengzhou (2013-2017)", and "Water Resource Bulletin of Ji'nan (2013-2017)") as basis, the underground water available at the base period (i.e., the GRACE-data-base years (2004-2009)) with which the underground freshwater avialble (FWA) from 1948 to 2016, or the sum of underground water available at the base period and the TWSC for any date of 1948 through 2016, can be calculated, as shown in Fig. 4-21.

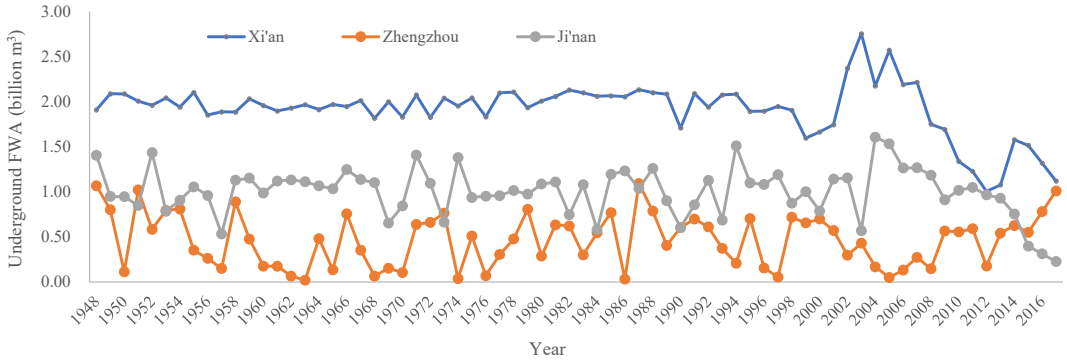

Fig. 4-21 Predicted underground FWA for the three representative cities from 1948 to 2016

Fig. 4-21 shows that the underground FWA from 1948 to 2016 fluctuates inter-annually with Xi'an (blue line) having the highest average of 1.92 billion m^3 and Zhengzhou (orange line) having the lowest average of 0.46 billion m^3. We validated them in the years (after the year 2002) when the bulletin of water resources is available but for the historical predicted values (e.g., before the year 2000) we did not validate because of the lack of data. What we did is to validate our model during 2002-2016 and use the validated model to predict the historical values.

4.3 Summary

This chapter estimated underground freshwater available (FWA) from 1948 to 2016 wherein the data series of GRACE TWSC (terrestrial water storage change) was extended from the last two decades to more than seven decades from 1948.

To begin with, environmental factors driving the variation of TWSC were determined via literature analysis and four scenarios. VIP method was used to screen out key driving factors with VIP>1.0 means great influence on TWSC. For the Scenario 1, the selected key driving factors include 7 (air temperature, glacier melt, soil moisture, terrestrial water storage, evapotranspiration, precipitation, transpiration) but varies in different periods; as to the Scenario 2, there are 7 factors including glacier melt, air temperature, direct evaporation from bare soil, precipitation, soil moisture from 0 to 200 cm in depth, runoff, precipitation minus ET which are of higher importance; as for Scenario 3, there are 10 factors including transpiration, evapotranspiration, air temperature, root zone soil moisture, terrestrial water storage, soil moisture from 0 to 200 cm in depth, precipitation, direct evaporation from bare soil, glacier melt, runoff which are of higher importance; for the Scenario 4, all the 11 environmental factors were selected.

Then, the selected factors in the four scenarios were used to verify and improve an artificial neural prediction model –LSTM-N (Long short-term memory network) wherein the optimized LSTM-N parameters were determined. For the problem of GRACE TWSC prediction, the optimized parameter "Unit" is 460, activation function is "Sigmoid" function, training epoch is 650 for the LSTM-N. Using the LSTM-N with the optimized parameters, the prediction performance of driving factor selected in the four scenarios was tested. Results show that the Scenario-4-based LSTM-N model has the highest R^2 (>0.8) in all the upper, middle and lower reaches of the YRB; all values of RMSE in the upper, middle and lower reaches are all smaller than 5 cm. Comparison of prediction value with GRACE observation shows that, LSTM-N

model in upper reach areas has the highest accuracy with a RMSE less than 0.1 cm, while in the middle reach it has a relatively lower accuracy with a RMSE less than 5.0 cm.

All these results imply that the Scenario-4-based LSTM-N model performs satisfactory in all the whole YRB, which was then employed to extend GRACE TWSC (or LWE) data series from 1948 to 2002 when the GRACE LWE monitoring is missed. Based on the long series of GRACE LWE data the corresponding underground freshwater available (FWA) were produced, with which the underground freshwater avialble (FWA) from 1948 to 2016 was calculated with Xi'an having the highest average of 1.92 billion m^3 and Zhengzhou (orange line) having the lowest average of 0.46 billion m^3. All these results can well serve for the prediction of underground FWA in future 2030 and 2050 in Chapter 6.

Chapter 5 Calculation of water consumption

Aiming at the third specific objective this chapter calculated the water consumption of three-sectors of household, industry and ecosystem. Household water consumption includes those in urban areas and rural areas. Industrial water consumption consists of water consumption in sectors making products for use in national development and routine daily life. Ecosystem water consumption includes evapotranspiration from urban green lands, from bare soil and from croplands. All these calculations lay solid basis for water consumption analysis in future 2030 and 2050 in Chapter 6.

In addition, water withdrawn consists of those from surface waters (river, lake, reservoir etc.), from underground and from other sources (sewage treated water, collected rainfall etc.). The water withdrawn from rivers and consumed by sectors is shown in Table. 5-1 taking the year 2016 as an example.

Table 5-1 Constitution of water withdrawn and consumed in the three cities in 2016 (data source: Water Resources Bulletin of Xi'an, Zhengzhou and Ji'nan)

	Water withdrawn Surface Underground Other	Water consumption Household Industry Ecosystem
Xi'an	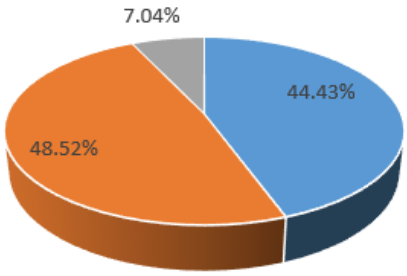	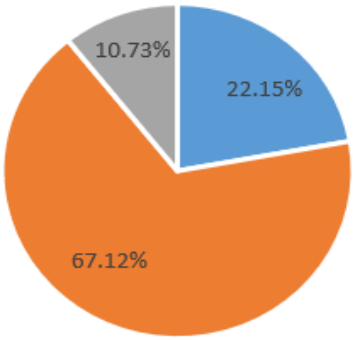
Zhengzhou	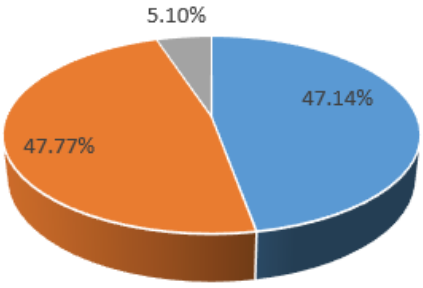	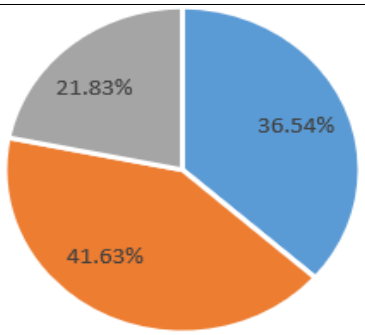
Ji'nan	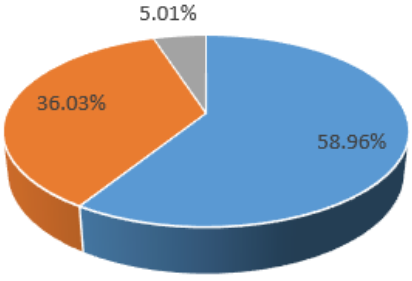	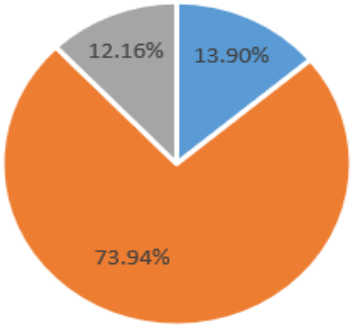

Table 5-1 shows that the three cities have similar structure of water withdrawn. Water from surface waters occupies 30-50% as that from underground 40-60%. From upstream (Xi'an) to downstream (Ji'nan) the percentages of surface water gradually lower (from 48.52% to 36.03%) but those of underground water increase slowly (from 44.43% to 58.96%). Contrary to water withdrawn, water consumed by sectors of household, industry and ecosystem varies but has no clear trend from upstream to downstream. In all the three cities, the percent of water consumed by industry is the highest (41.63%-73.94%) and that by ecosystem is the lowest (10.73%-21.83%) which suggests that most water resources in the YRB are consumed by industry.

5.1 Estimation of water quantity sustaining household

5.1.1 Population change in the study area and representative cities

This section uses LandScan global population data to analyze the change in representative cities of Xi'an, Zhengzhou, and Jinan, and uses local statistical data to verify them. The correlation between the statistical data and Landscan data is about 0.8, e.g., we collected the statistical pop data of zhengzhou from 2001 to 2015 and compared the data with those from landscan as shown in Fig. 5-1 (a). As Landscan has longer time series of pop data, we selected landscan pop for this study. To keep consistent with GRACE TWS dataset, population dataset of 2003 through 2016 in the study area were used, as shown in the following Fig. 5-1 (b).

Fig. 5-1 shows that there are abrupt-increased points from 2011 to 2012 in the three cities. The essential reason is that with the development of rurual areas in the YRB, the agricultural activities need less and less labourers and therefore the surplus labourers in rurual areas flow into urban areas in big cities, results of which is the population increase in urban areas (Yang et al., 2012). To revegetate degraded ecosystems, the semi-arid Loess Plateau in China started the 'Grain to Green' large-scale revegetation programme since 1999 (Feng et al., 2016). This to some extent resulted in fewer crop land and therefore much more surplus labourers flowing into urban areas. In other words, the abrupt increase of population from 2011 to 2012 in the three cities is the result of rurual areas development in the YRB and large-scale revegetation programme since 1999.

5.1.2 Assessment of water quantity sustaining household for representative cities

We use the formula Pop*(water use per person) to estimate water quantity sustaining household for the three representative cities, as shown in Fig. 5-2.

Fig. 5-2 shows slightly increasing trend in water quantity sustaining household for the three representative cities along with the increase of population (Fig. 5-1). What is worthing noticing is that the water consumption for household takes on abrupt increase from the year 2011 to 2012 due to the change in the population (Fig.33) in the corresponding period. Generally, Xi'an has the highest amount of water consumption for household as Ji'nan has the lowest one. Compared Fig. 5-2 and Fig. 5-1 shows the water consumption for household is essentially affected by the population.

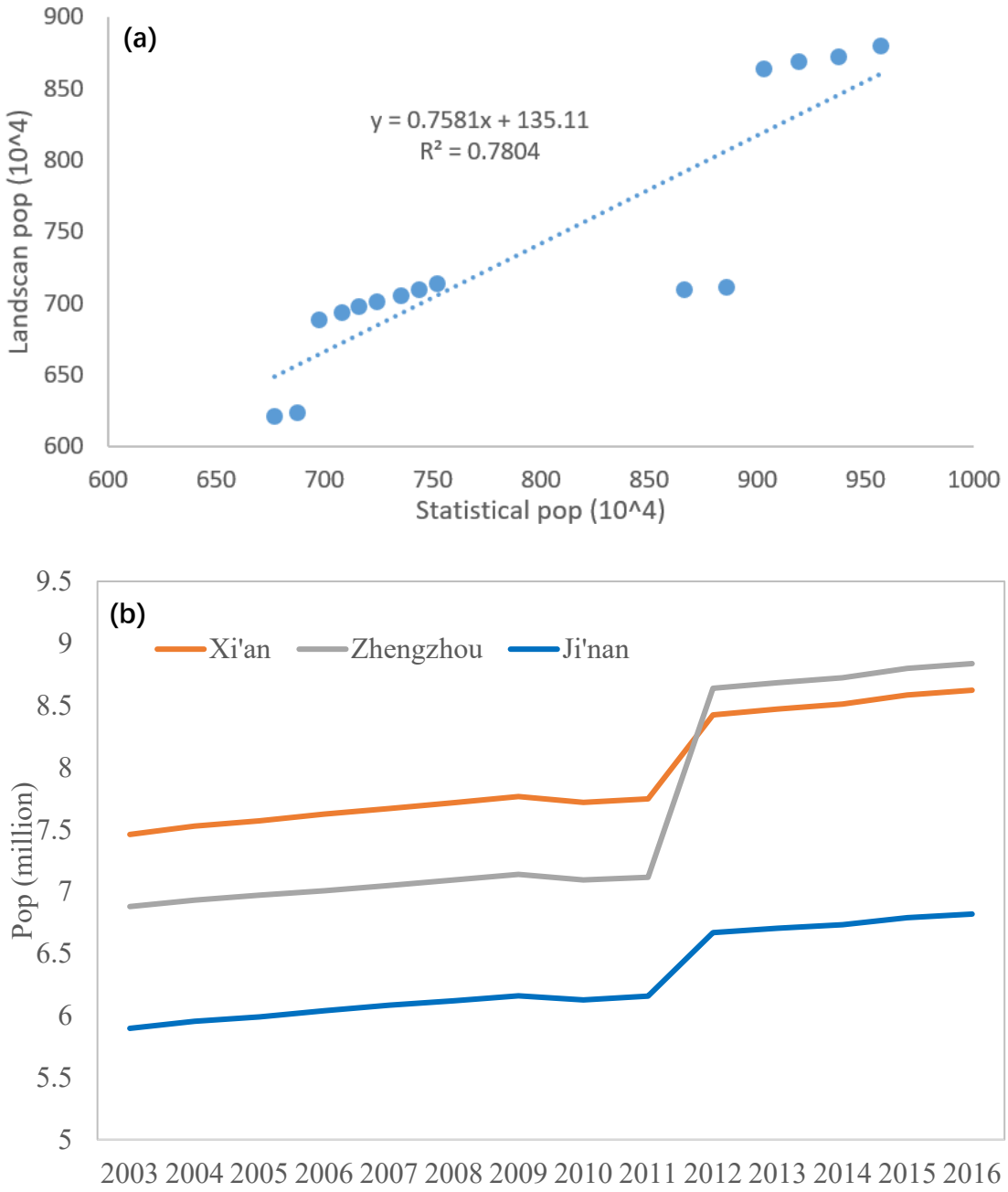

Fig. 5-1 Population trend in the three cities.

At the same time, the variable water use per person also affects the change of water consumption for household. Polcies for water saving decreases the water quantity, e.g., 2004 and after 2010 in Zhengzhou, and after 2014 in the rest cities, as shown in Fig. 5-2.

5.2 Estimation of water quantity for industry

5.2.1 Industrial Gross Domestic Product (GDP) in representative cities

From local statistic book in the three representative cities, industrial GDP can be obtained. This chapter is to analyze the temporal change in the three cities. Industrial GDP in 2003 throuth 2016 was plotted in Fig. 5-3.

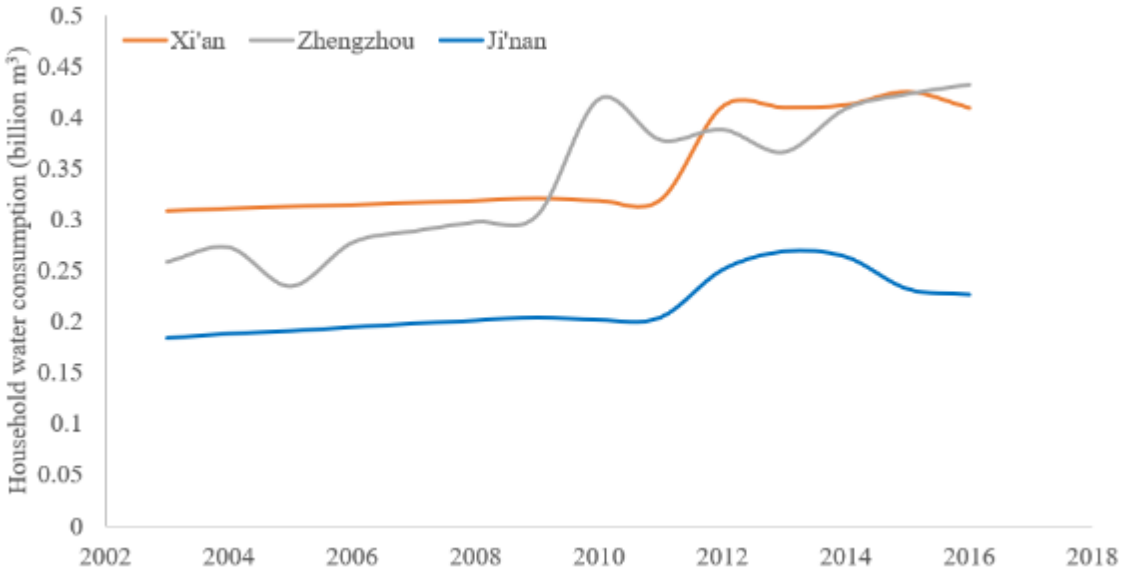

Fig. 5-2 Water quantity sustaining household for the three representative cities

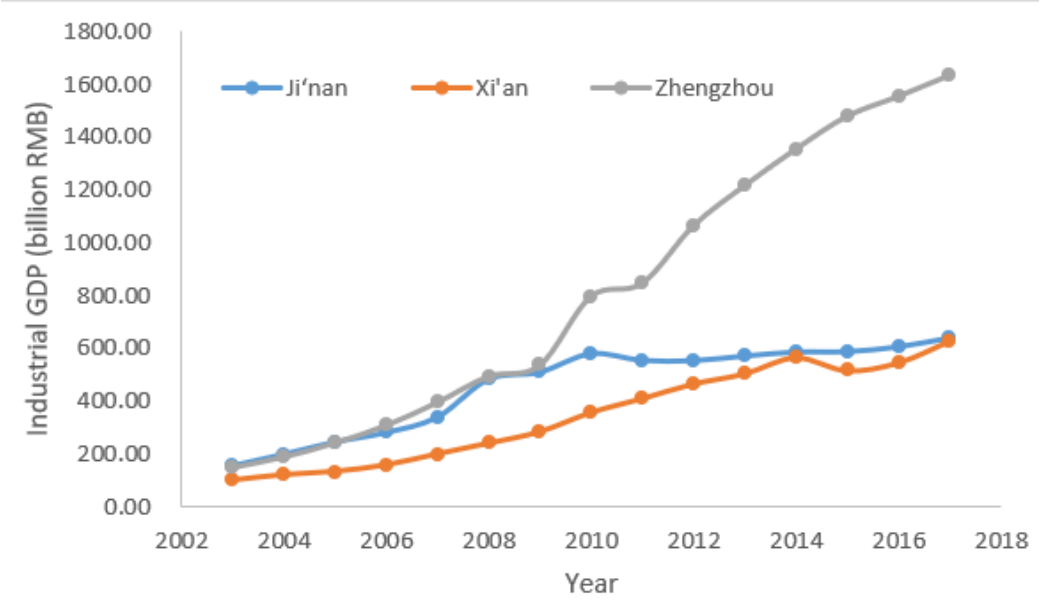

Fig. 5-3 Industrial GDP for the three representative cities

Fig. 5-3 shows a generally increase trend for the three cities. Especially, Zhengzhou has the higest as Xi'an has the lowest increase velocity in this period. The GDP of Zhengzhou was multiplicated by 8 in 16 years whereas in the same period the increase GDP of Xian and Jinan is only by 3. The reason is that the new economic zone of Zhengzhou was established in the year 2009 which was given preferential policies on tax by the local government. The new economic zone attracted a lot of manufactural industries as well as great amount of population (Li and Xu, 2015). The manufactural industries created precedentedly high GDP which made the GDP of Zhengzhou increased by 8 times in 16 years.

5.2.2 Estimation of water quantity for industry in representative cities

Using Eq. 5-1 to estimate water quantity for industry for the three representative cities.

Water consumption per GDP was shown in Fig. 5-4 which continuely decreasing in the period of 2003 through 2016. Meanwhile, it has the reverse order compared with GDP in the three cities (Fig. 5-3), i.e., Zhengzhou has the lowest while Xi'an has the highest one (Fig. 5-4). The revserse orders of GDP and water consumption per GDP resulted in fluctuated water quantity for industry, as shown in Fig. 5-5.

$$\text{Water quantity for industry} = \text{GDP} * (\text{water consumption per GDP}) \quad (5\text{-}1)$$

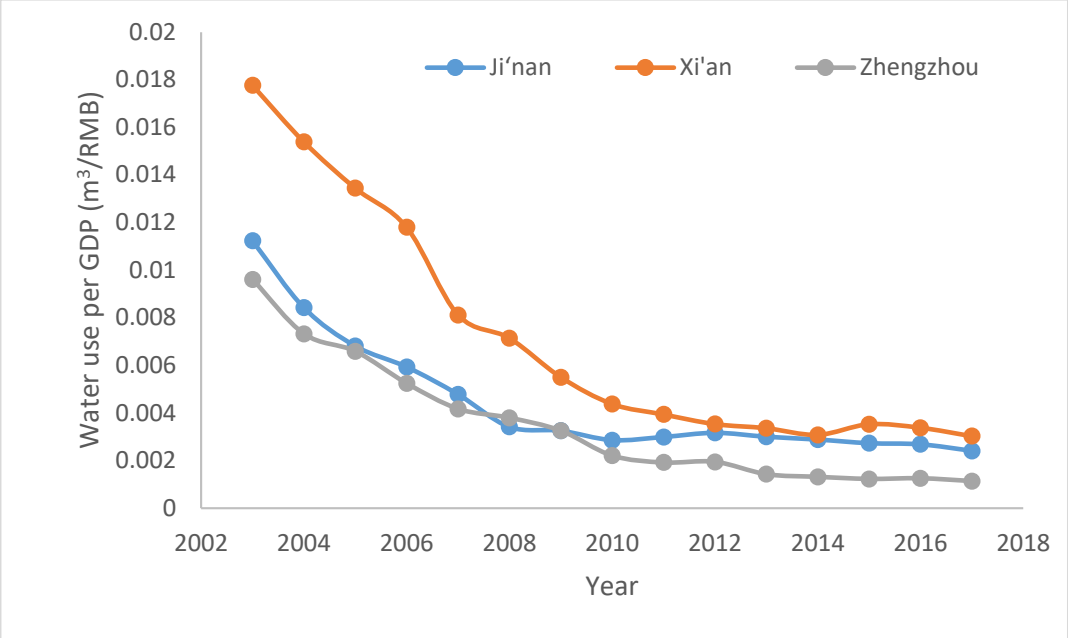

Fig. 5-4 Water use per industrial GDP

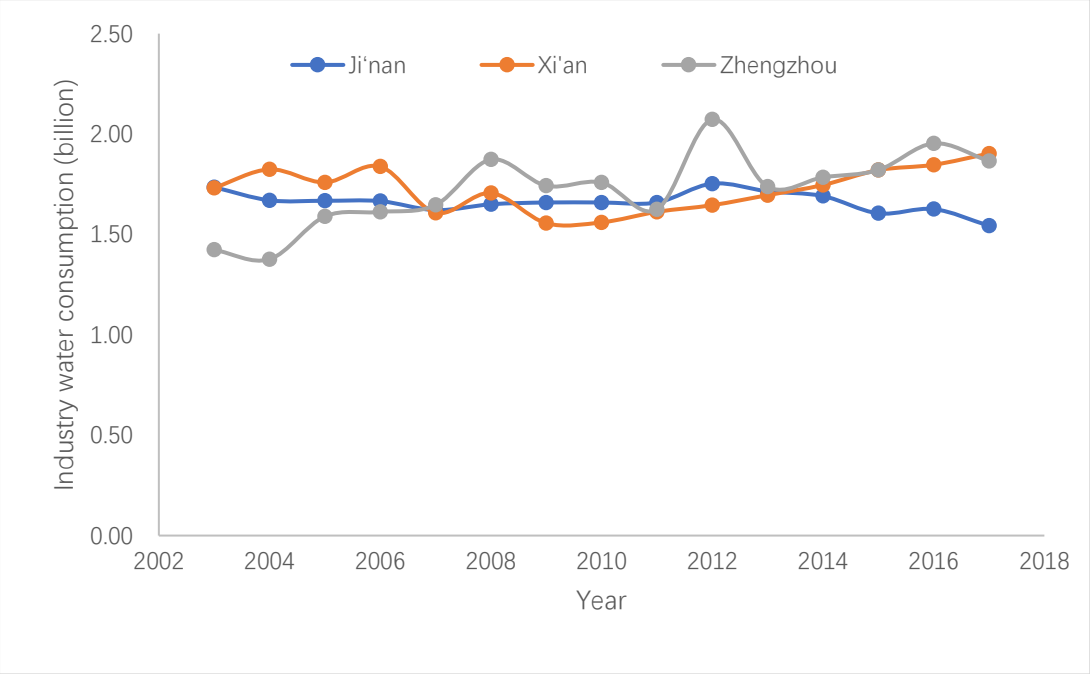

Fig. 5-5 Industrial water consumption for the three representative cities

Zhengzhou had a fabulous increase of industrial GDP since the establishment of the

new economic zone in 2009. But with the gradually decrese of water use per GDP (Fig. 5-4) the water use efficiency in Zhengzhou is higher and higher. In other words, the water is exploited better and better because the adoption of much more new water-saving, reusing, and treating techniques.

Fig. 5-5 shows fluctuated processes of industrial water consumption for the three representative cities due to the reversed order of GDP and water consumption per GDP. Generally, the three cities have almost the same process and quantity of industrial water consumption fluctuated around 1.6 billlion m^3. On average, Zhengzhou has the higest (1.73 billlion m^3) while Ji'nan has the lowest one (1.66 billlion m^3). Generally, the variation processes of industrial water consumption in the three cities are generally stable except for the Zhengzhou City. The variation of Zhengzhou is fluctuated year after year although the water use per industrial GDP (Fig. 5-4) had been decresing gradually because the adoption of much more new water-saving, reusing, and treating techniques since the establishment of the new economic zone in 2009. After three years development, the new economic zone performed better and better leading to an abrupt in 2012 and afterward stable increase of the industrial GDP, which resulted in a peak in 2012 and stable increase in the water consumption.

5.3 Estimation of water quantity consumed by ecosystems

5.3.1 Assimilation of evapotranspiration results from GLDAS data with MODIS imageries

To use MODIS retrieved ET value to rectify GLDAS ET modelling to make them able to represent the whole study area over the period of 2002 through 2016.

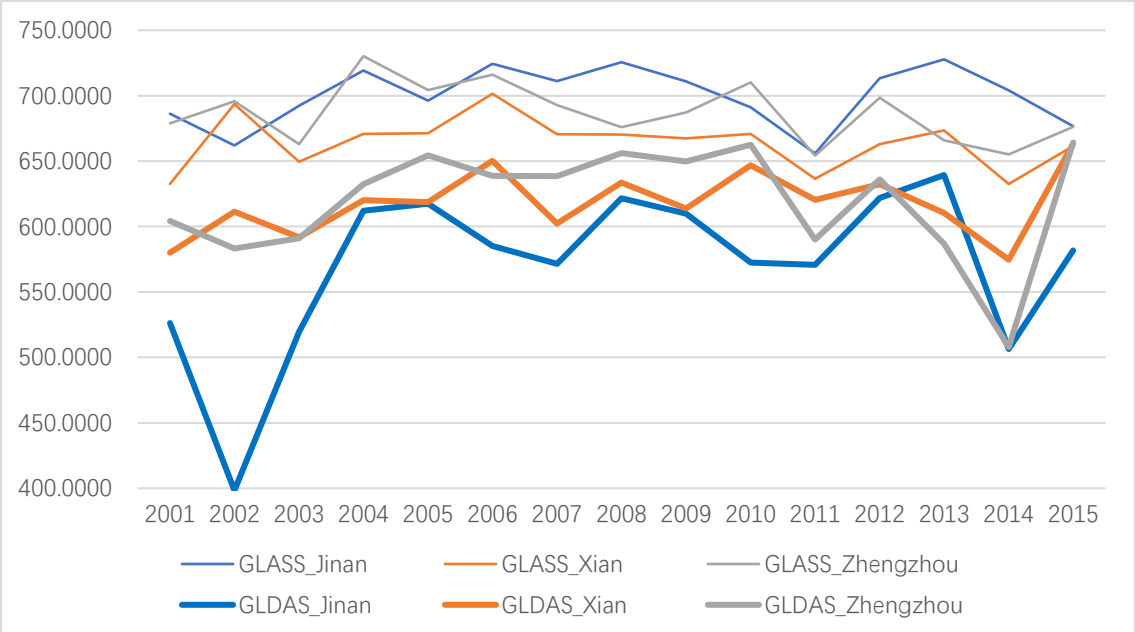

Fig. 5-6 Comparesion of GLASS ET with GLDAS ET in three cities

MODIS retrieved ET has been collected by a Chinese dataset (GLASS) (http://www.geodata.cn) produced by Yang's team from Beijing Normal University. Here, the MODIS retrieved ET values from GLASS dataset (Yao et al., 2014) in the three cities were

compared with the corresponding GLDAS ET, whereby correlations were established, as shown in Fig. 5-6 and 5-7.

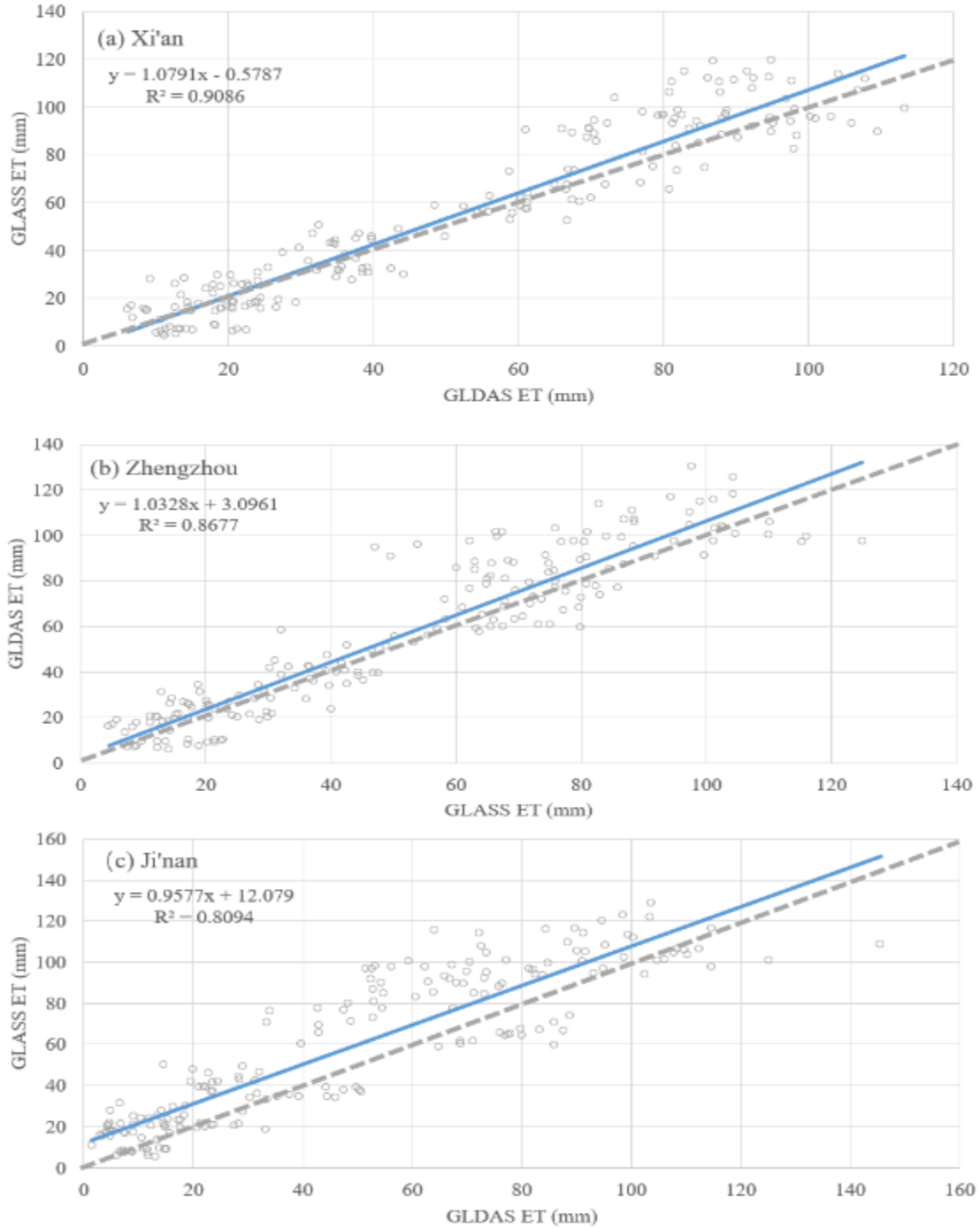

Fig. 5-7 Monthly GLASS ET vs monthly GLDAS ET in three cities with gray dash line being 1:1 line.

Fig. 5-6 shows the annual GLASS ET values are greater than the GLDAS ET values in the three representative cities. Differences between the annual GLASS and GLDAS ET values are the biggest in Jinan (average: 129 mm) while the least in Xi'an (average: 46 mm). The research of Chang et al. (2017) shows that the precipitation in 2002 is exceptionally low which resulted in abnormal low ET in GLDAS data in 2002 (Fig. 5-6) as the climate of Jinan is very arid and its ET is largely limited by water available. Likely, much lower precipitation in 2014 (Chang et

al., 2017) resulted in abnormally low ET in 2014. Results suggest that there are certain uncertainties in both of the GLASS and GLDAS data. If somebody want to analyse the bias between the two datasets, he has to firstly collect the ground-observed ET data in Ji'nan during 2001-2015. But as all know that ground-observed ET data are not publicly available in China. Though it is difficult, we looked through literatures and found that the precipitation in 2002 is exceptionally low which resulted in abnormal ET in GLDAS data in 2002 as the climate of Jinan is very arid and its ET is largely limited by water available.

Fig. 5-7 shows that the monthly GLASS ET is slightly greater than monthly GLDAS ET in all the three cities, Xi'an, Zhengzhou, and Ji'nan. They have significantly linear relationship (R^2=0.81-0.91, as shown in Fig. 5-7 a-c). Hence, using these linear relationships for the three cities in Fig. 5-7, one can improve the GLDAS ET accuracy from 1948-2016 in the three cities.

5.3.2 Estimating water consumed by ecosystems based on evapotranspiration data

This section estimates ET in the three representative cities based on the above rectified GLDAS ET data, as shown in Fig. 5-8.

Fig. 5-8 Annual rectified GLDA ET in three cities with upper being the water consumption and lower the evapotranspiration rate (ET) in the unit of mm.

For the ecosystem water consumption (Fig. 5-8 upper), Xi'an and Ji'nan have similar values (average: 7.13 and 7.11 billion m^3) while the zhengzhou has the least one (average: 5.05 billion m^3). The difference is because of the different area of the three cities (Xi'an, Ji'nan and Zhengzhou: 10752, 10244 and 7446 km^2). In other words, the three cities have similar evapotranspiration rate (averaged ET: 709, 702 and 723 mm, lower figure in Fig. 5-8), but the larger size of Xi'an and Ji'nan resulted in higher ecosystem water consumption, and *vice versa* in Zhengzhou.

5.4 Estimation of total water consumption

By summing up the above three water consumption for household, industry and ecosystem, one can get the total water consumption from 2003 to 2016, as shown in Fig. 5-9.

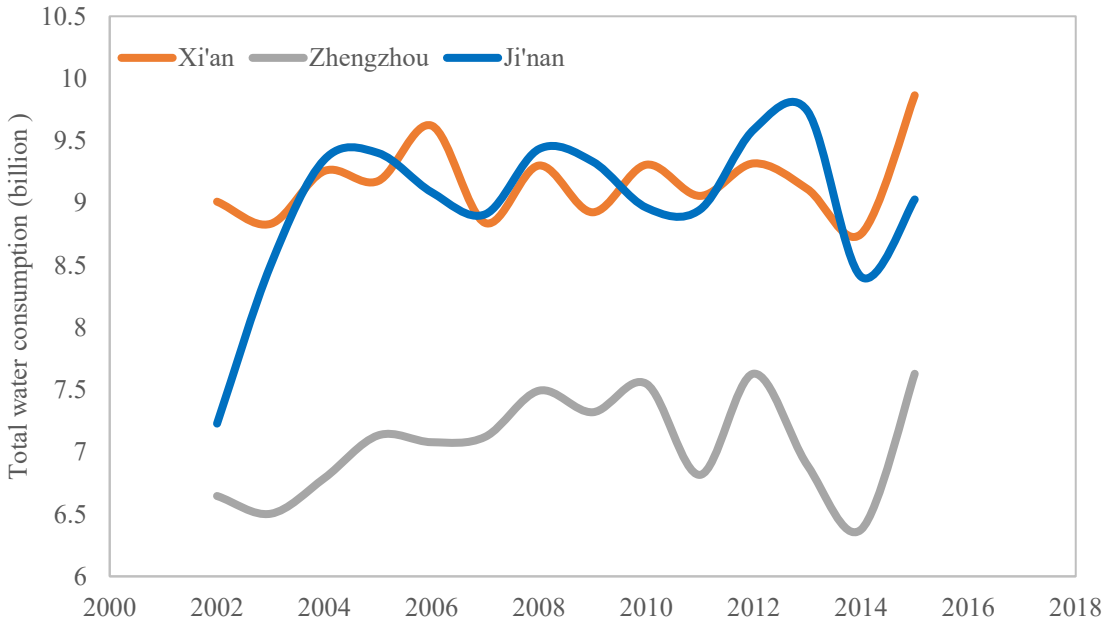

Fig. 5-9 Total water consumption in the three cities.

Fig. 5-9 shows that the total water consumption in the three cities fluctuated in the period. Xi'an and Ji'nan have similar processes with average values of 9.17 and 8.99 billion m^3 as Zhengzhou has the lowest value of 7.07 billion m^3. The process of total water consumption is similar with that of ecosystem water consumption (Fig. 5-8) with ratios of ecosystem to total water consumption ranging from 71.45% to 79.06%. Ratios of household to total water consumption are the lowest ranging from 2.35% to 4.66%.

The abnormality of total water consumption in 2014 is caused by the abnormal ET in the three cities as shown in Fig. 5-6 where the GLDAS ET in the three cities had an abnormal decrease in 2014. As ET or ecosystem water consumption occupies more than 70% of total water consumption, the variation process of total water consumption is dominated by the ET instead of population change which is obvious when we compare Fig. 5-9 with Fig. 5-8.

5.5 Summary

This chapter calculated water consumption of household, industry and ecosystem. During the same period with GRACE data from 2003 to 2016, household water consumption in the

three representative cities of Xi'an, Zhengzhou and Ji'nan takes on slightly increasing trend along with the increase of population. It is essentially affected by the variation of population. Xi'an has the highest amount of water consumption for household (0.35 billion m^3 on average) as Ji'nan has the lowest one (0.21 billion m^3 on average).

Industrial water consumption during 2003-2016 in the three cities fluctuates around 1.60 billlion m^3 showing no obvious increase or decrease trend. On average, Zhengzhou has the higest (1.73 billlion m^3) while Ji'nan has the lowest one (1.66 billlion m^3). For the ecosystem water consumption, Xi'an and Ji'nan have similar values (average: 7.13 and 7.11 billion m^3) while the zhengzhou has the least one (average: 5.05 billion m^3). The different area of the three cities (Xi'an, Ji'nan and Zhengzhou: 10752, 10244 and 7446 km^2) resulted in the difference of ecosystem water consumption among them.

All in all, the total water consumption in the three cities fluctuated in the period as Xi'an and Ji'nan have similar processes with average values of 9.17 and 8.99 billion m^3 as Zhengzhou has the lowest value of 7.07 billion m^3. The ecosystem water consumption dominates the total water consumption with ratios of ecosystem to total water consumption ranging from 71.45% to 79.06%.

Chapter 6 Prediction of urban drought in 2030 and 2050

This chapter aims to predict urban drought in the two future years of 2030 and 2050 including prediction of freshwater available and water consumption. The former was achieved by setting up ANN (Artificial Neural Network) with surface freshwater available estimated in Chapter 3 and environmental factors, presented in CMIP5 (Coupled Model Intercomparison Project Phase 5) scenarios, influencing the variation of surface freshwater. CMIP5 IPCC scenarios of RCP 2.6, RCP 4.5 and RCP 8.5 were used where principal environmental factors in 2030 and 2050 are presented. The latter, or future water consumption, for household/industrial/ecosystem, was predicted based on models established in Chapter 5 and predicted basis data presented in published literatures.

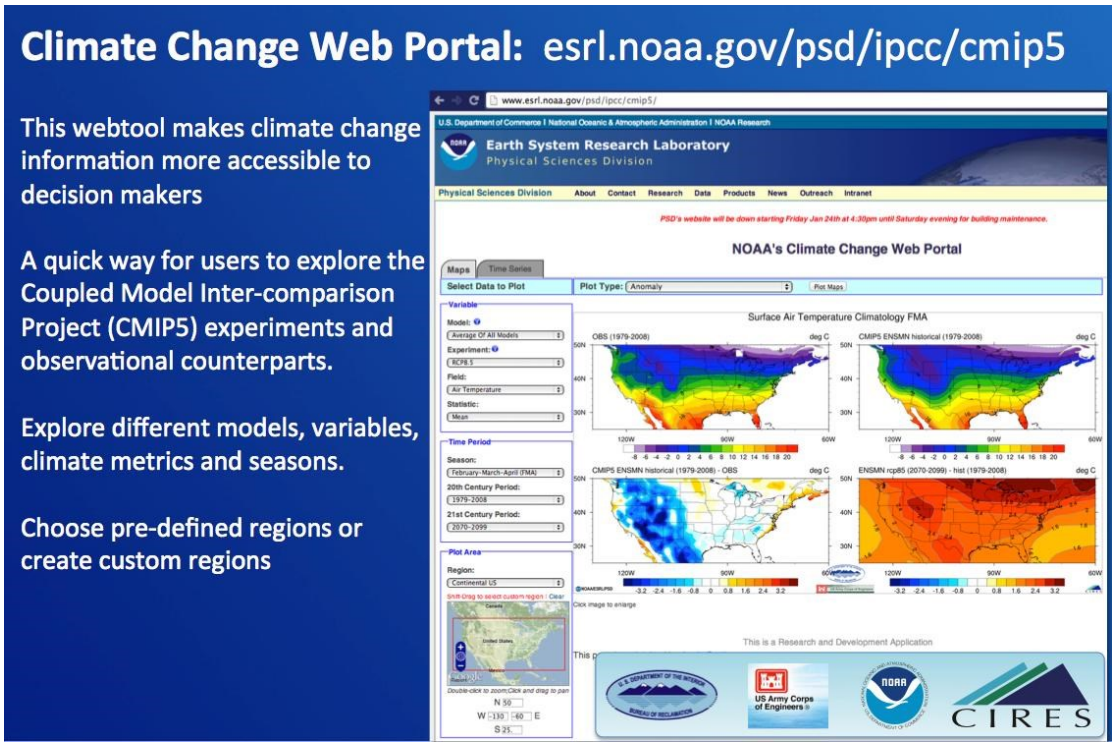

Fig. 6-1 CMIP5 website http://www.psl.noaa.gov/ipcc/

RCP2.6, RCP4.5 and RCP8.5 are respectively representative concentration pathways, which approximately result in a radiative forcing of 2.6, 4.5 and 8.5 W m^{-2} at year 2100, relative to pre-industrial conditions. RCPs are time-dependent, consistent projections of emissions and concentrations of radiatively active gases and particles. We selected four variables highly related to drought (Precipitation, Near-Surface Air Temperature, Evaporation, Evaporation from Canopy) from CMIP 5. Details can be found in Table 6-1.

Table 6-1 Four variables highly related to drought selected from CMIP 5

Long name	Units	Comment	Variable name	Standard name
Precipitation	kg m^{-2} s^{-1}	At surface; includes both liquid and solid phases from all types of clouds (both large-scale and convective)	pr	precipitation_flux
Near-Surface Air Temperature	K	Normally, the temperature should be reported at the 2 meter height	tas	air_temperature
Evaporation	kg m^{-2} s^{-1}	At surface; flux of water into the atmosphere due to conversion of both liquid and solid phases to vapor (from underlying surface and vegetation)	evspsbl	water_evaporation_flux
Evaporation from Canopy	kg m^{-2} s^{-1}		evspsblveg	water_evaporation_flux_from_canopy

Source: https://esgf-node.llnl.gov/search/cmip5/

6.1 Prediction of freshwater available

6.1.1 Establishment of relationship between environmental factors and surface FWA to predct future surface FWA

Envrionmental factors directly related to the variation of surface FWA, which are accessible in IPCC CMIP5 model and scenarios, include precipitation, evapotranspiration, near-surface air temperature. In addition, when making time slice the CMIP5 selected the year 2030 as the representative year to simulate a future decade covering the years 2026-2035, which implies the year 2030 is an important point in the CMIP5 simulations. Besides, the three secnarios all take the year 2100 as the simulation base year. Half of the the current century (2050) is the focus in many fields when studying climate change (Marks, 2019; Mastini et al., 2021; Polli et al., 2021; Robertson et al., 2021). Therefore, this study selected the year 2030 and 2050 as the base year to predict future urban drought.

To predict future urban drought, future freshwater quantity needs to be predicted. Via the way of establishing ANN (LSTM-N) model taking environmental factors as input and surface FWA as output, this section used envirionmental factors in 2030 and 2050 in three CMIP5 IPCC scenarios of RCP 2.6, RCP 4.5 and RCP 8.5 to estimate freshwater available, as shown in Fig. 6-2, Fig. 6-3 and Fig. 6-4.

LSTM-N is one of the most important deep learning models. By using gate cells, LSTM-N avoids the problem of gradient degradation. It has been widely used in many fields, especially in time series modeling, including speech recognition, natural language processing and sequence prediction. Simplified LSTM-N is very effective for modeling time series. In addition to time series modeling, LSTM-N can also be applied to modeling nonlinear systems (Yu et al., 2019a; Yu et al., 2019b). This algorithm could avoid the interference of the redundant information in the output of the bottom layer to the effective information in the upper layer. In

the term of speech-based emotion recognition task, the weighting on the time dimension reflects the difference of emotion saturation among periods, while that on the feature dimension reflects the distinguishability of different features (Xie et al., 2019).

A LSTM-N model with the optimal parameters (Unit": 460, activation function: "sigmoid", and training epoch: 650) are established to forcast future streamflow, or surface FWA, under the three climate scenarios by taking the environment factors of precipitation, evapotranspiration, near-surface air temperature as input. Historical data of the environment factors in CMIP5 and historical surface FWA from 1948 to 2016 predicted in the Chapter 3 are used to train the LSTM-N model.

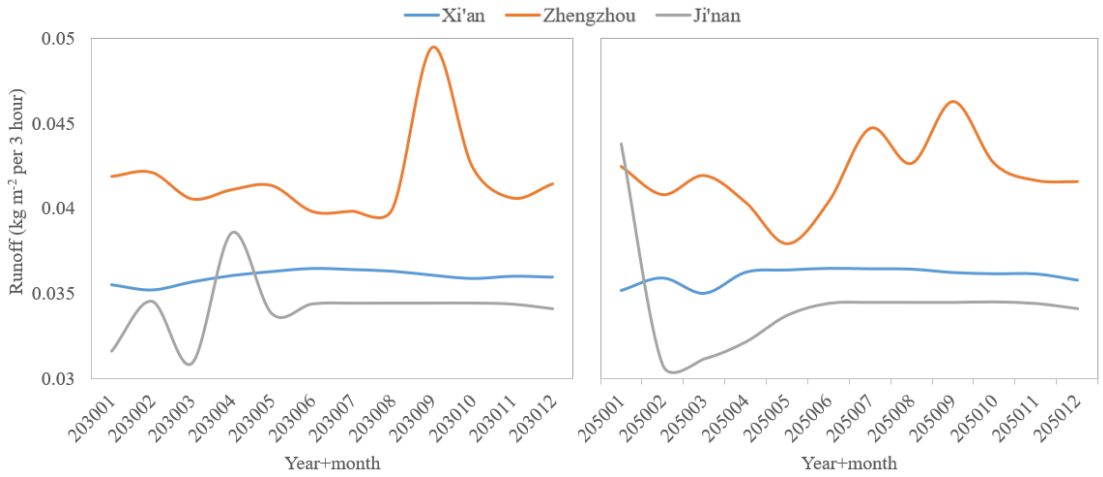

Fig. 6-2 Surface runoff in 2030 (Left) and 2050 (Right) under Scenario RCP 2.6

Fig. 6-2 shows the monthly surface runoff predicted by using the LSTM-N model under scenario RCP 2.6. The variation process of surface runoff within 2030 and 2050 is similar. Surface runoff in Xi'an in both 2030 and 2050 changes steadily among the 12 months, that in Ji'nan fluctuates a little in the first half year but becomes steady in the second half, while that in Zhengzhou fluctuates intensively especially in the wet season (June through September). The peak appears in Septermber in both 2030 and 2050 as there appears a valley in May of 2050.

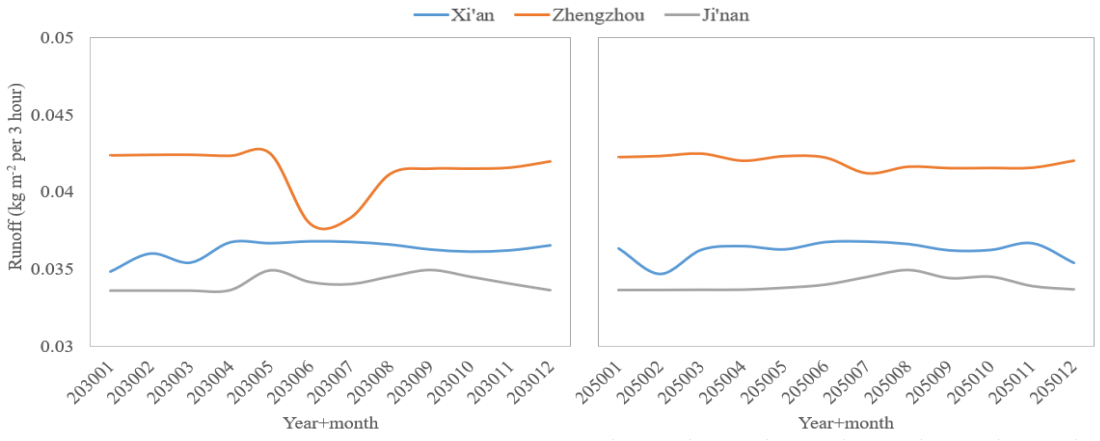

Fig. 6-3 Surface runoff in 2030 (Left) and 2050 (Right) under Scenario RCP 4.5

Fig. 6-3 shows the predicted monthly surface runoff processes in 2030 and 2050 under scenario RCP 4.5 are similar. The surface runoff in both Xi'an and Ji'nan in the two years

changes steadily, while that in Zhengzhou fluctuates a little in June of 2030 and changes steady throughout the whole year 2050.

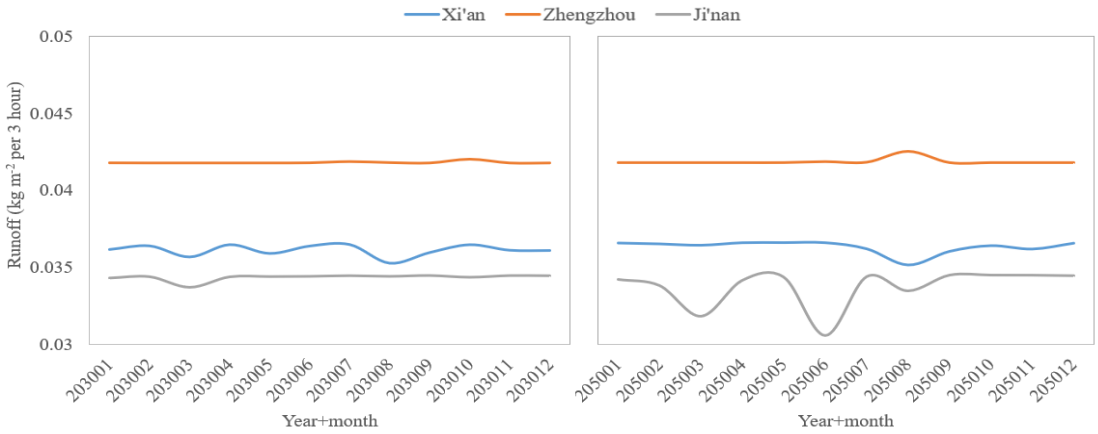

Fig. 6-4 Surface runoff in 2030 (Left) and 2050 (Right) under Scenario RCP 8.5

Fig. 6-4 shows the predicted monthly surface runoff processes in 2030 and 2050 under scenario RCP 8.5 are a little different. The surface runoff in both Xi'an and Zhengzhou in the two years changes steadily, while that in Ji'nan changes steady in 2030 but fluctuates a little in 2050 especially in the first half of the year.

Comparison of Fig. 6-2- Fig. 6-4 shows that different radiative forcing of 2.6, 4.5 and 8.5 W m^{-2} under scenario RCP 2.6, RCP 4.5 and RCP 8.5 change the future runoff pattern in 2030 and 2050. With the increase of radiative forcing from 2.6 to 8.5 W m^{-2}, the surface runoff flunctuation frequency is gradually lessened (e.g., Zhengzhou). At the same time, there appears a trend of regional drought with the increasing of the radiative forcing, e.g., Ji'nan in 2050 under RCP 8.5. In other words, with the increase of radiative forcing, the three cities have a possibility of changing from wet to dry climate, especially in the low reaches of the Yellow River (Zhengzhou and Ji'nan). The lowest radiative forcing (2.6 w m^{-2}) resulted in the highest fluctuation frequency in surface runoff in 2030 and 2050. In other words, a higher radiative forcing reduces the frequency of floods and makes runoff steady throughout a year.

Analysis also shows that with the increase of radiative forcing, the three cities have a possibility of changing from wet to dry climate, especially in the low reaches of the Yellow River (Zhengzhou and Ji'nan). This resulted in the near opposite results, especially in lower-reach cities, Zhengzhou and Ji'nan while the upper-reach Xi'an has a little change.

Overall, monthly surface runoff predicted was similar, fluctuating around average value of 0.036, 0.042 and 0.034 kg m^{-2} per 3-hour respectively in 2030 and in 2050 in Xi'an, Zhengzhou and Ji'nan, as shown in Table 6-2. In other words, Xi'an, Zhengzhou and Ji'nan will have up to 1.14, 0.91 and 2.03 billion m^3 surface freshwater for consumption in 2030 and 2050.

Table 6-2 predicted LWE and runoff in 2030 and 2050 (LWE in cm and runoff in kg m-2 per 3 hour)

IPCC Scenario	Year	Averaged LWE (cm)			Averaged Runoff (kg m^{-2} per 3-h)		
		Xi'an	Zhengzhou	Ji'nan	Xi'an	Zhengzhou	Ji'nan
RCP 2.6	2030	-0.225	-0.828	-2.185	0.036	0.042	0.034
	2050	-0.277	0.023	-1.465	0.036	0.042	0.034
RCP 4.5	2030	-0.121	-0.218	-2.132	0.036	0.041	0.034
	2050	-0.295	-0.216	-2.137	0.036	0.042	0.034
RCP 8.5	2030	-0.257	-0.206	-1.646	0.036	0.042	0.034
	2050	-0.616	-0.519	-1.649	0.036	0.042	0.034

6.1.2 Establishment of relationship between environmental factors and underground FWA to predict future underground FWA

This section predicted future LWE variation via the way of establishing ANN model taking environmental factors as input and LWE as output. It used envirionmental factors in 2030 and 2050 in the three CMIP5 IPCC scenarios to estimate monthly LWE variation in 2030 and 2050, based on which underground FWA was estimated. The predicted monthly LWE is shown in Fig. 6-5, Fig. 6-6 and Fig. 6-7.

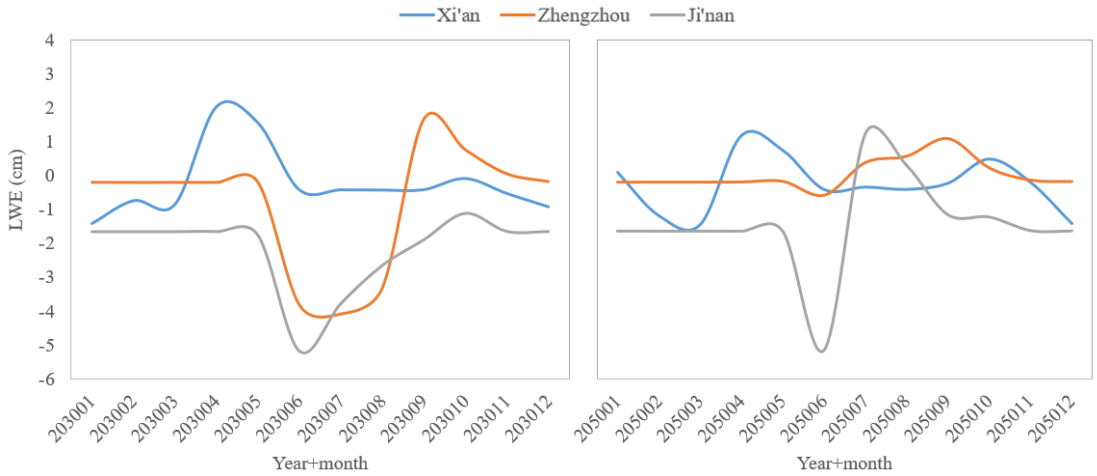

Fig. 6-5 LWE in 2030 (Left) and 2050 (Right) under Scenario RCP 2.6

Fig. 6-5 shows the monthly LWE predicted by using the LSTM-N model under scenario RCP 2.6. The variation process of LWE within 2030 and 2050 is similar. Difference of 2030 and 2050 in Zhengzhou is a little large during the wet season of June, July and August. LWE in all the three cities in both of the two future year fluctuates intensively especially in lower reaches (Zhengzhou and Ji'nan). LWEs of 2030 and 2050 in the three individual cities change similarly except for Zhengzhou which LWE appears a valley during the period of June, July and August of 2050.

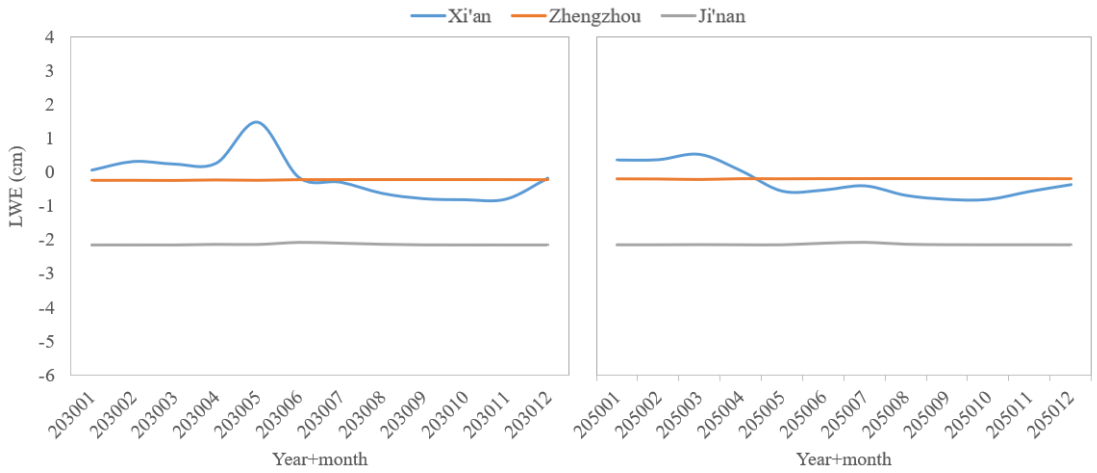

Fig. 6-6 LWE in 2030 (Left) and 2050 (Right) under Scenario RCP 4.5

Fig. 6-6 shows the predicted monthly LWE under scenario RCP 4.5 for both 2030 and 2050 changes steadily instead of fluctuates intensively uner RCP 2.6. The variation process between 2030 and 2050 is similar. Both in lower reaches of Zhengzhou and Ji'an, the LWE for the two future years changes very little. LWE in Xi'an fluctuates but with a smaller magnitude than that under RCP 2.6.

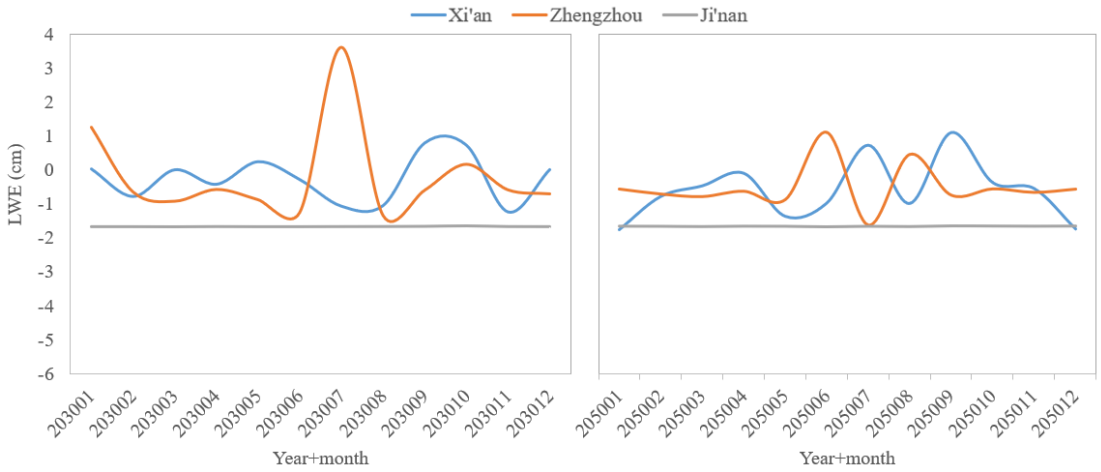

Fig. 6-7 LWE in 2030 (Left) and 2050 (Right) under Scenario RCP 8.5

Fig. 6-7 shows the predicted monthly LWE under scenario RCP 8.5 for both 2030 and 2050 fluctuates intensively, especially in the upper reaches of Xi'an and Zhengzhou. As for Zhengzhou, the fluctuating magnitude of LWE in 2030 is lager than that in 2050. What is worth noticing is that LWE in the low reach of Ji'nan has no change during the whole year of both 2030 and 2050.

Comparison of Fig. 6-5- Fig. 6-7 shows that with the increase of radiative forcing under scenario RCP 2.6, RCP 4.5 and RCP 8.5, the LWE firstly changes smaller and then fluctuates inversely in most of the three cities, which is more evident in the upper reaches (Xi'an and Zhengzhou). In the down reach Ji'nan, the LWE changes from frequently fluctuating to without any change during both 2030 and 2050. Generally, the fluctuating magnitude in the three cities in 2030 is larger than in 2050.

Overall, monthly LWEs predicted under scenario RCP 2.6, RCP 4.5 and RCP 8.5 vary greatly, with RCP 2.6 having the biggest variation range from -5 to 2 cm monthly and RCP 4.5 the smallest range from -2 to 1.5 cm monthly. Generally, LWE in all the three cities in both 2030 and 2050 decreases fluctuating below 0 in most months. In other words, underground water available in the three cities in 2030 and 2050 will continuously decrease. LWEs in the three cities will respectively decrease at a rate of 0.20, 0.42 and 1.99 cm on average in 2030. Similarly, in 2050 they will decrease 0.40, 0.24 and 1.75 cm. Ji'nan has the greatest decrease rate. All the three RCPs predicted similar LWE decrase rate (~0.8 cm on average).

By using data of underground water available (UFWA) in the three cities from "Water Resource Bulletin" (2002-2016), the averaged UFWA in the GRACE-data-base years (2004-2009) was acquired with the equation $UFWA_{base} = \sum_{k=2002}^{2016}(UFWA_i + LWE_i)/14$. With the averaged UFWA for the base year and based on the LWE variation in 2030 and 2050, underground water available was estimated. Results show that Xi'an, Zhengzhou and Ji'nan will have 0.87-0.90, 1.04-1.06 and 0.33-0.40 billion m^3 underground freshwater for consumption in 2030, and 0.91-1.00, 1.04-1.05 and 0.30-0.40 billion m^3 in 2050.

In summary, Xi'an, Zhengzhou and Ji'nan will have 2.01-2.04, ~1.95 and 2.36-2.43 billion m^3 freshwater for consumption in 2030, and 2.05-2.14, 1.95-1.96 and 2.33-2.43 billion m^3 in 2050. According to data from "Water Resource Bulletin" (2002-2016) of Xi'an, Zhengzhou and Ji'nan, the average values of freshwater available including surface and undergournd water resources are respectively 1.89-4.46, 0.75-2.50 and 0.79-2.57 billion m^3 which justified the reasonableness of caculated freshwater available above.

6.2 Prediction of water consumption

6.2.1 Future water consumption by household

This section uses population projections to predict population in the three cities and uses prediction data from published lieteratures to estimate water consumption for household in 2030 and 2050.

Population projections are attempts to show how the human population living today will change in the future. These projections are an important input to forecasts of the population's impact on this planet and humanity's future well-being. Models of population growth take trends in human development, and apply projections into the future. These models use trend-based-assumptions about how populations will respond to economic, social and technological forces to understand how they will affect fertility and mortality, and thus population growth (Wikipedia, 2021a).

The UN Population Division has calculated the future population of the world's countries, based on current demographic trends. Current (2020) world population is 7.8 billion. The 2019 report projects world population in 2050 to be 9.7 billion people, and possibly as high as 11 billion by the next century, with the following estimates for the top 14 countries in 2020, 2050, and 2100 (Wikipedia, 2021a). Population prediction for China can be plotted in Fig. 6-8 with data from UN.

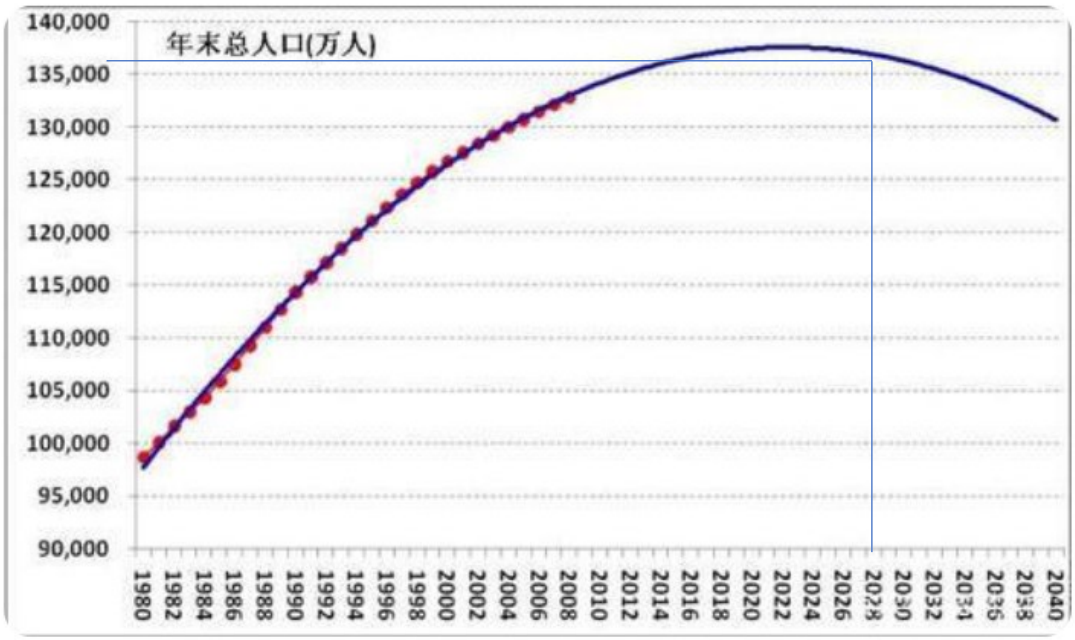

Fig. 6-8 Future population in China

(Source: https://baijiahao.baidu.com/s?id=1663031362737011917&wfr=spider&for=pc)

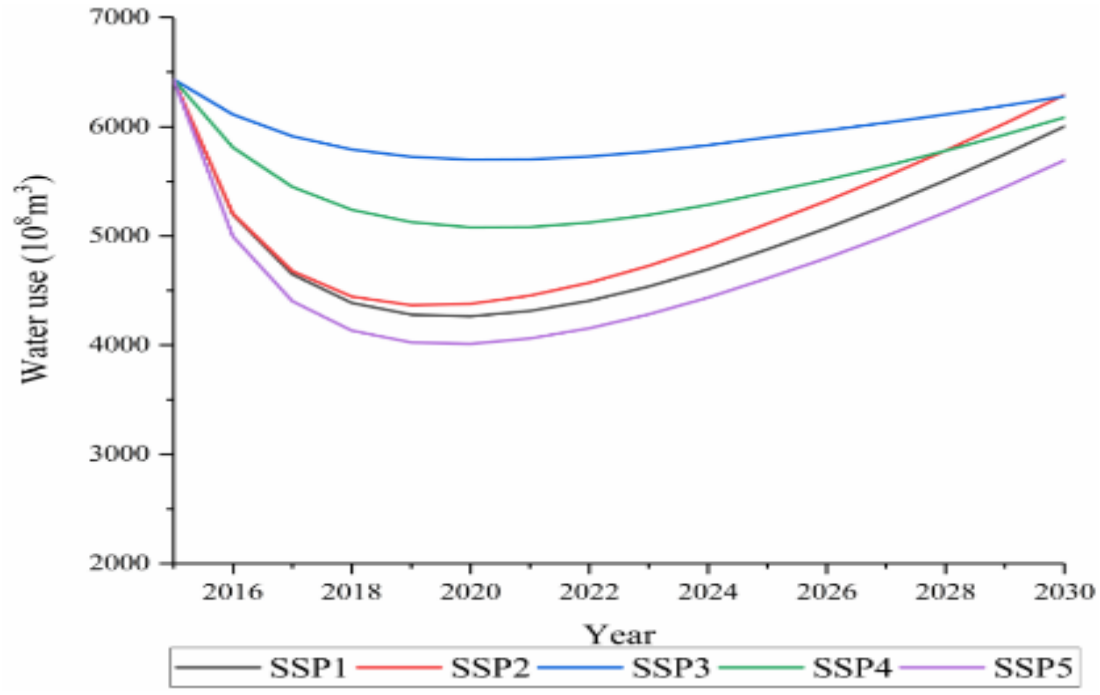

Fig. 6-9 Trends of China's total water use from 2015 to 2030 under the shared socioeconomic pathways (SSPs) (From Guo et al. 2021).

Fig. 6-8 shows than population in China will decrease to ~136,500 million. With this rate, population in 2050 will decrese to ~121,000 million. For Xi'an, Zhengzhou and Ji'nan, population will inevitably decrease in future. Assuming the three cities have the same rate with China, their population in 2030 will be ~8.7, 7.9, 6.8 million and in 2050 will be 5.7, 4.5 and 3.9 million.

With the change of population, the water use per captia will also change. Guo et al. (2021)

investigated the water use efficiency of China revealing that by 2030 China water use efficiency will increase by 0.88-0.93 times compared with 2015. In other words, water use in China will be 0.88-0.93 times of that in 2015, as shown in Fig. 6-9.

Assuming household water consumption in the three has the same increase rate with that in China water use, household water consumption in Xi'an, Zhengzhou and Ji'nan will be 0.88-0.93 times of that in 2015. In other words, household water consumption will be 0.37-0.40, 0.37-0.39 and 0.20-0.22 billion m^3 respectively in Xi'an, Zhengzhou and Ji'nan, as shown in Table 6-3.

Table 6-3 Household water consumption in 2030 (billion m^3)

City	2015-base	2030-min	2030-max
Xi'an	0.42	0.37	0.40
Zhengzhou	0.42	0.37	0.39
Ji'nan	0.23	0.20	0.22

Table 6-4 Percentage change of the WF of consumption relative to 2000. 'A': WF of agricultural products, 'D': WF of domestic water supply, 'I': WF of industrial products and 'T' : WF of totoal WF; 'CHI': China (Ercin et al., 2012).

Region	S1				S2				S3				S4			
	A	D	I	T	A	D	I	T	A	D	I	T	A	D	I	T
USA	29	24	112	41	83	57	69	80	29	-1	50	30	39	12	28	36
Canada	48	26	95	54	91	58	52	83	5	1	55	13	14	13	38	18
WEU	19	-3	112	28	52	22	65	52	-27	-23	52	-19	-24	-13	12	-20
JPK	11	-20	113	19	39	1	50	38	-36	-36	58	-26	-29	-28	15	-25
ANZ	172	40	107	171	201	77	62	199	20	12	73	20	5	26	13	5
EEU	12	-24	1024	143	45	0	285	75	-47	-39	438	17	-41	-30	419	20
FSU	6	-18	975	61	39	10	268	51	-44	-34	366	-20	-37	-24	340	-15
MDE	198	44	720	207	309	88	229	294	99	15	436	106	153	32	152	146
CAM	100	21	865	115	165	63	264	163	9	-3	490	20	24	13	292	30
SAM	117	24	722	126	181	66	204	177	21	-1	370	27	29	15	231	32
SAS	128	38	1206	143	214	85	313	212	27	11	1399	49	55	28	676	64
SEA	96	32	769	117	160	76	169	156	2	6	317	13	16	22	338	27
CHI	79	-12	1391	113	117	16	205	116	-29	-29	346	-18	-25	-19	771	-3
NAF	65	43	811	81	122	90	298	125	25	14	881	45	50	32	171	52
SSA	353	122	1415	355	538	183	334	531	179	78	969	181	263	101	486	262
RoW	212	-9	893	240	274	11	211	259	37	-27	366	52	51	-20	400	67
World	112	18	596	130	180	55	157	175	18	-6	308	30	38	8	259	46

As to future water use in 2050, Ercin and Hoekstra (2012) conducted the first global water footprint scenario study in 2050. It explores how the water footprint of humanity will change towards 2050 under four alternative scenarios, which differ from each other in terms of specific trajectories for the main drivers of change. The four scenarios they constructed, along two axes, represent two key dimensions of uncertainty: globalisation versus regional self-sufficiency, and economy-driven development versus development driven by social and environmental objectives. The two axes create four quadrants, each of which represents a scenario: global markets (S1), regional markets (S2), global sustainability (S3) and regional sustainability (S4).

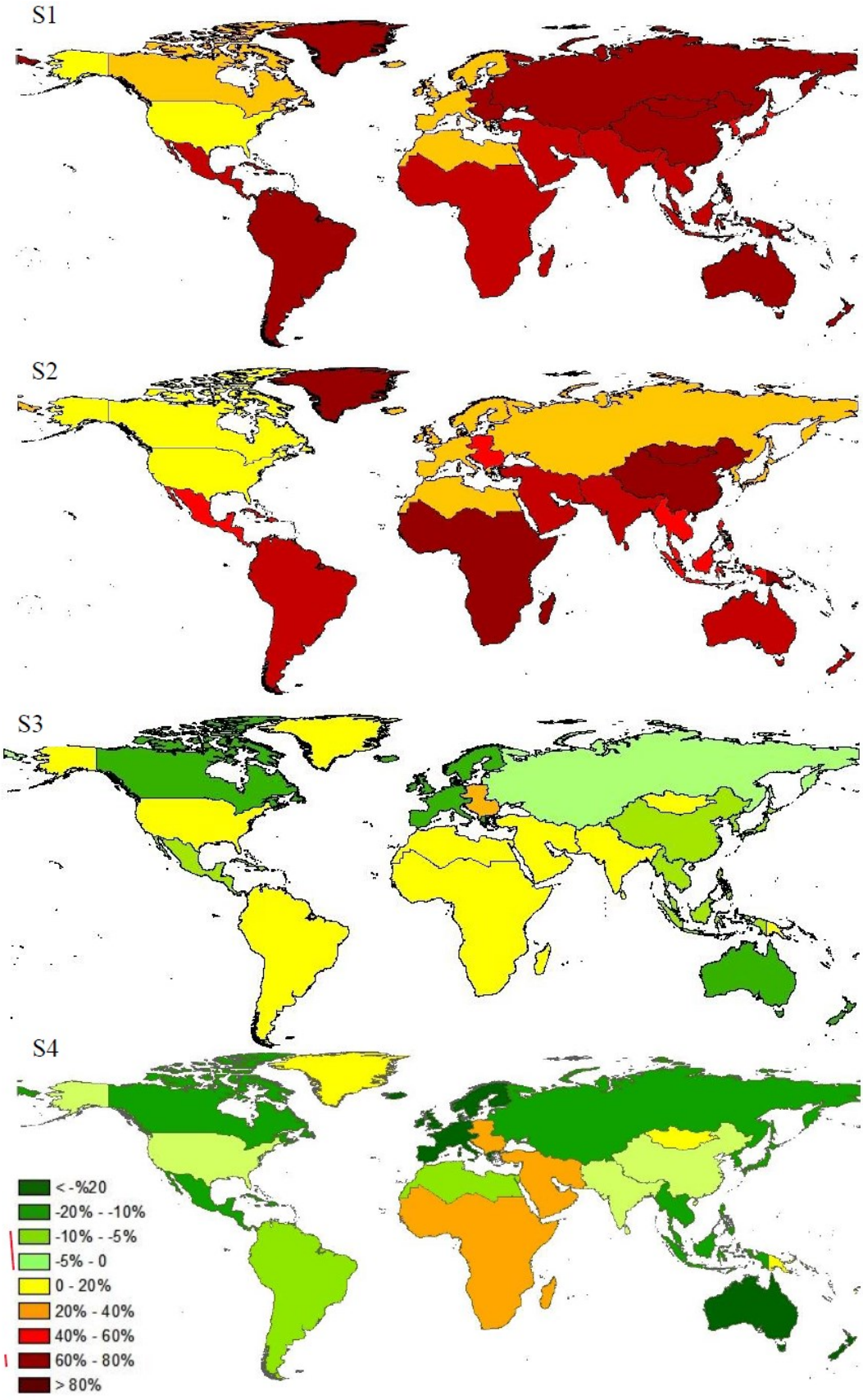

Fig. 6-10 Percentage change of the WF of consumption per capita relative to 2000 (Ercin et al., 2012)

Climate change effects are partially addressed in their study. They implicitly included the impact of climate change on production and trade patterns, but they excluded CO_2 fertilization effects in yields and climate change effects on crop water use. In addition, they assumed a homogeneous and single industrial sector in estimating the water footprint of industrial production and consumption. Their analysis shows that water footprints can radically change from one scenario to another and are very sensitive to the drivers of change, as shown in Table 6-4 and Fig. 6-10. Results show that the largest component of the total Water Footprint (WF) of consumption is green (67-81% per scenario), followed by grey (10- 20%) and blue (7-13%). Consumption of agricultural products has the largest share in the WF of consumption, namely 85-93% for all scenarios. The share of domestic water supply is 2-3% and of industrial products 4-13%.

A water footprint shows the extent of water use in relation to consumption by people. The water footprint of an individual, community or business is defined as the total volume of fresh water used to produce the goods and services consumed by the individual or community or produced by the business. Water use is measured in water volume consumed (evaporated) and/or polluted per unit of time. A water footprint can be calculated for any well-defined group of consumers (e.g., an individual, family, village, city, province, state or nation) or producers (e.g., a public organization, private enterprise or economic sector), for a single process (such as growing rice) or for any product or service (Wikipedia, 2021b).

For domestic water supply, or household water consumption in China (CHI), the four scenarios show variant percentage change of -12%, 16%, -29%, -19% in 2050 (Table 6-4). On average, household water consumption in 2050 will be decrased by 11% relative to 2000. With this rate, one can estimate that household water consumption in 2050 will be 0.20-0.32, 0.22-0.35 and 0.12-0.20 billion m^3 in Xi'an, Zhengzhou and Ji'nan with the base in 2000 being 0.28, 0.31 and 0.17 billion m^3 (Table 6-5).

Table 6-5 Household water consumption in 2050 in the four scenarios (billion m^3)

City	S1	S2	S3	S4
Xi'an	0.24	0.32	0.20	0.22
Zhengzhou	0.27	0.35	0.22	0.25
Ji'nan	0.15	0.20	0.12	0.14

6.2.2 Future water consumption by industry

Industrial water consumption can be calculated by using the formula (industrial GDP) * (water consumption per GDP). This section estimates future water consumption by industry by using published literatures where GDP and water consumption per GDP in 2030 and 2050 was forecasted or calculated.

As for future GDP, the Organization for Economic Co-operation and Development (OECD) is an international organisation that works to build better policies for better lives. Recently years OECD predicted GDP trend for all countries across over the world. GDP data in 2020, 2030 and 2050 in China are from OECD, as shown in Fig. 6-11 and Fig. 6-12.

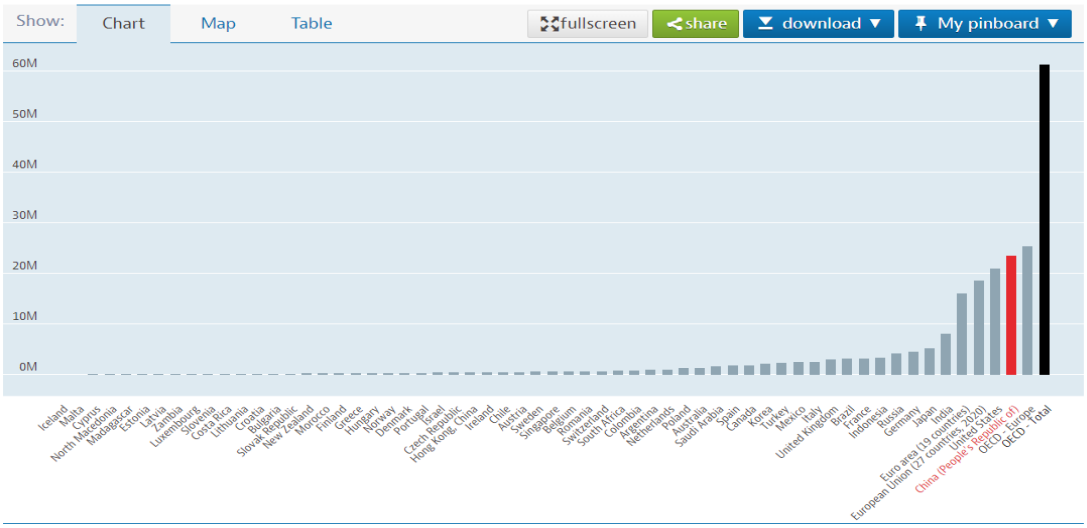

Fig. 6-11 Gross domestic product (GDP)Total, Million US dollars, 2020 or latest available Source: https://data.oecd.org/gdp/gross-domestic-product-gdp.htm#indicator-chart

Data in Fig. 6-11 shows that Chinese GDP is US$ 23 547 026 Million in 2020. Generally, GDP is the standard measure of the value added created through the production of goods and services in a country during a certain period. This indicator is based on nominal GDP (also called GDP at current prices or GDP in value) and is less suited for comparisons over time, as developments are not only caused by real growth, but also by changes in prices and PPPs (Purchasing Power Parities) (OECD, 2021). China Real GDP long-term forecast are shown in Fig. 6-12 where real GDP in 2030 and 2050 are acquired.

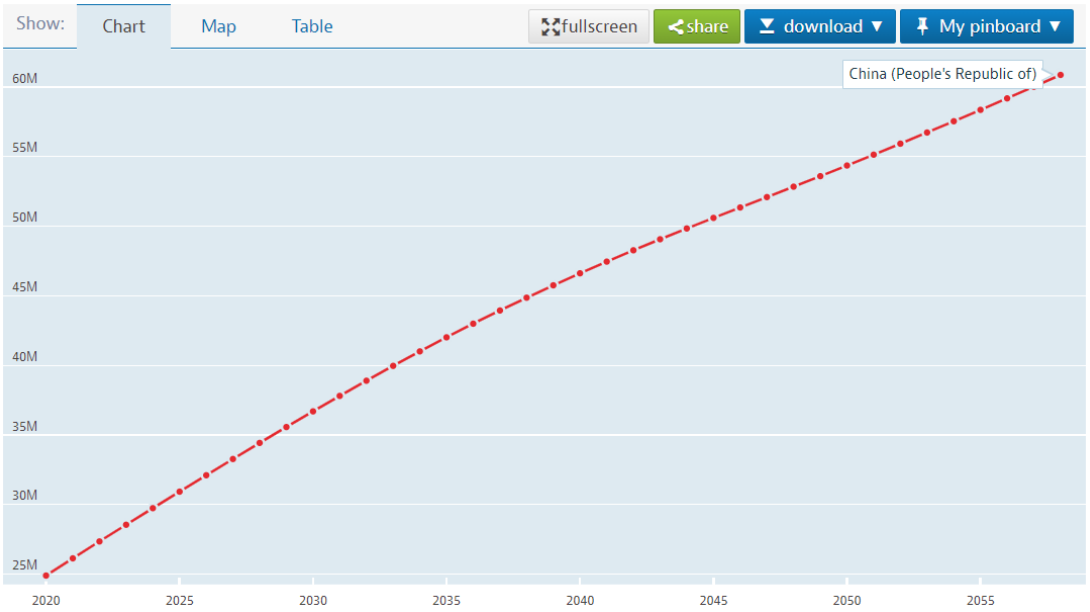

Fig. 6-12 China Real GDP long-term forecast Total, Million US dollars, 2020-2058. Source: https://data.oecd.org/gdp/real-gdp-long-term-forecast.htm#indicator-chart

As to OECD (2021), real GDP is GDP given in constant prices and refers to the volume level of GDP. Forecast in Fig. 6-12 is based on an assessment of the economic climate in individual countries and the world economy, using a combination of model-based analyses and expert judgement. This indicator is measured in growth rates compared to previous year. Trend

gross domestic product (GDP), including long-term baseline projections (up to 2060), in real terms. Forecast is based on an assessment of the economic climate in individual countries and the world economy, using a combination of model-based analyses and expert judgement. This indicator is measured in USD at constant prices and PPPs of 2010 (OECD, 2021). From data of Fig. 6-12, one can get real GDP in China: US$ 24896 for 2020, 36693 for 2030, and 54357 billion for 2050. In other words, GDP in 2030 and 2050 will be 1.47 and 2.18 times of that in 2020. With this rate, GDP in the three reprensentative cities of Xi'an, Zhengzhou and Ji'nan will be 1018.73, 2643.06 and 978.96 billion RMB in 2030, and will be 1510.76, 3919.64 and 1451.79 billion RMB in 2050.

Table 6-6 GDP in 2030 and 2050 in the three cities (billion RMB)

City	2020-base	2030	2050
Xi'an	693.01	1018.73	1510.76
Zhengzhou	1798.00	2643.06	3919.64
Ji'nan	665.96	978.96	1451.79

As to the water consumption in 2030, Meng et al. (2021) forecasted annual water consumption in 31 regions of China with future increase scenario of GDP which can be used in this study to estimate future water consumption per GDP. They estimated futute water consumption combined the economic development with the relevant data of regional GDP if the growth rates of regional GDP in the middle and lower reaches of the Yellow River, e.g., Henan, Shaanxi and Shandong, are all 5% and 10%, as shown in Table 6-7.

Table 6-7 water consumption under different GDP increase scenarios of 5% and 10% (From Meng et al., 2021) in billion m^3.

Region	GDP growth rate	2019	2020	2021	2022	2023	2024	2025	City name
Shaanxi	5%	9.12	9.21	9.3	9.38	9.47	9.56	9.65	Xi'an
	10%	9.15	9.3	9.46	9.63	9.83	10.04	10.27	
He'nan	5%	24.17	25.01	25.94	26.97	28.08	29.29	30.59	Zhengzhou
	10%	24.26	25.38	26.8	28.51	30.52	32.85	35.52	
Shandong	5%	21.21	21.17	21.13	21.08	21.04	21.01	20.97	Ji'nan
	10%	21.21	21.17	21.13	21.09	21.05	21.01	20.98	

Table 6-6 indicates that in 2030 GDP will increase by 47% of that in 2020. In other words, GDP in Xi'an, Zhengzhou and Ji'nan will increase in a rate of 4.7% every year which approximately equals to 5%. Based on Table 6-7, water consumption in 2030 under 5% GDP growth rate can be derived as 10.18, 35.70 and 20.68 billion m^3 in Shaanxi, He'nan and Shandong where Xi'an, Zhengzhou and Ji'nan locate. In other words, water consumption in 2030 under 5% GDP growth rate will be 1.10, 1.43 and 0.98 times of that in 2020 in three regions. Assuming Xi'an, Zhengzhou and Ji'nan have the same increase rate of industrial water consumption with their located region, industrial water consumption per GDP in 2030 should be 0.75, 0.97 and 0.66 times of that in 2020. Based on water consumption per GDP in Fig. 5-4, water consumption per GDP in 2030 can be estimated as 0.0017, 0.0008 and 0.0012 m^3/RMB.

Thus based on Table 6-6, industrial water consumption in 2030 should be 1.73, 2.11 and 1.17 billion m^3.

Likely, water consumption in 2050 should be calculated based on the scenario of 5% GDP growth rate since GDP in 2050 will be 2.18 times of that in 2020 or will have 3.9% increase rate per year. In the same way as in 2030, industrial water consumption per GDP in 2050 should be 0.59, 1.05 and 0.43 times of that in 2020. Based on water consumption per GDP in Fig. 5-4, water consumption per GDP in 2050 can be estimated as 0.0013, 0.00084 and 0.00077 m^3/RMB. Thus, based on Table 6-6, industrial water consumption in 2050 should be 1.96, 3.29 and 1.12 billion m^3.

6.2.3 Future water consumption by ecosystem

Future water consumpiton by ecosystem in Xi'an, Zhengzhou and Ji'nan in 2030 and 2050 was estimated by using the evaporation from soil and transpiration (ET) under three IPCC scenarios of RCP 2.6, RCP 4.5 and RCP 8.5. The monthly ET processes in 2030 and 2050 under the three IPCC scenarios are shown respectively in Fig. 6-13, Fig. 6-14 and Fig. 6-15.

Under IPCC scenarios RCP 2.6, the annal ecosystem water consumption (EWC) in three cities in 2030 is 2-15% higher than that in 2050. In other words, ecosystem will consume more water in 2030 than in 2050 in all the three representative cities. Under IPCC scenario RCP 4.5, annal EWCs in three cities in 2030 are 0.3-13% higher than those in 2050. Under IPCC scenario RCP 8.5, annal EWCs in the two cities in 2030 are 2-4% higher than those in 2050. Annal EWCs in Zhengzhou in 2030 are 1.4% lower than those in 2050, as shown in Table 6-8. In other words, ecosystem will consume more water in 2030 than in 2050 in Xi'an and Ji'nan but consume less water in Zhengzhou in 2030.

Table 6-8 Annual EWC under IPCC scenraios in 2030 and 2050 (billion m^3)

IPCC Scenario	City	2030	2050
RCP 2.6	Xi'an	15.45	15.19
	Zhengzhou	12.72	11.08
	Ji'nan	13.21	12.59
RCP 4.5	Xi'an	15.00	14.05
	Zhengzhou	11.87	10.47
	Ji'nan	12.15	12.11
RCP 8.5	Xi'an	14.78	14.25
	Zhengzhou	10.91	11.06
	Ji'nan	12.27	12.09

To summary, under IPCC scenarios of RCP 2.6, RCP 4.5 and RCP 8.5, ecosystem in most of the three cities will consume more water in 2030 than in 2050 in all the three representative cities. In 2030, ecosystem will consume water quantity ranging from 14.78-15.45, 10.91-12.72 and 12.15-13.21 billion m^3 respectivley in Xi'an, Zhengzhou and Ji'nan. In 2050, EWC will be 14.05-15.19, 10.47-11.08 and 12.09-12.59 billion m^3 respectively in the three cities. Abroadly, EWC in 2030 is slightly higher than in 2050. Compared EWC under the three scenarios (RCP

2.6, RCP 4.5 and RCP 8.5), future EWC under RCP 2.6 is the highest (15.32, 11.90 and 12.90 billion m^3 for Xi'an, Zhengzhou and Ji'nan) as that under RCP 8.5 is the lowest (14.52, 10.98 and 12.18 billion m^3).

All in all, total quantity of water consumed by household, industry and ecosystems in Xi'an, Zhengzhou and Ji'nan in 2030 will be 17.23, 14.31, 14.06 billion m^3 on average, and in 2050 will be 16.84, 14.35, 13.62 billion m^3 on average, as shown in Table 6-9.

Table 6-9 Water consumption in 2030 and 2050 (billion m3)

Water user	City	2030	2050
Household	Xi'an	0.37-0.40	0.20-0.32
	Zhengzhou	0.37-0.39	0.22-0.35
	Ji'nan	0.20-0.22	0.12-0.20
Industry	Xi'an	1.73	1.96
	Zhengzhou	2.11	3.29
	Ji'nan	1.17	1.12
Ecosystem	Xi'an	14.78-15.45	14.05-15.19
	Zhengzhou	10.91-12.72	10.47-11.08
	Ji'nan	12.15-13.21	12.09-12.59
Total	Xi'an	16.88-17.58	16.21-17.47
	Zhengzhou	13.39-15.22	13.98-14.72
	Ji'nan	13.52-14.60	13.33-13.91

According to data from "Water Resource Bulletin" (2002-2016) of Xi'an, Zhengzhou and Ji'nan, the average values of water consumption including that of household, industry, ecosystem and other are respectively 1.61-1.96, 0.70-2.02 and 1.01-1.83 billion m^3. The values are far less than what is predicted in 2030 and 2050. Among them, the maximal water consumption for household is 0.43, 0.57 and 0.42 billion m^3 respectively; and that for industry is 1.31, 1.53, 1.43 billion m^3; for ecosystem is 0.27, 0.51 and 0.25 billion m^3. Compared these data with those in Table 6-9, one can find that in future household water consumption decreases, and industrial one increases or changes little; but ecosystem water consumption in Table 6-9 is ~30-60 times of values from "Water Resource Bulletin" (2002-2016) the reason for that the latter takes account of only water quantity irrigating vegetation disregarding the ecosystem health stuatus. In fact, vegetation maintaining stable evapotranspiration suggest they are alive or maintain health to some extent. Evaporation from bare land or soil and transpiration from vegetation add up to total evapotranpiration used in this study. Though "Water Resource Bulletin" does not estimate or not fully considered the water quantity evapotranspirated by ecosystem, the ecosystem evaportranspiration does not stop. Therefore, the evapotranspirated water should be fully considered as it comes from the freshwater available or unavailable. The truth is freshwater available will decrease if freshwater unavailable is consumed greatly. In this sense, this study uses evaportranspiration to estimate ecosystem water consumption is feasible.

6.3 Future urban drought in the year 2030 and 2050

With predictions of freshwater available and water consumption in 2030 and 2050, one

can estimate urban drought in the three representative cities with the urban drought formula (the ratio of water consumption to water available). Following this, urban drought in 2030 and 2050 was estimated, as shown in Table 6-10, which shows that urban drought is the severest in Xi'an (greater than 8.0 on average) and less severe in Ji'nan (less than 6.0 on average) in both 2030 and 2050. Urban drought severity in 2030 is a little higher than in 2050. Using real ecosystem evapotranspiration as ecosystem water consumption in this study raises the urban drought ratio more than 6 times of that disregarding ecosystem evapotranspiration. If only consider water irrigating vegetation as ecosystem water consumption, the ratio in 2030 and 2050 will be ~1.2 which can be solved by adopting water-saving techniques along with diverting and transferring water from other water-abundant areas in southern, such as the Yangtze River.

Table 6-10 Urban drought in 2030 and 2050

City	2030	2050
Xi'an	8.27-8.75	7.57-8.52
Zhengzhou	6.87-7.81	7.13-7.55
Ji'nan	5.56-6.19	5.49-5.97

6.4 Summary

This chapter predicted urban drought in 2030 and 2050 via estimation of freshwater available and water consumption. ANN (Artificial Neural Network) prediting future freshwater available was set up by combining surface freshwater available estimated in Chapter 3 and environmental factors presented in CMIP5 IPCC scenarios: RCP 2.6, RCP 4.5 and RCP 8.5. Future water consumptionwas predicted based on models established in Chapter 5 and published literatures.

As for future freshwater available, Xi'an, Zhengzhou and Ji'nan will have 2.01-2.04, ~1.95 and 2.36-2.43 billion m^3 freshwater for consumption in 2030, and 2.05-2.14, 1.95-1.96 and 2.33-2.43 billion m^3 in 2050. In details, there will have up to 1.14, 0.91 and 2.03 billion m^3 surface freshwater, and 0.87-0.90, 1.04-1.06 and 0.33-0.40 billion m^3 underground freshwater for consumption in 2030, and 0.91-1.00, 1.04-1.05 and 0.30-0.40 billion m^3 in 2050 in the three cities. For the underground water (evaluated using LWE), Ji'nan has the greatest decrease rate. All the three RCPs predicted similar LWE decrase rate (~0.8 cm on average).

As to future water consumption in 2030 and 2050, total quantity of water consumed by household, industry and ecosystems in Xi'an, Zhengzhou and Ji'nan in 2030 will be 17.23, 14.31, 14.06 billion m^3 on average, and in 2050 will be 16.84, 14.35, 13.62 billion m^3 on average. Ecosystem water consumption (EWC) dominates the total water consumption (81-90% in 2030 and 75-91% in 2050). Under CMIP5 IPCC scenarios of RCP 2.6, RCP 4.5 and RCP 8.5, ecosystem in most of the three cities will consume more water in 2030 than in 2050 in all the three representative cities. In 2030, ecosystem will consume water quantity ranging from 14.78-15.45, 10.91-12.72 and 12.15-13.21 billion m^3 respectivley in Xi'an, Zhengzhou and Ji'nan, as in 2050, ecosystem will consume 14.05-15.19, 10.47-11.08 and 12.09-12.59 billion

m^3 Respectively. Future EWC under RCP 2.6 is the highest (15.32, 11.90 and 12.90 billion m^3 for Xi'an, Zhengzhou and Ji'nan) as that under RCP 8.5 is the lowest (14.52, 10.98 and 12.18 billion m^3). The ratios of household water consumption to total are the smallest, being 1.0-3.0% in 2030 and 1.0-2.0% in 2050.

The magnitude of the ratio of water consumption to freshwater available suggests the degree of urban drought. In both 2030 and 2050, urban drought is the severest in Xi'an (with the ratio greater than 8.0 on average) and less severe in Ji'nan (less than 6.0 on average). Urban drought severity in 2030 is a little higher than in 2050. Adaption of real ecosystem evapotranspiration as ecosystem water consumption raises the ratio up to ~6 times of that disregarding ecosystem evapotranspiration. In other words, if ecosystem evapotranspiration is not taken into account in estimation of total water consumption, the ratio of urban drought in 2030 and 2050 will be ~1.2 which can be easily solved by combing water-saving techniques and water diversion from water-abundant areas such as the Yangtze River.

Chapter 7 Conclusions and perspectives

Urban drought threats the welfare of human beings and the sustainability of the socio-economic development of cities. To reduce risks induced by urban drought, future risk of freshwater available and water consumption is urgently necessitated to be studied at urban scales. When assessing urban drought in previous researches many scholars took precipitation, soil moisture, evapotranspiration etc. as basis to calculate urban drought, yet less consideration is put on runoff concentration process (or streamflow) flowing by cities within a watershed. However, streamflow is significantly important for accurately estimate TWSC (terrestrial water storage change) –the most important partition for estimation of freshwater available. In addition, lack of long series of monitoring on freshwater available (streamflow and groundwater storage) hinders accurately predicting future freshwater available. Therefore, it is urgently necessitated to produce long series data of freshwater available to predict future urban drought with water consumption and freshwater availability. Therefore, this thesis developed a framework for the assessment and prediction of urban drought in the year 2030 and 2050. To begin with, surface freshwater available was estimated by developing two new method to retrieve streamflows via satellite imageries for dry and wet seasons; secondly, underground freshwater available was estimated via key driving factors identification and model prediction; finally, water consumption at urban scale was calculated and urban drought in 2030 and 2050 was analyzed. The study was conducted taking as the study area the Yellow River Basin, China, taking as examples big cities with population great than 5 million-- Jinan, Zhengzhou, Xi'an.

7.1 Main conclusions

(i) Two new methods for estimation of surface freshwater available (SFWA) in data-scarce areas were developed. The first one was named VHR-AMHG (Virtual Hydraulic Radius at-many-stations hydraulic geometry), and the second one was named transcaled spatial C/M method. The first one has a higher accuracy in dry season yet the second one is more accurate in wet season. The first one uses only river water width while the second one relies solely on the reflectance of soil and water to retrieve streamflow. Results showed that the relative error calculated from VHR-AMHG was 16.80%. Comparison of application in dry and wet seasons suggests that the VHR-AMHG method has a higher accuracy in dry season yet lower in wet season. Relative error from transcaled spatial C/M method is 19.00% for the whole year, 14.56% in flood seasons and 20.88% in non-flood seasons, suggesting the performance of the transcaled spatial C/M method has higher precision in flood seasons. Using the two methods coupled with NASA GLDAS runoff dataset, long-termed streamflow (1948-2018) for the three representative cities (Xi'an, Zhengzhou and Ji'nan) was estimated, laying foundation for SFWA prediction in future 2030 and 2050. Xi'an and Zhengzhou have almost the same averaged streamflow value (~1000 m^3/s) from 1948 to 2018, and Jinan has a lower averaged streamflow value (~600 m^3/s).

(ii) A new framework for estimating long series of underground freshwater available (UFWA) was developed. UFWAs in the three representative cities were estimated and their data series were extended from the last two decades to nearly 70 yrs long. Meanwhile, environmental factors driving the variation of underground water, where VIP method was used. From the scale

of the whole study area—the Yellow River basin, or in the Scenario 3, four factors inclusive of air temperature, precipitation, evapotranspiration, and transpiration are responsible for the variation of underground water variation; under Scenario 2, there produced 7 key driving factors ncluding glacier melt: air temperature, direct evaporation from bare soil, precipitation, soil moisture from 0 to 200 cm in depth, runoff, precipitation minus ET; for Scenario 3, there are 10 factors including transpiration, evapotranspiration, air temperature, root zone soil moisture, terrestrial water storage, soil moisture from 0 to 200 cm in depth, precipitation, direct evaporation from bare soil, glacier melt, runoff are of higher importance; for the Scenario 4, all the 11 environmental factors were selected. The selected factors in the four scenarios were then used to verify and improve an artificial neural prediction model –LSTM-N (Long short-term memory network) wherein the optimized LSTM-N parameters were determined. For the problem of GRACE TWSC prediction, the optimized parameter "Unit" is 460, activation function is "Sigmoid" function, training epoch is 650 for the LSTM-N. The LSTM-N with the optimized parameters was used to predict the variation of underground water variation in data-absent area and data-absent period (1948-2002). Comparison of prediction value with GRACE observation shows that, LSTM-N model in upper reach areas has the highest accuracy with a RMSE less than 0.1 cm, while in the middle reach it has a relatively lower accuracy with a RMSE less than 5.0 cm. With the Scenario-4-based LSTM-N model GRACE TWSC (or LWE) data series from 1948 to 2002 were predicted, based on which the underground freshwater avialble (FWA) from 1948 to 2016 was calculated: Xi'an has the highest average of 1.92 billion m^3 and Zhengzhou (orange line) has the lowest average of 0.46 billion m^3. All these results can well serve for the prediction of underground FWA in future 2030 and 2050.

(iii) Water consumption of household, industry and ecosystem was calculated by using the three newly-developed models. For the household water consumption, LandScan global population data was used to analyze the change in representative cities of Xi'an, Zhengzhou, and Jinan, and using local statistical data to verify them. Comparison of the three cities shows that Xi'an has the highest household water consumption (0.35 billion m^3 on average) while Ji'nan has the lowest one (0.21 billion m^3 on average). As to industrial water consumption, GDP (Gross Domestic Product) in the three cities continued increasing from 2003 to 2016 yet water use per GDP gradually decreasing from 0.010-0.018 m^3/RMB (or Chinese Yuan) to 0.001-0.004 m^3/RMB during the same period, results of which is fluctuation of industry water consumption (1.60 billion m^3 on average). For the ecosystem water consumption, MODIS derived ET (evapotranspiration) was used to rectify GLDAS modeled ET to make the latter able to represent the whole study area. Results show that, Zhengzhou has the lowest water consumption for ecosystem (average: 5.05 billion m^3) yet Xi'an has the highest value (average: 7.13 billion m^3). Larger size of Xi'an resulted in higher ecosystem water consumption and vice versa for Zhengzhou.

(iv) Drought situation of the three representative cities in 2030 and 2050 was predicted based on CMIP5 (Coupled Model Intercomparison Project Phase 5) scenarios. Generally, drought severity in 2030 for the three cities is a little higher than in 2050 among which, drought in Xi'an in 2030 is the most severe (with the ratio greater than 8.0 on average) in the three representative cities since it has the highest ecosystem water consumption yet relatively lower water supply in 2030. Freshwater available plus water consumption makes urban drought ratio. As for future

freshwater available, Xi'an, Zhengzhou and Ji'nan will have 2.01-2.04, ~1.95 and 2.36-2.43 billion m^3 freshwater for consumption in 2030, and 2.05-2.14, 1.95-1.96 and 2.33-2.43 billion m^3 in 2050. As to future water consumption in 2030 and 2050, total quantity of water consumed by household, industry and ecosystems in Xi'an, Zhengzhou and Ji'nan in 2030 will be 17.23, 14.31, 14.06 billion m^3 on average, and in 2050 will be 16.84, 14.35, 13.62 billion m^3 on average. Real ecosystem evapotranspiration being taken as ecosystem water consumption raises up the ratio. If it is not adopted, the ratio of urban drought in 2030 and 2050 will be ~1.2 which can be easily solved by combing water-saving techniques and water diversion from water-abundant areas such as the Yangtze River.

7.2 Perspectives

This study estimated surface and underground freshwater available by coupling NASA GLDAS dataset, GRACE satellite imageries, and TM / MODIS as well as Sentinel satellite imageries. Meanwhile two new methods were developed for streamflow retrieval; a framework was presented for estimation of underground freshwater available. When retrieving streamflow, the coarser spatial resolution of satellite imageries used in this study (spatial resolution ranging from 10 m to 30 m) reduced the accuracy of streamflow estimation. The reason is because for small rivers e.g. with water width less than 40 m, even an error of 10 m in river water width (25% error) plus much more error in water height could result in large bias in flow area and then larger in streamflow estimation. In future, more satellite imageries with higher spatial resolution and ground monitoring on streamflow corresponding to satellite-passby time should be introduced to improve the estimation precision, e.g., very high-resolution imageries such as Chinese Gaofen (spatial resolution: 1m) or Erupean Astrium Pleiades NEO (spatial resolution: 0.3 m) etc. Similarly, short-term series of GRACE monitored LWE (less than 200 months) limited training effect of LSTM-N model. In future, more LWE data other than GRACE monitoring should be collected to improve the model training effect. When extending the GRACE data series, only 11 environmental factors were considered, much more environmental factors should be considered to further improve prediction accuracy.

In addition, with drought seemingly more commonplace, entrepreneurs are using information on soil moisture from SMOS and data from other satellites to generate commercial data products for the insurance market, ultimately bringing benefits to farmers. But the omission of surface runoff in their estimation of drought makes the methods have difficulties in application into urban areas. In future, combining SMOS data and methods developed in this study to make SMOS estimated drought applicable to urban areas is a promising research field which will be of great help for urban development. Moreover, estimation of streamflow from SWOT water surface observations is difficult because of the correlated influence of flow controls on the observable water surface signatures, which may be solved when in situ depth/discharge data are available. Howerever, the fusion of Landsat/Sentinel-2 and CubeSats holds great promise for future hydrologic application, even with the advent of SWOT because the relatively low temporal/spatial resolutions (for Landsat and Sentinel-2) or low radiometric data quality (for Planet) limit the applications of these data sets used alone. Their fusioncan be an approach to enhance their ability to estimate discharge (Feng et al., 2019). In future, using the streamflow estimation methods in this study with the SWOT monitorings could be attempted to improve the accuracy of streamflow estimation by using SWOT.

Water consumption of household, industry and ecosystem at urban scale was estimated in this study. But only simple statistical method relying on statistical data were designed. Actually, in many areas across the world, statistical data were hard to collected. In future, the method should be improved to keep applicable in data-scarce regions. More important, all methods developed in this study should be applied to other regions than the Yellow River basin across the world, such as France and other European contries so as to make the methods be further tested and improved. what should be noticed is that uncertainties in CMIP5 dataset undoubtedly resulted in uncertainties in results of this project and in future in-depth analysis on CMIP5 dataset should be conducted to reduce the uncertainties in the current results.

References

Abu-Bakar, H., Williams, L., & Hallett, S. H. (2021). A review of household water demand management and consumption measurement. *Journal of Cleaner Production*, 292,1-19. doi:10.1016/j.jclepro.2021.125872

Allen, R. G., Pereira, L. S., Raes, D., & Smith, M. (1998). Crop evapotranspiration-Guidelines for computing crop water requirements-FAO Irrigation and drainage paper 56. Food and Agriculture Organization of the United, Rome, 300(9), D05109,PP50.

Amazirh, A., Er-Raki, S., Chehbouni, A., Rivalland, V., Diarra, A., Khabba, S., & Merlin, O. (2017). Modified Penman–Monteith equation for monitoring evapotranspiration of wheat crop: relationship between the surface resistance and remotely sensed stress index. *Biosystems Engineering*, 164,68-84.

Amitai, E., Llort, X., Sempere-torres, D. (2009). Comparison of TRMM radar rainfall estimates with NOAA next-generation QPE. *Journal of the Meteorological Society of Japan*, 87A,109-118.DOI:10.2151/jmsj.87a.109.

Andreadis, K. M., Clark, E. A., Lettenmaier, D. P., & Alsdorf, D. E. (2007). Prospects for river discharge and depth estimation through assimilation of swath-altimetry into a raster-based hydrodynamics model. *Geophysical Research Letters*, 34(10),1-5. doi:10.1029/2007gl029721

Ang, B. W. (2004). Decomposition analysis for policymaking in energy: which is the preferred method? *Energy Policy*, 32(9),1131-1139. doi:10.1016/s0301-4215(03)00076-4

Arbués, F., García-Valiñas, M., & Martínez-Espiñeira, R. Estimation of residential water demand: a state-of-the-art review. *The Journal of Socio-Economics*, 32(1),81-102.

Athanasiadis, A., Placido, D., Maas, S., Brown, B. A., Lowenhaupt, K., & Rich, A. (2005). The crystal structure of the Z beta domain of the RNA-editing enzyme ADAR1 reveals distinct conserved surfaces among Z-domains. *Journal of Molecular Biology*, 351(3), 496-507.

Ayiguli·Aikebaier, Shu, L., Lu, C., Zhang, G., & Li, W. (2015). Study on city gross industrial water consumption accounting method. *Water Resources Protection*, 31(3),108-111.

Baik, J., Zohaib, M., Kim, U., Aadil, M., & Choi, M. (2019). Agricultural drought assessment based on multiple soil moisture products. *Journal of Arid Environments*, 167,43-55. doi:10.1016/j.jaridenv.2019.04.007

Barthel, R., Janisch, S., Schwarz, N., Trifkovic, A., Nickel, D., Schulz, C., & Mauser, W. (2008). An integrated modelling framework for simulating regional-scale actor responses to global change in the water domain. *Environmental Modelling & Software*, 23(9),1095-1121. doi:10.1016/j.envsoft.2008.02.004

Basani, M., Isham, J., & Reilly, B. (2008). The determinants of water connection and water consumption: empirical evidence from a Cambodian household survey. *World*

Development, 36(5),953-968. doi:10.1016/j.worlddev.2007.04.021

Beck, R., Zhan, S., Liu, H., Tong, S., Yang, B., Xu, M., & Wang, S. (2016). Comparison of satellite reflectance algorithms for estimating chlorophyll-a in a temperate reservoir using coincident hyperspectral aircraft imagery and dense coincident surface observations. *Remote Sensing of Environment*, 178,15-30.

Bettadpur, S. (2007). CSR Level-2 processing standards document for product release 04. *Rep. GRACE* ,327-742.

Bhaduri, B., Bright, E., Coleman, P., & Dobson, J. (2002). LandScan. *Geoinformatics*, 5(2), 34-37.

Biancamaria, S., Lettenmaier, D. P., & Pavelsky, T. M. (2016). The SWOT mission and its capabilities for land hydrology. *Surveys in Geophysics*, 37(2),307-337. doi:10.1007/s10712-015-9346-y

Birkinshaw, S. J., Bathurst, J. C., & Robinson, M. (2014). 45 years of non-stationary hydrology over a forest plantation growth cycle, Coalburn catchment, Northern England. *Journal of Hydrology*, 519,559-573. doi:10.1016/j.jhydrol.2014.07.050

Bjerklie, D. M., Birkett, C. M., Jones, J. W., Carabajal, C., Rover, J. A., Fulton, J. W., & Garambois, P.-A. (2018). Satellite remote sensing estimation of river discharge: application to the Yukon River Alaska. *Journal of Hydrology*, 561,1000-1018. doi:10.1016/j.jhydrol.2018.04.005

Bonnema, M. G., Sikder, S., Hossain, F., Durand, M., Gleason, C. J., & Bjerklie, D. M. (2016). Benchmarking wide swath altimetry-based river discharge estimation algorithms for the Ganges river system. *Water Resources Research*, 52(4),2439-2461. doi:10.1002/2015wr017296

Brakenridge, G. R., Nghiem, S. V., Anderson, E., & Chien, S. (2005). Space-based measurement of river runoff. *Eos, Transactions American Geophysical Union*, 86(19), 185-188.

Brakenridge, G. R., Nghiem, S. V., Anderson, E., & Mic, R. (2007). Orbital microwave measurement of river discharge and ice status. *Water Resources Research*, 43(4),1-16.

Brakenridge, R., & Anderson, E. (2006). MODIS-based flood detection, mapping and measurement: the potential for operational hydrological applications. In Transboundary floods: reducing risks through flood management (pp. 1-12): *Springer*.

Broomhead, D. S. , & Lowe, D. . (1988). Multivariable functional. interpolation and adaptative networks. *Complex Systems*, 2, 321-355.

Bryant, E. A., Young, R. W., Price, D. M., & Short, S. A. (1992). Evidence for pleistocene and holocene raised marine deposits, Sandon Point, New South Wales. *Australian Journal of Earth Sciences*, 39(4), 481-493. doi:10.1080/08120099208728040

Bureau of Economic Analysis (BEA) (2006). What is Industry Value Added?. *https://www.bea.gov/help/faq/184*

Cai, X. M., & Rosegrant, M. W. (2004). Optional water development strategies for the Yellow River basin: balancing agricultural and ecological water demands. *Water Resources Research*, 40(8),1-11. doi:10.1029/2003wr002488

Canton, H. (2021). Organisation for Economic Co-Operation and Development—OECD. In The Europa Directory of International Organizations 2021 (pp. 677-687). Routledge.

Cao, Y., Nan, Z., & Cheng, G.(2015). GRACE gravity satellite observations of terrestrial water storage changes for drought characterization in the arid land of northwestern China. *Remote Sensing*, 7(1),1021-1047, 10.3390/rs70101021

Chang, X.D., Xu, Z.X. et al. (2017). Spatiotemporal variations in precipitation in Ji'nan, China. *Journal of Beijing Normal University*, 53(05),567-574.

Chen, J. L., Famiglietti, J. S., Scanlon, B. R., & Rodell, M. (2016). Groundwater storage changes: present status from GRACE observations. *Surveys in Geophysics,* 37(2), 397-417. doi:10.1007/s10712-015-9332-4

Chen, J. L., Wilson, C. R., Blankenship, D., & Tapley, B. D. (2009). Accelerated Antarctic ice loss from satellite gravity measurements. *Nature Geoscience*, 2(12),859-862. doi:10.1038/ngeo694

Chen, J., Wilson, C., Ries, J., & Tapley, B. (2013). Rapid ice melting drives Earth's pole to the east. *Geophysical Research Letters*, 40(11), 2625-2630.

Chen, Y., Hao, X., Li, W., Chen, Y., Ye, Z., & Zhao, R. (2008). An analysis of the ecological security and ecological water requirements in the inland river of arid region. *Advances in Earth Science*, 23(7), 732-738.

Chen, Z. M., Chen, G. Q., Zhou, J. B., Jiang, M. M., & Chen, B. (2010). Ecological input-output modeling for embodied resources and emissions in Chinese economy 2005. *Communications in Nonlinear Science and Numerical Simulation*, 15(7), 1942-1965. doi:10.1016/j.cnsns.2009.08.001

Chen, Z., Jiang, W., Wu, J., Chen, K., Deng, Y., Jia, K., & Mo, X. (2017). Detection of the spatial patterns of water storage variation over China in recent 70 years. *Scientific Reports*, 7(1), 1-9.

Chi, D., Wang, H., Li, X., Liu, H., & Li, X. (2018). Estimation of the ecological water requirement for natural vegetation in the Ergune River basin in Northeastern China from 2001 to 2014. *Ecological Indicators*, 92,141-150. doi:10.1016/j.ecolind.2017.04.014

Chu, J., Wang, C., Chen, J., & Wang, H. (2009). Agent-Based residential water use behavior simulation and policy implications: a case-study in Beijing City. *Water Resources Management*, 23(15), 3267-3295. doi:10.1007/s11269-009-9433-2

Clarke, G. P., Kashti, A., McDonald, A., & Williamson, P. (1997). Estimating small area demand for water: a new methodology. *Journal of the Chartered Institution of Water and Environmental Management*, 11(3), 186-192.

Cole, G., & Stewart, R. A. (2013). Smart meter enabled disaggregation of urban peak water demand: precursor to effective urban water planning. *Urban Water Journal,* 10(3), 174-194. doi:10.1080/1573062x.2012.716446

Costa, J. E., Cheng, R. T., Haeni, F. P., Melcher, N., Spicer, K. R., Hayes, E., Barrick, D. (2006). Use of radars to monitor stream discharge by noncontact methods. *Water Resources Research*, 42(7),1-14. doi:10.1029/2005wr004430

Costa, J. E., Spicer, K. R., Cheng, R. T., Haeni, P. F., Melcher, N. B., Thurman, E. M., Keller, W. C. (2000). Measuring stream discharge by non-contact methods: a proof-of-concept experiment. *Geophysical Research Letters*, 27(4), 553-556. doi:10.1029/1999gl006087

Dingman, S. L. (2007). Analytical derivation of at-a-station hydraulic–geometry relations. *Journal of Hydrology*, 334(1-2), 17-27.

Dobson, J. E., Bright, E. A., Coleman, P. R., Durfee, R. C., & Worley, B. A. (2000). LandScan: a global population database for estimating populations at risk. *Photogrammetric engineering and remote sensing*, 66(7), 849-857.

Dobson, J., Bright, E., Coleman, P., & Bhaduri, B. (2003). LandScan: a global population database for estimating populations at risk. *In Remotely Sensed Cities* (V., pp. 267-281). London: Taylor & Francis.

Döll, P., Mueller Schmied, H., Schuh, C., Portmann, F. T., & Eicker, A. (2014). Global-scale assessment of groundwater depletion and related groundwater abstractions: combining hydrological modeling with information from well observations and GRACE satellites. *Water Resources Research*, 50(7), 5698-5720.

Donchyts, G., Baart, F., Winsemius, H., Gorelick, N., Kwadijk, J., & Van De Giesen, N. (2016). Earth's surface water change over the past 30 years. *Nature Climate Change*, 6(9), 810-813.

Durand, M., Gleason, C. J., Garambois, P. A., Bjerklie, D., Smith, L. C., Roux, H., Vilmin, L. (2016). An intercomparison of remote sensing river discharge estimation algorithms from measurements of river height, width, and slope. *Water Resources Research*, 52(6), 4527-4549. doi:10.1002/2015wr018434

Ercin, A. E., Aldaya, M. M., & Hoekstra, A. Y. (2012). The water footprint of soy milk and soy burger and equivalent animal products. *Ecological Indicators,* 18,392-402. doi:10.1016/j.ecolind.2011.12.009

Ezquerro, P., Guardiola-Albert, C., Herrera, G., Antonio Fernandez-Merodo, J., Bejar-Pizarro, M., & Boni, R. (2017). Groundwater and subsidence modeling combining geological and multi-satellite SAR data over the Alto Guadalentin Aquifer (SE Spain). *Geofluids*,1-17. doi:10.1155/2017/1359325

Fan, Q. (2017). Landscape pattern evolution and habitat suitability evaluation of the Yellow River basin. *Dissertation of Ludong University*.PP83

Feng, D., Gleason, C. J., Yang, X., & Pavelsky, T. M. (2019). Comparing discharge estimates

made via the BAM algorithm in high-order Arctic rivers derived solely from optical CubeSat, Landsat, and Sentinel-2 data. *Water Resources Research*, 55(9), 7753-7771.

Feng, M., Sexton, J. O., Channan, S., & Townshend, J. R. (2016). A global, high-resolution (30-m) inland water body dataset for 2000: first results of a topographic–spectral classification algorithm. *International Journal of Digital Earth*, 9(2), 113-133.

Feng, X., Fu, B., Piao, S., Wang, S., Ciais, P., Zeng, Z., Wu, B. (2016). Revegetation in China's Loess Plateau is approaching sustainable water resource limits. *Nature Climate Change*, 6(11), 1019-1022. doi:10.1038/nclimate3092

Fisher, C. K., Pan, M., & Wood, E. F. (2020). Spatiotemporal assimilation–interpolation of discharge records through inverse streamflow routing. *Hydrology and Earth System Sciences*, 24(1), 293-305.

Florczyk A.J., Corbane C., Ehrlich D., Freire S., Kemper T., Maffenini L., Melchiorri M., Pesaresi M., Politis P., Schiavina M., Sabo F., Zanchetta L.(2019), GHSL data package 2019, EUR 29788 EN, Publications Office of the European Union, Luxembourg, 2019, ISBN 978-92-76-13186-1, doi:10.2760/290498, JRC 117104

Flörke, M., Kynast, E., Bärlund, I., Eisner, S., Wimmer, F., & Alcamo, J. (2013). Domestic and industrial water uses of the past 60 years as a mirror of socio-economic development: a global simulation study. *Global Environmental Change*, 23(1), 144-156.

Friedl, M., Pernicka, M., & Steininger, H. (2010). The phase 1 upgrade of the CMS Pixel Front-End Driver. *Journal of Instrumentation*, 5(12),1-6. doi:10.1088/1748-0221/5/12/c12054

Fu, G. B., Chen, S. L., Liu, C. M., & Shepard, D. (2004). Hydro-climatic trends of the Yellow River basin for the last 50 years. *Climatic Change*, 65(1-2), 149-178. doi:10.1023/B:CLIM.0000037491.95395.bb

Galan, J. M., Lopez-Paredes, A., & del Olmo, R. (2009). An agent-based model for domestic water management in Valladolid metropolitan area. *Water Resources Research*, 45(5),1-17. doi:10.1029/2007wr006536

Gao, D. W., & Sun, X. R. (2000). A shunt active power filter with control method based on neural network. Paper presented at the International Conference on Power System Technology (POWERCON 2000), Univ Western Australia, Perth, Australia.

Gao, H. F., Bai, J. H., Deng, X. Y., Lu, Q. Q., & Ye, X. F. (2018). Short-term effects of tidal flooding on soil nitrogen mineralization in a Chinese tidal salt marsh. *Physics and Chemistry of the Earth*, 103, 3-10. doi:10.1016/j.pce.2017.04.002

Getirana, A. C. V., & Peters-Lidard, C. (2013). Estimating water discharge from large radar altimetry datasets. *Hydrology and Earth System Sciences*, 17(3), 923-933. doi:10.5194/hess-17-923-2013

Giurco, D., Carrard, N. R., McFallan, S., Nalbantoglu, M., Inman, M., Thornton, N. L., & White, S. (2008). Residential end-use measurement guidebook: a guide to study design,

Sampling and Technology.

Gleason, C. J., & Smith, L. C. (2014). Toward global mapping of river discharge using satellite images and at-many-stations hydraulic geometry. *Proceedings of the National Academy of Sciences of the United States of America*, 111(13),4788-4791. doi:10.1073/pnas.1317606111

Gleason, C. J., & Wang, J. (2015). Theoretical basis for at-many-stations hydraulic geometry. *Geophysical Research Letters*, 42(17), 7107-7114. doi:10.1002/2015gl064935

Gleason, C. J., Smith, L. C., & Lee, J. (2014). Retrieval of river discharge solely from satellite imagery and at-many-stations hydraulic geometry: sensitivity to river form and optimization parameters. *Water Resources Research*, 50(12), 9604-9619. doi:10.1002/2014wr016109

Gleason, C. J., Wada, Y., & Wang, J. (2018). A Hybrid of optical remote sensing and hydrological modeling improves water balance estimation. *Journal of Advances in Modeling Earth Systems*, 10(1), 2-17. doi:10.1002/2017ms000986

Gosling, S. N., & Arnell, N. W. (2011). Simulating current global river runoff with a global hydrological model: model revisions, validation, and sensitivity analysis. *Hydrological Processes*, 25(7), 1129-1145. doi:10.1002/hyp.7727

Government Gazette.(2010). Declaration of the Pollution Control Department-Design Criteria for Wastewater Collection System and Community Wastewater Treatment System.(Vol. 127) .Thailand.

Guerreiro, S. B., Dawson, R. J., Kilsby, C., Lewis, E., & Ford, A. (2018). Future heat-waves, droughts and floods in 571 European cities. *Environmental Research Letters*, 13(3),1-10. doi:10.1088/1748-9326/aaaad3

Guo, J.L.,Ding,G.Y,Yang,X,Tang,Y.Z,Zhang,H.R,Pang,R.W.Dai.L,Q. (2021). Comparison of temporal and spatial accuracy of precipitation products from multi-source satellites in the Yangtze River basin. *South-to-North Water Transfers and Water Science & Technology*. (11), 1-17.

Guo, Y., Huang, S., Huang, Q., Wang, H., Fang, W., Yang, Y., & Wang, L. (2019). Assessing socioeconomic drought based on an improved Multivariate Standardized Reliability and Resilience Index. *Journal of Hydrology*, 568, 904-918. doi:10.1016/j.jhydrol.2018.11.055

Guo, Y., Huang, S., Huang, Q., Wang, H., Wang, L., & Fang, W. (2019). Copulas-based bivariate socioeconomic drought dynamic risk assessment in a changing environment. *Journal of Hydrology,* 575, 1052-1064. doi:10.1016/j.jhydrol.2019.06.010

Guo, Y., Li, S., Liu, R., & Zhang, J. (2021). Relationship between landscape pattern and water quality of the multi-scale effects in the Yellow River Basin. *Journal of Lake Sciences*, 33(3), 737-748.

Han, L.Y., Zhang, Q., Ma, P. L., Wang, Y. H., Huang, T., Jia, J. Y., Bai, B. (2021) Characteristics

of drought disasters risk in the Yellow River Basin Under the climate warming. *Journal of Desert Research*, 41(04), 225-234.

He, T., Liang, S. L., Wang, D. D., Cao, Y. F., Gao, F., Yu, Y. Y., & Feng, M. (2018). Evaluating land surface albedo estimation from Landsat MSS, TM, ETM plus, and OLI data based on the unified direct estimation approach. *Remote Sensing of Environment*, 204, 181-196. doi:10.1016/j.rse.2017.10.031

Hernandez, E. A., & Uddameri, V. (2014). Standardized precipitation evaporation index (SPEI)-based drought assessment in semi-arid south Texas. *Environmental Earth Sciences*, 71(6), 2491-2501.

Hiroko, B., Rodell, M., & Huang, J. (2016). GLDAS Noah Land Surface Model L4 Monthly 0.25 x 0.25 Degree V2.1.

Hirpa, F. A., Hopson, T. M., De Groeve, T., Brakenridge, G. R., Gebremichael, M., & Restrepo, P. J. (2013). Upstream satellite remote sensing for river discharge forecasting: Application to major rivers in South Asia. *Remote Sensing of Environment*, 131, 140-151. doi:10.1016/j.rse.2012.11.013

Hobbins, M. T., Wood, A., McEvoy, D. J., Huntington, J. L., Morton, C., Anderson, M., & Hain, C. (2016). The Evaporative Demand Drought Index. Part I: linking drought evolution to variations in Evaporative demand. *Journal of Hydrometeorology*, 17(6), 1745-1761. doi:10.1175/jhm-d-15-0121.1

Hochreiter, S., & Schmidhuber, J. (1997). Long short-term memory. *Neural Computation*, 9(8), 1735-1780. doi:10.1162/neco.1997.9.8.1735

Hoffert M I, Miller G. (1986). Missile Defense: cost of Space-Based Laser. *Science*, 234(4780), 1057-1060. doi:10.1126/science.234.4780.1056-a

Houborg, R., Rodell, M., Lawrimore, J., Li, B., Reichle, R., Heim, R., ... & Zaitchik, B. F. (2010, July). Using enhanced GRACE water storage data to improve drought detection by the US and North American Drought Monitors. In 2010 IEEE International Geoscience and Remote Sensing Symposium (pp. 710-713). IEEE.

Hu, W., Tian, J., & Chen, L. (2021). Assessment of sustainable water stewardship and synergistic environmental benefits in Chinese industrial parks. *Resources Conservation and Recycling*, 170,1-12. doi:10.1016/j.resconrec.2021.105589

Huang, C., Chen, Y., Zhang, S., & Wu, J. (2018). Detecting, extracting, and monitoring surface water from space using optical sensors: a review. *Reviews of Geophysics*, 56(2), 333-360.

Huang, S., Huang, Q., Chang, J., Zhu, Y., Leng, G., & Xing, L. (2015). Drought structure based on a nonparametric multivariate standardized drought index across the Yellow River basin, China. *Journal of Hydrology*, 530, 127-136. doi:10.1016/j.jhydrol.2015.09.042

Huang, S., Huang, Q., Leng, G., & Liu, S. (2016). A nonparametric multivariate standardized drought index for characterizing socioeconomic drought: a case study in the Heihe

River Basin. *Journal of Hydrology*, 542, 875-883. doi:10.1016/j.jhydrol.2016.09.059

Huete, A. (2016). ECOLOGY Vegetation's responses to climate variability. *Nature*, 531(7593), 181-182. doi:10.1038/nature17301

Jensen, J. R. (1986). Introductory digital image processing: a remote sensing perspective. Univ. of South Carolina, Columbus,65-65. doi: 10.1080/10106048709354084

Jiang, L., Jiapaer, G., Bao, A., Guo, H., & Ndayisaba, F. (2017). Vegetation dynamics and responses to climate change and human activities in Central Asia. *Science of the Total Environment*, 599, 967-980. doi:10.1016/j.scitotenv.2017.05.012

Jiang, S. H., Ren, L. L., Yong, B., Yang, X. L., & Shi, L. (2010). Evaluation of high-resolution satellite precipitation products with surface rain gauge observations from Laohahe basin in northern China. *Water Science and Engineering*, 3(4),405-417. DOI:10.3882/j.issn.1674-2370.2010.04.004.

Jung, H. C., Hamski, J., Durand, M., Alsdorf, D., Hossain, F., Lee, H., Hoque, A. K. M. Z. (2010). Characterization of complex fluvial systems using remote sensing of spatial and temporal water level variations in the Amazon, Congo, and Brahmaputra Rivers. *Earth Surface Processes and Landforms*, 35(3), 294-304. doi:10.1002/esp.1914

Kaewmai, R., Grant, T., Eady, S., Mungkalasiri, J., & Musikavong, C. (2019). Improving regional water scarcity footprint characterization factors of an available water remaining (AWARE) method. *Science of the Total Environment*, 681, 444-455. doi:10.1016/j.scitotenv.2019.05.013

Khan, M. S., Liaqat, U. W., Baik, J., & Choi, M. (2018). Stand-alone uncertainty characterization of GLEAM, GLDAS and MOD16 evapotranspiration products using an extended triple collocation approach. *Agricultural and Forest Meteorology*, 252, 256-268. doi:10.1016/j.agrformet.2018.01.022

Kim, D., & Rhee, J. (2016). A drought index based on actual evapotranspiration from the Bouchet hypothesis. *Geophysical Research Letters*, 43(19), 10277-10285. doi:10.1002/2016gl070302

Kim, D., Lee, H., Jung, H. C., Hwang, E., Hossain, F., Bonnema, M., Getirana, A. (2020). Monitoring river basin development and variation in water resources in transboundary Imjin River in North and South Korea using remote sensing. *Remote Sensing*, 12(1),1-19. doi:10.3390/rs12010195

Knyazikhin, Martonchik, JV, Myneni, RB, Diner, SW. (1998). Synergistic algorithm for estimating vegetation canopy leaf area index and fraction of absorbed photosynthetically active radiation from MODIS and MISR data. *Journal of Geophysical Research: Atmospheres*, 1998, 103(D24), 32257-32275. doi: 10.1029/98JD02462

Knyazikhin, Y., Glassy, J., Privette, J. L., Tian, Y., & Running, S. W. (1999). MODIS Leaf Area Index (LAI) and Fraction of Photosynthetically Active Radiation absorbed by vegetation (FPAR) product (MOD15) algorithm theoretical basis document.

http://eospso. gsfc. nasa. gov/atbd/modistabls. heml, 1999.

Kong, L., Zhang, L., & Lv, J. (2014). Accurate prediction of protein structural classes by incorporating predicted secondary structure information into the general form of Chou's pseudo amino acid composition. *Journal of Theoretical Biology*, 344, 12-18.

Kun, D. (2008). Remote sensing image classification based on multi-source data. *Northwest Agriculture and Forestry University in Shanxi Province*.

Lee, L. C., Liong, C.-Y., & Jemain, A. A. (2018). Partial least squares-discriminant analysis (PLS-DA) for classification of high-dimensional (HD) data: a review of contemporary practice strategies and knowledge gaps. *Analyst*, 143(15), 3526-3539.

LeFavour, G., & Alsdorf, D. (2005). Water slope and discharge in the Amazon River estimated using the shuttle radar topography mission digital elevation model. *Geophysical Research Letters*, 32(17),1-5. doi:10.1029/2005gl023836

Leopold, L. B., & Maddock, T. (1953). The hydraulic geometry of stream channels and some physiographic implications (Vol. 252): US Government Printing Office.

Li, C.M. and Xu, X. (2015). Advices for the establishment of new cities in China from the viewpoint of Zhengzhou New Economic Zone. *Social Observation*, 20,50-51.

Li, H., Li, H., Wang, J., & Hao, X. (2019). Extending the ability of near-infrared images to monitor small river discharge on the northeastern Tibetan Plateau. *Water Resources Research*, 55(11), 8404-8421.

Li, X. H., Feng, G., Zhao, C. Y., & Shi, F. Z. (2016). Characteristics of soil infiltration in the Tarim River floodplain. *Environmental Earth Sciences*, 75(9), 1-7. doi:10.1007/s12665-016-5573-x

Li, X. M. (1988). Relations of the vegetation distribution to heat and water in Xinjiang. *Arid Zone Research*, 5, 41-46.

Li, X., Liu, S., Ma, M., Xiao, Q., Liu, Q., Jin, R., Wang, S. (2012). HiWATER:an Integrated Remote Sensing Experiment on Hydrological and Ecological Processes in the Heihe River Basin. *Advance in Earth Sciences*, 27(5), 481-498.

Liang, S., Fang, H., Chen, M., Shuey, C. J., Walthall, C., Daughtry, C., Strahler, A. (2002). Validating MODIS land surface reflectance and albedo products: methods and preliminary results. *Remote Sensing of Environment*, 83(1-2), 149-162.

Lin, M., Biswas, A., & Bennett, E. M. (2019). Spatio-temporal dynamics of groundwater storage changes in the Yellow River Basin. *Journal of Environmental Management*, 235, 84-95.

Ling, H., Guo, B., Xu, H., & Fu, J. (2014). Configuration of water resources for a typical river basin in an arid region of China based on the ecological water requirements (EWRs) of desert riparian vegetation. *Global and Planetary Change*, 122, 292-304. doi:10.1016/j.gloplacha.2014.09.008

Liu, H., Lu, N., Jiang, H., Qin, J., & Yao, L. (2020). Filling gaps of monthly Terra/MODIS daytime land surface temperature using discrete cosine transform method. *Remote Sensing*, 12(3),1-16. doi:10.3390/rs12030361

Lu, S., Pei, L., & Bai, X. (2015). Study on method of domestic wastewater treatment through new-type multi-layer artificial wetland. *International Journal of Hydrogen Energy*, 40(34), 11207-11214.

Lu, S., Wu, B., Yan, N., Li, F., Wen, M., & Wang, J. (2010). Progress in river runoff monitoring by remote sensing. *Advance in Earth Sciences*, 25(8), 820-826.

Lv, C. H. (1998). Characteristics of drought and flooding hazards in the reaches of Yellow River. *Journal of Arid Land Resources and Environment*, (01), 2-7.

Lv, M., Ma, Z., & Yuan, N. (2021). Attributing terrestrial water storage variations across China to changes in groundwater and human water use. *Journal of Hydrometeorology*, 22(1), 3-21.

Lv, M., Ma, Z., Chen, L., & Peng, S. (2019). Evapotranspiration reconstruction based on land surface models and observed water budget components while considering irrigation. *Journal of Hydrometeorology*, 20(11), 2163-2183.

Lv, M., Ma, Z., Li, M., & Zheng, Z. (2019). Quantitative analysis of terrestrial water storage changes under the grain for green program in the Yellow River basin. *Journal of Geophysical Research-Atmospheres*, 124(3), 1336-1351. doi:10.1029/2018jd029113

Lv, M., Ma, Z., Yuan, X., Lv, M., Li, M., & Zheng, Z. (2017). Water budget closure based on GRACE measurements and reconstructed evapotranspiration using GLDAS and water use data for two large densely-populated mid-latitude basins. *Journal of Hydrology*, 547, 585-599.

Marks, A. B. (2019). (Carbon) Farming our way out of climate change. *Denver Law Review* , 97, 497-556.PP60

Massonnet, D., Rossi, M., Carmona, C., Adragna, F., Peltzer, G., Feigl, K., & Rabaute, T. (1993). The displacement field of the landers earthquake mapped by radar interferometry. *Nature*, 364(6433), 138-142. doi:10.1038/364138a0

Mastini, R., Kallis, G., & Hickel, J. (2021). A green new deal without growth?. *Ecological Economics*, 179,1-9, 106832.

McKee, W. H., & McKevlin, M. R. (1993). Geochemical processes and nutrient-uptake by plants in hydric soils. *Environmental Toxicology and Chemistry*, 12(12), 2197-2207.

Mehran, A., AghaKouchak, A., Nakhjiri, N., Stewardson, M. J., Peel, M. C., Phillips, T. J., Ravalico, J. K. (2017). Compounding impacts of human-induced water stress and climate change on water availability. *Scientific Reports*, 7(1), 1-9.

Mehran, A., Mazdiyasni, O., & AghaKouchak, A. (2015). A hybrid framework for assessing socioeconomic drought: linking climate variability, local resilience, and demand. *Journal of Geophysical Research-Atmospheres*, 120(15), 7520-7533.

doi:10.1002/2015jd023147

Memon, F. A., & Butler, D. (2006). Water consumption trends and demand forecasting techniques.Published by IWA Publishing. ISBN:1843390787

Meng, X., Tu, L., Yan, C., & Wu, L. (2021). Forecast of annual water consumption in 31 regions of China considering GDP and population. *Sustainable Production and Consumption*, 27, 713-736. doi:10.1016/j.spc.2021.01.036

Mohan, G., Chapagain, S. K., Fukushi, K., Papong, S., Sudarma, I. M., Rimba, A. B., & Osawa, T. (2021). An extended Input-Output framework for evaluating industrial sectors and provincial-level water consumption in Indonesia. *Water Resources and Industry*, 25,1-20. doi:10.1016/j.wri.2021.100141

Mück, M., Klotz, M., & Taubenböck, H. (2017). Validation of the DLR global urban footprint in rural areas: a case study for Burkina Faso. Paper presented at the 2017 Joint Urban Remote Sensing Event (JURSE),1-4.

Myneni, R. B., Keeling, C. D., Tucker, C. J., Asrar, G., & Nemani, R. R. (1997). Increased plant growth in the northern high latitudes from 1981 to 1991. *Nature*, 386(6626), 698-702. doi:10.1038/386698a0

Narasimhan, B., & Srinivasan, R. (2005). Development and evaluation of Soil Moisture Deficit Index (SMDI) and Evapotranspiration Deficit Index (ETDI) for agricultural drought monitoring. *Agricultural and Forest Meteorology*, 133(1-4), 69-88. doi:10.1016/j.agrformet.2005.07.012

Nguyen, K. A., Stewart, R. A., Zhang, H., Sahin, O., & Siriwardene, N. (2018). Re-engineering traditional urban water management practices with smart metering and informatics. *Environmental Modelling & Software*, 101, 256-267. doi:10.1016/j.envsoft.2017.12.015

Nie, N., Zhang, W., Chen, H., & Guo, H. (2018). A global hydrological drought index dataset based on gravity recovery and climate experiment (GRACE) data. *Water Resources Management*, 32(4), 1275-1290.

Nie, R. (2008). Study on the water utilization allocation of Shaanxi Pronvince of Yellow River. Master Dissertation of Northwest A&F University.PP74

Palazzo, J., Liu, O. R., Stillinger, T., Song, R., Wang, Y., Hiroyasu, E. H. T., Tague, C. (2017). Urban responses to restrictive conservation policy during drought. *Water Resources Research*, 53(5), 4459-4475. doi:10.1002/2016wr020136

Papa, F., Durand, F., Rossow, W. B., Rahman, A., & Bala, S. K. (2010). Satellite altimeter-derived monthly discharge of the Ganga-Brahmaputra River and its seasonal to interannual variations from 1993 to 2008. *Journal of Geophysical Research-Oceans*, 115(C12),1-19. doi:10.1029/2009jc006075

Parker, J. M., & Wilby, R. L. (2013). Quantifying household water demand: a review of theory and practice in the UK. *Water Resources Management*, 27(4), 981-1011.

doi:10.1007/s11269-012-0190-2

Paul, P. K., Kumari, B., Gaur, S., Mishra, A., Panigrahy, N., & Singh, R. (2020). Application of a newly developed large-scale conceptual hydrological model in simulating streamflow for credibility testing in data scarce condition. *Natural Resource Modeling*, 33(4),1-27. doi:10.1111/nrm.12283

Pavelsky, T. M., Durand, M. T., Andreadis, K. M., Beighley, R. E., Paiva, R. C. D., Allen, G. H., & Miller, Z. F. (2014). Assessing the potential global extent of SWOT river discharge observations. *Journal of Hydrology*, 519,1516-1525. doi:10.1016/j.jhydrol.2014.08.044

Pekel, J.-F., Cottam, A., Gorelick, N., & Belward, A. S. (2016). High-resolution mapping of global surface water and its long-term changes. *Nature*, 540(7633), 418-422.

Pellet, V., Aires, F., Papa, F., Munier, S., & Decharme, B. (2020). Long-term total water storage change from a Satellite Water Cycle reconstruction over large southern Asian basins. *Hydrology and Earth System Sciences*, 24(6), 3033-3055.

Pericli, A., & Jenkins, J. O. (2015). Review of current knowledge : smart meters and domestic water usage. *Foundation for Water Research*.PP60

Phillips, I. D., & McGregor, G. R. (1998). The utility of a drought index for assessing the drought hazard in Devon and Cornwall, South West England. *Meteorological Applications*, 5(4), 359-372.

Polli, B. A., da Nóbrega Cunha, C. D. L., de Almeida, R. C., & Gobbi, M. (2021). Evaluation of the impacts caused by wind field and freshwater flow variations due to climate change on the circulation of the Paranaguá Estuarine Complex, Brazil. *Regional Studies in Marine Science*, 47,1-13, 101933.

Pujol, L., Garambois, P.-A., Finaud-Guyot, P., Monnier, J., Larnier, K., Mose, R., Paris, A. (2020). Estimation of multiple inflows and effective channel by assimilation of multi-satellite hydraulic signatures: the ungauged anabranching Negro river. *Journal of Hydrology*, 591,1-24, 125331.

Ramillien, G., Biancale, R., Gratton, S., Vasseur, X., & Bourgogne, S. (2011). GRACE-derived surface water mass anomalies by energy integral approach: application to continental hydrology. *Journal of Geodesy*, 85(6), 313-328.

Ramillien, G., Frappart, F., Gratton, S., & Vasseur, X. (2015). Sequential estimation of surface water mass changes from daily satellite gravimetry data. *Journal of Geodesy*, 89(3), 259-282.

Ramillien, G., Seoane, L., Frappart, F., Biancale, R., Gratton, S., Vasseur, X., & Bourgogne, S. (2012). Constrained regional recovery of continental water mass time-variations from GRACE-based geopotential anomalies over South America. *Surveys in Geophysics*, 33(5), 887-905.

Robertson, J. C., Randrup, K. V., Howe, E. R., Case, M. J., & Levin, P. S. (2021). Leveraging

the potential of nature to meet net zero greenhouse gas emissions in Washington State. *The Journal of Life & Environmental Sciences*, 9, 1-25,e11802.

Rodell, M., Houser, P. R., Jambor, U., Gottschalck, J., Mitchell, K., Meng, C. J., Toll, D. (2004). The global land data assimilation system. *Bulletin of the American Meteorological Society*, 85(3), 381-394. doi:10.1175/bams-85-3-381

Royal Irrigation Department (RID). (2011). Work manual No.8/16: assessing water consumption by sectors. Available online: *http://irrigation.rid.go.th/rid10/om/Work%20Manual/manual-08*.pdf(accessed on 17 October 2012).

Royal Irrigation Department (RID). (2017). Work manual: 15-minute runoff predictions from rain radar of thai meteorological department. Bangkok, Thailand.

Rukonuzzaman, M., & Nakaoka, M. (2001, November). Single-phase shunt active power filter with adaptive neural network method for determining compensating current. In IECON'01. 27th Annual Conference of the IEEE Industrial Electronics Society (Vol. 3, pp. 2032-2037). IEEE.

Schaaf, C. B., Gao, F., Strahler, A. H., Lucht, W., Li, X., Tsang, T., Muller, J.-P. (2002). First operational BRDF, albedo nadir reflectance products from MODIS. *Remote Sensing of Environment*, 83(1-2), 135-148.

Shabanov, N. V., Knyazikhin, Y., Baret, F., & Myneni, R. B. (2000). Stochastic modeling of radiation regime in discontinuous vegetation canopies. *Remote Sensing of Environment,* 74(1), 125-144. doi: 10.1016/S0034-4257(00)00128-0

Sharmeela, C., Mohan, M. R., & Uma, G. (2003, October). Line harmonics reduction using neural based controller for shunt active filters. In TENCON 2003. Conference on Convergent Technologies for Asia-Pacific Region (Vol. 4, pp. 1554-1557). IEEE.

Shen, C., Wang, S., & Liu, X. (2016). Geomorphological significance of at-many-stations hydraulic geometry. *Geophysical Research Letters*, 43(8), 3762-3770.

Shi, L., He, Q. Q., Yang, J., et al. (2019). Downscaling modeling of the GPM IMERG precipitation product and comparative analysis in the Fujian-Zhejiang-Jiangxi region. *Journal of Geo-Information Science*, 21(10): 1642-1652.

Shiklomanov, I. (2000). World water resources and water use: present assessment and outlook for 2025 (supplemented by CD-ROM: Shiklomanov, I., World freshwater resources, available from: International Hydrological Programme, UNESCO, Paris). *World Water Scenarios: Analysing Global Water Resources and Use, Earthscan Publications, London.*

Shu, Y., Li, H., & Lei, Y. (2018). Modelling groundwater flow with MIKE SHE using conventional cimate data and satellite data as model forcing in Haihe Plain, China. *Water*, 10(10),1-19. doi:10.3390/w10101295

Shukla, S., & Wood, A. W. (2008). Use of a standardized runoff index for characterizing

hydrologic drought. *Geophysical Research Letters*, 35(2),1-7. doi:10.1029/2007gl032487

Singh, S. P., Singh, B., & Kumar, U. (2013). Water management strategies for achieving food security. Paper presented at the 4th International Conference on Environmental Science and Development (ICESD), *ScienceDirect APCBEE procedia*, 5, 423-428.

Smith, L. C., Isacks, B. L., Bloom, A. L., & Murray, A. B. (1996). Estimation of discharge from three braided rivers using synthetic aperture radar satellite imagery: potential application to ungaged basins. *Water Resources Research*, 32(7), 2021-2034. doi:10.1029/96wr00752

Smith, L. C., Isacks, B. L., Forster, R. R., Bloom, A. L., & Preuss, I. (1995). Estimation of discharge from braided glacial rivers using ers-1 synthetic-aperture radar - first results. *Water Resources Research*, 31(5), 1325-1329. doi:10.1029/95wr00145

Sonderlund, A. L., Smith, J. R., Hutton, C. J., Kapelan, Z., & Savic, D. (2016). Effectiveness of smart meter-based consumption feedback in curbing household water use: knowns and unknowns. *Journal of Water Resources Planning and Management*, 142(12),1-13. doi:10.1061/(asce)wr.1943-5452.0000703

Song, C., Ke, L., Pan, H., Zhan, S., Li, K., & Ma, R. (2018). Long-term surface water changes and driving cause in Xiong'an, China: from dense Landsat time series images and synthetic analysis. *Science Bulletin*, 63(11), 708-716. doi:10.1016/j.scib.2018.05.002

Song, P., Liu, Y., & Liu, Y. (2011). Advances in Satellite Retrieval of Terrestrial Surface Water Parameters. *Advance in Earth Sciences*, 26(7), 731-740.

Song, X. (2017). Study on production water footprint of main grain crops in the Yellow River Basin. North China Electric Power University(Beijing).

Song, Y. D., Wang, R. H., & Peng, Y. S. (2002). Water resources and ecological conditions in the Tarim Basin. *Science in China Series D-Earth Sciences*, 45, 11-17. doi:10.1007/bf02878383

Spinoni, J., Barbosa, P., De Jager, A., McCormick, N., Naumann, G., Vogt, J. V., Mazzeschi, M. (2019). A new global database of meteorological drought events from 1951 to 2016. *Journal of Hydrology-Regional Studies*, 22,1-24. doi:10.1016/j.ejrh.2019.100593

Stagge, J. H., Tallaksen, L. M., Gudmundsson, L., Van Loon, A. F., & Stahl, K. (2015). Candidate distributions for climatological drought indices (SPI and SPEI). *International Journal of Climatology*, 35(13), 4027-4040.

Syvitski, J. P., Morehead, M. D., Bahr, D. B., & Mulder, T. (2000). Estimating fluvial sediment transport: the rating parameters. *Water Resources Research*, 36(9), 2747-2760.

Tao, J. H., Yang, J., Ma, C. X., Li, J. F., Du, K. Q., Wei, Z., Deng, X. Y. (2020). Cellulose nanocrystals/graphene oxide composite for the adsorption and removal of levofloxacin hydrochloride antibiotic from aqueous solution. *Royal Society Open Science*, 7(10),1-24. doi:10.1098/rsos.200857

Tapley, B. D., Bettadpur, S., Watkins, M., & Reigber, C. (2004). The gravity recovery and climate experiment: mission overview and early results. *Geophysical Research Letters*, 31(9), 121-124. doi:10.1029/2004gl019920

Tarpanelli, A., Amarnath, G., Brocca, L., Massari, C., & Moramarco, T. (2017). Discharge estimation and forecasting by MODIS and altimetry data in Niger-Benue River. *Remote Sensing of Environment*, 195, 96-106.

Tarpanelli, A., Barbetta, S., Brocca, L., & Moramarco, T. (2013a). River discharge estimation by using altimetry data and simplified flood routing modeling. *Remote Sensing*, 5(9), 4145-4162.

Tarpanelli, A., Brocca, L., Barbetta, S., Faruolo, M., Lacava, T., & Moramarco, T. (2015). Coupling MODIS and radar altimetry data for discharge estimation in poorly gauged river basins. *IEEE Journal of Selected Topics in Applied Earth Observations and Remote Sensing*, 8(1), 141-148.

Tarpanelli, A., Brocca, L., Lacava, T., Melone, F., Moramarco, T., Faruolo, M., Tramutoli, V. (2013b). Toward the estimation of river discharge variations using MODIS data in ungauged basins. *Remote Sensing of Environment*, 136, 47-55. doi:10.1016/j.rse.2013.04.010

Tarpanelli, A., Santi, E., Tourian, M. J., Filippucci, P., Amarnath, G., & Brocca, L. (2018). Daily river discharge estimates by merging satellite optical sensors and radar altimetry through artificial neural network. *Ieee Transactions on Geoscience and Remote Sensing*, 57(1), 329-341.

Tate, J. (2000). Water supply in the UK: towards a more sustainable future? *Sustainable Development*, 8(3), 155-164.

Tayfur, G. (2021). Discrepancy precipitation index for monitoring meteorological drought. *Journal of Hydrology*, 597,1-12. doi:10.1016/j.jhydrol.2021.126174

Torres, R., Snoeij, P., Geudtner, D., Bibby, D., Davidson, M., Attema, E., Rostan, F. (2012). GMES Sentinel-1 mission. *Remote Sensing of Environment*, 120, 9-24. doi:10.1016/j.rse.2011.05.028

Trenberth, K. E., Dai, A., Van Der Schrier, G., Jones, P. D., Barichivich, J., Briffa, K. R., & Sheffield, J. (2014). Global warming and changes in drought. *Nature Climate Change*, 4(1), 17-22.

Twine, T. E., Kustas, W., Norman, J., Cook, D., Houser, P., Meyers, T., Wesely, M. (2000). Correcting eddy-covariance flux underestimates over a grassland. *Agricultural and Forest Meteorology*, 103(3), 279-300.

Valkering, K. P., van den Bekerom, M. P. J., Kappelhoff, F. M., & Albers, G. H. R. (2009). Complications after tomofix medial opening wedge high tibial osteotomy. *The journal of knee surgery*, 22(3), 218-225.

Vicente-Serrano, S. M., Lopez-Moreno, J. I., Begueria, S., Lorenzo-Lacruz, J., Azorin-Molina,

C., & Moran-Tejeda, E. (2012). Accurate computation of a streamflow drought index. *Journal of Hydrologic Engineering*, 17(2), 318-332. doi:10.1061/(asce)he.1943-5584.0000433

Vishwakarma, B. D., Zhang, J., & Sneeuw, N. (2021). Downscaling GRACE total water storage change using partial least squares regression. *Scientific data*, 8(1), 1-13.

Vorosmarty, C. J., Willmott, C. J., Choudhury, B. J., Schloss, A. L., Stearns, T. K., Robeson, S. M., & Dorman, T. J. (1996). Analyzing the discharge regime of a large tropical river through remote sensing, ground-based climatic data, and modeling. *Water Resources Research*, 32(10), 3137-3150. doi:10.1029/96wr01333

Wahr, J., Swenson, S., Zlotnicki, V., & Velicogna, I. (2004). Time-variable gravity from GRACE: first results. *Geophysical Research Letters*, 31(11),1-4. doi:10.1029/2004gl019779

Wang, L., Zuo, Z., & Fu, J. (2014). Bus arrival time prediction using RBF neural networks adjusted by online data. *Procedia-Social and Behavioral Sciences,* 138, 67-75.

Wang, S. Y., Ding, C. B., & Liu, J. S. (2009). Landscape evolution in the Yellow River Basin using satellite remote sensing and GIS during the past decade. *International Journal of Remote Sensing*, 30(21), 5573-5591. doi:10.1080/01431160802687482

Wang, W., Shao, Q., Peng, S., Xing, W., Yang, T., Luo, Y., Xu, J. (2012). Reference evapotranspiration change and the causes across the Yellow River basin during 1957-2008 and their spatial and seasonal differences. *Water Resources Research*, 48(5),1-27. doi:10.1029/2011wr010724

Wang, X., Luo, Y., Zhang, Q., Cai, P., & Zhang, M. (2017). Construction of mean air temperature datasets with high temporal and spatial resolution in oasis-desert region: A case study of Sangong River basin on the northern slope of Tianshan Mountains. *Geographical Research*, 036(1), 49-60.

Wang, Y. Y., Long, A. H., Xiang, L. Y., Deng, X. Y., Pei, Z., Yang, H., Yang, L. (2020). The verification of Jevons' paradox of agricultural Water conservation in Tianshan District of China based on Water footprint. *Agricultural Water Management*, 239,1-12. doi:10.1016/j.agwat.2020.106163

Wang, Y., Xiao, H. L., & Lu, M. F. (2009). Analysis of water consumption using a regional input-output model: model development and application to Zhangye City, Northwestern China. *Journal of Arid Environments*, 73(10), 894-900. doi:10.1016/j.jaridenv.2009.04.005

Wikipedia, (2021a). Projections of population growth. *https://en.wikipedia.org/wiki/Projections_of_population_growth*. Accessed by 15/07/2021.

Wikipedia, (2021b). Water footprint. *https://en.wikipedia.org/wiki/Water_footprint*. Accessed by 20/07/2021.

Williamson, P., Mitchell, G., & McDonald, A. T. (2002). Domestic water demand forecasting: a static microsimulation approach. *Journal of the Chartered Institution of Water and Environmental Management*, 16(4), 243-248.

Willis, R. M., Stewart, R. A., Panuwatwanich, K., Williams, P. R., & Hollingsworth, A. L. (2011). Quantifying the influence of environmental and water conservation attitudes on household end use water consumption. *Journal of Environmental Management*, 92(8), 1996-2009. doi:10.1016/j.jenvman.2011.03.023

Wu, H., & Li, Z.-L. (2009). Scale Issues in Remote Sensing: a Review on Analysis, Processing and Modeling. *Sensors*, 9(3), 1768-1793. doi:10.3390/s90301768

Wu, J., Chen, X., Love, C. A., Yao, H., Chen, X., & AghaKouchak, A. (2020). Determination of water required to recover from hydrological drought: perspective from drought propagation and non-standardized indices. *Journal of Hydrology*, 590,1-33. doi:10.1016/j.jhydrol.2020.125227

Wu, R., Liu, Y., & Xing, X. (2021). Evaluation of evapotranspiration deficit index for agricultural drought monitoring in North China. *Journal of Hydrology*, 596,1-16. doi:10.1016/j.jhydrol.2021.126057

Xie, J., Xu, Y. P., Wang, Y., Gu, H., Wang, F., & Pan, S. (2019). Influences of climatic variability and human activities on terrestrial water storage variations across the Yellow River basin in the recent decade. *Journal of Hydrology*, 579,1-15, 124218.

Xing, Z., Wang, Y., Gong, X., Wu, J., Ji, Y., & Fu, Q. (2018). Calculation of Comprehensive Ecological Flow with Weighted Multiple Methods Considering Hydrological Alteration. *Water*, 10(9),1-17.

Xu, J., Chen, Y., Li, W., & Dong, S. (2008). Long-term trend and fractal of annual runoff process in mainstream of Tarim River. *Chinese Geographical Science*, 18(1), 77-84. doi:10.1007/s11769-008-0077-6

Xu, K. Q., Zhang, J. Q., Watanabe, M., & Sun, C. P. (2004). Estimating river discharge from very high-resolution satellite data: a case study in the Yangtze River, China. *Hydrological Processes*, 18(10), 1927-1939. doi:10.1002/hyp.1458

Yan, J. J., Zhang, G. P., Deng, X. Y., Ling, H. B., Xu, H. L., & Guo, B. (2019). Does climate change or human activity lead to the degradation in the grassland ecosystem in a mountain-basin system in an arid region of China? *Sustainability*, 11(9),1-15. doi:10.3390/su11092618

Yan, K., Park, T., Yan, G. J., Chen, C., Yang, B., Liu, Z., Myneni, R. B. (2016). Evaluation of MODIS LAI/FPAR product collection 6. Part 1: consistency and improvements. *Remote Sensing*, 8(5),1-16. doi:10.3390/rs8050359

Yang, F., Xia, Z., Yu, L., & Guo, L. (2012). Calculation and analysis of the instream ecological flow for the Irtysh River. In B. Zhou (Ed.), 2012 International Conference on Modern Hydraulic Engineering (Vol. 28, pp. 438-441).

Yang, J., & Du, X. (2017). An enhanced water index in extracting water bodies from Landsat TM imagery. *Annals of GIS*, 23(3), 141-148. doi:10.1080/19475683.2017.1340339

Yang, W. Z., Huang, D., Tan, B., Stroeve, J. C., Shabanov, N. V., Knyazikhin, Y., Myneni, R. B. (2006b). Analysis of leaf area index and fraction of PAR absorbed by vegetation products from the terra MODIS sensor: 2000-2005. *Ieee Transactions on Geoscience and Remote Sensing*, 44(7), 1829-1842. doi:10.1109/Tgrs.2006.871214

Yang, W. Z., Tan, B., Huang, D., Rautiainen, M., Shabanov, N. V., Wang, Y., Myneni, R. B. (2006a). MODIS leaf area index products: from validation to algorithm improvement. *Ieee Transactions on Geoscience and Remote Sensing*, 44(7), 1885-1898. doi:10.1109/Tgrs.2006.871215

Yang, W., Shabanov, N. V., Huang, D., Wang, W., Dickinson, R. E., Nemani, R. R., Myneni, R. B. (2006c). Analysis of leaf area index products from combination of MODIS Terra and Aqua data. *Remote Sensing of Environment*, 104(3), 297-312. doi:10.1016/j.rse.2006.04.016

Yao, C.L. (2017). Natural- and human-induced impacts on regional terrestrial water storage changes from GRACE and hydro-meteorological data. *Ph. D Dissertation of Wuhan University*.PP144

Yao, H. B., Ge, J., Wang, C. F., Wang, X., Hu, W., Zheng, Z. J., Yu, S. H. (2013). A flexible and highly pressure-sensitive graphene–polyurethane sponge based on fractured microstructure design. *Advanced Materials*, 25(46), 6692-6698.

Yao, Y., Liang, S., Li, X., Hong, Y., Fisher, J. B., Zhang, N., Feng, F. (2014). Bayesian multimodel estimation of global terrestrial latent heat flux from eddy covariance, meteorological, and satellite observations. *Journal of Geophysical Research-Atmospheres*, 119(8), 4521-4545. doi:10.1002/2013jd020864

Yao, Y., Liang, S., Qin, Q., & Wang, K. (2010). Monitoring drought over the conterminous United States using MODIS and NCEP Reanalysis-2 data. *Journal of Applied Meteorology and Climatology*, 49(8), 1665-1680. doi:10.1175/2010jamc2328.1

Yi, S., Jun, C.-P., Jo, K.-n., Lee, H., Kim, M.-S., Lee, S. D., Lim, J. (2020). Asynchronous multi-decadal time-scale series of biotic and abiotic responses to precipitation during the last 1300 years. *Scientific Reports*, 10(1),1-10. doi:10.1038/s41598-020-74994-x

Yin, W., Hu, L., Zheng, W., Jiao, J. J., Han, S.-C., & Zhang, M. (2020). Assessing underground water exchange between regions using GRACE data. *Journal of Geophysical Research-Atmospheres*, 125(17),1-42. doi:10.1029/2020jd032570

Yu W, Li X, Gonzalez J (2019a). Fast training of deep LSTM networks. Paper presented at the 16th International Symposium on Neural Networks. *Springer*, 3-10.

Yu, Y., Si, X., Hu, C., & Zhang, J. (2019b). A review of recurrent Neural Networks: LSTM Cells and network architectures. *Neural Computation*, 31(7), 1235-1270. doi:10.1162/neco_a_01199

Yuan, X.-C., Wei, Y.-M., Pan, S.-Y., & Jin, J.-L. (2014). Urban household water demand in Beijing by 2020: an Agent-Based Model. *Water Resources Management*, 28(10), 2967-2980. doi:10.1007/s11269-014-0649-4

Zaidman, M. D., Rees, H. G., & Young, A. R. (2002). Spatio-temporal development of streamflow droughts in northwest Europe. *Hydrology and Earth System Sciences*, 6(4), 733-751. doi:10.5194/hess-6-733-2002

Zhang, C., Yang, S., Zhao, C., Lou, H., Zhang, Y., Bai, J., Zhang, Y. (2018). Topographic data accuracy verification of small consumer UAV. *Journal of Remote Sensing*, 22(1), 185-195.

Zhang, G. H., Feng, G., Li, X. H., Xie, C. B., & Pi, X. Y. (2017). Flood effect on groundwater recharge on a typical Silt Loam Soil. *Water*, 9(7), 1-15. doi:10.3390/w9070523

Zhang, J., Xu, K., Kamey ama, S., Watanabe, M., Chen, X., & Sun, C. (2004). Estimation of river discharge using TOPEX/Poseidon altimeter data. *Acta Geographica Sinica*, 59(1), 95-100.

Zhang, P., Deng, X. Y., Long, A. H., Xu, H. L., Ye, M., & Li, J. F. (2019). Change in spatial distribution patterns and regeneration of Populus euphratica under different surface Soil Salinity conditions. *Scientific Reports*, 9(1),1-12. doi:10.1038/s41598-019-42306-7

Zhang, Y. (2003). Research on the ecological and environmental water requirementsof the highland and river channel in the Yellow River Basin. Beijing: Beijing Normal University Institute of Environmental Science, 1-200.

Zhang, Y. S., Lu, X., Liu, B. Y., Wu, D. T., Fu, G., Zhao, Y. T., & Sun, P. L. (2021). Spatial relationships between ecosystem services and socioecological drivers across a large-scale region: a case study in the Yellow River Basin. *Science of the Total Environment*, 766,1-16. doi:ARTN 14248010.1016/j.scitotenv.2020.142480

Zhang, Y., & Yang, Z. (2002). Minimum ecological water requirement of forestland in Huang-Huai-Hai area. *Journal of Soil and Water Conservation*, 16(2), 72-75.

Zhang, Y., Zheng, H., Fath, B. D., Liu, H., Yang, Z., Liu, G., & Su, M. (2014). Ecological network analysis of an urban metabolic system based on input-output tables: model development and case study for Beijing. *Science of the Total Environment*, 468, 642-653. doi:10.1016/j.scitotenv.2013.08.047

Zhang, Z., Liu, H., Zuo, Q., Yu, J., & Li, Y. (2021). Spatiotemporal change of fractional vegetation cover in the Yellow River Basin during 2000-2019. *Resources Science*, 43(4), 849-858.

Zhao, C. S., Zhang, C. B., Yang, S. T., Liu, C. M., Xiang, H., Sun, Y., Yu, Q. (2017). Calculating e-flow using UAV and ground monitoring. *Journal of Hydrology*, 552, 351-365. doi:10.1016/j.jhydrol.2017.06.047

Zhao, C., Pan, T., Dou, T., Liu, J., Liu, C., Ge, Y., Lim, R. (2019). Making global river

ecosystem health assessments objective, quantitative and comparable. *Science of the Total Environment*, 667,500-510.

Zhao, X., Liang, S. L., Liu, S. H., Yuan, W. P., Xiao, Z. Q., Liu, Q., Yu, K. (2013). The Global Land Surface Satellite (GLASS) remote sensing data processing system and products. *Remote Sensing*, 5(5), 2436-2450. doi:10.3390/rs5052436

Zheng, X., Huang, G., Li, J., Liu, L., Zhang, X., & Pan, X. (2021). Development of a factorial water policy simulation approach from production and consumption perspectives. *Water Research*, 193,1-17. doi:10.1016/j.watres.2021.116892

Zhong, J., & Wang, R. (2006). Multi-temporal remote sensing change detection based on independent component analysis. *International Journal of Remote Sensing*, 27(9-10), 2055-2061. doi:10.1080/01431160500444756

Zhou, H., Zhang, X., Xu, H., Ling, H., & Yu, P. (2012). Influences of climate change and human activities on Tarim River runoffs in China over the past half century. *Environmental Earth Sciences*, 67(1), 231-241. doi:10.1007/s12665-011-1502-1

Zhou, K. (2020). Droughtassessment and prediction in the Yellow River Basin. *Dissertation of Xi'an University of Technology*.PP79

Zhou, S., Wang, J., Xu, Z., Sun, Y., & Wang, T. (2015). Analysis and assessment on performance of Yellow River Water quantity allocation scheme in Shandong Province. *Yellow River*, 37(4), 66-68.

Zhu, Y. (2019). Remote sensing estimation of vegetation net primary productivity and its response to climate change in the Yellow River Basin from 1992 to 2015. *Dissertation of Changan University*.PP70

Zhu, Y., Zhang, J., Zhang, Y., Qin, S., Shao, Y., & Gao, Y. (2019). Responses of vegetation to climatic variations in the desert region of northern China. *Catena*, 175, 27-36. doi:10.1016/j.catena.2018.12.007.

Publications

[1] **Zhao, C. S**., Pan, T. L., Xia, J., Yang, S. T., Zhao, J., Gan, X. J., & Ding, S. Y. (2019). Streamflow calculation for medium-to-small rivers in data scarce inland areas. *Science of The Total Environment*, 693, 133571.

[2] **Zhao, C.S**., Shao, N.F., Yang, S.T., Xiang, H., Lou, H.Z., Sun, Y., Yang, Z.Y., Zhang, Y., Yu, X.Y., Zhang, C.B., & Yu, Q. (2018). Identifying the principal driving factors of water ecosystem dependence and the corresponding indicator species in a Pilot City, China. *Journal of Hydrology*, 556 :488–499.

[3**] Zhao, C.,** Pan, T., Dou, T., Liu, J., Liu, C., Ge, Y., Zhang, Y., Yu, X., Mitrovic, S. and Lim, R. (2019). Making global river ecosystem health assessments objective, quantitative and comparable. *Science of The Total Environment*. 667: 500-510.

[4] **Zhao, C.S**., Yang, Y., Yang, S.T., Xiang, H., Wang, F., Chen, X., Zhang, H.M. and Yu, Q. (2019). Impact of spatial variations in water quality and hydrological factors on the food-web structure in urban aquatic environments. *Water Research*. 153: 121-133.

[5] **Zhao, C.S**., Shao, N.F., Yang, S.T., Ren, H., Ge, Y.R., Zhang, Z.S., Feng, P. and Liu, W.L. (2019). Quantitative assessment of the effects of human activities on phytoplankton communities in lakes and reservoirs. *Science of The Total Environment*. 665: 213-225.

[6] Yang, S., Guan, Y., **Zhao, C.***, Zhang, C., Bai, J., & Chen, K. (2019). Determining the influence of catchment area on intensity of gully erosion using high-resolution aerial imagery: A 40-year case study from the Loess Plateau, northern China. *Geoderma*, *347*, 90-102.

[7] **Zhao, C.S.**, Shao, N.F., Yang, S.T., Ren, H., Ge, Y.R., Feng, P., Dong, B.E. and Zhao, Y. (2019). Predicting cyanobacteria bloom occurrence in lakes and reservoirs before blooms occur. *Science of The Total Environment*. 670: 837-848.

[8] **Zhao, C**.S., Yang, Y., Yang, S.T., Xiang, H., Zhang, Y., Wang, Z.Y., Chen, X. and Mitrovic, S.M. (2019). Predicting future river health in a minimally influenced mountainous area under climate change. *Science of The Total Environment*. 656: 1373-1385.